



THE UNIVERSITY OF QUEENSLAND
AUSTRALIA

**Alternative methods for geomechanical characterisation of sub-bituminous coal,
Surat Basin, Australia**

Karina Jorge Barbosa
BEng(Min), MSc(Geotch)

*A thesis submitted for the degree of Doctor of Philosophy at
The University of Queensland in 2019
School of Earth and Environmental Sciences*

Abstract

This thesis examines alternative methods for testing the geomechanical behaviour of subbituminous coal that is a target for coal seam gas extraction as well as mining in the Surat Clarence-Moreton basins in eastern Australia. Although the coal seams can vary from <1 m and >10 m, the coal is thin bedded and interbedded with mudstones and tuffaceous claystones that contribute to its strength anisotropy both in compression and tension. Uniaxial Compressive Strength tests are commonly conducted on standard size core and scaled to the rock mass for predicting borehole stability, whereas indirect tensile strength tests are needed to model response to fracture stimulation. For prediction of rock behaviour, the critical parameters for fracture initiation and propagation might be hardness or fracture toughness, and these properties are not commonly available or are derived from empirical correlation to compressive strength results. Because coal is an inherently fractured rock, smaller specimens might be required to test a truly intact material.

The approach of this thesis was to go back to the basics to understand the rock material as an intact specimen. This study showed that alternative laboratory tests to derive rock parameters such as Uniaxial Compressive Strength on mini-cylinder specimens, fracture toughness and tensile strength using Short Impact Load Cell on mini-core specimens and chips/irregular-particles, and hardness testing using a Shore Scleroscope provide reliable geomechanical information obtained at the scale of interest. The experimental work was performed and evaluated using a certain number of specimens to obtain statistical sets and/or controlled specimens to draw correlations between data available on the literature, when possible. Tests were conducted on different coal lithotypes and stone to capture the heterogeneity based on composition. Tests were also conducted on fabricated 3D-printed sandstone to investigate the validity of calculations and performance of the different shape, size, and fabric orientation free from the natural variability of the material. These tests provided a valuable contribution for low rank, sub-bituminous coals; moreover, the same approach can be extended to other coal ranks and rock material.

A relationship between coal specimen size and its uniaxial compressive strength was verified for mini-cylinder specimens. The intact coal strength for the mini-cylinder specimens was upscaled to larger sizes and to the rock mass, with resulting properties comparable to coal data tested on other ranks available in the literature. In each of the short impact load cell tests, size and shape was varied and used to inform the upscaling. Despite the short impact load cell results being affected by the varying sizes, shapes, and fabric orientation of the specimens, it is a promising test to obtain the tensile strength and fracture toughness of shape-controlled specimens, as well as to observe their failure characteristics. Specific fracture energy estimated from short impact load cell utilizing heterogeneous rock of irregular-particles or shaped specimens can be correlated

to fracture toughness, whereas for homogeneous 3D-printed sandstone, the specific fracture energy can be widely different for specimens of distinct shape. For the short impact load cell tests, ultra-high speed camera was used to capture fracture initiation and propagation. Last, because fracture propagation might find a pathway through the matrix and natural fractures of coal, microscopical observation was used to understand the brittle-ductile behaviour of sub-bituminous coal organic components (macerals and microlithotypes) and inorganic components (in particular clay minerals that were often much softer than the coal).

Overall, the investigations provided confidence in the geomechanical properties derived and failure criterion for coal and interbedded rock material utilizing non-conventional experiments and provide alternatives that can be used in the coal seam gas and mining industries. For both industries, the rock characterisation requires a site-specific investigation to develop a realistic representation for numerical modelling simulations. This thesis shows that small scale specimens can be used, and tests for deformation in tension, such as SILC, and simple indentation tests can capture the brittle and ductile characteristics of sub-bituminous coal for engineering behaviour. Together these data can inform future numerical models of rock mass behaviour during drilling and reservoir stimulation for gas extraction.

Declaration by author

This thesis *is composed of my original work, and contains* no material previously published or written by another person except where due reference has been made in the text. I have clearly stated the contribution by others to jointly-authored works that I have included in my thesis.

I have clearly stated the contribution of others to my thesis as a whole, including statistical assistance, survey design, data analysis, significant technical procedures, professional editorial advice, financial support and any other original research work used or reported in my thesis. The content of my thesis is the result of work I have carried out since the commencement of my higher degree by research candidature and does not include a substantial part of work that has been submitted *to qualify for the award of any* other degree or diploma in any university or other tertiary institution. I have clearly stated which parts of my thesis, if any, have been submitted to qualify for another award.

I acknowledge that an electronic copy of my thesis must be lodged with the University Library and, subject to the policy and procedures of The University of Queensland, the thesis be made available for research and study in accordance with the Copyright Act 1968 unless a period of embargo has been approved by the Dean of the Graduate School.

I acknowledge that copyright of all material contained in my thesis resides with the copyright holder(s) of that material. Where appropriate I have obtained copyright permission from the copyright holder to reproduce material in this thesis and have sought permission from co-authors for any jointly authored works included in the thesis.

Publications included in this thesis

Peer-reviewed journal paper

BARBOSA, K., ESTERLE, J., RUEST, M., 2016. A workflow to build a model investigating coal cleat upscaling conditioned by the lithotype. The Australian Petroleum Production and Exploration Association (APPEA) Journal - Brisbane, Australia, 56, 331-340.

- Partially incorporated as Chapter 2.

BARBOSA, K., CHALATURNYK, R., BONFILS, B., ESTERLE, J., and CHEN, Z., 2019 Testing impact load cell calculations of material fracture toughness and strength using 3D-printed sandstone. Geotechnical and Geological Engineering, 1-32 <https://doi.org/10.1007/s10706-019-01073-y>

- incorporated as Chapter 4.

BARBOSA, K., ESTERLE, J., BONFILS, B., and CHEN, Z., 2019. The use of short impact load cell to derive geomechanical properties of sub-bituminous coal and mudstone. Journal of Natural Gas Science and Engineering. 72, 103-118 <https://doi.org/10.1016/j.jngse.2019.103018>

- incorporated as Chapter 5.

-

BARBOSA, K., ESTERLE, J., WETERING, N.V.D., and CHEN, Z., Shore hardness measurements of sub-bituminous coal by microlithotypes. Manuscript accepted for publication at the International Journal of Coal Geology.

- incorporated as Chapter 6.

Submitted manuscripts included in this thesis

BARBOSA, K., ESTERLE, J., and CHEN, Z., Scaling compressive strength from mini-cylinder specimens of sub-bituminous coal. Submitted manuscript is under review at the Rock Mechanics and Rock Engineering.
- incorporated as Chapter 3.

Other publications during candidature

No other publications.

Contributions by others to the thesis

Prof. Joan Esterle (principal supervisor) advised, commented and edited the submitted manuscripts as well as the draft versions of this thesis. Professor Esterle obtained funding from UQ Centre for Coal Seam Gas (CCSG) and its industry members: APLNG, Arrow Energy, Santos (2011 – 2021), and Shell/QGC (2011 – 2017) for financial support of PhD scholarship (UQ Project number: 017851; RM number: 2015000765), and the KOGAS (UQ Project number 019465; RM number: 2016001957).

Dr Zhongwei Chen (associate supervisor) advised, commented and edited the submitted manuscripts as well as the draft versions of this thesis.

Prof. Rick Chalaturnyk proposed the experiment using 3D-printed sandstone and supported the fabrication of 3D-printed specimens, reviewed, discussed and edited the manuscript incorporated in Chapter 4.

Dr Benjamin Bonfils provided the training on the short impact load cell, advised on the analyses of results, reviewed, discussed and edited the manuscripts incorporated in Chapter 4 and Chapter 5.

Ms Nikola Van De Wetering assisted with the microlithotype identification, reviewed, discussed and edited the manuscripts incorporated in Chapter 6.

In addition to my co-authors (outlined above), the following people have contributed to this thesis:

- ❖ Dr Kevin Hodder from the University of Alberta, in Canada, fabricated all 3D-printed sandstone specimens tested for uniaxial compressive strength and short impact load cell in Chapter 4 of this thesis.
- ❖ Mr Davide Pistellato recorded the videos with the ultra-high-speed camera utilized in Chapter 4 of this thesis.
- ❖ Dr Sandra Rodrigues and Ms Nikola Van De Wetering assisted with petrographic analyses and microlithotype identification in Chapter 3 and Chapter 6 of this thesis.
- ❖ Dr Helen Schultz and Ms Suzi Moore provided valuable assistance on proof-reading all the submitted manuscripts incorporated in this thesis.
- ❖ Anonymous reviewers of the manuscripts for their constructive comments.

Statement of parts of the thesis submitted to qualify for the award of another degree

None.

Research Involving Human or Animal Subjects

No animal or human subjects were involved in this research.

Acknowledgements

First of all, I would like to thank and express my deep appreciation to my supervisors, Prof. Joan Esterle and Dr Zhongwei Chen, for their guidance, technical contributions, and suggestions throughout this work. Also, thanks are extended to Dr Benjamin Bonfils for his invaluable assistance and motivation and Prof. Rick Chalaturnyk for his open mind and technical advice.

I also recognize the relevance of key people that assist me during this journey and wish to express my gratitude to: Dr Marc Ruest for his initial support on this research; Dr Christopher Leonardi and Dr Dion Weatherley for their helpful discussions and constructive criticism; Dr Kevin Hodder for the fabrication of all 3D-printed sandstone specimens; Dr Sandra Rodrigues and Ms Nikola Van De Wetering for assisting with the petrographic analysis and microlithotypes; Mr Davide Pistellato for recording the videos with the ultra-high speed camera; Dr Helen Schultz and Ms Suzi Moore for their precious time and effort to assist on proof-reading.

I would like to express thanks to the UQ Centre for Coal Seam Gas (CCSG) and its industry members: APLNG, Arrow Energy, Santos, and Shell/QGC, as well as the KOGAS for their financial support on this project. An acknowledgement is extended to The University of Queensland and the School of Earth and Environmental Sciences for creating the opportunity for me to pursue my studies, as well as the School of Mechanical and Mining Engineering, and the Advanced Engineering Building for their laboratory facilities and resources. Additionally, I must thank the mining company New Hope mine for providing the coal and mudstone samples utilized in this research. Also, thanks for The UQ Julius Kruttschnitt Minerals Research Centre (JKMRC) for providing resources to conduct laboratory tests on SILC.

My colleagues and friends at The University of Queensland and PhD peers are thanked for their on-going encouragement, motivation, and persistence. They all gave me the strength that I needed. Because research is about digging out the unknown, explore the creativity, and taking short steps into a long walk.

Finally, I would like to thank my beautiful and lovely family for their support, particularly my mother for her strong believe in education and learning. A most special thank you to my gorgeous daughter for my everyday laugh and bright. Mum is so proud of you, 'Clarinha'.

Financial support

This research was financially supported by the UQ Centre for Coal Seam Gas (CCSG) and its industry members: APLNG, Arrow Energy, Santos (2011 – 2021), and Shell/QGC (2011 – 2017) (UQ Project number: 017851; RM number: 2015000765). The KOGAS (UQ Project number 019465; RM number: 2016001957) also provided funding assistance.

Keywords

geomechanical, low rank coal, short impact load cell, 3D-printed rock, strength, specific fracture energy, hardness, microlithotype

Australian and New Zealand Standard Research Classifications (ANZSRC)

ANZSRC code: 091402 Geomechanics and Resources Geotechnical Engineering, 50%

ANZSRC code: 091405 Mining Engineering, 25%

ANZSRC code: 091406 Petroleum and Reservoir Engineering, 25%

Fields of Research (FoR) Classification

FoR code: 0403, Geology, 25%

FoR code: 0912, Materials Engineering, 25%

FoR code: 0914, Resources Engineering and Extractive Metallurgy, 50%

*To inspiring woman's Evania, Adriana and
my daughter Clara Gabriela my forever love, soul and rock.*

TABLE OF CONTENTS

TABLE OF CONTENTS	XII
LIST OF FIGURES.....	XV
LIST OF TABLES.....	21
LIST OF SYMBOLS AND ABBREVIATIONS.....	22
CHAPTER 1: INTRODUCTION	
1.1 COAL SEAM GAS	23
1.2 RESEARCH CHALLENGE: CSG IN THE SURAT BASIN – LOW RANK COAL.....	26
1.3 HYPOTHESIS	27
1.4 AIMS AND OBJECTIVES OF THE RESEARCH.....	27
1.5 FORMAT OF THE THESIS	28
CHAPTER 2: BACK TO THE BASICS TO UNDERSTAND COAL	
2.1 INTRODUCTION.....	30
2.2 COAL CHARACTER	31
2.2.1 Uniqueness of coal	31
2.3 BASIN CHARACTERISTICS	35
2.3.1 Geological characterization of Surat Basin	35
2.4 RESERVOIR CHARACTERISTICS.....	37
2.4.1 Gas and production in Surat Basin	37
2.4.2 Coal mining: lessons learned.....	38
2.4.3 Reservoir modelling.....	40
2.5 EXPERIMENTAL CHARACTERISATION OF COAL MECHANICAL PROPERTIES.....	41
2.5.1 Uniaxial Compression Strength.....	43
2.5.2 Short Impact Load Cell	43
2.5.3 Shore Scleroscope Rebound Hardness	45
2.6 SUMMARY	46
CHAPTER 3: MINI-CORE SPECIMENS SCALED	
3.1 INTRODUCTION.....	49
3.2 BACKGROUND	53
3.3 RESEARCH METHODOLOGY	54
3.3.1 Sample collection	54
3.3.2 Specimen preparation.....	55
3.3.3 Uniaxial compression test equipment.....	57
3.3.4 Coal characterisation	58

3.4	EXPERIMENTAL RESULTS AND DISCUSSION.....	59
3.4.1	Failure mode.....	59
3.4.2	Results of strength and Young’s modulus by ply.....	59
3.4.3	Mini-cylinder specimen strength by quality.....	63
3.4.4	Coal mass strength from mini-cylinder specimen.....	65
3.4.5	Mini-cylinder specimen UCS values by maceral subgroup.....	69
3.5	CONCLUSIONS AND RECOMMENDATIONS.....	73

CHAPTER 4: 3D-PRINTED SANDSTONE

4.1	INTRODUCTION.....	77
4.2	BACKGROUND.....	79
4.3	3D-PRINTED SANDSTONE SPECIMENS.....	79
4.4	SPECIFICATION OF SILC TESTING SPECIMENS.....	81
4.5	SHORT IMPACT LOAD CELL APPARATUS AND TESTING.....	84
4.6	SILC CALCULATION METHODOLOGY.....	87
4.6.1	Determination of cross-sectional areas at contact bodies.....	87
4.6.2	Determination of fracture force.....	90
4.6.3	Determination of fracture energy for different settings/conditions.....	91
4.6.4	Estimation of specific fracture energy.....	94
4.6.5	Estimation of ‘apparent’ stiffness or Young’s modulus.....	94
4.6.6	Estimation of the tensile strength.....	94
4.6.7	Estimation of the compressive strength.....	95
4.7	UCS APPARATUS AND TESTING.....	96
4.8	RESULTS OF UCS TESTING.....	97
4.9	RESULTS OF SILC TESTING.....	100
4.9.1	Fracture mechanism.....	100
4.9.2	Typical force-time profile.....	104
4.9.3	Analysis of SILC results.....	106
4.9.4	Interpretation of mechanical properties from SILC tests.....	110
4.9.5	Assessment of compressive strength from SILC tests.....	114
4.10	CONCLUSIONS AND RECOMMENDATIONS.....	116

CHAPTER 5: SILC ON COAL AND MUDSTONE

5.1	INTRODUCTION.....	120
5.2	SHORT IMPACT LOAD CELL TEST SETTINGS AND OUTPUT.....	122
5.3	SAMPLING.....	123
5.3.1	Sample collection.....	123
5.3.2	Specimen preparation.....	123
5.4	SILC FAILURE MODE.....	127
5.4.1	Coal.....	127
5.4.2	Mudstone.....	129

5.5	DATA PROCESSING METHODS	130
5.6	SILC RESULTS ON MINI-CORE SPECIMENS OF COAL	132
5.6.1	Influence of drop mass and height combinations on mini-core specimens of coal	133
5.6.2	Aspect ratio effect on mini-core specimens of coal	134
5.6.3	Lithotype effect on mini-core specimens of coal	136
5.6.4	Orientation of bands relative to impact loading on mini-core specimens of coal	139
5.7	SILC RESULTS ON IRREGULAR-PARTICLES OF COAL AND MUDSTONE.....	141
5.7.1	Size and lithology/lithotype effect on irregular-particles of coal and mudstone.....	142
5.8	COMPARISON OF IRREGULAR PARTICLES AND MINI-CORE SPECIMENS ON COAL.....	144
5.9	CONCLUSIONS AND RECOMMENDATIONS	148

CHAPTER 6: LITHOTYPES AND MICROLITHOTYPES MATTER

6.1	INTRODUCTION.....	152
6.2	RESEARCH METHODOLOGY	153
6.2.1	Hardness testing	153
6.2.2	Sample collection	154
6.2.3	Specimen preparation.....	155
6.2.4	Hardness testing procedure	155
6.2.5	Microscopic analysis	156
6.3	RESULTS AND DISCUSSION.....	157
6.3.1	Correlation between hardness and microlithotype for specimens from the open cut mine.....	157
6.3.2	SH behaviour of vitrite for specimens from the open cut mine	161
6.3.3	Correlation between hardness and microlithotype for specimens from borehole	162
6.3.4	Comparison of SH values across specimens	165
6.4	CONCLUSIONS AND RECOMENDATIONS	167

CHAPTER 7: SYNTHESIS, CONCLUSIONS AND FUTURE WORK

7.1	SUMMARY AND SIGNIFICANCE	169
7.2	MAIN FINDINGS FROM THIS RESEARCH	171
7.3	CONCLUDING REMARKS	174
7.4	RECOMMENDATIONS FOR FUTURE WORK.....	176

LIST OF REFERENCES :

APPENDIX I

APPENDIX II

APPENDIX III

LIST OF FIGURES

	Page
Figure 1	Schematic representation of coal seam gas extraction.....24
Figure 2	a) Map of CSG reserves and gas infrastructure in eastern Australia (EDR - economic demonstrated resources, PJ - petajoules) (Australian government – Department of environment and energy - website), and b) top 10 LNG exporting countries in 2017 (billion cubic feet) (APPEA - website).25
Figure 3	Simplified diagrams showing progressive changes of vitrinite group macerals during coalification from bituminous to anthracite (% vol. m.) (Stach et al., 1982).33
Figure 4	(a) Schematic representation of core specimen, (b) Cross section view of bright band with face and butt cleat mineralised (modified Gray 2015 ACARP C23014).34
Figure 5	Surat Basin structure, tectonic elements, Walloon coal outcrop/subcrop (Hamilton, 2014).35
Figure 6	Idealised diagram showing the appearance of coal at different scales (Trueman and Medhurst, 1994).39
Figure 7	Influence of specimen size on the strength of intact rock (after Hoek-Brown, 1980).50
Figure 8	Illustration of Walloon Coal Measures showing variation in lithological units, and typical interbedded and banded nature of the plies (ruler stick is 50 cm long) (highwall photo courtesy of New Hope Mine).51
Figure 9	Stratigraphic column for the Surat Basin (McKellar, 1998), and the Walloon Subgroup (Hamilton et al., 2012).52
Figure 10	Preparation steps to achieve the mini-cylinder specimen shape and size.....55
Figure 11	Example of one mini-cylinder being verified for the cylindrical profile of lateral walls.56
Figure 12	Examples of mini-cylinder specimens (not on scale) derived from PC8-B and classified by visual appearance (a) no defect, (b) minor defect, (c) pervasive defect, (d) long defect.56
Figure 13	Photograph of the UCS testing machine used for mini-cylinder specimens.58
Figure 14	Examples of mini-cylinder specimens previously tested for UCS and prepared for petrographic analysis (blocks sized 50x30x12 mm).58
Figure 15	Schematic and photographic fracture patterns for failure modes observed on coal mini-cylinder specimens under uniaxial compression.59
Figure 16	Example of the stress-strain monitoring result for mini-cylinder specimen PC6-D #11, #12, and #13, where (AB) is abrupt burst and (LV) is less violent.61
Figure 17	UCS results versus maximum strain using mini-cylinder specimens of all sizes for distinct plies of sub-bituminous coal.61
Figure 18	The relationship between normalised UCS and mini-cylinder specimen size for distinct plies of sub-bituminous coal.62
Figure 19	Effect of mini-cylinder specimen size on measurements of elastic modulus for distinct plies of sub-bituminous coal.63
Figure 20	The relationship between normalised UCS and mini-cylinder specimen size when separated by quality/appearance for sub-bituminous coal.64

Figure 21	Photos of ‘non-intact’ mini-cylinder specimens showing quality and size/diameter for sub-bituminous coal.....	65
Figure 22	Influence of specimen size for sub-bituminous coal compared with other scaling curves in the literature.....	67
Figure 23	Influence of rank and UCS using distinct types of coal with size extrapolated to 50 mm specimen at the top curve, and 300 mm specimen at the bottom curve. Results are from this study (pink circles) and literature reported values (as noted in the legend).....	68
Figure 24	Petrographic analysis shown the stacked percentage distribution of macerals subgroup levels and mineral matter for each epoxy sample.....	69
Figure 25	Representative photomicrographs (10x objective in air, ~50x magnification; all white light except c) of macerals composing the different coal lithotypes and the banding structure.....	70
Figure 26	The samples utilised for petrographic analysis are highlighted in the graphic showing the relationship between normalised UCS and mini-cylinder specimen diameter.....	71
Figure 27	(a) strength vs suberinite percentage; (b) strength vs telinite plus collotelinite percentage for sub-bituminous coal. Note that results were represented for the three distinct plies (PC6-D in light blue, PC8-B in orange, and PC8-WB in light grey colour) tested as either ‘intact’(x) or ‘non-intact’ (Δ) mini-cylinder specimens.....	72
Figure 28	Sample PC8-B #2 zoom in and schematic texture appearance. The block is 50x30x12 mm. The zoom in is from a stitched photomosaic collected at 50x magnification.	73
Figure 29	Relationship between mean particle fracture energy and mean particle tensile strength of 2.0-2.8 mm particles of various materials (from Tavares 1997).	78
Figure 30	3DP specimens fabricated to be tested: a) AutoCAD design, and b) shape, size and orientation of each specimen as printed.	81
Figure 31	3DP specimens schematic illustration of shapes: a) when manufactured into the printing job box; and potential bedding orientation when specimen is impacted: b) cylinder printed vertically: 0°, c) cylinder printed horizontally: 0°–90°, d) sphere: 0°–180°, e) flattened sphere: 90°, and f) ellipsoid: 0°–90°.	82
Figure 32	Setup of the SILC testing system.	84
Figure 33	A photograph of the ultrahigh-speed digital camera phantom v2011.	86
Figure 34	Illustration of dynamic interaction of the striker and the sphere-shaped specimen showing no fracture during a SILC test.	87
Figure 35	Illustration of the bodies in contact for ‘Group A’: a) striker, ‘group A’ specimen, and rod during breakage in the SILC test, b) evidence for striker against the ‘group A’ specimen, c) the ‘group A’ specimen against the rod, and d) the force-time profile of a sphere-shaped specimen that did not failure.	88
Figure 36	Illustration of the bodies in contact for ‘Group B’: a) striker, ‘group B’ specimen, and rod during breakage in the SILC test (Bonfils, 2017), b) evidence for striker against the ‘group B’ specimen, c) the ‘group B’ specimen against the rod and d) the force-time profile of a cylinder-shaped specimen that did not failure.	89
Figure 37	Example of force-time profile of 3DP sphere-shaped specimen with 10 mm in diameter (striker of 2 inches in diameter, 535.25 g) and recorded impact at time equal to 0, 399, 699 and 933 μ s. Regions I to IV are described in the text.....	91
Figure 38	The INSTRON 4505 load system.	97

Figure 39	Failure modes observed on 3DP specimens under uniaxial compression a) 21.6 mm specimens, b) 12.3 mm specimens (zoom in photography), and c) example of the axial stress-strain curve for 3DP sandstone (21.6 mm diameter).....	98
Figure 40	UCS test results for 3DP sandstone specimens of different diameter.....	98
Figure 41	UCS strengths of three sedimentary sandstone rocks (Hawkins 1998) versus 3DP sandstone.....	100
Figure 42	a) Transition between shear and tensile failure modes in 3DP sandstone, modified from the illustration by Li and Wong (2013), b) crack propagation on cylinder-shape specimen diametrically loaded, c) specimen splitting, d) edges from shear failure.....	101
Figure 43	Fracturing process and failure pattern: a) cylinder-shaped specimen (12.2 mm) split into two halves; b) sphere-shaped specimen (5.2 mm) indented and compressed; c) ellipsoid-shaped specimen (12.4 mm) split into three fragments; d) flattened sphere-shaped specimen (10.2 mm) split into two halves, and e) sphere-shaped specimen (10.2 mm) show surface chipping. Selected frames from ultrahigh-speed camera phantom v2011.....	103
Figure 44	Summary of fragmentation characteristics generated by 3DP specimens tested with SILC.....	104
Figure 45	Pattern fracture for major fragments of 3DP with ≈ 12.2 mm diameter: a) cylinder-shaped specimens printed horizontal and b) sphere-shaped specimens.....	104
Figure 46	Example of force-time curve of 3DP sandstone with ≈ 10 mm diameter and fractured under same impact conditions: a) cylinder-shaped specimen printed horizontal, and b) flattened sphere-shaped specimen.....	105
Figure 47	Cumulative distributions of force at first fracture of: a) sphere-shaped, b) flattened sphere, c) ellipsoid, d) cylinder printed vertical, and e) cylinder printed horizontal.....	107
Figure 48	Cumulative distribution of the specific fracture energies: a) irregular crushed particles versus cylinder-shaped specimens of basaltic rock (Bonfils 2017), b) cylinder-shaped specimens of basaltic rock versus cylinder-shaped specimens of 3DP.....	108
Figure 49	Variation of median force at first fracture with specimen size for 3DP specimens.....	109
Figure 50	Impact of fabric orientation on the fracture force for cylinder-shaped specimens.....	110
Figure 51	Variation of median fracture energy with specimen size for 3DP sandstone.....	111
Figure 52	Variation of median corrected specific fracture energy with specimen size for 3DP sandstone.....	112
Figure 53	Variation of median ‘Young’s Modulus’ with specimen size for 3DP sandstone.....	112
Figure 54	Variation of median tensile strength with specimen size for 3DP sandstone.....	113
Figure 55	Variation of average uniaxial compressive strength and average tensile strength ratio with specimen size for 3DP sandstone.....	114
Figure 56	Median results for 3DP of ‘group A’ and ‘group B’ specimens: a) circular contact area for striker versus specimen, b) circular contact area for specimen versus rod, c) elliptical contact area for striker versus specimen, and d) rectangular contact area for specimen versus rod.....	115
Figure 57	Variation of median compressive strength for ‘group A’ and ‘group B’ of 3DP sandstone.....	115
Figure 58	Comparison of the strength ratios between SILC method (σ_{cSILC}) and standard UCS method (σ_{cUCS}) for ‘group A’ and ‘group B’ of 3DP sandstone.....	116

Figure 59	Variation in coal strength relative to rank as estimated by carbon content. From Palmer et al, 2005 cited in Deisman, 2016.....	121
Figure 60	Illustration of samples shape preparation into mini-core specimens of coal tested on SILC.	124
Figure 61	Illustration of the DWT used for fragmentation of distinct size distribution and varied energy in preparation for the irregular-particle specimens of coal tested on SILC.	125
Figure 62	Evidence of ductile deformation for mudstone during fragmentation. a) before DWT test, b) after DWT test.	126
Figure 63	Illustration of irregular single-particles of mudstone tested on SILC.	126
Figure 64	The force-time profile for mini-core specimens drilled perpendicular to band and their conditions before (cylinder-shape) and after (fragments) the SILC test.	128
Figure 65	Impact signal showing the force-time profile for irregular-particles of sub-bituminous coal with 9.5 mm in height on SILC test.	129
Figure 66	Impact signal of two irregular-particles of mudstone with 9.5 mm in height showing the force-time profile from SILC test.	130
Figure 67	Example of impact signal showing the force-time profile where the first fracture was selected for sub-bituminous coal: (a) mini-core specimen with 11.7 mm in diameter, (b) irregular-particle with 9.5 mm in diameter.	131
Figure 68	Cumulative distributions of Young's modulus for PC8-B mini-core specimens drilled perpendicular to band and compared for impact velocity variation on SILC test.	133
Figure 69	Cumulative distributions of tensile strength for PC8-B mini-core specimens drilled perpendicular to band and compared for impact velocity variation on SILC test.	134
Figure 70	Cumulative distributions of correct specific fracture energy for PC8-B mini-core specimens drilled perpendicular to band and sorted by ratio on SILC test.	135
Figure 71	Cumulative distributions of Young's modulus for PC8-B mini-core specimens drilled perpendicular to band and sorted by ratio on SILC test.	136
Figure 72	Cumulative distributions of correct specific fracture energy for PC8-B with aspect ratio of 0.9:1 and PC6-D with aspect ratio from 0.9:1 to 1.1:1, all mini-core specimens drilled perpendicular to band.	137
Figure 73	Cumulative distributions of tensile strength PC8-B with aspect ratio of 0.9:1 and PC6-D with aspect ratio from 0.9:1 to 1.1:1, all mini-core specimens drilled perpendicular to band.	138
Figure 74	Cumulative distributions of correct specific fracture energy for PC8-B and PC8-WB both with an aspect ratio from 0.9:1 to 1.1:1, all mini-core specimens drilled parallel to band.	138
Figure 75	Cumulative distributions of tensile strength for PC8-B and PC8-WB both with an aspect ratio from 0.9:1 to 1.1:1, all mini-core specimens drilled parallel to band.	139
Figure 76	Cumulative distributions of correct specific fracture energy for PC8-B with aspect ratio of 0.9:1 drilled perpendicular to band and PC8-B with aspect ratio from 0.9:1 to 1.1:1 drilled parallel to band.	140
Figure 77	Cumulative distributions of tensile strength for PC8-B with aspect ratio of 0.9:1 drilled perpendicular to band and PC8-B with aspect ratio from 0.9:1 to 1.1:1 drilled parallel to band.	140

Figure 78	Variation of median fracture force against specimen diameter for irregular-particles of coal plies PC6-D, PD8-BLA and mudstone.....	142
Figure 79	Variation of median tensile strength for irregular-particles of coal plies PC6-D, PD8-BLA and mudstone by size.	143
Figure 80	Variation of median fracture energy for irregular-particles of coal plies PC6-D, PD8-BLA and mudstone by size.	144
Figure 81	Median values of cumulative distributions of fracture energy for PC6-D and PD8-BLA for lots of irregular particles retained at 3.35 mm mesh size.	145
Figure 82	Variation of median tensile strength for sub-bituminous coal on SILC influenced by shape.....	146
Figure 83	Variation of median fracture force for sub-bituminous coal on SILC influenced by shape.	146
Figure 84	Variation of median fracture energy for sub-bituminous coal on SILC influenced by shape.....	147
Figure 85	Variation of median corrected specific fracture energy for sub-bituminous coal on SILC influenced by shape.	147
Figure 86	SSRH versus VR (%) on confined (epoxy block) specimens, separated by coal maceral (CM) where MCM stands for Moranbah Coal Measures; FCCM for Fort Cooper Coal Measures, and RCM for Rangal Coal Measures (Klawitter et al., 2015).....	153
Figure 87	Shore scleroscope rebound hardness made by IMAI SIKENKI Co.....	154
Figure 88	SH conversion table - IMAI SIKENKI Co. equipment, in red values from the original conversion table, and in green values extrapolated for SH > 80.....	154
Figure 89	Photographs of polished coal blocks illustrating a) transect, and b) selected lithotype within a block.	156
Figure 90	Ply PC6-D, specimen M5 tested for SH in a transect. a) photomicrographs 1, 2, 3, and 4 representing the sections across the whole specimen as per photo of polished coal surface (c); b) graphic sequence of indentations in terms of Shore hardness (SH); and d) SH values plotted on a histogram. Note that carbominerite areas highlighted on photomicrographs 1, 2, and 3 correspond to drop on SH values as observed in the graphic sequence of indentations.....	158
Figure 91	Ply PC8-WB, specimen M1 tested for SH in a transect. a) photomicrographs 1 and 2 representing the sections across the whole specimen as per photo of polished coal surface (c); b) graphic sequence of indentations in terms of SH; and d) SH values plotted on a histogram.....	159
Figure 92	Ply PC8-B, specimen M2 tested for SH in a transect. a) photomicrographs 1, 2, and 3 representing the sections across the whole specimen as per photo of polished coal surface (c); b) graphic sequence of indentations in terms of SH; and d) SH values plotted on a histogram.....	160
Figure 93	Shore hardness limits for clarite and carbominerite in fine controlled specimens from open cut mine.....	160
Figure 94	Representative photomicrographs of SH indentation on vitrite for the following specimens: a) PC8-B#M3; b) PC6-D #M9; c) PC8-B #6a, lower SH value; d) PC8-B #6a, medium SH value; and e) PC8-B #6a, higher SH value.....	162
Figure 95	Guluguba-2, specimen GG-16, Taroom Coal Measures, 415.5m depth. a) graphic sequence of indentations in terms of SH for the transects; b) SH values plotted on a histogram; c) representative photomicrographs for visualization of microlithotype as it occurred along the transects; and d) the polished coal surface	

	showing location of transects as well as distinct lithotypes delineated. Note that the blue transect follows along the specimens' central axis, then an orange one offsets the central axil towards the left side, while the light grey one offsets the central axil towards the right side.....	163
Figure 96	Guluguba-2, specimen GG-27 (unknown depth). a) graphic sequence of indentations in terms of SH for the transects; b) SH values plotted on a histogram; c) representative photomicrographs for visualization of microlithotype as it occurred along the transects; and d) the polished coal surface showing location of transects.....	164
Figure 97	Shore hardness limits for clarite in selected lithotypes of specimens from borehole Guluguba-2. Cross symbols represent the average.....	165
Figure 98	Shore hardness for specimens tested in this study compared with Klawitter et al. (2015) database.....	167
Figure 99	Variation of mean fracture energy for irregular-particles of coal plies PC6-D, PD8-BLA, 3D-printed sphere-shaped specimens, and mudstone by size, all tested on SILC.....	199
Figure 100	Representative photomicrographs of SH indentation on clarite and carbominerite showing the banding structure for specimens of open cut mine.....	205
Figure 101	Representative photomicrographs of SH indentation on vitrite and carbominerite showing the banding structure for specimens of Guluguba-2.....	205
Figure 102	Representative photomicrographs of SH indentation for clarite (average/ standard deviation) at Guluguba-2.....	206
Figure 103	Guluguba-2, Juandah Coal Measures, specimens tested for Shore hardness.	207
Figure 104	Guluguba-2, Taroom Coal Measures, specimens tested for Shore hardness.	207
Figure 105	Guluguba-2, unknown depth, coal specimens tested for Shore hardness.....	208

LIST OF TABLES

	Page
Table 1	Rank class in terms of maximum vitrinite reflectance (Ward, 1984).....31
Table 2	Correlation between terms of banded coal (Stopes, 1919 and AS2519-1993).....32
Table 3	Summary of mini-cylinder specimens tested and their mechanical properties.....60
Table 4	Normalized UCS extrapolated to equivalent 50 mm diameter core.....71
Table 5	Summary of the 3DP specimens' shape, dimensions and impact conditions tested.....83
Table 6	Summary of the rod and striker parameters.....85
Table 7	Summary of UCS tests of the 3DP specimens.....97
Table 8	Mechanical properties of 3DP sandstone obtained from UCS tests.....99
Table 9	Number of specimens used to conduct SILC tests following the rock material and specimen features.....127
Table 10	List of parameters obtained using SILC, the example illustrates experiments on sub-bituminous coal.....132
Table 11	Number of specimens and testing conditions per location.....156
Table 12	Summary of SH values measured conditional to microlithotype.....157
Table 13	Summary of UCS measurements on 3D-printed sandstone from UCS test.....194
Table 14	Summary for SILC test results on 3D-printed sandstone.....196
Table 15	Summary of fracture characteristics for mini-cylinder specimens (11.7 mm in diameter, aspect ratio varying from 0.9:1 to 1.1:1) of coal on SILC. Impact conditions utilising a 535.25 g strike dropped from 63.1 mm in height.....198
Table 16	Summary of fracture characteristics for irregular-particles (retained at 3.35, 4.75, 6.7, and 9.5 mm mesh sized) of coal plies PC6-D, PD8-BLA and mudstone on SILC.....198
Table 17	Fracture characteristics for irregular-particles of sub-bituminous coal PC6-D on SILC.....200
Table 18	Fracture characteristics for irregular-particles of sub-bituminous coal PD8-BLA on SILC.....201
Table 19	Fracture characteristics for irregular-particles of mudstone on SILC.....202
Table 20	Summary of specimens from open cut mine tested for SH hardness in a transect line.....203
Table 21	Summary of specimens from borehole Gulugula-2 tested for SH in a transect line.....203
Table 22	Summary of specimens from borehole Gulugula-2 tested for SH on selected lithotype.....204

LIST OF SYMBOLS AND ABBREVIATIONS

CH ₄	Gas methane
CBM	Coal Bed Methane
CSG	Coal Seam Gas
d.a.f.	dry-ash-free
E'	fracture energy
EDR	economic demonstrated resources
F _c	fracture force
fps	frames per second
HGI	Hardgrove Grindability Index
GPa	gigapascal
'group A'	sphere, flattened sphere, and ellipsoid-shaped specimens
'group B'	cylinder-shaped specimens
lbf/in ²	psi or Pound-force per square inch
'intact'	mini-core specimens with no visible or minor defects
K _{Ic}	mode I fracture toughness
kWh/t	kilowatt-hours per metric ton
L/D	length-to-diameter ratio
μs	Microsecond or one millionth of a second
MPa	megapascal
'non-intact'	mini-core specimens with pervasive and long defects
PC8-B	C8 ply banded
PC8-WB	C8 ply banded with white marks comprising clay lenses
PC6-D	C6 ply dull
PD8-BLA	D8 ply banded low ash
PJ	petajoules
R _o (max)	maximum vitrinite reflectance
SEM	Scanning Electron Microscope
SH	Shore hardness
SILC	Short Impact Load Cell
SSRH	Shore Scleroscope Rebound Hardness
UCS	Uniaxial Compressive Strength

INTRODUCTION

1.1 COAL SEAM GAS

Demand for reliable energy resource tends to increase even further with advanced technologies and automation in the near future. Globally, Coal Seam Gas (CSG) which is also named Coal Bed Methane (CBM) is an extremely large energy resource with substantial economic benefits. The natural gas (Liquefied Natural Gas) extracted from CSG is vastly used for cooking and heating homes and buildings, as well as in industrial processes with power stations that generates electricity. Natural gas is used to make plastic and fabric for clothing; it is a fuel substitute for cars, trucks and industrial vehicles; also indispensable for production of industrial and chemical fertilizers.

It is underneath the ground, about 200 to 1000 meters below surface, that CSG may be economically explored using available tools and technology. The natural gas is found in coal deposits, of which the highly inflammable gas methane (CH_4) is the major component and secondarily the carbon dioxide, nitrogen, and trace amounts of higher hydrocarbon gases occur in variable proportions (Flores, 2014). Coal deposits are formed slowly from organic matter under suitable conditions (heat and pressure) buried at depths, over periods of up to several hundred million years. Meanwhile, the gases components formed in a near-liquid state, whether thermogenic or biogenic, can mostly be held onto the internal surfaces. These internal surfaces include porous systems, small and regularly spaced cleats, and larger-scale joints. In this scenario 95% of the gas is stored within micro-porous and only 5% within the natural fractures. The variety of plant debris and the climatic conditions influence the constituents and the structure of the coal-forming as well as the gas volumes stored.

Drilling wellbores through these complex and highly heterogeneous layers of coal seam allows for the natural gas to be explored (Figure 1). Traditionally, the wellbore is drilled vertical and it is protected with cement and steel casing. During production, the gas is released from unconventional CSG by lowering the pressure (drilling and continuously pumping off water). The main pathway for gas to flow out of the coal is through the internal surfaces or natural fractures (porous structure, cleats, and joints). In high quality CSG deposits, the natural fractures are permeable enough to allow the free gas or the gas saturated with water contained within the seams to flow through this fracture system. Except by those areas identified by high natural permeability as well as deep underground boreholes, the unconventional gas extraction needs to be artificially stimulated in order to successfully achieve a commercial production. For that, a controlled process such as hydraulic fracture (also named fracture stimulation or fracking) is usually applied to increase the coalbed permeability. During this process, injection of water (or another fluid) under high pressure via wells is utilized to open the existing natural fractures and to create new ones in the coal to increase gas production. In order to target prominent coal seams or to work on optimization of fracking design, it is critical to understand the geomechanical behaviour of the reservoir and the surrounding rocks at the microscale.

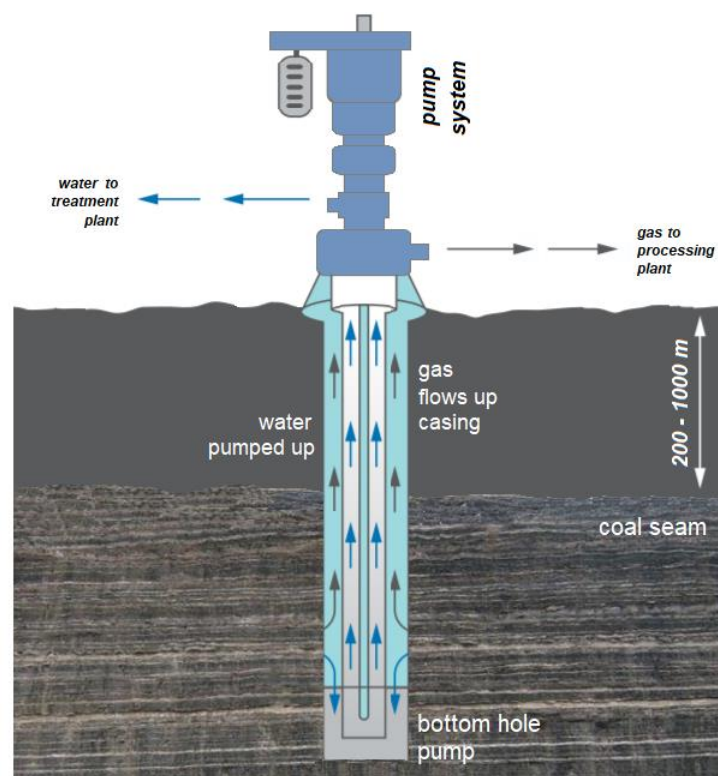


Figure 1 Schematic representation of coal seam gas extraction.

As a means of highlighting the relevance of the gas industry, it is observed that growth in Australia’s natural gas production (LNG and domestic use) increased by 16% in 2018 compared with 2017. While production has more than doubled over the last five years (APPEA, 2019). Figure 2a provides an overview of CSG reserves and infrastructure in eastern Australia where large reserves of CSG occur (Australian government - Department of environment and energy - website). In 2018, the production of natural gas from coal seams represented 1,303.0 billion cubic feet for Queensland (QLD), against 5.0 billion cubic feet in New South Wales, Australia (source: Energyquest). Notice that the CSG production in the Bowen (Permian Coal Measures) and Surat (Jurassic Walloon Coal Measures) basins represents more than 90% of the total gas produced in the state. Also, data from BP statistical review of world energy has placed Australia between the top 10 leading export of LNG in 2017 (APPEA - website) (Figure 2b).

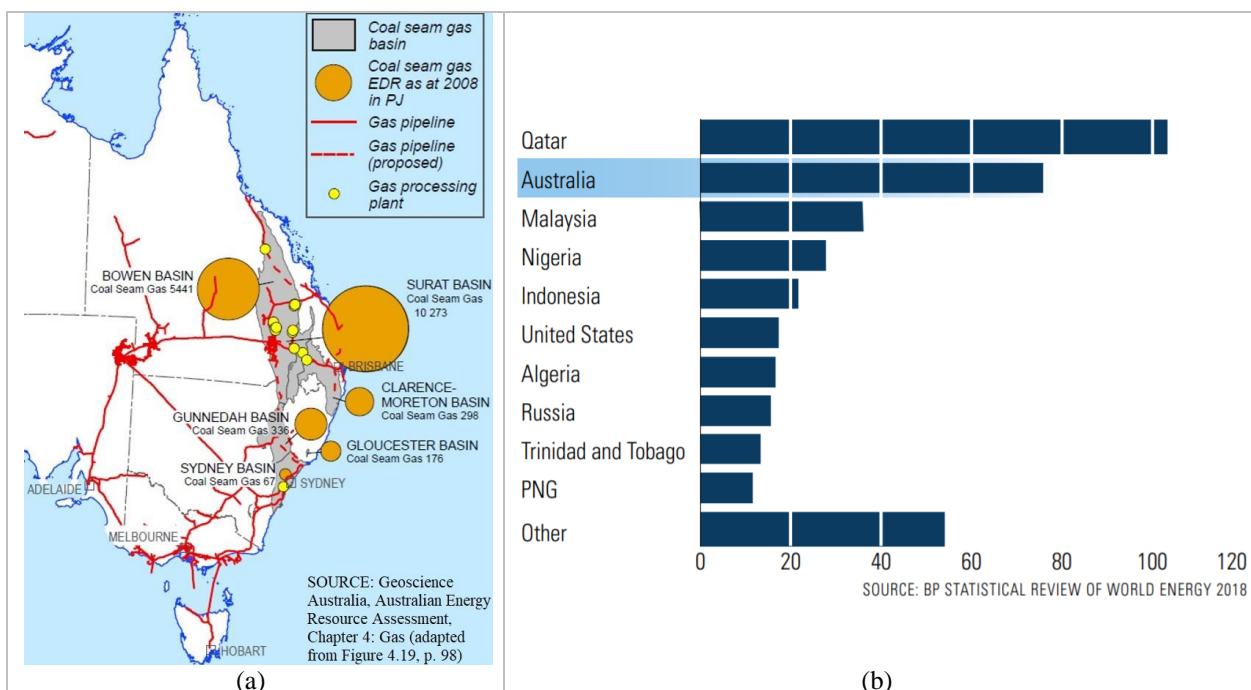


Figure 2 a) Map of CSG reserves and gas infrastructure in eastern Australia (EDR - economic demonstrated resources, PJ - petajoules) (Australian government – Department of environment and energy - website), and b) top 10 LNG exporting countries in 2017 (billion cubic feet) (APPEA - website).

This study focuses on low rank, sub-bituminous coal from Surat-Clarence-Moreton basins, a complex geological and geotechnical environment where the depositional sequence of lithotypes and non-coal partings, such as claystones and mudstones, vary in thickness from millimetre to metre scale, in eastern Australia. Their distribution also changes vertically and laterally within a coal seam. This environment is very different from broad mining extraction on medium rank coal.

The thick seams on medium rank coal allow for layers with varying proportions of natural fractures, lithotypes, and mineral matter to be disregarded or averaged for the specimen, then large excavations and big volumes of rock removal comprise the geomechanical appraisals and guide the laboratory tests conducted.

In another hand, the level of understanding involving rock characterization for the oil and gas industries, particularly low rank coal in the Surat Basin, must be thought at the micro-scale. In this case, more rational approach to improve gas extraction is an understanding of the rock dominant breakage mode and/or the micro-process occurring inside the coal contrasting with the interbedded material. For that, a series of relevant and practical laboratory experiments are carried out under controlled, reproducible conditions, and utilizing smaller specimens' size. This provides more realistic range of input data for numerical modelling approach to handle the behaviour of such a complex and heterogeneous system.

1.2 RESEARCH CHALLENGE: CSG IN THE SURAT BASIN – LOW RANK COAL

Almost without exception, understanding, measuring, and representing the reservoir properties are the major technical challenge for bringing CSG economically recoverable and feasible to market. Associated gaps within the gas industry, when appraising the reservoir properties, includes the ability to approach a complex geological and geotechnical environment. Coal geomechanical properties such as compressive and tensile strength, and fracture toughness vary with respect to the proportion of natural fractures, discontinuities (faults, dykes), and the moisture (rank) as well as composition of the intact rock which is encapsulated in the lithotype classification (brightness of coal).

The higher moisture coals of the Surat Basin are also texturally very different, consisting of multiple thin packages of <0.5 to 10 meters coal beds, stacked into groups of many metres. The coals are jointed and cleats are poorly developed at low rank, except for some incipient cleats in the few bright bands. Within each bed, the coals can be sub-divided into even thinner (centimetre to decimetre scale) lithotypes that are separated by partings of rock or claystone or mudstone. These characteristics show distinct geotechnical and gas flow behaviours, which are yet to be clarified. Therefore, general assumption about coal rock mass varying between 6 to 12 MPa is a misleading approach for this Basin. For site-dependent properties, the issue to overcome core

sample difficulties, including to recover, source, and measure on laboratory, might be to reproduce the scale of interest.

Then questions to be investigated in this thesis are: what is expected when testing intact specimens of sub-bituminous coal, where cleats are poorly developed, furthermore, if induced fractures are removed to avoid misleading interpretations? How can the interactions and distributions of lithotypes and microlithotypes help to better understand this scenario? Last, how to deal with a sedimentary environment which is very complex with juxtaposition of strong and weak rock mass overprinted by structures such as faults and joint sets?

1.3 HYPOTHESIS

The hypothesis to be tested is that coal exhibit both brittle and ductile behaviour, particularly low rank coal with abundant claystone partings. The scale of observation to address intact strength of coal, is better small, perhaps below the inherent flaw size, to microscopically. Geomechanical characterization of coal obtained through those sizes and/or non-traditional experimental methods may demonstrate the influence of structural features and composition/lithotypes, or microstructural features and microlithotypes on coal behaviour.

1.4 AIMS AND OBJECTIVES OF THE RESEARCH

The aim of this research is to investigate the applicability and validity of alternative laboratory tests to provide characterization for the sub-bituminous coals of the Surat-Clarence-Moreton basins. This thesis addresses the characterization of the mechanical and comminutive properties such as strength, fracture energy, elastic modulus, and hardness. The experimental laboratory tests are planned to be performed on smaller rock specimens. Influence of shape and size are also for consideration, while fracture opening, and propagation are attempted to be observed. Ultimately, this research brings together geological, geotechnical and metallurgical knowledge for resources matters and develops better alternative to obtain input data for CSG reservoir simulations.

1.5 FORMAT OF THE THESIS

The thesis is made up of one volume; it has seven chapters, and three appendixes. The chapters comprise details for the assessment and results, focus on geological, geotechnical, and metallurgical characterization of the coals, and the appendixes with supporting material and methodologies followed.

The titles and outline of chapters are arranged in the following sequence:

Chapter 1 - Introduction: presents the relevance of this study for the CSG, the thesis objectives, and address an outline of each chapter.

Chapter 2 – Back to the basics to understand coal: This chapter summarizes some fundamental information for coal reservoir geomechanics. The main characteristics of coal composition and structure from grain to macro scale are addressed. It also introduces the laboratory experiments performed here. (This chapter contains parts of a peer-review APPEA Journal).

Chapter 3 – Mini-core specimens scaled: This chapter describes preparation of the mini-core specimens and the laboratory experiments of uniaxial compressive strength (UCS) using nonstandard size for sub-bituminous coal. The applicability of results is discussed by comparison with bituminous coal. (This chapter is a submitted manuscript).

Chapter 4 – A test of fracture, shape, and size using 3D-printed sandstone: In this chapter 3D-printed sandstone is utilized to demonstrate the mechanical properties of homogeneous and intact material. The known properties were used to test calculations/estimations of material properties for specimens of different size, shape and fabric in a Short Impact Load Cell (SILC) test. The experimental procedures and results are presented in detail. (This chapter is published at the Geotechnical and Geological Engineering).

Chapter 5 – SILC on coal and mudstone: This chapter contain details of the Short Impact Load Cell (SILC) on coal and mudstone. It explores the influence of loading direction, specimen size, and shape on estimation of mechanical properties. Comparisons between coal and mudstone are presented and discussed. (This chapter is published at the Journal of Natural Gas Science and Engineering).

Chapter 6 – Lithotypes and microlithotypes matter: This chapter highlights the dependence of microlithotype and hardness on sub-bituminous coal. Description of the test and results of Shore

Scleroscope Rebound Hardness (SSRH/SH) are presented. (This chapter is accepted for publication at the International Journal of Coal Geology).

Chapter 7 – Discussion, conclusions and future work: This chapter summarizes and discusses the most significant outcomes of the experimental work conducted in the context of CSG exploring low rank coal reservoirs. It also identifies some of the gaps in knowledge and proposes themes for further work.

BACK TO THE BASICS TO UNDERSTAND COAL

2.1 INTRODUCTION

Coal is a heterogeneous, highly complex sedimentary rock (Koenig and Stubbs, 1986; Wold et al, 1995), which cannot be characterized by a particular grain size since it contains more macerals (fibres) than minerals (grains) (Buzzi et al., 2014). The depositional environment and the burial history of the coal are critical to understand the gas composition, gas content, density, diffusivity, permeability, and gas storage capacity. The physical, chemical, and hydrological properties of coal make it a unique and site-specific rock type. Various features are pertinent to the mechanical behaviour of coal seam and rock mass strata including, for instance, the internal surfaces or natural fractures (porous and cleats accounting for fluid pressure and impacting the success of fracture stimulation techniques); the increase in depth extraction (reflecting on stability of wellbores, multilateral wells, etc.); the thickness of the coal (if multiple thin-bedded zones or massive coal); the lateral continuity and connectivity of the coal seams and the surrounding strata (variable production rate); the pre-existing geological structures (compartmentalising a reservoir vertically and horizontally), the in-situ stress conditions/tectonic stress; and the effects on land subsidence. In summary, that is how interesting the source rock and the environment for coal seam gas (CSG) reservoir can be.

In this chapter, considerations and knowledge-driven approach to address the coalbed geological and geomechanical conditions at the relevant scale, that will influence reservoir performance, are described. Basic important concepts of coal rank, lithotype, matrix, porous, and cleats are highlighted. Followed by an overview of the geology in the Surat Basin, the environment of this study. Then, geomechanics aspects are pointed out, including those involving rock behaviour,

composition, and structure, which require further knowledge are presented. Last, a quick overview is given of the laboratory experiments utilized for rock characterization in this thesis.

2.2 COAL CHARACTER

2.2.1 Uniqueness of coal

Distinct basins are controlled by the degree of diageneses, the depositional history of the units, and the tectonic evolution which contribute to make coal a unique and again, site-specific rock. At first, it is important to classify the coal rank which is similar to a measure of the level of metamorphism (degree of diagenesis) that exists in inorganic rocks (Ward, 1984). The coal rank generally increases in direct correlation to temperature, depth of burial (pressure), geothermal gradient, and the length of time the organic material remains in a given regime (Ward, 1984). The coal macroscopic appearance varies from brown to black depending on the rank; specifically, brown coal is of low rank (i.e. lignite) and black coal is of higher rank (i.e. from bituminous to anthracite). Sub-bituminous coal, which is of interest in this thesis, is reported brown (George, 1975) and black (Stopes, 1919; Schopf, 1960; Davis, 1978) as it is transitional. The maximum vitrinite reflectance, referred to as percentage $R_o(\text{max})$, is the most common measured property related to the structure of organic combinations in the coal and it is used as rank indicator (Table 1).

Table 1 Rank class in terms of maximum vitrinite reflectance (Ward, 1984).

Rank	Type	% $R_o\text{max}$
Low-rank coal	Sub-bituminous	< 0.47
Medium-rank coal	High volatile bituminous C	0.47-0.57
	High volatile bituminous B	0.57-0.71
	High volatile bituminous A	0.71-1.10
	Medium volatile bituminous	1.10-1.50
	Low volatile bituminous	1.50-2.05
High-rank coal	Semi-anthracite	2.05-3.00 (approx.)
	Anthracite	> 3.00

The composition and character of a coal seam is determined by the available organic units and sediments (inorganic fraction such as mineral matter) which also influence on the continuity and spatial variation of the seams. Coal lithotype, a macroscopic visual method, is used for characterization of the organic compositional differences within and between coal seams that, along with thermal maturity show the chemical and physical properties of the coal (Stopes, 1919). This concept was first proposed by Stopes (1919) to include the four “ingredients”, namely, vitrain,

clarain, durain, and fusain, the main constituents in hand specimens of banded bituminous coals. Then, lithotypes refer to multi-layers recognizable with varying thinner bright (vitreous vitrain bands) relative to thicker dull (durain bands) proportions as classified by various authors (Stopes, 1919; Thiessen and Sprunk, 1935; Cady, 1942; Schopf, 1960; Davis, 1978; Diessel, 1982; Stach et al. 1982; Hower et al., 1990; AS2519, Standards Association of Australia, 1993). The alternations of lithotype bands produce textures which have distinctive colour, luster, fracture, and thickness (Hower et al., 1990). Geological characterization and mapping techniques can be utilized for describing the layered and blocky appearance of coal in terms of lithotype. The classification schemes and correlation between terms followed by Stopes (1919) and Standards Association of Australia (1993) are presented below (Table 2).

Table 2 Correlation between terms of banded coal (Stopes, 1919 and AS2519-1993).

Stopes' lithotypes	Australian standard brightness profiles		Proportion of bright bands (%)
	Category	Description	
Vitrain	C1 (B)	Bright	> 90%
Clarain	C2 (Bb)	Bright banded with minor dull	60% - 90 %
“Duro-clarain”	C3 (IB)	Inter-banded bright and dull	40% - 60 %
“Claro-durain”	C4 (Db)	Dull banded	10% - 40 %
Durain	C5 (Dmb)	Dull with minor bright	1% - 10 %
Durain	C6 (D)	Dull	< 1%
Fusain	(F)	Fibrous	-

DULL → BRIGHT

By zooming into the lithotype, one can then describe coal in terms of microlithotypes. The microlithotype method of classification is performed under the microscope. It is utilized for characterisation of the natural associations of maceral groups (vitrinite, liptinite and inertinite) and mineral matter at specific proportions, to name the maceral subgroups that occur within the coalbed. Microlithotypes are classified into three groups based on the number of maceral: (i) monomaceral consist of one maceral group, for instance the vitrite (>95% vitrinite) or inertite (>95% inertinite); (ii) bimaceral consist of two maceral groups, for instance clarite, durite, or vitrinertite; (iii) trimaceral consist of three maceral groups, for instance duroclarite, clarodurite or vitrinertoliptite.

Now that concepts such as rank and maceral groups are remembered, further explanation about the microstructural features or structures forming the intact coal rock (Zhao et al., 2014a; Potyondy, 2015) are presented. It happens that throughout the coalification process the vitrinite group macerals

changes from bituminous to anthracite in terms of volatile matter (Stach et al., 1982; Flores, 2014). Other geophysical factors such as compaction and water expulsion also change during this process of increasing rank. This reduces the porosity in coal and a minimum is reached between medium volatile bituminous to low volatile bituminous coal (Taylor et al., 1998; Rodrigues and Lemos de Sousa, 2002). The coal porous structure includes micro-porous, mesoporous, and macro-porous varying from a few Angstroms to frequently over a micrometer in size. The macro-porous system is known as the primary porosity. The secondary porosity develops when the molecular structure through coals of a higher rank changes and a meso- and micro-porous system starts to form (Rodrigues and Lemos de Sousa, 2002). Micro-porous system is predominant with the main group vitrinite which presents the largest potential for methane gas generation. Opposing to that, the macro-porous system is predominant with the main group inertinite and has reduced potential for gas production (Scott, 2002). Figure 3 shows the structures of coal during various stages of coalification, the molecular (upper level) changes and the physical (lower level) changes.

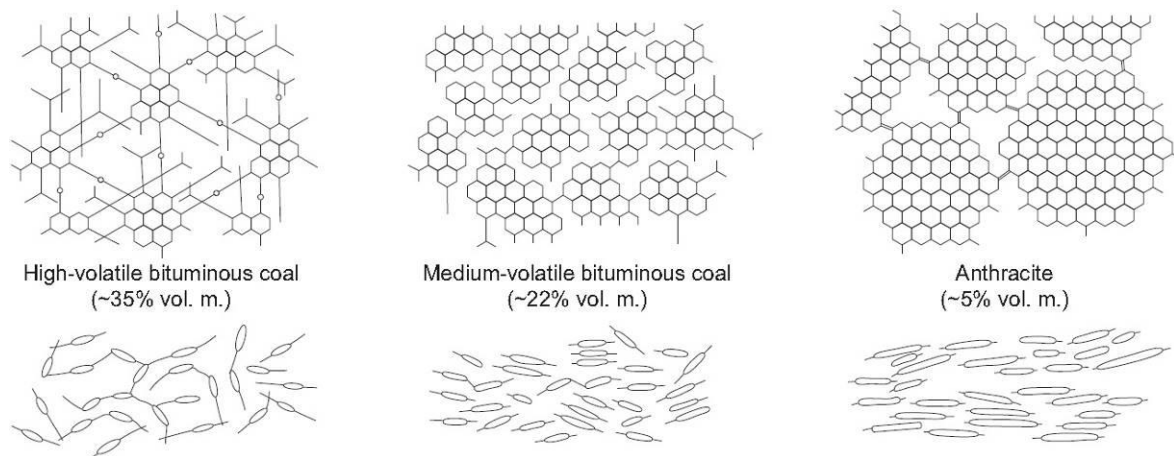


Figure 3 Simplified diagrams showing progressive changes of vitrinite group macerals during coalification from bituminous to anthracite (%vol. m.) (Stach et al., 1982).

Following that, the coalbed structure comprises a matrix of complex heterogeneous porous structure, broken up by macroscopic natural fractures at all scales. Then, confined to the dull and brighter layers (bands) are well-defined distributed networks of natural fractures known as cleat (Ting, 1977a; Dawson and Esterle, 2010). Non to poorly banded coals derived from fine-grained macerated plant fragments tend to have fewer, more widely spaced cleats than banded coals that contain higher proportions of better-preserved plant matter. Cleats are essentially shrinkage cracks formed from the volume loss of moisture during coalification (Ting, 1982) and matrix porosity (Gentzis et al, 2006).

A cleat set is comprised by face cleats (earliest formed, more prominent set) and orthogonal butt cleats, which generally end at the boundaries of face cleats (Dron, 1925; Kulander et al., 1990; Laubach and Tremain, 1991; Li et al., 2004). Figure 4 illustrates a schematic representation and cross section view of real cleat set (face and butt cleat) for a bright band coal (C1 category, Table 2) which is quite evident due mineralisation.

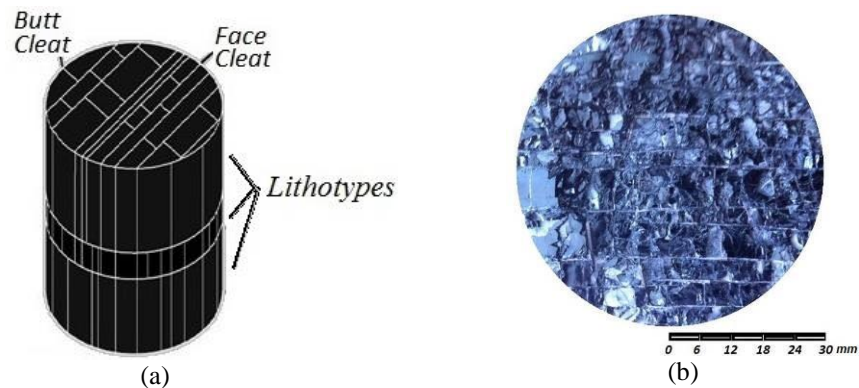


Figure 4 (a) Schematic representation of core specimen, (b) Cross section view of bright band with face and butt cleat mineralised (modified Gray 2015 ACARP C23014).

Overall, the spacing between cleats tends to be quite uniform, from millimetres to centimetres scale or even decimetres. The cleat height and spacing varies with the rheology and thickness of the different layers or bands within the coal (Gamson et al, 1993). The thicker the bright coal lithotype, the lower the cleat frequency in bituminous coal (Tremain et al., 1991; Close, 1993; Law, 1993; Laubach et al., 1998; Su et al., 2001). Better estimates of cleat frequency might be calculated if the distribution of coal microlithotype layers are known, and the apparent relationship between coal height and cleat spacing for specific cleats within a given coal rank are taken into consideration (Dawson and Esterle, 2010). The cleat aperture is typically less than 0.1 mm (Kulander et al., 1990; Laubach et al., 1998). It is well recognised that cleat spacing decreases from sub-bituminous to medium volatile bituminous coal and increases throughout the anthracite coal rank (Ammosov and Eremin, 1963; Ting, 1977b).

Moreover, there is a strong relationship between cleat orientation and regional stresses relative to banding. According to Gentzis et al (2006), the orientation of the natural fractures records the in-situ stress at burial depth. Often face cleats are perpendicular to the least compressive principal stress, whereas butt cleats are parallel to the axis of the original local compression, approximately (Hancock and Engelder, 1989). The cleat can be overprinted through changes in tectonic stress over the geological history of the basin (Pattison et al, 1996). According to Su et al. (2001) different development stages of face and butt cleats results in distinct network patterns.

2.3 BASIN CHARACTERISTICS

2.3.1 Geological characterization of Surat Basin

The Surat Basin is a broad intra-cratonic downwarp that covers an area of about 300,000 km² in south-eastern Queensland into north-eastern New South Wales, Australia (Rigby and Kantsler, 1987). The structural axis of the basin is along the Mimosa Syncline which is an axial trough in the centre of the basin that contains the thickest preserved section. The Mimosa Syncline is slightly offset from the axis of the underlying Permo-Triassic Taroom trough of the Bowen Basin (Figure 5). The thick-skinned, meridional Moonie-Goondiwindi and Burunga-Leichhardt thrust fault systems, formed by a contractional event called the Goondiwindi Event, comprise a series of discrete fault segments with displacement transfer zones in between (Korsch et al., 1998; Hamilton, 2014). Movement along these fault systems likely impacted on the depositional architecture of units underlying the Walloon Subgroup (Sliwa and Esterle, 2008; Hamilton, 2014).

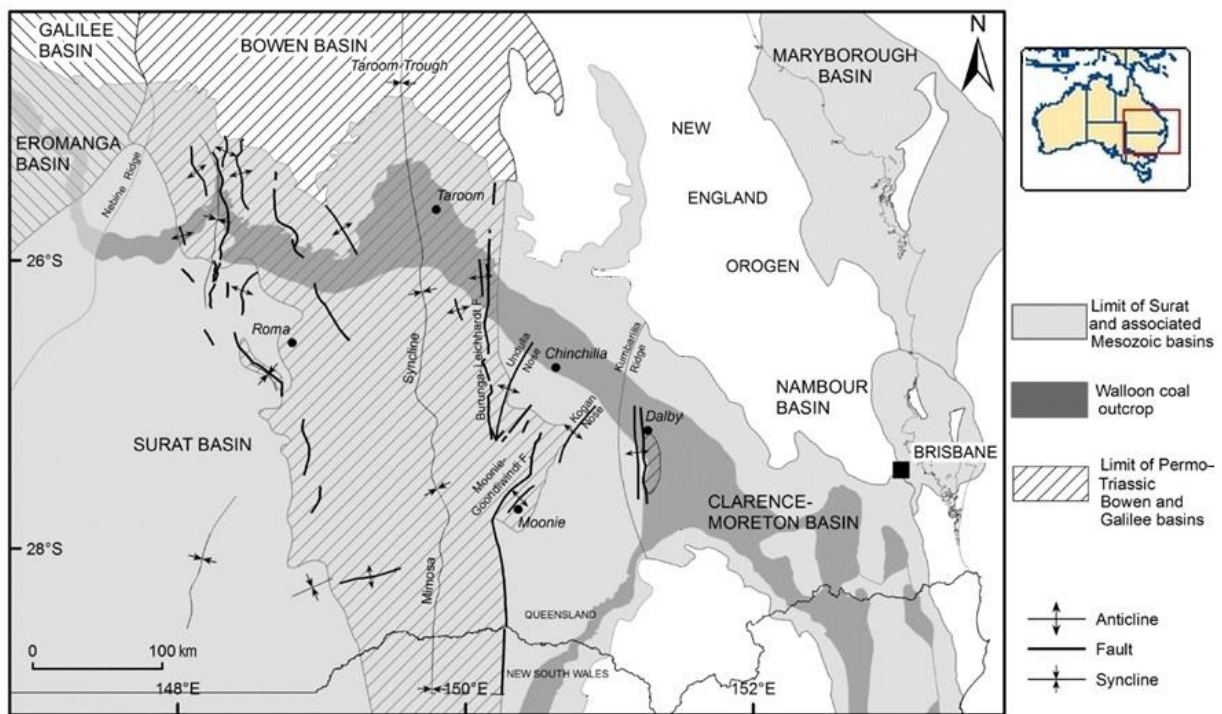


Figure 5 Surat Basin structure, tectonic elements, Walloon coal outcrop/subcrop (Hamilton, 2014).

The basin sequence comprises a non-marine Jurassic succession overlain by a mixed non-marine and marine Early Cretaceous succession (Green et al., 1997). Sedimentation within the Surat Basin initiated in the Late Triassic to Early Jurassic, after a phase of contractional deformation and widespread erosion in the Middle to Late Triassic causing a peneplanation of basins and basement

rocks of eastern Australia (Exon, 1976; Fielding et al., 1990; Korsch and Totterdell, 1996; Korsch et al., 2009; Hoffman et al., 2009), which also resulted in deposition of the quartzose Precipice Sandstone. Throughout the Jurassic and early Cretaceous, several episodes of fluvial-lacustrine-coal swamp sedimentation occurred as the basin gently subsided, resulting in the deposition of the Evergreen to Bungil Formations. According to Gallagher (1990), subsidence was described as generally consistent throughout most of the Jurassic, but slightly increased during the Late Jurassic and Early Cretaceous. Exon (1980) recorded a series of six sedimentary cycles, each comprising a basal sandy succession that grades into increasingly labile (<50% quartz) units at the top of the cycles. In summary, each cycle begins with the deposition of craton-derived quartzose (>50% quartz) sandstones deposited in fluvial environments, then continues with deposition of finer-grained, volcanoclastic-rich sandstones, which are often associated with tuffs, carbonaceous mudstones and coals (Veevers, 1984; Hawlader, 1990; Waschbusch et al., 2009).

It is recognised that the regional variation of the coal strata is mainly controlled by the depositional environment. The deposits of the Surat Basin are lateral equivalents to sediments in the Eromanga Basin further west. The eastern margin Surat Basin stratigraphic pile is significantly thinner than further west, as per interpretations evolved from outcrop and subsurface studies. Thick, north-south trending channelised sandstone units (e.g. Precipice Sandstone, Hutton Sandstone) underlie broader, sheet and wedge-shaped units containing finer-grained meandering stream and lacustrine deposits (e.g. Evergreen Formation, Walloon Subgroup) (Sliwa and Esterle, 2008; Hamilton, 2014).

Uncertainty surrounds the causal tectonic mechanism(s) (structural settings) driving basin evolution and subsidence in the Surat and adjacent Mesozoic basins (Hoffmann et al., 2009) occur, as different propositions have been presented by various authors (Russell and Gurnis, 1994; Fielding, 1996; Yago and Fielding, 1996; Waschbusch et al., 1999, 2009; Korsch and Totterdell, 2009; Korsch et al., 2009; Matthews et al., 2011; Smith et al., 2017). Also, the internal architecture of the Walloon Subgroup of the Surat Basin is still target for research (Hentschel, 2018).

Because part of the rock material utilized in this thesis was collected at the Clarence-Moreton Basin, it is pertinent to explain that this Basin borders the Surat Basin in the south-east (Figure 3). Its Late Triassic to Middle Jurassic sediments are continuous with the Surat Basin across the Kumbarilla Ridge (Day et al., 1983; Jell, 2013). Although the adjacent Clarence-Moreton Basin to the east was likely a foreland basin associated with a volcanic arc in the Jurassic, the absence of volcanic arc related rocks rather supports an extensional depositional setting for the Surat Basin (Yago and Fielding, 2015). As proposed by Fielding (1996) and Yago and Fielding (1996), an

active intraplate rifting with the onset of rifting of the eastern margin of the Australian plate occurred. In this way, the coal measures of the Walloon Subgroup in the Clarence-Moreton and Surat Basins are laterally equivalent and have been referred as low rank for this thesis purposes.

2.4 RESERVOIR CHARACTERISTICS

2.4.1 Gas and production in Surat Basin

The CSG distribution is influenced by the coal rank and structure (Lucia, 1983; Laubach et al., 1998; Su et al., 2001; Scott, 2002; Dawson and Esterle, 2010). The coals of the Middle Jurassic Walloon Subgroup (i.e. the youngest unit) along the north-eastern margin of the Surat Basin, are of low rank sub-bituminous, and the vitrinite reflectance range from approximately 0.5-0.4% Ro up section (with some values reaching 0.7% Ro) (Scott et al., 2007; Hamilton et al., 2012). Along the western margin of the basin the composition and rank still needs to be validated. The coals of the Walloon Subgroup are vitrinite-rich (62 to 91 vol. % mmf) with abundant liptinite and high mineral matter contents (Scott et al., 2007). On a maceral subgroup level, telovitrinite is the most common one. Amongst the liptinite group macerals, suberinite and cutinite are common (Khavari-Khorasani, 1987; Pacey, 2011; Hentschel, 2013). Higher inertinite content occur within the upper coal measures providing evidence of desiccation and oxidation by fires (Leblang et al., 1981; Scott et al., 2007; Hentschel, 2013). In high vitrinite coals, the micro-porous system and cleat formation are both predominate which provides optimal environment for gas generation.

Gas contents (dry-ash-free; d.a.f.) vary significantly, for instance, in the eastern Surat Basin the gas content range from 1-15 m³/tonne d.a.f. and average 5.36 ± 2.5 m³/tonne d.a.f. (Hamilton et al., 2012). The most prospective area for CSG occur down-dip and adjacent to the Walloon subcrop edge, where high permeability exists and it refer to the connectivity of the pore structure as well as the passage of a pore fluid through the opening of micro-fractures/cleats inside the rock. These are the areas where the compression is offset by tensional forces. However, general observation is that CSG in Surat Basin have reduced permeability at a given depth or pressure, where cleats are mineralised and became blocked mostly by fine clay minerals infilling the face cleats (Faraj et al., 1996). Note that increase of the confining pressure reduces both the porosity and the permeability due to elastic closure of pre-existing microcracks (Brace et al., 1968; Turner and Secor, 1974; Zoback and Byerlee, 1975) in the low-porosity rocks. Though in porous rocks the correlation

between porosity and permeability changes is not as well defined. Nevertheless, those areas might require some technique such as hydraulic fracture to increase production.

Overall, the CSG is produced from multiple coal seam groups across the Middle Jurassic Walloon Subgroup. Despite a decrease of net coal thickness towards the Roma Shelf and the Nebine Ridge, the CSG production has extended westwards (Hentschel, 2018). In producing areas, the Walloon Subgroup is typically 350 m thick and contains an average of 30 m of net coal with average coal ply thickness about 40-30 cm (widespread coal due deposition in an intra-cratonic setting), that is interbedded with a range of clay-rich, and fluvio-lacustrine lithological units. The coals are dull or dull banded with bright bands that are commonly only 1 mm in thickness (frequency of 64.6%) (Hentschel, 2018). Thicker bright bands are rare and only occur with increase in depth (Afonso, 2014) in the lower seams of the Lower Taroom Coal Measures and the upper seams of the Lower Juandah Coal Measures (Hentschel, 2018). While sub-bituminous coal is considered to show the first developments of cleats (Law, 1993), the cleats are poor in this Basin. Moreover, the butt cleat spacing does not increase as much as the face cleat spacing with variation on stress conditions (Afonso, 2014).

The Surat Basin CSG reservoir is water saturated meaning the water provides the reservoir pressure that holds gas in the adsorbed state (perfect equilibrium system). Then water starts being pumped, the reservoir produces only water as a primary mechanism of pressure reduction. During this single-phase flow (production of water), the gas content of the reservoir is below the sorption isotherm curve (i.e. the relationship of pressure and the capacity of a given coal to hold gas at a constant temperature). When the reservoir pressure falls and the gas production initiates, there is a two-phase flow of gas and water which is controlled by (i) desorption of gas from the coal matrix, (ii) diffusion to the cleat system, and (iii) flow through fractures. During production it is important to keep the lowest practical pressure in order to maintain the relationship between gas desorption and reservoir pressure.

2.4.2 Coal mining: lessons learned

For geological and geotechnical characterization of coal and sedimentary rocks comprising the reservoir, the mining background is used as reference. Notable the success of mining designs and appraisals rely on measurement and quantification of strengths and deformations of rocks done through laboratory experiments (e.g. uniaxial compressive strength, triaxial test, tensile strength, and Brazilian test) and numerical modelling simulations. Some of the knowledge developed

highlights that rank class, lithotype, and cleat frequency influence the coalbed mechanical behaviour (Medhurst, 1996; Medhurst and Brown, 1998; Scholtès et al, 2011; Poulsen and Adhikary, 2013), and that the greater the density of defects (micro-defects, structural features, and fractures) the weaker the rock behaves. Furthermore, natural fractures and bedding planes represent the main weak components of anisotropy inherent to duller and brighter layers that influence coal strength (Bieniawski, 1968a; Bieniawski and Van Heerden, 1975). At the same time, the natural fractures and porous of coal are responsible for effects of fluid pressure and gas content changes within those structures. A reason that measurement of coal strength might be affected by the confining pressure of the laboratory tests (Medhurst, 1996). Also, it should be mentioned that coal is a material that has the ability to sustain some load beyond their peak strength. Nevertheless, more than five decades ago, Hobbs (1964) reported the wide variation of measured strength test results on coal.

The coal complexity is illustrated in Figure 6 where a transition from intact to a typical cleated seam is presented by Trueman and Medhurst (1994). The combined effect of density and distribution of cleats planes in failure per lithotype within a coal seam play a role to understanding the scale effects (i.e. influence of size and structure of the tested specimen) on coal when investigating the mechanical property estimates of laboratory tests (Medhurst, 1996). For the field-scale strength, the general knowledge is that it reduces while the deformability increases as a function of increase in total defects with increase in specimen volume (Brady and Brown 1985; Hoek and Brown, 1980; Brown, 2008). Ideally, experimental laboratory tests should be performed on intact specimens (Hoek and Brown, 1982; Bieniawski and Bauer; 1982) while results can be useful to describe the rock behaviour.

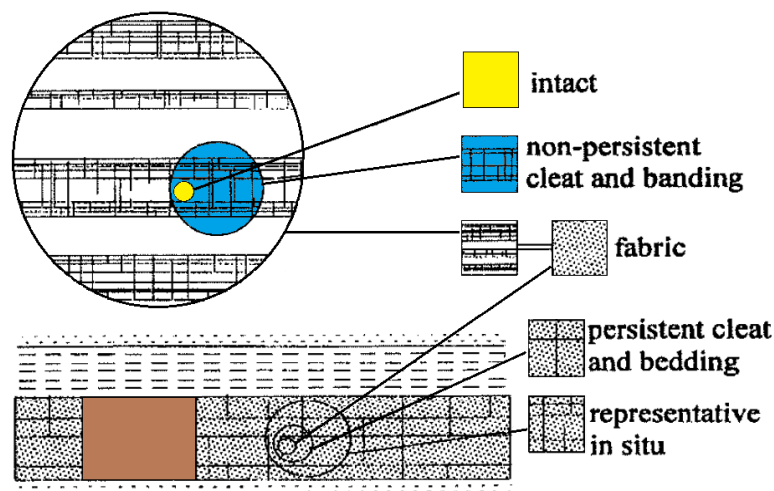


Figure 6 Idealised diagram showing the appearance of coal at different scales (Trueman and Medhurst, 1994).

In this attempt to describe the rock behaviour, the relationship between stress and strain in a rock material observed in laboratory might be explained using constitutive laws such as: linearly elasticity, elastic-plasticity, poroelasticity, or viscoelasticity. The linear elasticity or linear deformation, which is based on the Hooke's law, describes the elongation of the isotropic material as linear proportional to the stress, according to the Young's modulus. The elastic-plastic occurs when an axial load is applied to the specimen and the material begins to deform in elastic plastic way, until some point when the applied deformation stops, the specimen is unloaded, and the material holds a permanent strain. The poroelasticity behaviour is well-understood for soil (Terzaghi, 1996) and it can be described as the forces acting on it; for instance, it shows the way in which changes in fluid pressure change the dimensions of the material within the confines of elastic behaviour. Then, the viscoelasticity which includes a time-dependent effect, refer to the behaviour of a rock containing pore fluid.

2.4.3 Reservoir modelling

Numerical modelling simulations are mathematical models governed by equations solved numerically once the associated boundaries and the initial conditions are informed. The algorithms used in numerical modelling can be quite complex, depending on the detail to which one would like to simulate. More advanced techniques allow for use of constitutive equations in addition to information about discontinuities (e.g. joints), microstructures, and their interactions within a model to be replicated, also taking the scale effects in account. Notice that, adjusting smaller-scale properties for CSG, which are typically attained through field or laboratory testing, into those of a larger scale for modelling can be challenge. An advantage of numerical analysis is to allow an understanding of complex rock behaviour by observing the effects of each individual parameter and rock structures inputted into the model.

Reservoir models are mainly used to analyse the following: (i) adsorption/desorption of gas to coal surfaces (Langmuir isotherm approach); (ii) dual porosity of coal seams; (iii) diffusion of gas from coal matrix to fracture systems (Fick's Law); (iv) multiphase flow (gas/water) in the fracture system (Darcy flow), and (v) shrinkage of the matrix due to gas desorption. Different reservoir models will utilized different approaches, e.g. empirical, equilibrium (pressure-dependent), non-equilibrium (pressure and time-dependent) models. Examples of software packages for reservoir models include: ECLIPSE model; Arenas 2004; FracMan; COMET3 model; Generalized Equation-of-State Model (GEM); Tech SIM; SIMEDWin; FLAMED model; PFLOTTRAN; Petrel; etc.

Following that, the modelling tools can be used to simulate a variety of scenarios. For example, simulations can be used to model the well integrity; to estimate gas production; to estimate issues associated to changes on design or well installation; to predict permeability; to assess hydraulic fracturing on coal seams; to simulate CO₂ storage; to simulate water-related impacts from production wells; to investigate the connectivity between coal seams; to predict the depressurisation of aquifers; to forecast recovery of aquifers when production terminates; to predict changes to groundwater quality and/or or connectivity to surface water; to estimate ground subsidence; etc.

All models are an attempt to represent the reality, they contain assumptions and/or simplifications that influence the level of confidence on the results. Limitations in computational resources may also constrain the amount of information that can be included in a numerical model. While the errors or uncertainties inherent within modelling results might be estimated, they tend to be attributed to field measurements and the complexity of natural systems. Therefore, the importance of adequately addressing geological and geomechanical behaviours of the coal and the surrounding rock with reference to their natural characteristics and mechanisms provides a better understanding of the fundamental mechanics of rock behaviour. Together with information of stress magnitude data (tectonic stress) (Cuthbertson, 1990; Hillis et al., 1998, 1999; Hillis and Reynolds, 2000, 2003; Reynolds et al., 2002, 2003; Zhao and Muller, 2001; Heidbach et al., 2010; Hamilton, 2014; Ziegler and Heidbach, 2017; Rajabi et al., 2017; Heidbach et al., 2018) which is essential for modelling calibration. Thus, a reservoir engineer can make an appropriate choice regarding the application of numerical methods for planning and design. Moreover, the models should be continuously revised and updated as more data become available.

Particularly for CSG reservoir, it is anticipated that the challenge to numerically simulate the Surat Basin is to understand the micro-mechanisms of coal as well as the mechanical characteristics of the surround strata. Then detailed coalbeds might be simulated by including the appropriate microstructural features of coal, the microstructural interactions within a model, the natural fractures, the geological structures, the stratigraphic rock sequence, and the in-situ stress regimes, all according the scale of the model.

2.5 EXPERIMENTAL CHARACTERISATION OF COAL MECHANICAL PROPERTIES

The response of the coal seam and the interbedded rock to a certain mechanism of breakage need to be investigated to derive the geomechanical properties of the materials. The parameters obtained by

breakage techniques either using quasi-static or dynamic process can be directly used in reservoir modelling simulations. Hence, it is worthwhile to elaborate on alternative methods of rock characterization, as an attempt to address the complexity of natural systems which are critical for numerical modelling simulations.

A comprehensive test largely used by the mining industry is the Uniaxial Compressive Strength (UCS), but an important issue to address for UCS testing is to obtain representative intact core samples. Following the motivation for understanding the compressive strength of the basin environment, it is pondered that the most fundamental element of a breakage mechanism, which is critical for fracture stimulation, is the breakage of a single particle. The phenomenological understanding of breakage of a single particle can be investigated using a metallurgical approach. In comminution, the fundamental properties of the fracture process occurring on particles loaded, mainly in compression, can be measured. The drop weight (DWT) test principle (Gross, 1938), is to establish a relationship between the net breakage energy and the new surface generated. However, the energy applied by the DWT is usually higher than the energy required for the first breakage of a particle. Over time, a number of variations for the DWT were developed. The Short Impact Load Cell (SILC), a further developed version of an instrumented DWT, can provide information for the primary breakage with the advantage of estimating tensile strength and fracture force. Another consideration is to conduct further interpretation on the continuity of crack propagation through distinct microlithotypes of low rank coal, which can be done using the Shore Scleroscope Rebound Hardness (SSRH).

The alternative laboratory experiments utilised in this thesis are the Uniaxial Compressive Strength (UCS), the Short Impact Load Cell (SILC), and the Shore Scleroscope Rebound Hardness (SSRH). The experimental work is used to measure fundamental properties of brittle and non-brittle materials such as strength (both compression and tension), Young's modulus, hardness, and fracture force. The experiments are used to explore the effects of size, shape, and/ or orientation of small specimens, while the fields of fracture (brittle) and flow (ductile) behaviour might be observed. Additionally, it is anticipated that some insight about porosity, and sensitive to grain size and to the presence of clay minerals might be captured for low rank, sub-bituminous coal. However, the tests should not fulfil the complexity of CSG production, such as the effects of volumetric change due swelling and shrinkage.

The following topics do not intended to be a comprehensive review of the alternative laboratory experiments utilised in this thesis, the focus is to give an introduction about the methods. Further discussion about the apparatus and testing will be given along the thesis.

2.5.1 Uniaxial Compression Strength

The uniaxial compressive strength (UCS) is a servo-control test which involves application of homogeneous stress, while it allows for measurements of lateral strain. The mechanism of breakage is a two-point contact, and the breakage occurs at slower stressing velocity. The UCS test is dominated by the elastic properties of the material under compression loading. When the contact between compression platens and the rock specimen occur, the force increases linearly with the deformation. Then, a progressive development of cracking might be observed during load until the fracture takes place, last the force drops rapidly. The time required to cause fracture depends on the deformation rate of load and the intrinsic properties of the rock specimen tested. In brittle rocks the servo-control tends to be more effective at smaller deformation rates (Peng, 1973; Houpert, 1974), and it tends to be abrupt as observed on a macroscopic scale.

The UCS test is used to determine the strength of the intact rock material and as such governs partially the strength of a rock mass. Typically, the UCS test is performed at standard size core, and intact rock specimens between discontinuities (means good quality samples) are required. Furthermore, the specimen length-to-diameter ratio is important as more uniform stress is expected for distances of up to roughly half a diameter from the specimen' ends when the behaviour is substantially elastic. Hawkes and Mellor (1970) showed an analysis of elastic stress distribution in a specimen tested for UCS with radial constraint at the ends, and demonstrated the relative intensity of stressed regions across the specimen tested (Hawkes and Mellor, 1970). But controversy exist about the sensitive to the platen or end effects conditions influencing the specimen to present a particular failure mode (e.g. axial splitting). Another general observation when measuring intact rock strength is that the tensile strength tend to be of the order of one-tenth of the uniaxial compressive strengths. These discussions about the need to test intact material, the specimen length-to-diameter ratio, failure modes, and compressive/tensile strength correlations, are all of interest when characterisation of the material is proposed to be performed for smaller specimens' sizes.

2.5.2 Short Impact Load Cell

The Short Impact Load Cell (SILC) test involves dynamic stress prior to fracture while the probability of fracture is based on the Griffith's theory. Following the Griffith's theory of fracture,

the strength of brittle rock material is governed by the initial presence of microcracks (Jaeger and Cook, 1979). Then, failure is likely to occur when the interatomic cohesion of the material is overcome by an oriented crack-like flaw (such as the natural fractures for coal), which gets extended beyond its maximum tensile stress component (Griffith, 1924). Note that, the Griffith's theory does not consider the effects of the closing cracks under load and the frictional effects that can arise (e.g. UCS test). Also, the Griffith's theory is claimed to refer only to the initiation of the failure on the scale of the cracks, not to crack propagation (Brace 1960; Brace and Bombolakis, 1963; Hoek and Bieniawski, 1965; Bieniawski, 1967a).

According to Gurney and Rowe (1948a, 1948b), an extension fracture must involve failure of bonding grain contact under local tensile stress. The macroscopic deformation is an integrated average of the localized deformation at all the grain contacts in elastic contact under normal loading. Furthermore, the extension fractures tend to originate in response to local tensile stresses around flaws, cleats, or heterogeneities in the coal arising in relation to axial splitting (Scholz et al., 1986). These natural fractures, flaws or heterogeneities provide a local net of tensile stress component through which the crack is propagating, similar to Jaeger and Cook (1979) description. Also, it is known that the direction of the natural fractures, flaws or heterogeneities into the specimen axis relative to the impact orientation, affect the plane of propagation and the crack orientation (Brace and Bombolakis, 1963; Bombolakis, 1964; Hoek and Bieniawski, 1965; Gramberg, 1965, 1970; Fairhurst and Cook, 1966; Holzhausen and Johnson, 1979).

Overall, the SILC test allows to explore of difference about fracture initiation and propagation for homogeneous and heterogeneous rock specimens, also influenced by the shape effect (random irregular particles and mini-core specimens), and sizes. At the contact between bodies, the shear localization involves the coalescence of clusters of such Hertzian contact stress which also depends on the interplay of dilatant (increase volume), and compactant (decrease volume) processes. This inelastic volume changes reflect changes in the structure (Bridgman, 1949) or microstructure of the rock associated with the deformation processes of pores or cracks. For homogeneous material the crack propagation is expected to be a single crack across the specimen. But for heterogeneous rock such as coal, the final fracture gets the contribution of other local natural fractures and cracks rather than the propagation of a single crack across the specimen. Likewise, fracture toughness is an important aspect of describing the fracture energy consumption rate required to create new surfaces in the comminution process (Bearman et al., 1989; Donovan, 2003). Donovan (2003) showed through experimental work for breakage of single particle (using High Energy Crushing Tests) that

there is a strong relationship between fracture toughness and specific comminution energy. According to Donovan (2003), the specific comminution energy required to reduce a rock particle to a given size increases with fracture toughness.

2.5.3 Shore Scleroscope Rebound Hardness

The Shore Scleroscope Rebound Hardness (SSRH) test is used for measurement of hardness, quite similar to a scratch hardness test, by promoting a local stress concentration at the material. Previously used for metals (gold, copper, lead, nickel, steel, etc) the SSRH might be used to test a varied of rock types, from brittle to ductile. Klawitter et al. (2015) showed the hardness of coal using the SSRH while the indentation pattern post-testing was observed with a scanning electron microscope (SEM). It was demonstrated that combination of both devices (SSRH and SEM) allows for observation of fracture propagation on microstructural features including grains, pores and microcracks such as cracks, cleats, and other fractures (with varied orientation, population, shape, etc.) on microscope scale. Though, it might be difficult to distinguishing between real (pre-existing) cracks and those introduced in the specimen preparation. Note that microcracks derive from differences in compressibility and thermal expansion of grains and macerals under pressure and temperature changes, while also affected by the tectonic stress.

Aspects of brittle behaviour into the micromechanics is well elaborated by Paterson and Wong (2005). The brittle behaviour involves failure following either small or large amounts of inelastic strain when compared with the elastic range. Griggs and Handin (1960) described two types of brittle failure: shear fracture and extension fracture. While a transition between the two types of brittle failure occurs when a gradual change in orientation of the failure surface can be observed (Brace, 1964; Hoskins, 1969). In a broad perspective, the micromechanics of brittle fractures can be differentiated between strongly and weakly cohesive porous rocks. It refers to an understanding of the growing or nucleate of microcracks, when stress concentration located at pore, cleats or flaws/cracks are eventually overcome by the applied stresses and result in tensile stress concentrations that lead to microcrack initiation. Therefore, a simple investigation using SSRH testing can provide significant information for hydraulic fracturing for the CSG, and observation of microcrack in the form of damage evolution (nucleation/propagation of cracks).

2.6 SUMMARY

In rock mechanics, the effect of scale and anisotropy of rock specimens has long been recognized, but there are various factors that influence coal (fracture, porous, microlithotypes, mineral matter, etc.) that are not individually captured. Therefore, it is not surprising that despite largely studied, the difficulties in interpreting the results from laboratory to those representatives of the in-situ when characterising the coal persist. Apart from different coal scale, the individual lithological layers forming the coal seam might vary in lateral persistence, thickness and for coal of different type and rank. Geomechanical quantification and characterization cannot be transferred across rank nor through boreholes, and measurement of rock properties deserves to be site-specific, as they consist critical information for modelling CSG reservoir.

A rational approach is to go back to the basics to investigate the coal and interbedding using alternative laboratory methods to test small specimens (<25 mm in diameter). Then, some important characteristics of coal, such as its unique structure and composition, might be accentuate. Description of the geological environment for the source rock of interest for gas extraction and the interbedded material are brought into context. An increase in exploration and production, also increasing depth, require a close looking into the rock itself. The shortcomings with regard to rock characterization, including extrapolation of database across basins or even neighbouring wellbores, are proved unsustainable. Particularly in the Surat Basin, the scale of interest to investigate hydraulic fracturing should consider small volumes of rock for contrasting geomechanical behaviours.

Chapter 3

MINI-CYLINDER SPECIMENS SCALED

Karina Barbosa (PhD candidate) conducted specimen preparation and testing, interpreted data, prepared figures and graphics, and wrote the manuscript.

Joan Esterle (Principal PhD supervisor) proposed the experiment, reviewed, discussed and edited the manuscript.

Zhongwei Chen (Associate PhD supervisor) provided the laboratory facilities, reviewed, discussed and edited the manuscript.

Summary

The variation of test results on laboratory measurements of coal strength are widely reported. For this unique rock, apart from its natural variability including structural features and bedding planes, justification is made that laboratory specimens of coal are not intact at sizes that were normally considered intact for other rocks. Supported by those observations, this chapter presents a series of test results for the unconfined compressive strength (UCS) test performed on intact mini-core specimens of low rank, sub-bituminous coal, across a range of sizes from 9.3 to 22.6 mm, and compared to data from larger sizes to investigate scaling approaches. This experimental study is designed to address intact properties of coal useful for borehole stability analyses by the coal seam gas industry, and to see if smaller, rather than larger core sizes can achieve reliable results. During a UCS test, the initial stage is known by closing/ collapse of pre-existing micro-cracks or porosity of the specimen, followed by a more or less linearly elastic section where stress and strain are proportional to each other. Next, as the stress increases, the rock specimen behaves plastically until the stress goes beyond the elastic limit of the rock. Then small cracks start to propagate into the specimen, and the deformation mechanisms take place (inelastic behaviour). Finally, the peak force is reached beyond which there is a weakening and the specimen fails. These mechanisms occur at any scale and are captured by the mini-core specimens tests.

Scaling compressive strength from mini-core specimens of sub-bituminous coal

Karina Barbosa^{ab}, Joan Esterle^{ab}, and Zhongwei Chen^c

- a. School of Earth and Environmental Sciences, The University of Queensland, St. Lucia 4072, QLD, Australia*
- b. UQ Centre for Coal Seam Gas, The University of Queensland, St. Lucia 4072, QLD, Australia*
- c. School of Mechanical and Mining Engineering, The University of Queensland, St. Lucia 4072, QLD, Australia*

Submitted manuscript to the Journal of Rock Mechanics and Rock Engineering

Abstract

This study presents the results of laboratory tests conducted on a series of mini-cylinder specimens to measure the uniaxial compressive strength of sub-bituminous coal, which is sparsely recorded in the public domain. The measurements were made on mini-cylinder specimens (non-standard) sized from 9.3 to 22.6 mm in diameter, sourced from the Surat-Clarence-Moreton Basin in Australia, an important region for coal mining and coal seam gas extraction. The tested specimens presented poorly developed cleats and were texturally classified as non to poorly banded, although the composition is rich in vitrinite group macerals. The inherent variability of experimental coal strength results was found to be related to the degree of fracturing of the mini-cylinder specimens of coal, either pre-existing or induced from specimen preparation, to fabric and texture. In contrast to expectations, the specimens analysed for petrographic showed minor dependence on coal lithotype. The results from the mini-cylinder specimens could be scaled to predict the behaviour of larger core sizes commonly used for testing mechanical variability and for estimating full seam rock mass strength.

Keywords: coal; geomechanics; uniaxial compressive strength; mini-cylinder specimens; lithotypes

3.1 INTRODUCTION

Coal is an anisotropic and heterogeneous material. Testing and modelling coal is challenging because its strength varies as a function of material properties such as:

- Rank or thermal maturity, grade or distribution and occurrence of mineral inclusions (Zhao et al., 2014a, 2014b; Gao et al., 2014);
- Lithotype or maceral composition (Ting, 1977; Rusnak, 2018);
- Texture and fabric that is manifested by the band and phyteral thickness, and the distribution and the volume variation of microstructures influenced by loading direction (Jaeger, 1971; Scholtès et al., 2011; Song et al., 2018);
- Organic molecules and the polycyclic aromatic hydrocarbon re-arrangements (Pan et al., 2013);
- Intensity of fracturing at different scales (Medhurst, 1996; Medhurst and Brown, 1998; Pan et al., 2013; Poulsen and Adhikary, 2013); and
- Rate of loading of testing device, specimen size and shape (Bieniawski, 1968a; 1968; Wagner, 1974; Bieniawski and Van Heerden, 1975).

The intensity of fracturing, or cleat, increases rapidly with coal rank from lignite to the sub-bituminous/high volatile bituminous threshold, but then stabilizes somewhat in the high volatile through low volatile bituminous rank (Law, 1993). For a given rank, increased cleating can also be associated with increased banding or occurrence of bright vitrain in coal lithotypes (Ting, 1977; Dawson and Esterle, 2010). Notice that, lithotypes allow for a description of coal types with the naked eye based simply on observation of the proportion of vitrain (Stopes, 1919; Taylor et al., 1998) and these will also correspond to variation in the maceral group percentages (Teichmüller, 1989) and their precursory plant tissues in the peat phase (e.g. Hower and Wagner, 2012). As a result, the higher the rank and the megascopic vitrain content, the more intense is the cleating for the boundaries described, and the weaker is the coal (Ting, 1977). The total coal porosity also tends to decrease with increasing coal maturity (Gurdal and Yalcın, 2001), at least up to low volatile bituminous rank (Rodrigues and Lemos de Sousa, 2002), and this affects the mechanical properties. Different coal lithotypes, that have different banding and natural fracture intensities, exhibit

different strengths, and this information can guide pillar design (Rusnak, 2018). In the absence of direct strength measurements other proxies of coal material behaviour, such as grindability, can be used to estimate coal strength (Colwell and Mark, 2005).

Core specimens are commonly used to test for coal mechanical strength, but they can be difficult as well as expensive to source and measure, in particular large diameter cores (Bieniawski, 1968; Medhurst, 1996; Hoek and Brown, 1997; Medhurst and Brown, 1998). Measurement of different core sizes allows one to scale upwards with the objective to emulate the rock mass that can contain more fractures than does intact rock used for testing. A common guide to scale test data to engineering design is the well-known normalised relationship proposed by Hoek and Brown (1980) where the rock mass is equal to $0.58 \sigma_{ci}$ for a 50 mm diameter core (σ_{ci} is the strength of the intact rock tested at standard size). The Hoek and Brown (1980) approximate relationship is based on reviewed data from the literature including UCS measurements on specimens from 10 to 200 mm diameter, mostly hard and unjointed intact rock (isotropic) only (Figure 7). Thus, Hoek and Brown (1997) attributed the reduction in strength with increased specimen size to failure through and around grains of the intact rock. For jointed rock mass when discontinuities are close to each other, the Generalized Hoek-Brown failure criterion is commonly applied. According to Laubscher and Jakubec (2001), the strength of heterogeneous rock depends on the rock block with micro-defects and defects, where the rock mass ranges from 0.65 to 0.32 σ_{ci} ; however, no reference to coal was made.

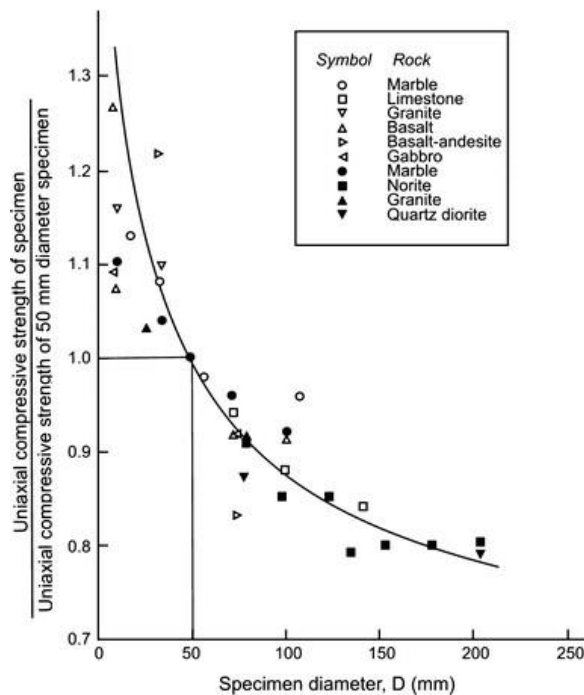


Figure 7 Influence of specimen size on the strength of intact rock (after Hoek-Brown, 1980).

Two recognized studies particularly conducted on scaling coal properties by increasing the specimen size while maintaining the specimen shape were conducted by Bieniawski (1968a) (bituminous coal from Witbank Colliery in South Africa) and Medhurst (1996) (medium rank, bituminous high volatile A from Moura Colliery in Australia with maximum vitrinite reflectance of 0.88% by Esterle, 1994). Medhurst explored the influence of different lithotypes, and illustrated the decrease in strength with increased vitrain banding. Overall, testing suites of small, standard and large-scale size specimens were conducted to measure the peak strength, mainly in bituminous rank coals (Bieniawski, 1968; Wagner, 1974; Bieniawski and Van Heerden, 1975; Medhurst, 1996; Medhurst and Brown, 1998; Song et al., 2018). However, strength data on lower rank sub-bituminous coal, which is rarely mined underground, is still sparse in the public domain.

The emergence of coal seam gas (CSG) exploration and exploitation in the sub-bituminous coals of the Jurassic age Walloon Coal Measures in the Surat-Clarence Moreton basin necessitated a study of coal strength for borehole stability and potential for fracture stimulation. The seams exhibit a variable contrast between thinly-bedded coal (<0.5 to 2 m, average thickness of 0.4 m), interbedded with carbonaceous tuff or claystone (Figure 8). The coals in this basin are jointed but cleats are poorly developed, except for some incipient cleats in the few bright bands or weakness planes created by the banding texture. There are multiple seams, better described as seam groups, distributed through the ~350 m thickness of the coal measures (stratigraphic framework in Figure 9). Therefore, the coal seams might be compared to multiple robust pillars (i.e., short in height with ‘infinite’ thickness) intercalated between softer (or less hard) material. However, the first issue was to obtain measurements of coal strength.



Figure 8 Illustration of Walloon Coal Measures showing variation in lithological units, and typical interbedded and banded nature of the plies (ruler stick is 50 cm long) (highwall photo courtesy of New Hope Mine).

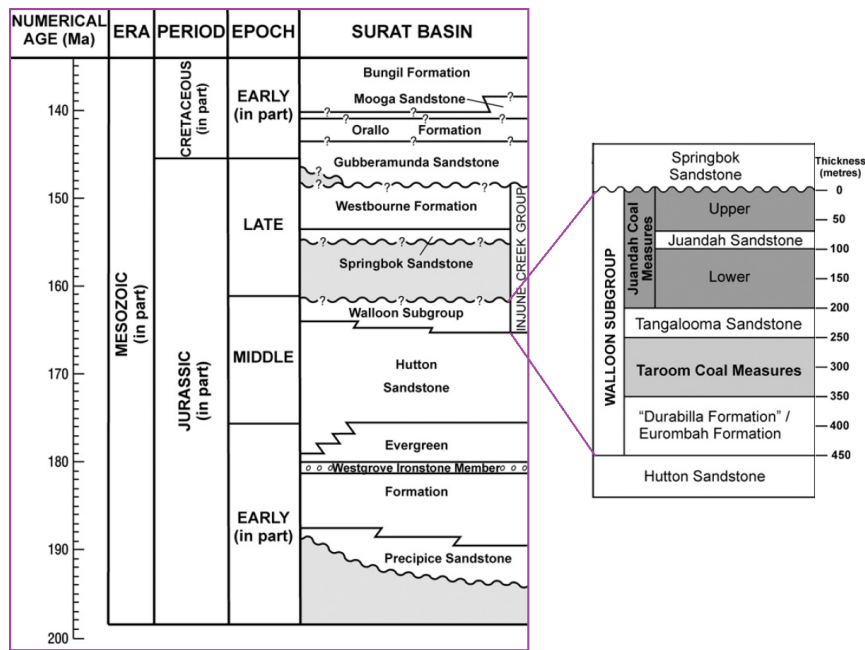


Figure 9 Stratigraphic column for the Surat Basin (McKellar, 1998), and the Walloon Subgroup (Hamilton et al., 2012).

As exploration core was unavailable, the objective of this study was to obtain geomechanical properties for the sub-bituminous Walloon coals using mini-cylinder specimens. In heterogeneous, fractured rock such as coal, smaller, rather than larger core specimens may be a better option to reflect the intact rock behaviour (Hoek, 1983). Logistically, smaller cores can also give flexibility for multiple specimens when exploration core is sparse, or specimens need collecting from outcrop or open cut coal mines. If the smaller cores can be scaled to the rock mass properties, then more specimens might be obtained to characterise the variability in the coal lithotypes through the measures. Although, it is also unknown whether coal lithotype (Stopes, 1919; Hower et al., 1990) has a strong influence on coal strength at lower ranks.

Laboratory unconfined compressive strength (UCS) testing was conducted on mini-cylinder specimens ranging from 9.3 to 22.6 mm diameter, fashioned from distinct lithotypes of the same low rank coal within a seam ply. The coal was difficult to core at the specimen test size, so cylinders were fashioned as described in the methods section. We explored the use of these mini-cylinder specimens to (i) more truly reflect intact rock on physical properties results (UCS and elastic modulus); (ii) improve the logistics of sampling for differences (or not) in behaviour between different lithotypes, that could later be assigned back to the full seam; (iii) scale the results to standard core sizes (50±10 mm diameter, ASTM D4543) and the rock mass; and (iv) verify the influence of maceral subgroup and mineral matter composition on strength in low rank coals.

3.2 BACKGROUND

Lithotypes refer to a classification of coal banding texture and organic composition at millimetre to centimetre scale (Stopes, 1919; Hower et al., 1990). According to Hower and Wagner (2012), it is not uncommon that the depositional sequence or arrangement and the thickness of lithotypes are highly variable. The coal organic composition and texture was inherited during peat deposition and reflects the starting size of the plant tissues and their degree of degradation in the peat stage. In coal petrography, the following maceral groups of vitrinite, liptinite and inertinite are analysed to capture the variation in organic composition (Teichmüller, 1989). Texture is captured at the maceral subgroup level, especially among the vitrinites for structured (telovitrinite) and unstructured (detrovitrinite and gelovitrinite) components (ICCP System 1994).

In rock mechanics, UCS is a key parameter to derive other fundamental geomechanical properties, such as friction angle, cohesion and tensile strength. However, it is recognised that the effect of scale (Bieniawski and Van Heerden, 1975) and strength anisotropy is influenced by the presence of cracks and fissures, bedding and lamination, pore pressure, environment, rate of loading, time effects, specimen size and shape (Bieniawski, 1967b, 1968a, 1968b). Indeed, the compressive strength of coal is one of the most difficult properties to establish experimentally (Bieniawski, 1968a) as it is organic in origin and has unique and variable constituents and properties (Hoek and Brown, 1997). Also, coal is site specific, and it is one of the few rock materials for which both laboratory and in-situ testing of small, standard, and large-scale size specimens were conducted to measure the peak strength (Bieniawski, 1968a; Wagner, 1974; Bieniawski and Van Heerden, 1975; Medhurst, 1996; Medhurst and Brown, 1998; Song et al., 2018).

For the rock mass scale in coal, Bieniawski (1968a) reported the estimates of unconfined compressive strength for coal pillars of various dimensions, based on extensive in-situ underground measurements. The cubic coal specimens of thirteen distinct sizes, ranging from small specimens to full pillars (19 to 2000 mm). Medhurst (1996) and Medhurst and Brown (1998) reported the results for a series of true triaxial compressive tests conducted in the laboratory. The cylindrical coal specimens of four distinct sizes (61, 101, 143, and 300 mm in diameter) with heights approximately twice the diameter size, and variable peak confining stresses. For those publications, the testing of large-scale specimens of coal result in strengths that are highly variable (i.e., exhibit a large amount of scatter). However, the peak strength remains constant for certain specimen sizes, i.e.,

independent of the specimen size if greater than 1.5 m (testing cubic shape 2:1 ratio) (Bieniawski, 1967b) and 1.0 m (testing cylindrical shape 2:1 ratio) (Medhurst, 1996).

Recently, Song et al. (2018) explored the microstructure-related effects of loading direction (i.e. varied dip of the bedding from 0° to 90°) from smaller to standard core specimens (25 to 75 mm in diameter) on strength of coal. The U-shape form of the relationship between UCS and anisotropy (Jaeger, 1971) showed that the contribution of microstructures on uniaxial compressive strength differs for different orientations of loading relative to anisotropy (Song et al., 2018). Song et al., (2018) attributed the decrease of coal strength with increasing specimen size to the enhanced microstructural volume of a larger specimen. It is supposed that the Wudong coal tested by Song et al. (2018) is either low volatile to anthracite coal which is considered hard coal, based on the moisture content ~1.8% reported.

If tested for small or standard size specimens then the laboratory results need to be adjusted or scaled to reproduce the field-scale strength of the rocks. It is well understood that rock mass input parameters used for design cannot be directly assigned from laboratory properties. Some popular means for scaling rock properties derived from testing intact rock to in-situ rock mass in a mining environment are done through visual observations such as the GSI (Geological Strength Index), and the MRMR (Mining Rock Mass Rating) systems. Unfortunately, the broadly applied GSI system is not applicable for quantification of the coal rock mass strength due to the coal heterogeneity bounded by blocks forming open joints, nor for borehole stability assessment due to scale effect (Medhurst and Brown, 1998; Kaiser et al., 2015). The last update of MRMR (Laubscher and Jakubec, 2001) showed interesting modifications when it abandoned the Rock Quality Designation (RQD) as an input parameter and included the concept of rock block strength, which accounts for the effect of cemented joints and veins.

3.3 RESEARCH METHODOLOGY

3.3.1 Sample collection

Samples targeted different coal lithotypes within seams exposed at an open cut mine extracting the Walloon Coal Measures. The coal is relatively blocky, allowing small to large samples (about 5×5×5 to 30×30×30 cm) to be collected from different plies with different lithotype composition. The coal at the sampling location is low rank, sub-bituminous with maximum vitrinite reflectance

of 0.56%. A total of three distinct plies were classified, sampled, and tested for this study, namely (i) C8 ply-banded (PC8-B), (ii) C8 ply “white marks” banded (PC8-WB), and (iii) C6 ply dull (PC6-D). The white marks are small lenses of clay distributed in the matrix of the coal. All three distinct plies were collected from the same pit location, while PC8-B and PC6-D were in the same bench. The density of the coal varies between ~ 1.3 and 1.5 g/cm^3 . Maceral analyses were used to confirm the sample composition.

3.3.2 Specimen preparation

Representative mini-cylinder specimens were fashioned from rectangular blocks using manual artisanal preparation (Figure 10). Attempts to drill/core different size specimens were unsuccessful with available tools. To overcome the technical limitation and minimize the damage to coal specimens, small intact pieces of coal were carefully cut into rectangular shapes/blocks. Then a rotating polishing plate (grinding surface) was used to completely smooth the edges of the rectangular piece until it was converted into mini-cylinder specimens. The mini-cylinder specimen length was cautiously established by trimming the excesses with a mini-saw machine, and the ends were again ground on a rotating polishing plate.

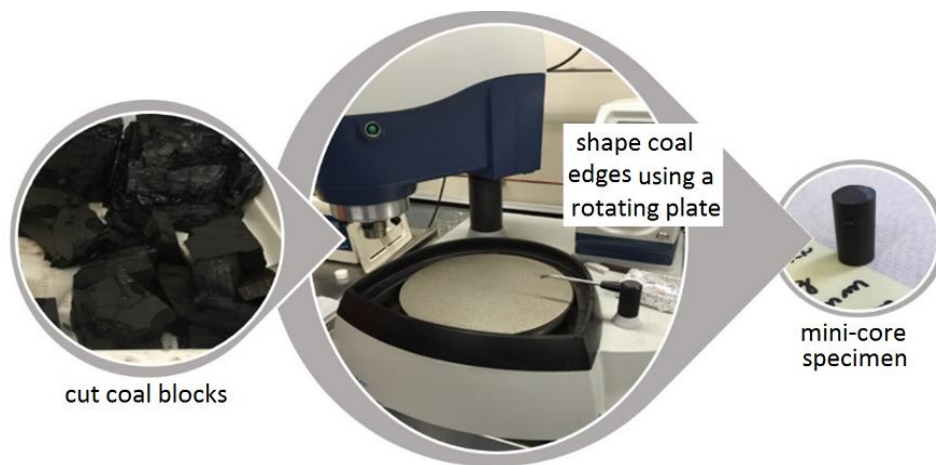


Figure 10 Preparation steps to achieve the mini-cylinder specimen shape and size.

All the specimens' dimensions were checked with a vernier caliper to ensure the cylindrical profile of lateral wall (Figure 11) and parallelism of the ends (base/top), which are crucial for such specimen size. The accuracy of each mini-cylinder was aimed at the second decimal place followed by constant check during the preparation. Each mini-cylinder specimen was then individually wrapped with wrap/film-plastic to avoid further moisture disturbance and oxidation.



Figure 11 Example of one mini-cylinder being verified for the cylindrical profile of lateral walls.

During this unconventional preparation, each mini-cylinder specimen was also verified to avoid imperfections on end- and wall-faces, which are crucial for such specimen size. Despite all the effort in specimen preparation, the nature of coal showed some defects (imperfections on ends/wall-faces) when grinding/polishing either through pre-existing or induced fractures. Therefore, not all mini-cylinder specimens of coal were considered pure ‘intact’ with no defects. Some mini-cylinder specimens contained single or multiple minor cracks and superficial damage, i.e., visible fractures particularly located at the end-faces, named minor defect. Other mini-cylinder specimens presented more prominent or notable damage, i.e., visible fractures located at wall-faces and/or end-faces, named pervasive or long defect. Even with sub-bituminous coal, the banded coal (PC8-B’s, Figure 12) tends to present more prominent defect or damage during specimen preparation. Approximately 65% of mini-cylinder specimens prepared from the PC8-B presented more prominent defect or damage, at both wall-faces and end-faces. Information about mini-cylinder specimens’ appearance were compiled (Table 3). This information was relevant and given the limited number of mini-cylinder specimens available for this study, it was decided to test all mini-cylinder specimens including those with pervasive and long defects (i.e., called ‘non-intact’ specimens). Last, it is acknowledged that sample bias has occurred by testing mini-cylinder specimens that survived the manual preparation process.

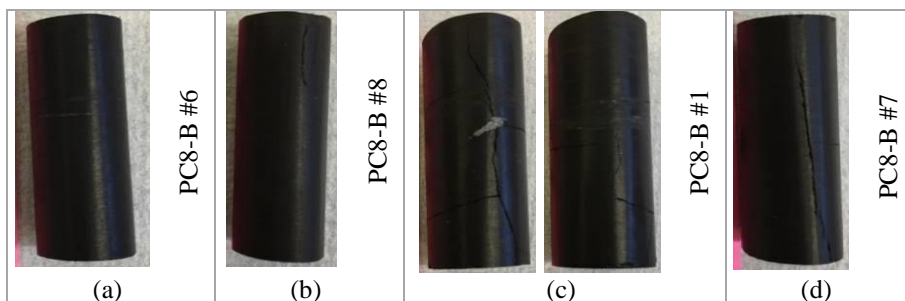


Figure 12 Examples of mini-cylinder specimens (not on scale) derived from PC8-B and classified by visual appearance (a) no defect, (b) minor defect, (c) pervasive defect, (d) long defect.

A total of 35 mini-cylinder specimens were prepared and they represent 17 at PC8-B, 5 at PC8-WB, and 13 at PC6-D. The diameter, length, and mass of each specimen was recorded and listed in Table 3. The mini-cylinder specimens were prepared with diameters ranging from 9.3 to 22.6 mm. However, the majority of the specimens' range between 9.3 and 16.5 mm since those with larger diameter (around 17 to 23 mm) were more likely to fail in preparation due to increased population of pre-existing fractures/ defects (Hoek and Brown, 1997). The mini-cylinder specimens presented a slenderness ratio (length-to-diameter ratio or L/D) of 2.3:1 in average (ranging from 1.9 to 2.7) following the standards (ASTM D7012-13). The slenderness ratio is significant to minimize the effect of frictional constraints at end-faces of mini-cylinder specimens i.e., by reducing the non-uniformity of the stress state in mini-cylinder specimens' centre part. The minimum number of specimens tested for each size was not pre-imposed, however it was attempted to have at least two mini-cylinder specimens for each size diameter. Overall, the mini-cylinder specimens were completed according to the ASTM (D2938-86/95; D4543-85; D7012-13), and ISRM (1999, 2007) guidelines and standards, except for the minimum diameter recommendation (47 or 54 mm according to ASTM or ISRM, respectively).

3.3.3 Uniaxial compression test equipment

All mini-cylinder specimens were loaded in uniaxial compression (axial load) using a fully automated digital machine. The machine is supplied with a load cell capacity ranging from 0 to 200 kN, digital display, user defined digital controls, software package, and real time graphic on screen (Figure 13). The mini-cylinder specimens were loaded in the direction perpendicular to the bedding planes (i.e., the angle between the loading direction and the orientation of the bedding plane was $\beta \approx 90^\circ$) to obtain the maximum strength values (Ramamurthy, 1993 and Song et al., 2018). Irregularities on both the platen and specimen end-faces that could potentially lead to local stress concentrations were checked prior to test commencement. The bearing faces of the upper and lower platens of the UCS testing machine were cleaned before placing the mini-cylinder specimen properly aligned on the lower platen.

The vertical displacement was measured from the lower platen by means of a 5 mm range linear variable differential transformer (or LVDT) mounted outside the cell. Axial load was continuously applied to produce a stress rate as constant as feasible throughout the test. The load cell was adjusted with ~100 kN to simulate quasi-static loading during each test. The stress rate selected was adhered to for all tests and the produced failure occurred in 1.5 to 4 minutes time-interval. Recording data started just before the mini-cylinder specimen was seated in the bearing parts of the

apparatus. The loading data/output, displacement, and time were directly recorded with a computer-based data acquisition system and analysed with an Excel spreadsheet. The laboratory experimental tests were undertaken in accordance with the ISRM guidelines (ISRM, 1979). It must be acknowledged that estimated values of UCS and Young's modulus reported elsewhere for coal or other rock material are all subjected to some influence explained through the difference in testing equipment and loading rates.



Figure 13 Photograph of the UCS testing machine used for mini-cylinder specimens.

3.3.4 Coal characterisation

The different lithotypes in this study were corroborated by petrographic characterisation of representative mini-cylinder specimens recovered after UCS testing was performed. A total of 11 mini-cylinder specimens that showed an axial splitting failure mode during the UCS test were prepared for petrographic analysis. Each of those specimens retained the full length of the original mini-cylinder specimen tested, whereas others had lost broken pieces and were incomplete for analysis. The 11 mini-cylinder specimens were confined into epoxy blocks sized 50×30×12 mm and polished for analysis (Figure 14). The petrographic analysis was performed at the University of Queensland, on a Leica DM 6000M microscope using the Hilgers' Diskus Fossil computer program by an accredited coal petrologist. The maceral subgroup level and reflectance analysis were performed in accordance with the ICCP System, 1994.



Figure 14 Examples of mini-cylinder specimens previously tested for UCS and prepared for petrographic analysis (blocks sized 50x30x12 mm).

3.4 EXPERIMENTAL RESULTS AND DISCUSSION

3.4.1 Failure mode

The observed failure mode on mini-cylinder specimens of coal was either powerful/violent, comparable to an abrupt burst with fragmentation into very small pieces, or less violent (similar to Bieniawski, 1968a description) with some warnings involving noise and crack burst that resulted in spalling of the specimen face. The fracture patterns observed from mini-cylinder specimens' post-UCS test were categorised into two, possibly three varieties: axial splitting (i.e., spalling from one face); double shear (i.e., at least one pyramid/cone type recovered); and multiple fracturing. The distinction between double shear and multiple fracturing is not very clear since not all fragments were recovered post-test. For those mini-cylinder specimens showing abrupt burst, it was inferred that double shear or multiple fracturing occurred, as most leftover fragments became unrecoverable. It was observed that about 32% of the coal mini-cylinder specimens could be categorized as axial splitting under uniaxial compression while others resulted in double shear or multiple fracturing. Each failure mode was presented schematically and photographically in Figure 15.

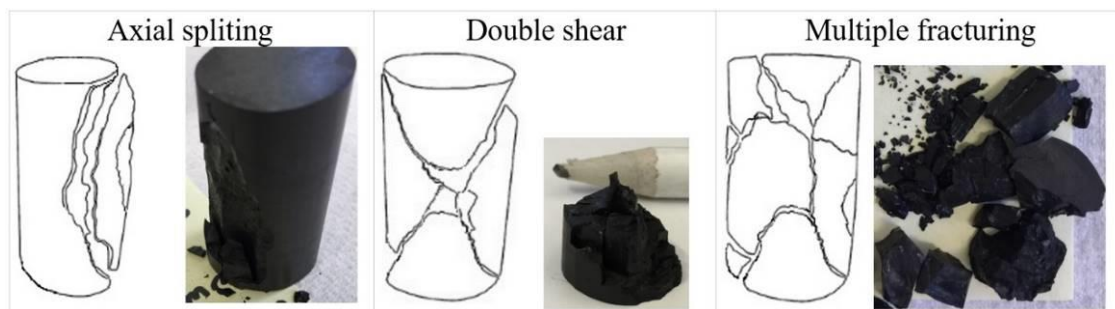


Figure 15 Schematic and photographic fracture patterns for failure modes observed on coal mini-cylinder specimens under uniaxial compression.

3.4.2 Results of strength and Young's modulus by ply

Individual information for mini-cylinder specimens of coal tested for UCS are summarised in Table 3. This table shows the three distinct plies (PC6-D in light blue, PC8-B in orange, and PC8-WB in light grey colour) where samples were collected, followed by information of mini-cylinder specimens that were prepared and tested. This information includes the specimen attributed number; mass; dimensions (diameter and length); slenderness ratio; compressive strength results; maximum strain results; estimated Young's Modulus; and visual appearance/quality (none, minor, pervasive, or long defect).

Table 3 Summary of mini-cylinder specimens tested and their mechanical properties.

Sample location	Number #	Mass	Diameter	Length	L/D	Strength	Normalised Strength (MPa)	Axial Strain (%)	Young's Modulus (GPa)	Appearance	Failure energy
		(g)	(mm)	(mm)	ratio	(MPa)					
PC6-D	4	23.9	23.7	43.8	1.9	48.08	59.84	2.04	2.59	(a)	(AB)
	5	13.8	17.8	42.3	2.4	54.61	52.85	2.02	2.71	(no)	(LV)
	8	6.4	13.5	31.9	2.4	70.98	69.09	2.57	3.02	(b)	(LV)
	2	3.3	11.9	24.0	2.0	72.20	82.34	2.76	3.09	(b)	(AB)
	7	6.7	14.1	32.1	2.3	72.88	73.63	2.80	3.04	(b)	(AB)
	3	3.8	12.7	23.6	1.9	74.76	92.53	3.08	2.96	(no)	(AB)
	9	6.0	13.8	32	2.3	78.96	78.32	3.15	2.95	(b)	(LV)
	6	6.0	13.6	32.3	2.4	84.33	81.67	3.00	3.21	(b)	(AB)
	12	2.8	10.7	24.2	2.3	90.86	92.40	3.37	3.37	(b)	(LV)
	13	3.0	10.8	24.5	2.3	93.88	95.18	3.29	3.04	(a)	(AB)
	11	2.8	10.8	24.8	2.3	94.31	94.46	3.24	3.02	(a)	(AB)
	10	3.1	11	25.5	2.3	101.23	100.44	3.72	3.04	(a)	(LV)
1	4.1	13.0	24.3	1.9	104.72	128.85	4.08	3.19	(a)	(AB)	
PC8-B	1	27.6	22.6	52.9	2.3	25.35	24.91	1.37	2.22	(c)	(AB)
	3	15.5	19.1	40.9	2.1	29.00	31.15	1.47	2.29	(c)	(LV)
	5	9.6	16.1	38.6	2.4	46.71	44.81	2.37	2.82	(d)	(AB)
	11	3.4	11.2	26.6	2.4	51.87	50.23	2.37	2.88	(d)	(LV)
	15	2.4	9.5	24.4	2.6	55.73	49.91	2.41	2.65	(d)	(AB)
	17	2.5	9.9	25.0	2.5	55.86	50.88	2.82	3.20	(d)	(LV)
	7	6.5	14.10	34.2	2.4	59.43	56.35	2.24	3.03	(d)	(AB)
	12	3.1	10.4	27.1	2.6	60.98	53.82	2.37	3.37	(d)	(AB)
	2	21.8	21.3	41.4	1.9	61.10	72.30	2.37	2.83	(b)	(LV)
	14	2.9	10.9	25.5	2.3	69.77	68.59	2.84	2.62	(d)	(AB)
	13	3.0	10.6	26.2	2.5	64.14	59.68	2.42	2.99	(d)	(AB)
	6	8.2	16.1	36.3	2.3	67.15	68.50	2.57	3.08	(a)	(AB)
	18	1.9	9.3	22.0	2.4	75.23	73.14	2.51	4.13	(d)	(AB)
	9	5.2	12.8	32.2	2.5	80.12	73.25	3.11	2.82	(a)	(AB)
	8	6.7	13.2	34.7	2.6	86.30	75.51	3.60	3.19	(b)	(AB)
16	2.3	9.4	25.5	2.7	105.05	89.07	4.08	2.87	(a)	(AB)	
10	4.5	12.3	27.5	2.2	110.50	113.67	6.89	3.21	(b)	(LV)	
PC8-WB	6	2.3	9.9	23.1	2.3	49.89	49.18	1.59	3.06	(b)	(AB)
	1	10.9	17.0	38.8	2.3	60.97	61.44	2.07	3.39	(a)	(LV)
	2	9.4	16.1	37.1	2.3	85.42	85.26	3.21	3.00	(a)	(AB)
	3	3.9	11.9	27.6	2.3	96.21	95.41	4.57	2.94	(a)	(AB)
	5	2.9	10.5	24.1	2.3	118.03	118.27	6.15	3.34	(a)	(AB)

Mini-cylinder *appearance* classified as (a) no defect, (b) minor defect, (c) pervasive defect, (d) long defect; and *failure energy* classified as (AB) abrupt burst, and (LV) less violent.

Figure 16 shows examples of typical stress-strain curve obtained from a UCS test conducted on a mini-cylinder specimen of sub-bituminous coal. No significant difference was observed for failure energy classified as abrupt burst or less violent. This example is referred to PC6-D #11, #12, and #13 (i.e., specimen location and specimen number), which were of similar dimensions (~10.8 mm diameter and ~24.5 mm length). The UCS result was ~94 MPa and Young's modulus was ~3.3 GPa (calculated as the average slope of the linear pre-peak portion of the stress-strain curve) (Figure 16).

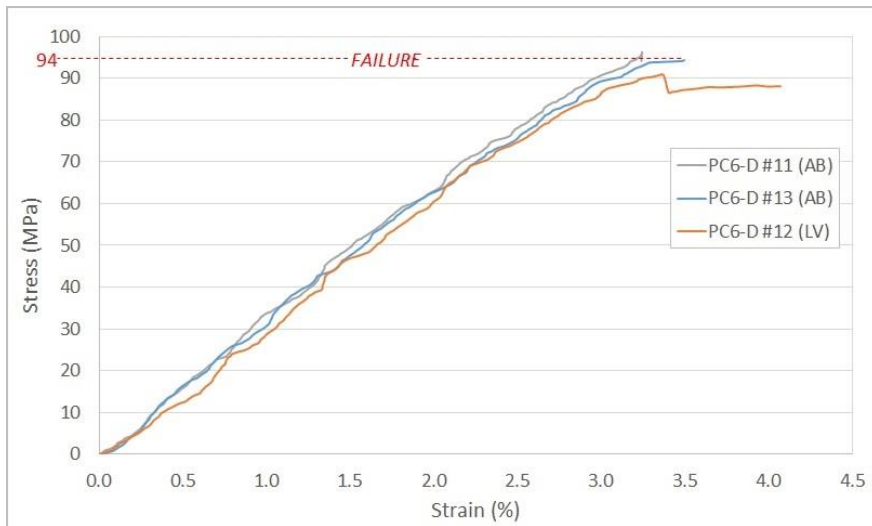


Figure 16 Example of the stress-strain monitoring result for mini-cylinder specimen PC6-D #11, #12, and #13, where (AB) is abrupt burst and (LV) is less violent.

Figure 17 illustrates quite good correlation involving all results for UCS versus maximum axial strain for the mini-cylinder specimens from three distinct plies. The trend appeared to be a linear increase in relation to each ply. Note that PC6-D and PC8-B seemed to be parallel trend lines except for a single point outside the curve (for PC8-B).

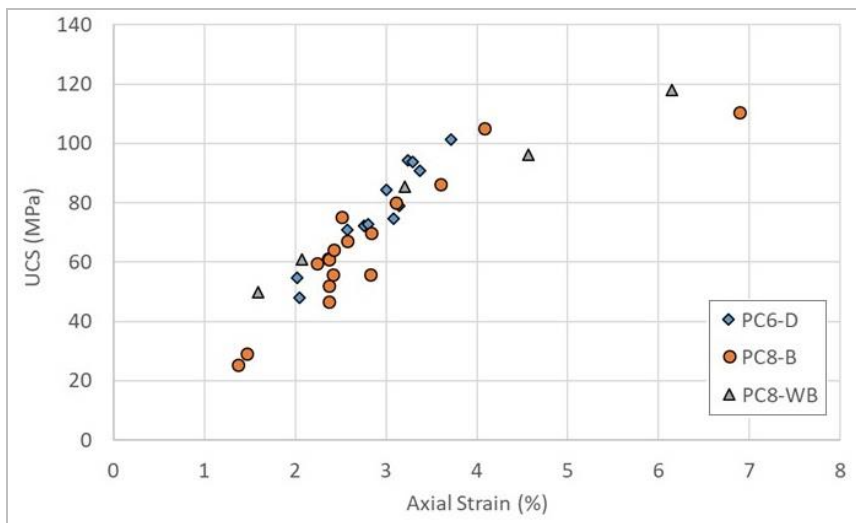


Figure 17 UCS results versus maximum strain using mini-cylinder specimens of all sizes for distinct plies of sub-bituminous coal.

Significant variation in UCS values was observed for mini-cylinder specimens with different size derived from three distinct plies. It was statistically confirmed that the variation in the slenderness ratio (L/D between 1.9:1 to 2.7:1) still resulted in accurate results. However, in order to manage precision the UCS values were ‘normalised’ with respect to a ratio of 2.3 (length-to-diameter) strength for standardization and comparison. The proposed normalised UCS data was calculated

using the measured UCS data from an actual slenderness ratio then converted into the 2.3 slenderness ratio as follows:

$$\sigma_{ci} = \sigma_c \times 2.3 / \left(\frac{L}{D}\right)_{test} \quad (1)$$

where the σ_{ci} parameter is the normalised UCS [MPa], σ_c is the strength from the UCS test [MPa], $\left(\frac{L}{D}\right)_{test}$ is the specimen ratio tested, 2.3 is the ratio of interest for comparison purpose.

Figure 18 shows the correlation between the normalised UCS and the mini-cylinder specimen size from the three distinct plies. The size dependency or scale effect observed by many authors is also dominant in these data. The UCS values generally decrease with increasing specimen size/diameter. Variability in the UCS results was also observed for mini-cylinder specimens of similar size. More significant dispersion was observed for specimens from PC8-B where reduction of the UCS might be attributed to the presence of pre-existing cracks/fractures. Overall, by looking at the population tested for each distinct ply, PC8-WB is the stronger one followed by PC6-D, and then PC8-B the weakest of the three plies (when majority of the tested specimens are taken into consideration).

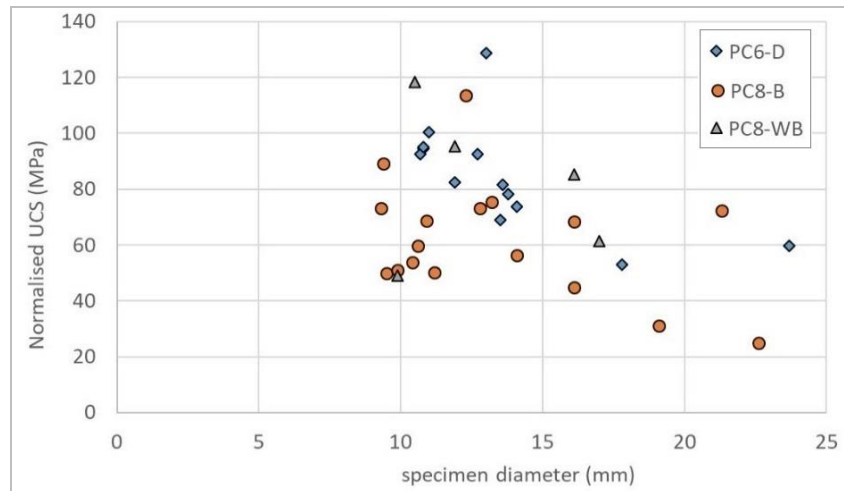


Figure 18 The relationship between normalised UCS and mini-cylinder specimen size for distinct plies of sub-bituminous coal.

For each mini-cylinder specimen, the vertical deformation was recorded to incorporate the Young's modulus (E_i) for laboratory tests carried out for sub-bituminous coal. Figure 19 illustrates a smooth trend of decreasing elastic modulus with increasing size/diameter of mini-cylinder specimen for PC6-D and PC8-B, however limited data was available to confirm similar behaviour for PC8-WB. The measurements indicated that the trend becomes constant at an approximated value of 2.6 GPa for PC6-D and PC8-B, and 3.0 GPa on average by taking the three plies into consideration. Both values were in agreement with laboratory tests reported for the same basin by Parotidis et al. (2016)

where E_i ranges from 2.0 to 3.2 GPa for varied depth (2.7 GPa in average). But the values were higher than elastic modulus estimation for medium rank (bituminous high volatile A) reported as approximately between 1.5 and 2.0 GPa by Medhurst and Brown (1998). Note that the Young's modulus is a critical property for numerical modelling influencing the CSG reservoir fracture simulation.

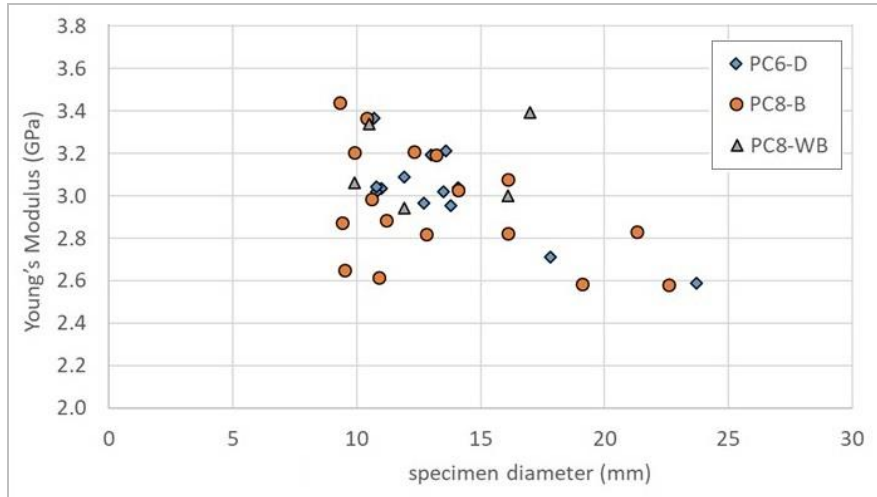


Figure 19 Effect of mini-cylinder specimen size on measurements of elastic modulus for distinct plies of sub-bituminous coal.

3.4.3 Mini-cylinder specimen strength by quality

The mini-cylinder specimens could be visually separated by quality/appearance, and because majority of them (about 85-90%) behaved in a similar way not strictly dependent on the ply (lithotype), they were grouped as either 'intact' or 'non-intact'. The 'intact' group referred to pure intact (no defect) or minor defect constrained at the bases (end-faces) meaning the centre part of the cylinder remained intact; 'non-intact' referred to long or more pervasive defects crossing the sidewalls (wall-faces) and/or the bases (end-faces).

Figure 20 shows the relationship between normalised UCS versus size of mini-cylinder specimens for distinct quality/appearance. For convenience of the reader, the two groups were denoted with x's (x) for 'intact' and triangles (Δ) for 'non-intact' mini-cylinder specimens. By plotting the results, a distinction was observed between both groups. Then, the data were analysed using the method of least squares regression. Fitting approximation was best achieved using the power regression. The fitting curves, which are not confidence intervals, were used to determine intervals for 'intact' or 'non-intact' mini-cylinder specimens for sub-bituminous coal. The data was confined by the upper and lower limit of UCS for 'intact', and 'non-intact' mini-cylinder specimens. The justification to

assume those limits is that the constants for the regression coefficients are significantly different. The equations correlating normalised UCS and mini-cylinder specimen size for ‘intact’ and ‘non-intact’ mini-cylinder specimens were as follows:

$$\sigma_{ci} = 1096.8 \times d^{-0.902} \quad \text{upper limit 'intact'} \quad (2)$$

$$\sigma_{ci} = 567.32 \times d^{-0.816} \quad \text{transition limit between 'intact' and 'non-intact'} \quad (3)$$

$$\sigma_{ci} = 345.86 \times d^{-0.828} \quad \text{lower limit 'non-intact'} \quad (4)$$

where the σ_{ci} parameter is the normalised UCS (MPa), and d is the specimen diameter (mm).

Figure 20 indicates the variability in UCS for laboratory tests conducted with ‘intact’ and ‘non-intact’ mini-cylinder specimens of sub-bituminous coal. For instance, using the above equations (2) to (4), normalised UCS might vary from 144 to 91 MPa for ‘intact’, and 91 to 54 MPa for ‘non-intact’ mini-cylinder specimens with 9.5 mm diameter; and from 69 to 47 MPa for ‘intact’, and 47 to 27 MPa for ‘non-intact’ mini-cylinder specimens with 21.5 mm diameter. If the UCS results were extrapolated to a standard core size of 50 mm diameter, then the expected variation would be approximately from 32 to 23 MPa for ‘intact’ coal and 23 to 14 MPa for ‘non-intact’ coal. It was observed that the spread in UCS results tended to decrease with increasing specimen size (scale effect). Although there is uncertainty in extrapolating the trend associated with a small population of data points, the minor variability on results allows for the data to be constrained by strength.

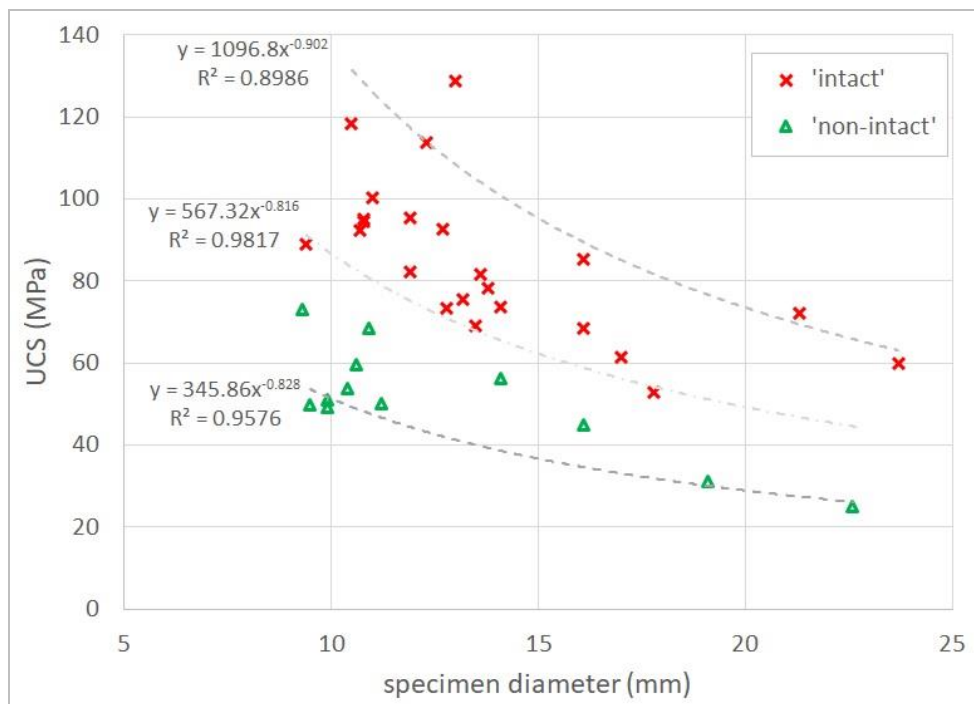


Figure 20 The relationship between normalised UCS and mini-cylinder specimen size when separated by quality/appearance for sub-bituminous coal.

Figure 21 illustrates each mini-cylinder specimen denoted ‘non-intact’ (which comprises 12 specimens) with their size/diameter, so one can refer back to Figure 20 for verification of the fracture pattern versus the upper or lower limits of ‘non-intact’.


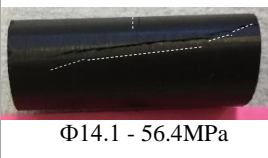
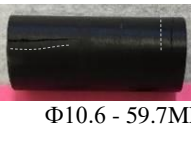
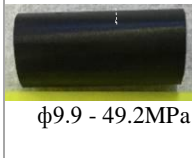
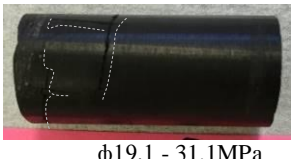
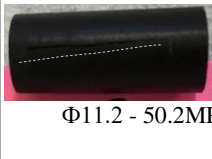
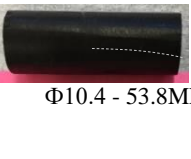
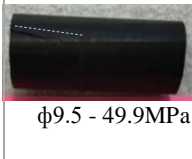
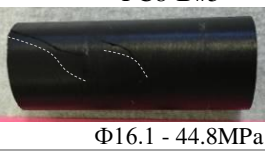
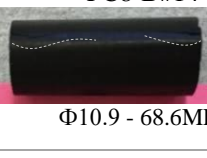


 <p>PC8-B#1 φ22.6 - 24.9MPa</p>	 <p>PC8-B#7 Φ14.1 - 56.4MPa</p>	 <p>PC8-B#13 Φ10.6 - 59.7MPa</p>	 <p>PC8-WB#6 φ9.9 - 49.2MPa</p>
 <p>PC8-B#3 φ19.1 - 31.1MPa</p>	 <p>PC8-B#11 Φ11.2 - 50.2MPa</p>	 <p>PC8-B#12 Φ10.4 - 53.8MPa</p>	 <p>PC8-B#15 φ9.5 - 49.9MPa</p>
 <p>PC8-B#5 Φ16.1 - 44.8MPa</p>	 <p>PC8-B#14 Φ10.9 - 68.6MPa</p>	 <p>PC8-B#17 φ9.9 - 50.9MPa</p>	 <p>PC8-B#18 φ9.3 - 73.1MPa</p>

Figure 21 Photos of ‘non-intact’ mini-cylinder specimens showing quality and size/diameter for sub-bituminous coal.

3.4.4 Coal mass strength from mini-cylinder specimen

The proposition that coal strength decreases with increased specimen size until it reaches a constant value (Hoek and Brown, 1997; Medhurst, 1996), leads to a commonly accepted rock mass strength to range between 5.4 and 7.4 MPa (Mark and Barton, 1996) i.e., based on their mining database for coal pillars, most likely to be medium rank coal. However, when trying to understand the geomechanical behaviour in lower rank sub-bituminous coal like the Walloon Coal Measures, a less generalised approach should be considered. For coal seam gas extraction, it is anticipated that the rock mass behaves like squat (short height and long thickness) coal ‘pillars’ instead of slender (long height and short thickness) ‘pillars’, therefore the coal deformation and the strength of the surrounding strata play an important role (Medhurst, 1996; Wagner and Madden, 1984). The strength of coal seam must be conditional to size. A thin seam is stronger and possibly more so than the carbonaceous mudstone or tuffaceous claystone in the strata.

First, the influence of specimen size on the strength of mini-cylinder specimens was demonstrated for the sub-bituminous coal. Then, the profile for mini-cylinder specimens is extrapolated to the rock mass using UCS measurements exclusively on ‘intact’ specimens (Figure 20 denoted with x’s which comprise 23 specimens). The results were extrapolated using a power function to show the

scale effect on mini-cylinder specimens. An asymptotic strength value for coal can be assumed equal to 1000 mm in height or 435 mm diameter (2.3:1 slenderness ratio). Similar to the Hoek and Brown (1980) approach, the data set of ‘intact’ mini-cylinder specimens calculated as normalised strength was reduced to dimensionless form by dividing individual strength values by the strength of a specimen 50 mm diameter. This process allowed for comparison with other experimental results in literature.

Figure 22 shows the influence of specimen size for low rank, sub-bituminous coal compared with proposed scaling curves from higher rank coals from the following authors: Hoek and Brown (1980), Laubscher and Jakubec (2001), Medhurst and Brown (1998) published by Poulsen and Adhikary (2013), and Song et al. (2018). Coal specimens from Poulsen and Adhikary (2013), Song et al. (2018), and mini-cylinder specimens were extrapolated using a power function. The Hoek and Brown (1980) approximate relationship was compiled with UCS data from the literature on competent rocks. Laubscher and Jakubec’s (2001) approach fit between the limits for sedimentary rock. Poulsen and Adhikary (2013) summarised the inferred UCS from triaxial tests conducted by Medhurst and Brown (1998) on medium rank bituminous coal. Last, the measurements from Song et al. (2018) were plotted here for UCS results of coal specimens with different sizes and 90° dip of the bedding relative to loading direction only (whereas tested for varied bedding).

Figure 22 shows that if one extrapolates the medium rank, bituminous high volatile A coal from Medhurst and Brown (1998) published by Poulsen and Adhikary (2013) back to an ‘intact’ mini-cylinder scale, they tend to behave parallel to the lower rank, sub-bituminous coals tested in this study. And when mini-cylinder specimens are scaled to the rock mass, the low rank coals appear slightly more competent (stronger) than medium rank coal (tested by Medhurst and Brown, 1998) (Figure 22). It is interesting to observe that, the strength of Chinese coals tested by Song et al. (2018) tend to follow the Hoek and Brown (1980) trend for rock rather than coal. In fact, it is assumed that Song et al. (2018) tested high rank coals; if so, the coals have less microporous structure which would justify the higher UCS. Being more or less competent would reflect the coal grindability and population of distinct banding and cleating. It is also noted that large-scale specimens should not be referred to as ‘intact’ because of coal specimen size and quality (flaws, defects, micro-cracks, discontinuities, and cleats, in significant proportion).

Based on the experimental results for low rank, the following equation can be used to calculate strength scaling to the rock mass (σ_a) of sub-bituminous coal. The fitted calculation provided a straight forward guide for low rank coal rock mass. It does not substitute for laboratory tests and

equally important is to consider the surrounding conditions influencing the coal rock mass and the evolution of rock characteristics during the water and gas extraction in a coal or CSG environment.

$$\sigma_d = \sigma_{ci} \times \left(\frac{d_{sample}}{d_{ply}} \right)^{0.82} \quad \text{low rank coal} \quad (5)$$

where σ_{ci} is the strength of the ‘intact’ rock specimen tested in laboratory, d_{sample} is the diameter (mm) of the tested specimens, and d_{ply} is the coal rock mass dimension. It is assumed a constant peak strength value for coal is reached for rock mass ~435 mm in diameter i.e., $d_{ply} < 435$ mm.

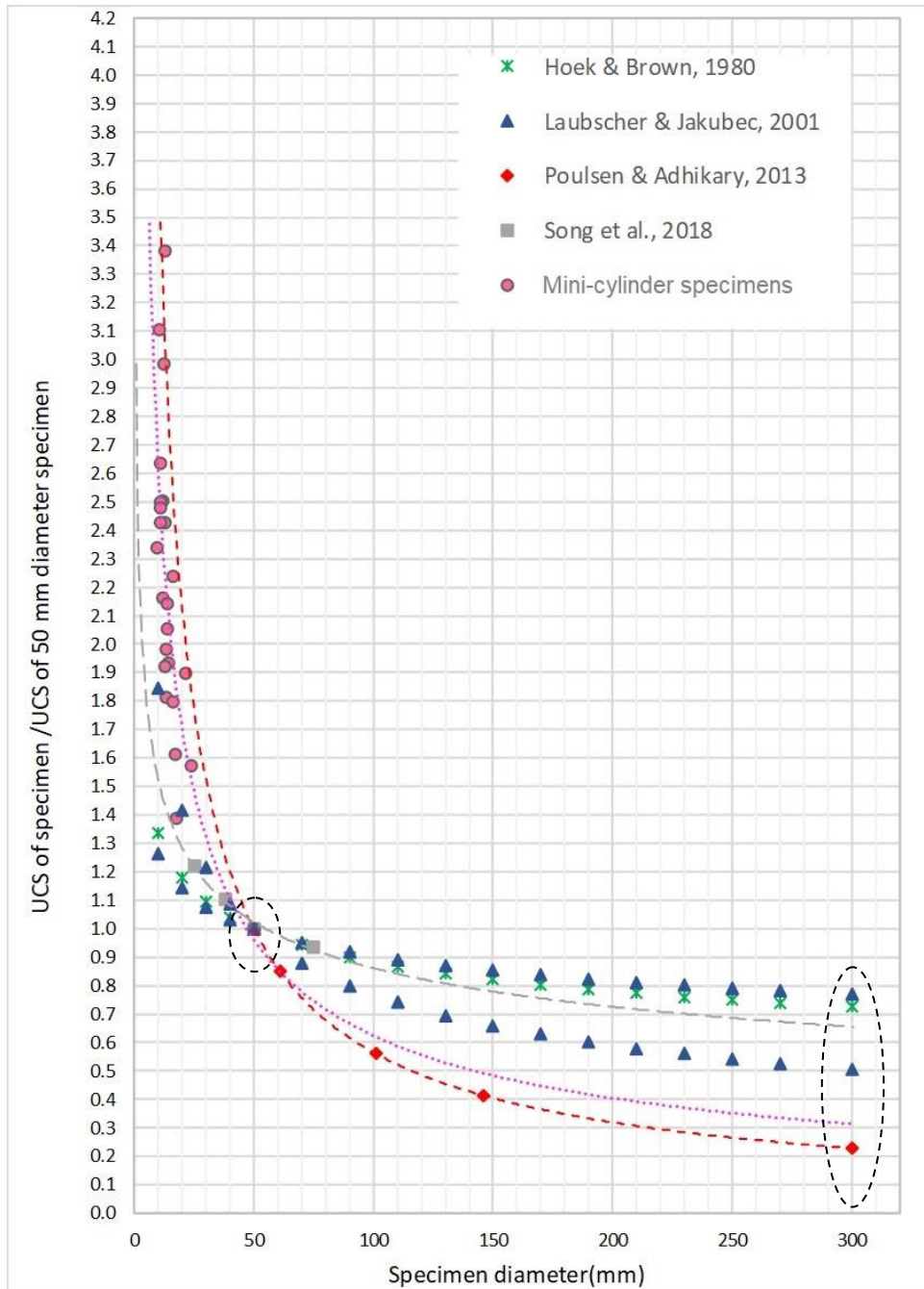


Figure 22 Influence of specimen size for sub-bituminous coal compared with other scaling curves in the literature.

Generally, the uniaxial compressive strength values indicate that the mechanical properties differ in various rock type and size (Figure 22). Particularly for coal, Figure 23 shows the rank effect observed from sub-bituminous to anthracite. Two graphics are plotted together using the mini-cylinder specimens tested here and data in the literature from Poulsen and Adhikary (2013), Song et al. (2013), and Pan et al. (2013), where the specimen size was extrapolated to 50 mm and 300 mm diameter. For specimens equivalent to 50 mm diameter, the coal strength increases from sub-bituminous to medium rank (bituminous high volatile), then there is a decrease towards bituminous medium, and after that an increase to high rank coal (anthracite) (Figure 23 see the top curve). However, if the coal specimen is about 300 mm diameter, then continuous increase in strength is expected with increasing rank (Figure 23 see the bottom curve). Note that interpretation is strongly influenced by limited data from Song et al. (2013). During gas production, if an analogy can be made that alteration in microporous, and molecular structure and/or orientation occurs over time of extraction, changing the coal across ranks, then it promotes change in the strength path. Because the Walloon Coal Measures in the Surat-Clarence Moreton basin are thinly bedded (i.e. not massive seam) an increase and decrease in coal strength is more likely to occur (Figure 23 the top curve).

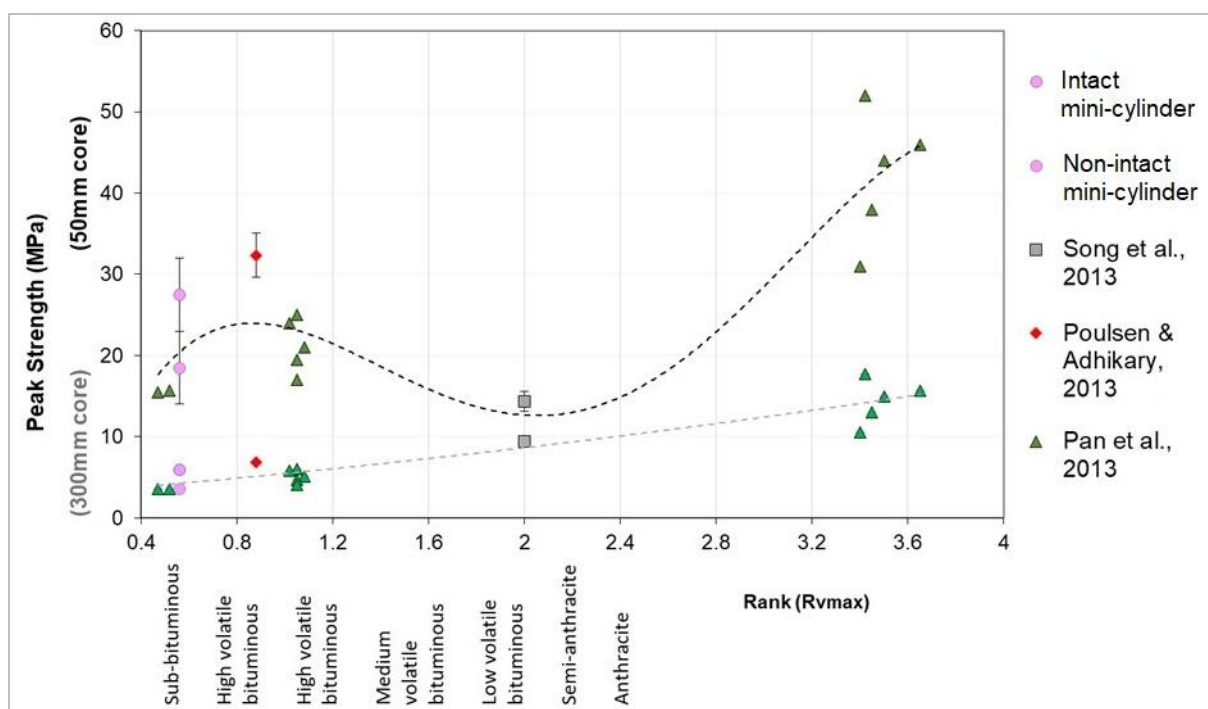


Figure 23 Influence of rank and UCS using distinct types of coal with size extrapolated to 50 mm specimen at the top curve, and 300 mm specimen at the bottom curve. Results are from this study (pink circles) and literature reported values (as noted in the legend).

3.4.5 Mini-cylinder specimen UCS values by maceral subgroup

According to Medhurst et al. (1995) considerations of 'brightness' allow one to differentiate between the mechanical characteristics of different coals. Petrographic analysis showing the stacked percentage distribution of maceral subgroups and mineral matter for 11 samples (i.e., mini-cylinder specimens of sub-bituminous coal classified as 'intact' and 'non-intact' when tested for UCS) are presented in Figure 24. Information about textural and compositional controls on coal or the lack of it were used to assist in the interpretation of UCS results. Data was organized by ply (PC6-D, PC8-WB, and PC8-B) followed by the attributed mini-cylinder specimen number (e.g. PC6-D #8). All lithotypes are dominated by high percentages of vitrinite group macerals (i.e., telinite, collotelinite, vitrodetrinite and gelinite), but the duller ply (PC6-D) contains a slightly lower proportion in exchange for a higher proportion of the liptinite group macerals (i.e., cutinite, sporinite, and suberinite). There is also a shift of more cutinite and sporinite (mean macerals associated with organic material originating from leaves) for samples from duller ply, than suberinite (i.e., organic material originating from waxy cells, structured tissue or bark originating from roots or stems in the peat phase) which accentuates structures in the banded coal (PC8-B) lithotypes.

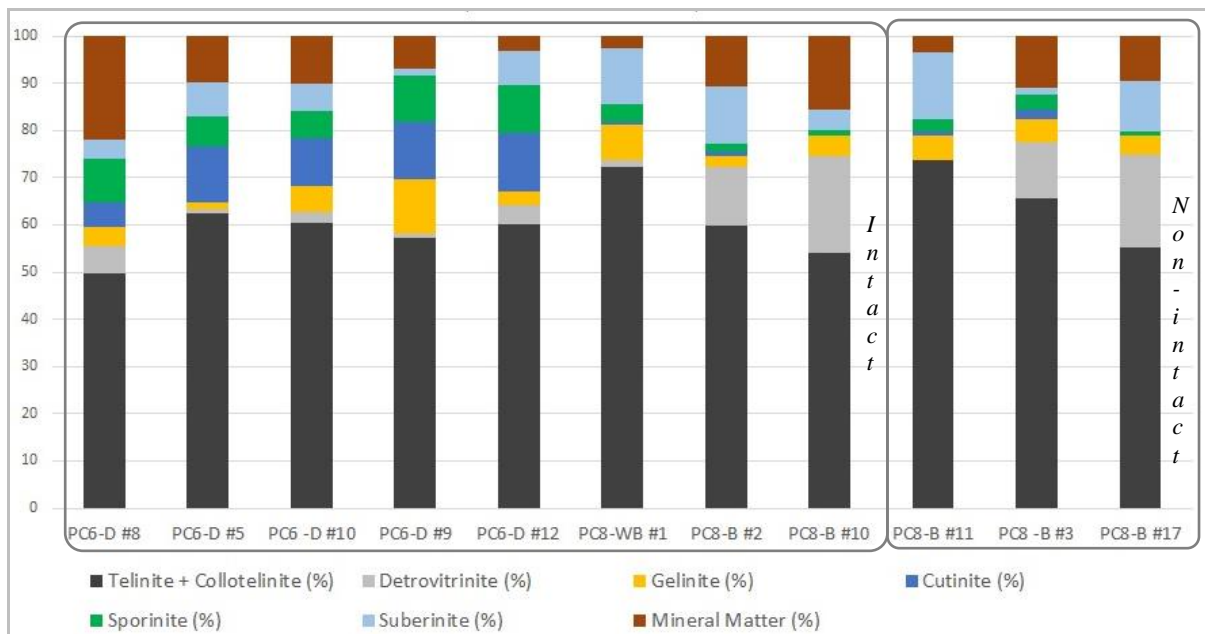
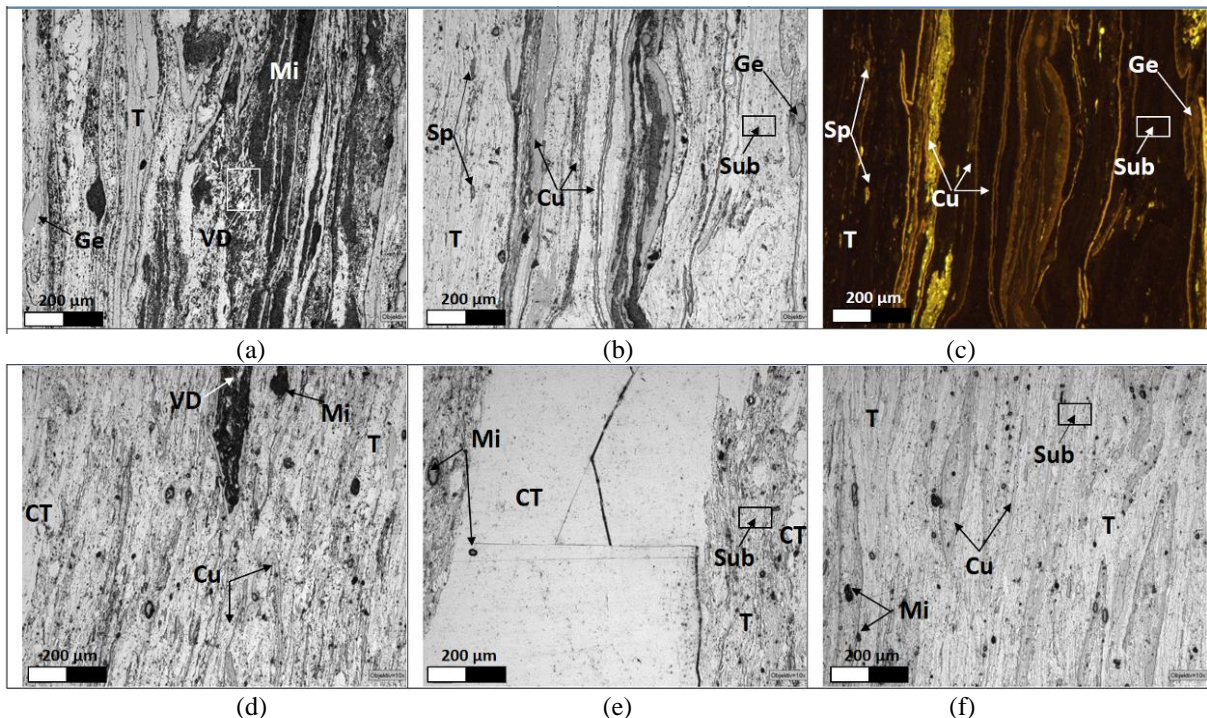


Figure 24 Petrographic analysis shown the stacked percentage distribution of macerals subgroup levels and mineral matter for each epoxy sample.

Overall, the macroscopic classification of duller and brighter coal was confirmed grossly by differences in the vitrinite and liptinite maceral type and proportion. For the samples analysed, duller presented ~60-70% vitrinite and ~20-30% liptinite, while brighter (i.e. banded) showed ~70-85% vitrinite and ~5-20% liptinite. The inertinite subgroup macerals were uncommon for these

coals. Because identification of desmocollinite (broken down/mushy plant material) was not evident, the subgroup level detrovitrinite was used. Mineral matter occurs in variable percentages across all the samples analysed.

Figure 25 shows representative photomicrographs (using a 10x objective in air, ~50x magnification) of macerals composing the different coal lithotypes and the banding structure arising from the presence of cutinite and suberinite mixed with structure vitrinite group macerals. Within the darker texture, very fine-grained mineral (clay) was observed infilling the cell spaces (Figure 25). The clay minerals occurred during the peat phase when the plants were still soft, so the peats were compacted around the minerals. Except for the image on the top right, obtained under blue light excitation, all images are taken in reflected white light. The images intended to illustrate the maceral subtypes; remember that all mini-cylinder specimens were loaded in the direction perpendicular to the bedding planes.



T: telinite, CT: collotelinite, Ge: gelinite, Sub: suberinite, Mi: mineral, Cu: cutinite, Sp: sporinite, VD: detrovitrinite

Figure 25 Representative photomicrographs (10x objective in air, ~50x magnification; all white light except c) of macerals composing the different coal lithotypes and the banding structure.

Next, the normalised UCS for these 11 samples (see location and attributed number highlighted in Figure 26) were extrapolated to an equivalent 50 mm diameter specimen in order to verify possible correlations by maceral subgroup level. The results of normalised UCS for ‘intact’ specimens

presented some strength variability where the two ‘intact’ mini-cylinder specimens of banded plies were 34.5 ± 0.5 MPa and the six ‘intact’ ones of dull ply exhibited 25.5 ± 2.5 MPa (Table 4). Because three samples prepared for PC8-B (#3, #11, and #17) included ‘non-intact’ specimens, it is anticipated that the cylinder quality together with other factors (flaws, mini-cracks, etc.) resulted in underestimated strength and consideration is made to avoid misrepresentation.

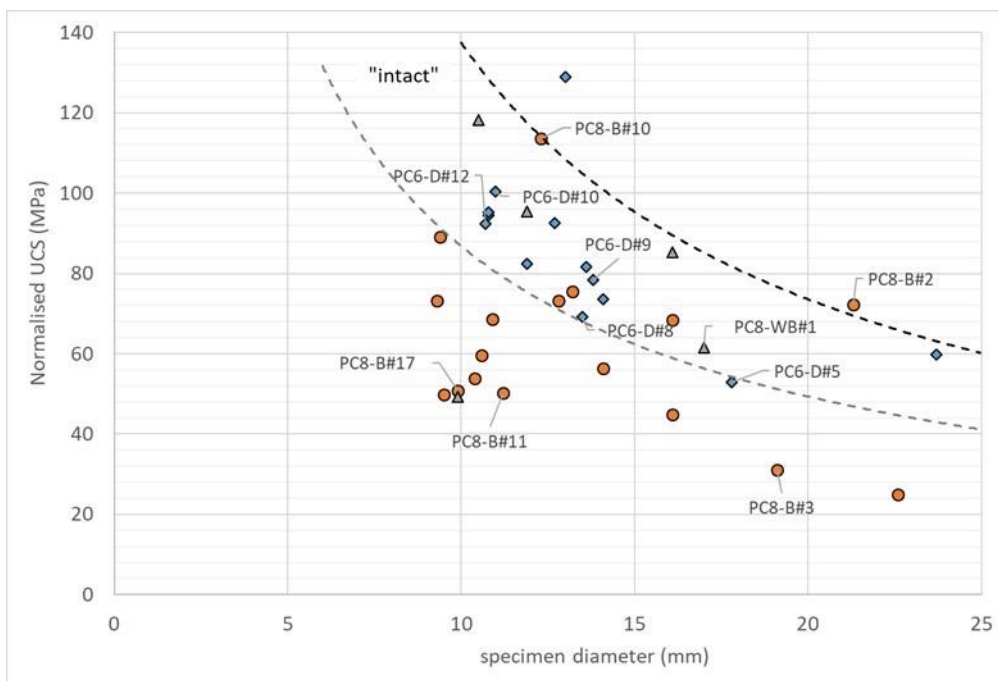


Figure 26 The samples utilised for petrographic analysis are highlighted in the graphic showing the relationship between normalised UCS and mini-cylinder specimen diameter.

Table 4 Normalized UCS extrapolated to equivalent 50 mm diameter core.

	‘intact’								‘non-intact’		
	PC8-B #2	PC8-B #10	PC6-D #10	PC6-D #9	PC6-D #12	PC8-WB #1	PC6-D #8	PC6-D #5	PC8-B #11	PC8-B #3	PC8-B #17
50mm UCS(MPa)	35.2	34.0	27.7	27.3	25.7	24.8	24.4	22.6	14.0	14.0	12.5

Cross plots of the normalised UCS versus the subgroup maceral distribution (for instance, strength versus suberinite percentage, and strength versus telinite plus collotelinite) were attempted for available samples (Figure 27). The cross plots were highlighted as ‘intact’ with x’s (x) and ‘non-intact’ with triangles (Δ) in order to assist the interpretation. First it was not expected that the banded ply was more competent than the duller ply. However, it is emphasized that the eight ‘intact’ samples observed for petrographic analysis do not comprise the entire population of ‘intact’ mini-cylinder specimens, but the ones that had enough retrievable portions of coal to make a representative polished block (Figure 14). Notice that other ‘intact’ mini-cylinder specimens of

banded ply (Figure 19) which were not analysed for petrography (i.e. unable to be assembled into an block) presented UCS values within the duller ply limits or slightly weaker.

In terms of the cross plots for available samples, it is suggested that tested low rank coal behaved similarly in terms of strength independent of lithotype (Figure 27). For instance, an increase of suberinite, which reflects increased micro banding, would promote a slight reduction in UCS. But this expected correspondence to suberinite content was not evident (Figure 27a). Also, observation of the structured maceral subgroup telovitrinite (telinite plus collotelinite) gives an expectation that samples with higher percentage are the weaker ones since they incorporate more incipient cleats. However, there is not a strong trend to conclude (Figure 27b). Neither was an increase in mineral matter potentially allowing for further uniaxial compression of the specimen evident. It seems that coal mechanical properties are more likely related to fabric and texture rather than the content of a particular maceral for these sub-bituminous samples. More so, the presence of fractures, natural or induced, were responsible for the lower strength values.

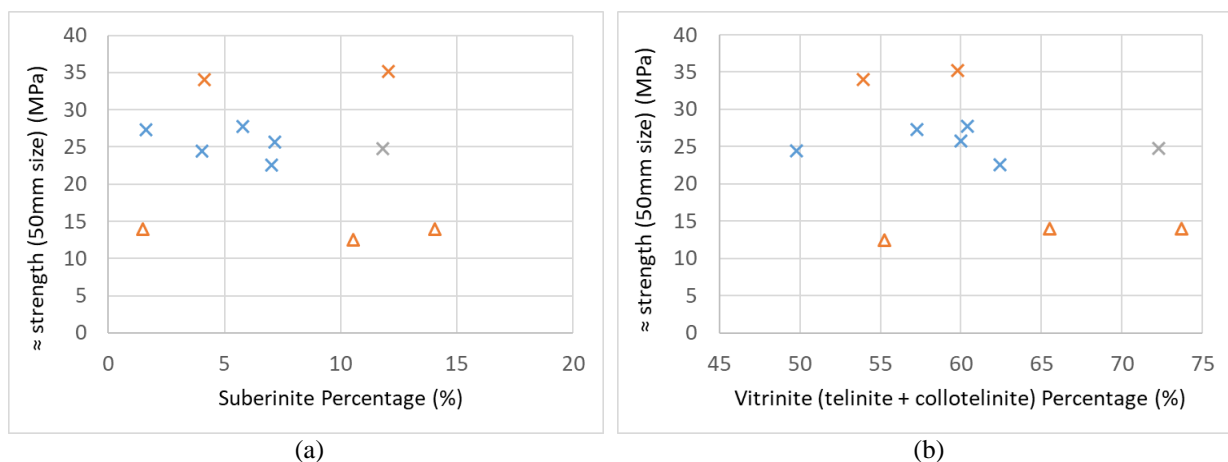


Figure 27 (a) strength vs suberinite percentage; (b) strength vs telinite plus collotelinite percentage for sub-bituminous coal. Note that results were represented for the three distinct plies (PC6-D in light blue, PC8-B in orange, and PC8-WB in light grey colour) tested as either ‘intact’(x) or ‘non-intact’ (Δ) mini-cylinder specimens.

Also, it is quite perplexing that both ‘intact’ PC8-B samples present the highest strength measurements. A schematic representation of PC8-B #2 is illustrated below (Figure 28). The photomicrographs are used to give some perception of representative texture comprising the mini-cylinder specimen. It seems that PC8-B #2 presents a diffuse texture, but more interesting is that the mini-cylinder specimens’ centre part is quite laminated which might contribute to improving its ability to be compressed.

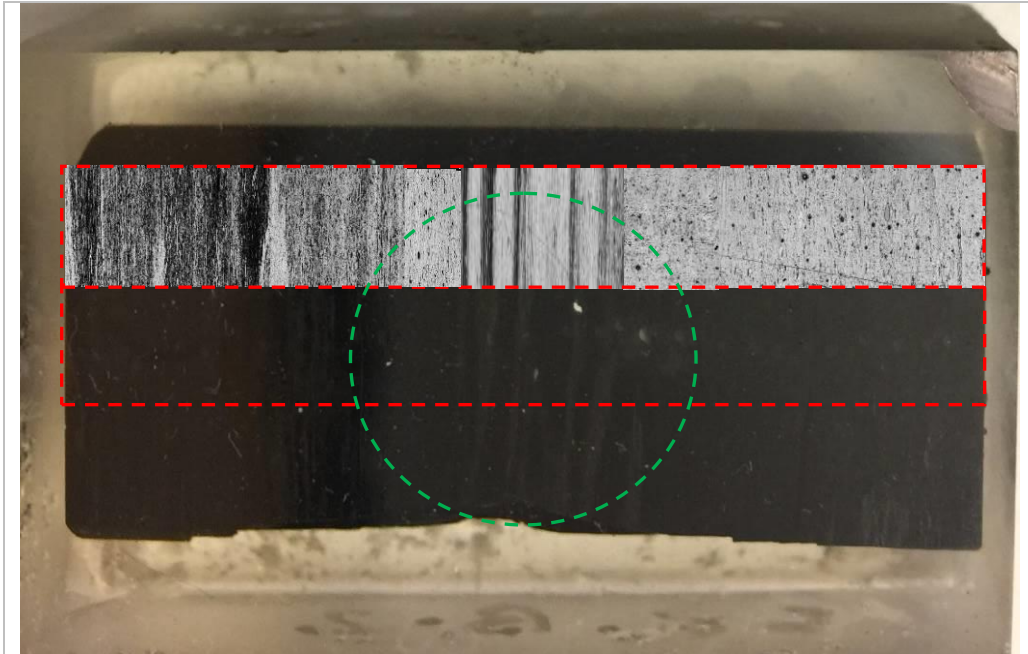


Figure 28 Sample PC8-B #2 zoom in and schematic texture appearance. The block is 50x30x12 mm. The zoom in is from a stitched photomosaic collected at 50x magnification.

3.5 CONCLUSIONS AND RECOMMENDATIONS

This study investigated the strength and elastic modulus properties using UCS laboratory testing on mini-cylinder specimens of sub-bituminous coal in the Walloon Coal Measures. It is promoted that for natural fractured rock such as coal the ‘intact’ rock tested needs to be of smaller size (from within an intact region of the coal) and without visible fractures (induced or pre-existing) rather than standard or larger core specimens, which encompass more natural structural discontinuities. Also, scaling using mini-cylinder provides an alternative approach to testing large cores if they are difficult to obtain. Where coring is unachievable, the fashioned mini-cylinder can be used. Coal visual appearance/quality and maceral composition were investigated to assist laboratory test data interpretation.

- The results for the UCS testing carried out for mini-cylinder specimens sized from 9.3 to 22.6 mm diameter (2.3:1 slenderness ratio) of low rank, sub-bituminous coal are more competent than bituminous coal.
- Failure mode for mini-cylinder specimens was axial split, double shear, or multiple fracture.

- The mini-cylinder specimens of sub-bituminous coal was quite sensitive to fracture intensity.
- A cylinder size equivalent 50 mm diameter gives an estimated 27.5 ± 4.5 MPa for ‘intact’ coal and 18.5 ± 4.5 MPa for ‘non-intact’. The well-known behaviour that laboratory scale unconfined strength reduces with increasing specimen size for non-homogeneous rock material such as coal is observed for mini-cylinder specimens. Coal scaling to the rock mass shows the dependence on rank.
- Measurements of the elastic modulus property showed a gentle trend of decreasing elastic modulus with increasing size/diameter of mini-cylinder specimen. The elastic modulus showed an approximated value of 2.6 GPa for sub-bituminous coal, which is consistent with laboratory tests reported in literature for standard size core.
- The coal maceral group composition showed similarities between the dull and banded plies, except for variation among the liptinite macerals. Because cross plots for sub-bituminous coal strength versus maceral subgroup distribution were inconclusive. It is assumed that the mechanical properties were more likely related to fabric and texture rather than the presence or absence of particular maceral subgroup. It is projected that sub-bituminous coal shows an elastic behaviour relative to more brittle and higher rank coals, e.g. Permian coals

For the CSG reservoir, it is suggested that coal strength behaviour might need to be observed in terms of the seam thickness and the contrast between layers for better comprehension, rather than a single scaling approach.

It is recommended further laboratory investigation of UCS using standard to large size specimens to compare to the scaling trend of mini-cylinder specimens for low rank. Also, further investigation is recommended to improve the confidence in the results using mini-cylinder specimens on different coal ranks, and rock types.

A TEST OF FRACTURE, SHAPE, AND SIZE USING 3D-PRINTED SANDSTONE

Karina Barbosa (PhD candidate) designed shape and size of specimens, conducted SILC and UCS tests, interpreted data, prepared figures and graphics, and wrote the manuscript.

Joan Esterle (Principal PhD supervisor) reviewed, discussed and edited the manuscript.

Zhongwei Chen (Associate PhD supervisor) reviewed, discussed and edited the manuscript.

Rick Chalaturnyk proposed the experiment, supplied the specimens, reviewed, and edited the manuscript.

Benjamin Bonfils escorted the experimental work, reviewed, discussed and edited the manuscript.

Summary

The Short Impact Load Cell (SILC) experiments are used in combination to characterize the deformation, fracture initiation and fragmentation behaviour of irregular-single particles and shaped specimens subjected to impact loading. This Chapter utilizes the 3D-printed sandstone, a fabricated relatively homogeneous material to test assumptions and calculations used in the test, as well as differences in SILC results based on specimen size, shape, and fabric orientation. An advantage of testing distinct sizes is that results can be upscaled to the size of interest. Ultrahigh-speed digital camera captured the test and was compared to the force-time profile to assist in interpretation of the SILC results. The expected failure mode of homogeneous, brittle material start with a shear fracture, in which the relative displacement is parallel to the fracture surface and progress with a displacement normal to the fracture surface, resulting in a well-defined planar feature when testing cylinder-shaped specimens. The perfect split not always occurred for sphere type shaped specimens which might fragment into three portions. SILC is pointed out as an alternative for the Brazilian tensile strength, where better approximations can be reached with cylinder-shaped specimens. However, the specific fracture energy required to reduce a homogeneous specimen to a given size can be widely different for specimens of distinct shape. A full description of the specimens tested, observations, and results are detailed below.

***Testing Impact Load Cell calculations of material fracture toughness and strength using
3D-printed sandstone***

Karina Barbosa^{ab}, Rick Chalaturnyk^{ef}, Benjamin Bonfils^d

Joan Esterle^{ab}, and Zhongwei Chen^c

- a. School of Earth and Environmental Sciences, The University of Queensland, Brisbane, Australia*
- b. UQ Centre for Coal Seam Gas, The University of Queensland, Brisbane, Australia*
- c. School of Mechanical and Mining Engineering, The University of Queensland, Brisbane, Australia*
- d. Julius Kruttschnitt Minerals Research Centre, The University of Queensland, Brisbane, Australia*
- e. Department of Civil and Environmental Engineering, The University of Alberta, Edmonton, Canada*
- f. Canadian Centre for Clean Carbon and Mineral Processing technologies, The University of Alberta, Edmonton, Canada*

Abstract

Short impact load cell (SILC) tests provide insight on the dynamic breakage behaviour of rocks. The measured impact force to first fracture of a rock specimen is used to calculate properties such as fracture toughness, tensile strength, and elastic modulus. To explore the repeatability and performance of the SILC test and verify the underlying assumptions for interpreting the test measurements, a comprehensive SILC testing program was conducted using additively manufactured (3D-printed) sandstone. 3D-printed sandstone specimens with known mechanical properties were used to indirectly determine the mechanical properties of specimens from SILC test measurements with respect to different sizes (from 5 to 12 mm diameter), shapes (sphere, flattened sphere, ellipsoid, and cylinder) and fabric orientations (i.e. angle variation of microstructures relative to the impact or loading direction). Unconfined compressive strength tests were also conducted on twin sets of various sized cylinder-shaped specimens to verify the estimation of compressive strength from the SILC test. Confidence in interpretation of SILC testing results is obtained by excluding the intrinsic material variability. Ultrahigh-speed digital camera was used to observe the fracture mechanism and to verify the force–time profiles against specimen physical response. Well-defined shaped specimens instead of irregular single-particles showed clear peaks corresponding to the force to first fracture on the force–time profiles. The study found that the minimum energy required to fracture the specimen, therefore the specimen strength, was strongly influenced by the shape effect.

Keywords: 3D-printed sandstone; impact breakage; geomechanical properties; scale effects

4.1 INTRODUCTION

Geomechanical strength and elastic modulus data necessary for numerical modelling simulations should be based on site specific investigations such as triaxial or uniaxial strength tests on intact core specimens. In many cases, obtaining intact core specimens is very challenging resulting significant uncertainty in the properties of a rock mass. Additional rock mass properties such as fracture toughness and tensile strength, which are required for hydraulic fracturing models in naturally fractured materials, e.g. coal, are also difficult to determine due to sampling challenges. Consequently, this study was motivated by a need to identify and validate alternative laboratory testing techniques to obtain reliable geomechanical data for natural rock systems.

In the mineral processing industry, an impact load cell (ILC) test method was developed for single-particle breakage studies of irregular and sphere-shaped specimens to reproduce comminution conditions existing in some full-scale milling operations. Data from the ILC has been used to calculate a number of parameters, such as the minimum energy required to fracture a particle, the strength and elastic modulus of particles, the net energy absorbed by the particle during the entire breakage event (Tavares, 1997), and fracture toughness (Bearman et al., 1989; Donovan, 2003). Factors affecting breakage include the particle size (Schonert et al., 1962; Schonert, 1986; Yashima et al., 1987; Tavares, 1997; Tavares and King, 1998a), as well as deformation rate and stressing velocity, stressing mechanism (abrasion, compression and one-point impact), and the ball/striker characteristics (Tavares, 1997). The ILC has also been used across a wide range of natural materials including minerals, metal ores and rocks (Tavares, 1997; Tavares and King, 1998a) and manufactured materials such as glass spheres (Baumgardt et al., 1975) (Figure 29). Recently, Bonfils (2017) introduced cylinder-shaped specimens to verify the shape variability and the intrinsic material variability against crushed single-particles of basalt, showing that the variance of the cumulative distribution of estimated properties was significantly reduced for cylinder-shaped specimens when compared with single-particles. Despite no previous use as a tool for geomechanical appraisals, the current study was undertaken to assess whether a modified ILC test, a short version of the impact load cell called the short impact load cell (SILC) could provide an alternative test method to capture geomechanical properties on drilling particles (or chips) and cylinder-shaped specimens, which could alleviate some sampling and testing issues requiring fully intact specimens.

This study explores the use of intact, quasi-identical, non-standard size and shaped sandstone specimens produced using novel 3D-printed (3DP) technology that uses sand as the print material. The mechanical properties of these specimens are determined from the short impact load cell (SILC) test. Additionally, the study provides a comparison between SILC values and the unconfined compressive strength (UCS) using twin sets of 3DP cylinder-shaped specimens, to test the correlation between these different methods of testing. The results from UCS are also compared with experimental results of Hawkins (1998), also followed by Masoumi et al. (2016) and Roshan et al. (2017). Furthermore, the 3DP specimens will improve understanding of the influence of shape, size and fabric relative to the impact (i.e., loading direction) when estimating mechanical properties, by taking away the intrinsic material variability. As an alternative to natural material for testing, the mechanical variation between printed specimens are expected to be minimized. It is the first stage to improved confidence in interpretation of results for geomechanical derived properties. Also, an ultrahigh-speed digital camera was used to verify the material response to impact interpreted by the force–time profiles.

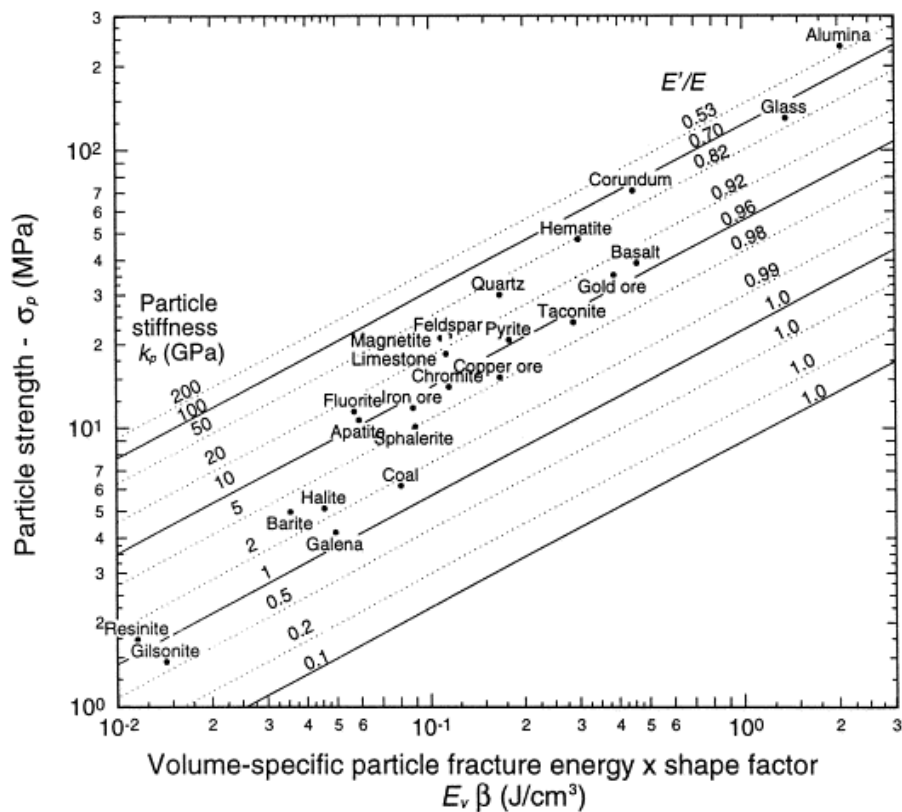


Figure 29 Relationship between mean particle fracture energy and mean particle tensile strength of 2.0-2.8 mm particles of various materials (from Tavares, 1997).

4.2 BACKGROUND

The effect of size on impact load test results has been reported for measurement of the particle strength and the energy at fracture of materials over a wide range of sizes (Schonert et al., 1962; Schonert, 1986; Yashima et al., 1987; Tavares, 1997; Tavares and King, 1998a). In brittle materials, it is observed that as particle size decreases, the particles usually become stronger (Tavares, 1997). This effect is explained by the probability of fracture based on Griffith's theory, which states that the probability of cracks being present in a solid decrease with a reduction in specimen size. However, the study from Hawkins (1998) on isotropic sandstone demonstrated that up to 54 mm in diameter, the inverse relationship is true and thereafter (from 54 to ~155 mm) the results of strength measurements decrease with increase of specimen size. Hawkins (1998) tested seven sedimentary rocks, cylinder-shaped, eight different diameters for each type of rock, 2:1 length-to-diameter ratio for uniaxial compressive strength (UCS), and all the results were reduced to dimensionless form relative to the strength of the 54mm diameter specimen. Masoumi et al (2016) and Roshan et al. (2017) also compared specimen-size dependence against Hawkins (1998) and similar results (i.e. ascending and descending trends) were found.

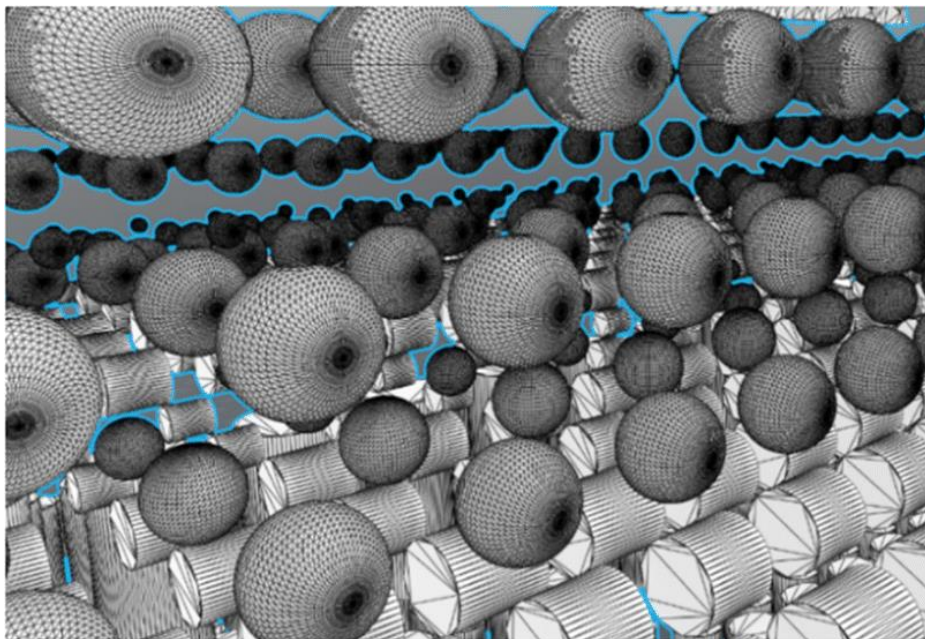
Unresolved fundamental issues on standard core are affected by several factors such as heterogeneity of the rock material that form a mechanical stratigraphy, bedding orientation, grain contact, moisture content, coring procedures introducing fractures, and others. Therefore, improved understanding of the influence of shape and size, by taking away the intrinsic material variability is the first stage to demonstrate the repeatability and performance of the Impact Load Cell test and this contributes to improved confidence in interpretation of results.

4.3 3D-PRINTED SANDSTONE SPECIMENS

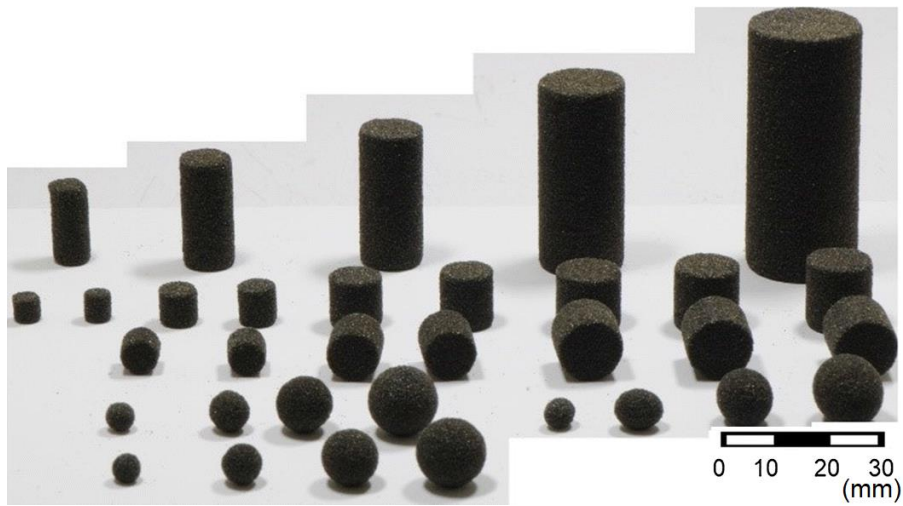
The 3D-printed (3DP) sandstone specimens were additively manufactured using an M-Flex sand printer in the GeoPRINT laboratory at the University of Alberta, Canada. The 3DP specimens are fabricated using silica sand and binder jetting technology which allows control over grain size, packing, mineralogy, cementing type and content, bedding orientation, and discontinuities. Hodder (2017) describes the 3DP process in detail and demonstrates that the geomechanical behaviour of these 3DP sandstones is dependent on three key aspects: silica sand, binder liquid (composed mostly of furfuryl alcohol), and activator (p-toluene sulphonic acid). For the current study, all

specimens were fabricated with 20% binder saturation (8 vol%) and post-cured at 80 °C for 24 h (Hodder, 2017; Primkulov et al., 2017). Every layer of sand grains applied in the printing was $\approx 250 \mu\text{m}$ thick, slightly greater than the typical $\approx 150 \mu\text{m}$ diameter of the sand grains. Each fabricated specimen is an assemblage of sand/grains located with a certain size distribution where they form bridges (connections) with the neighbouring grains. For specimens fabricated with these specifications, the UCS of cylinder-shaped 3DP specimens with 25.4 mm in height and 12.7 mm diameter was reported as $23.0 \pm 2.5 \text{ MPa}$ and Young's modulus $\approx 1.3 \text{ GPa}$ (Hodder, 2017) and $\approx 1.9 \text{ GPa}$ (Primkulov et al., 2017). The difference in the Young's modulus results may be due to the different testing equipment and loading rates used in the two experiments (Hodder, 2017). These properties are used as reference for the current study.

3DP allows a variety of shapes (cylinders, spheres, flattened spheres and ellipsoids) of varying sizes to be printed. These specimen configurations are initially designed using AutoCAD and this file is converted to STL format which is sent to the M-Flex printer. Figure 30 illustrates the AutoCAD design and one of each 3DP specimen considering shape, size and printing orientation. Each shape was tested at four distinct sizes with average diameters of 5.2 mm, 7.3 mm, 10.1 mm, and 12.2 mm. A total of 550 specimens comprising 330 cylinder-shaped specimens (printed in vertical and horizontal orientations) and 220 specimens between sphere, flattened sphere, and ellipsoid-shaped were successfully tested following the SILC test methodology. The mass, length and diameter of each specimen was measured individually and recorded prior to testing.



(a)



(b)

Figure 30 3DP specimens fabricated to be tested: a) AutoCAD design, and b) shape, size and orientation of each specimen as printed.

4.4 SPECIFICATION OF SILC TESTING SPECIMENS

Relative to the silica sand grains of the specimens and the post-cured binder, it is anticipated that the binder/grain interface will provide a weaker zone for dynamic fracture during a SILC test. Consequently, fracture of the specimens is likely to consist of rupture and sliding along grain–grain interfaces. Based on the study by Hodder (2017), it is assumed no pre-existing cracks are present in the 3DP specimens that will contribute to the failure during the SILC test.

During the 3DP process, the print head dispenses binder on the sand bed in parallel layers from bottom to top and so understanding the influence of fabric or bedding orientation was important (Figure 31a). The fabric effect refers to the angle variation of microstructures relative to the impact or loading direction, and to produce this effect, cylinder-shaped specimens were printed in a vertical direction relative to parallel sand layers while others were printed in the horizontal direction. All cylinder-shaped specimens were diametrically loaded/impacted to failure during the test. Therefore, a cylinder-shaped specimen printed in the vertical direction would have a well-controlled bedding orientation of 0° when the specimen is impacted (Figure 31b). While the cylinder-shaped specimen printed in horizontal direction had a non-controlled (or unknown) bedding orientation which can vary from 0° to 90° when the specimen is impacted, as the first printed layers cannot be identified or tracked during the test (Figure 31c). The sphere-shaped specimen also presented a non-controlled bedding orientation which can vary from 0° to 180° when the specimen is impacted (Figure 31d). The flattened sphere-shaped specimen was an attempt to slightly flatten the sphere at base and top

surfaces to potentially track the bedding layers and promote control of fabric or bedding orientation to be 90° when the flattened sphere-shaped specimen was impacted (Figure 31e). Identification of this only slightly flattened surface was difficult on 3DP specimens and alternate methods should be investigated in future studies. Elliptical-shaped specimens, where no attempt was made to flatten parts of the surface, also had a non-controlled bedding orientation, which can vary from 0° to 90° , relative to the impact direction (Figure 31f).

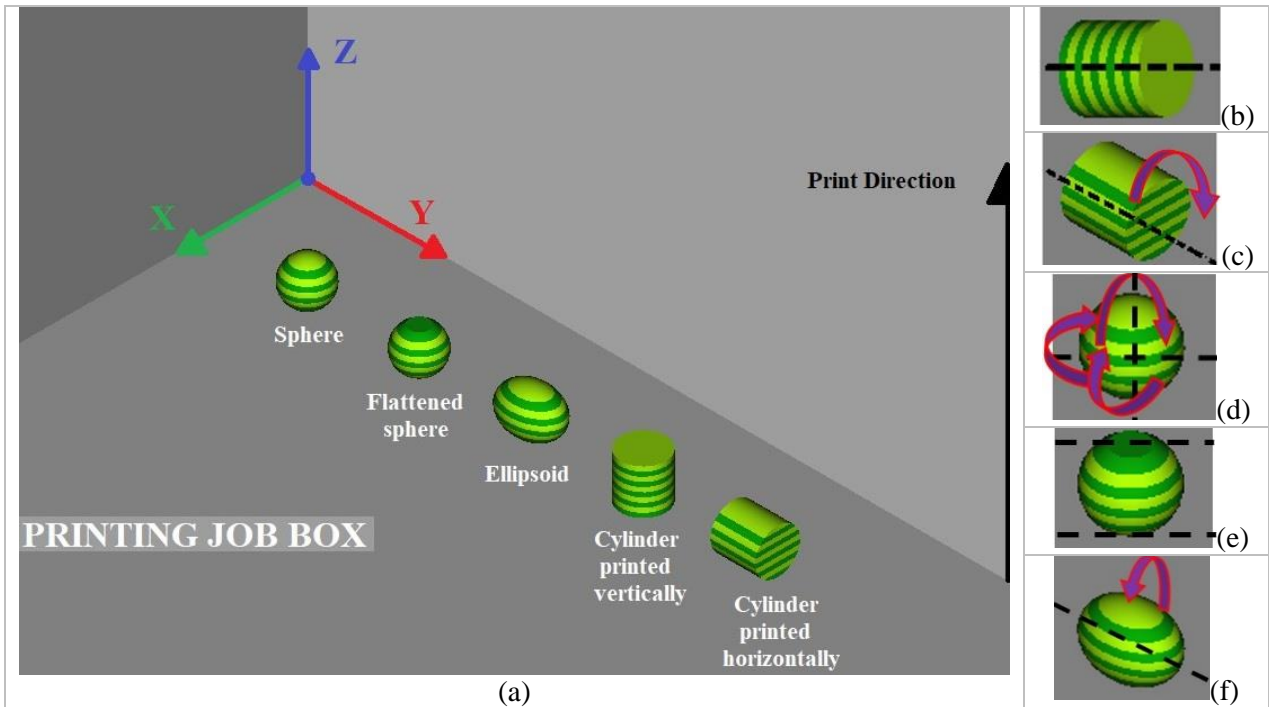


Figure 31 3DP specimens schematic illustration of shapes: a) when manufactured into the printing job box; and potential bedding orientation when specimen is impacted: b) cylinder printed vertically: 0° , c) cylinder printed horizontally: 0° – 90° , d) sphere: 0° – 180° , e) flattened sphere: 90° , and f) ellipsoid: 0° – 90° .

This study also assessed the impact of slenderness ratio [i.e., length-to-diameter ratio (L/D)] on cylinder-shaped specimen properties determined using SILC test. The SILC testing recommendation is that cylinder specimens should be prepared at a 1:1 ratio. Since 3DP sandstone specimens can be printed at distinct ratios, cylinder-shaped specimens were fabricated for vertical and horizontal orientations having slenderness ratios of 0.9/1, 1/1, and 1.1/1. Table 5 presents a summary of the range of specimens of given shapes and sizes (ratio was included when applicable), and the impact conditions investigated, to validate geomechanical properties of 3DP sandstone specimens from the SILC test. Note that 3DP sphere, flattened sphere, and ellipsoid-shaped specimens are named ‘group A’, and 3DP cylinder-shaped specimens are named ‘group B’ (Table 5).

Table 5 Summary of the 3DP specimens' shape, dimensions and impact conditions tested.

Shape	Cylinder-shaped specimens printed vertically (Group B)								
Diameter (mm)	5.31	5.32	7.38	7.38	10.18	10.22	12.35	12.36	12.4
Ratio (length/diameter)	1:0.98	1:1.07	1:0.98	1:1.04	1:0.98	1:1.07	1:0.88	1:0.99	1:1.07
N (number of tests)	21	25	25	26	26	26	16	16	16
Striker Mass (g)	535.25		535.25		535.25		535.25		
Drop Height (mm)	25.07		63.33		100		125.11		
Photo									
Shape	Cylinder-shaped specimens printed horizontally (Group B)								
Diameter (mm)	-	-	7.2	7.19	9.98	10.01	12.21	12.15	12.1
Ratio (length/diameter)	-	-	1:1.01	1:1.12	1:1.02	1:1.11	1:0.92	1:1.02	1:1.12
N (number of tests)	-	-	19	19	19	19	19	19	19
Striker Mass (g)	-	-	535.25		535.25		535.25		
Drop Height (mm)	-	-	63.33		100		125.11		
Photo	-	-							
Shape	Sphere-shaped specimens (Group A)								
Diameter (mm)	5.1	7.2		10.0	12.2				
N (number of tests)	20	20		20	17				
Striker Mass (g)	535.25	535.25		535.25	1399.8				
Drop Height (mm)	25.07	63.33		100	100				
Photos									
Shape	Flattened sphere-shaped specimens (Group A)								
Diameter (mm)	5.2	7.4		10.2	12.1				
N (number of tests)	18	20		20	18				
Striker Mass (g)	535.25	535.25		535.25	1399.8				
Drop Height (mm)	25.07	63.33		100	100				
Photos									
Shape	Ellipsoid-shaped specimens (Group A)								
Diameter (mm)	5.3	7.4		10.1	12.4				
Ratio (length/ diameter)	1:1.17	1:1.20		1:1.22	1:1.24				
N (number tested)	18	18		18	13				
Striker Mass (g)	535.25	535.25		535.25	1399.8				
Drop Height (mm)	25.07	63.33		100	100				

4.5 SHORT IMPACT LOAD CELL APPARATUS AND TESTING

The SILC test apparatus used in this study, as shown in Figure 32, is located at the Julius Kruttschnitt Mineral Research Centre (JKMRC), Australia. The apparatus has a cold-rolled rod composed of 2 pieces: the main rod with strain gauges attached, and a small anvil. The four semiconductor 540Ω strain gauges (Micron Instruments SS-080-050-500P-S4) are installed on the rod (119.3 ± 0.01 mm below the top) in a standard Wheatstone bridge configuration. Small changes in resistance of the strain gauges are converted into a voltage (Bourgeois and Banini, 2002) and the output voltage is amplified (HBM ML10B module), then used for signal conditioning, and bridge balancing. The precision of the force measurement obtained with the calibration depends on the resolution of the data acquisition system (PCI data card with 14-bits resolution and sampling rate of 2.5 MB/s was used). Detailed description for this SILC apparatus was published by Bourgeois and Banini (2002).

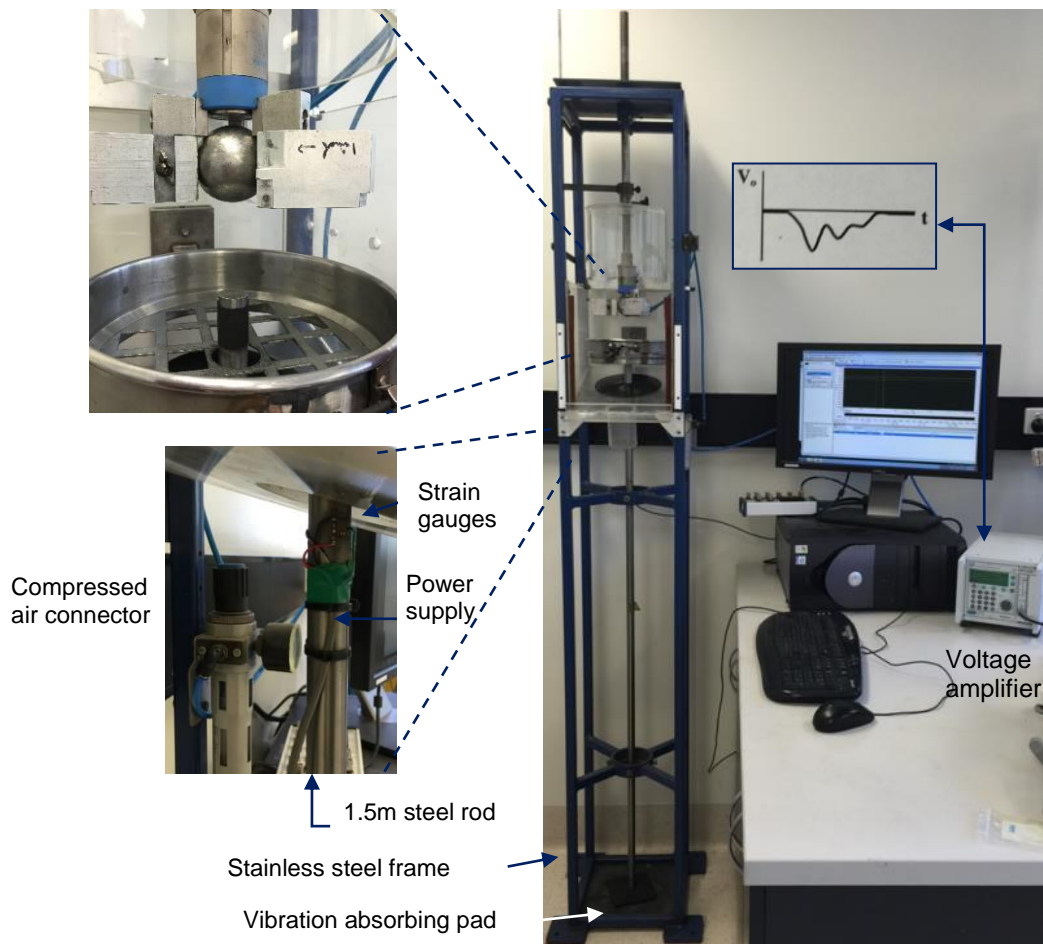


Figure 32 Setup of the SILC testing system.

Stainless steel balls of different sizes were available as the strikers. Details of the striker mass and drop height, which define the loading rate or impact conditions, utilized to carry out the tests are shown in Table 5. The impact energy level was determined by selecting combinations of striker mass and drop height and subjecting each specimen to impact breakage. Typically, the radius of curvature of the striker is considerably larger than that of the tested specimen. If couple specimens remaining unbroken after being subjected to impact, the impact energy level needs to be increased in order to fracture the specimens without inducing significant over-breakage. Because incremental damage during impact loading is irreversible, specimens that did not fracture by impact were rejected from the analyses. As noted in Table 5, large specimens (12.2 mm diameter) shaped sphere, flattened sphere, and ellipsoids required a striker mass of 1399.8 g and a 100 mm drop height to induce failure. While large cylinder shaped specimens (12.2 mm diameter) required a striker mass of 535.25 g and a 125.11 mm drop height. According to Saeidi (2016), the primary breakage function is material dependent, therefore it do not vary if particles are fractured by distinct impact conditions.

The force to voltage ratio is calibrated with dropping a striker (1 in. or 25.4 ± 0.05 mm diameter and 100 mm drop height) directly on the steel rod (see Table 6 for further detail about rod and striker). Calibration is required before the SILC test starts. Then, testing can be performed using a selected striker which is released from a known drop height onto one specimen sitting on top of the SILC anvil/rod. During the test, the compressive strain wave resulting from the impact travels down the rod and strains the solid-state gauges producing a change in resistance. The voltage output is directly proportional to the force applied on the rod, which is then recorded as a function of time. An ultrahigh-speed digital camera (Phantom v2011) was used to record of extremely short-duration (microseconds) of failure events taking place during the SILC tests. Still-images from these videos are provided in this study.

Table 6 Summary of the rod and striker parameters.

Stainless steel	Rod	Striker (ball calibration)
Diameter	19.99±0.01 mm	25.4±0.05 mm
Length	1500.00±0.05 mm	-
density	7805.51±39.57 kg/m ³	7.783 g/cm ³
Young's modulus	211.34±0.22 GPa	203.49 GPa
Poisson ratio	0.29	0.29
Young's modulus (elastic modulus)	230 GPa	230 GPa

In terms of testing and data analysis, the SILC test can be used for measuring the (Bourgeois and Banini, 2002):

- (1) specimen compression under dynamic conditions;
- (2) compressive force acting on the specimen at the instant of the fracture which allows for: measure of tensile strength and estimation of the yield strength; and
- (3) energy absorbed by the specimen as a function of time by combining the dynamic measurements of force and specimen compression, which allows for the determination of:
 - energy-at-first-fracture (or fracture energy) which is the minimal strain energy absorbed/stored by the specimen subjected to impact load prior to fracture and
 - energy absorption during fragmentation which is the total energy absorbed by the specimen and the generated fragments during a single-impact event.

For further details of the SILC device construction, calibration and calculations can be found in King and Bourgeois (1993), Tavares (1997), Tavares and King (1998b, 2004), Bourgeois and Banini (2002), and Bonfils (2017).

Breakage events taking place during the SILC test are extremely fast (microseconds), so it was of interest to visually monitor the experiments. An ultrahigh-speed digital camera was utilised to capture fracture propagation in 3D-printed sandstone specimens during the SILC test. The equipment utilized was the Phantom v2011, the monochrome device in Figure 33. The videos were recorded at 33.3 μ s intervals with resolution acquisition of 768 x 768, while the play speed could be adjusted from 0.1 to 100 fps for detailed visualisation.



Figure 33 A photograph of the ultrahigh-speed digital camera phantom v2011.

4.6 SILC CALCULATION METHODOLOGY

It is known that the maximum contact pressure between two surfaces (striker and specimen or specimen and anvil/rod) depends on: type of curvature between contact surfaces, radius of curvature, magnitude of contact force, and elastic modulus and Poisson's ratio of contact surfaces. The SILC calculation methodology is a function of the specimen shape and the contact geometry.

Figure 35 illustrates the typical interactions that occur between the striker, the sphere-shaped specimen, and the anvil/rod for a test where the specimen does not fracture. Figure 35a shows the approach of the striker towards a sphere-shaped specimen resting on the anvil. At impact, the specimen compresses and the anvil displaces downward (Figure 35b, c). Following this downward movement, rebound of the entire set (striker, specimen, and anvil) occurs, as shown in Figure 35d. Impact signatures at the contact surfaces at the top (striker-specimen) and base (specimen-anvil) of a specimen occur highlighting plastic deformation and geometry changes at the contact surfaces (Figure 35e, f). After the first impact, the sphere-shaped specimen underwent rotation in the air (Figure 35g), relative to its initial position, to finally be impacted by the striker again (Fig. 4h). For this test, no visible fracture or chipping occurred.

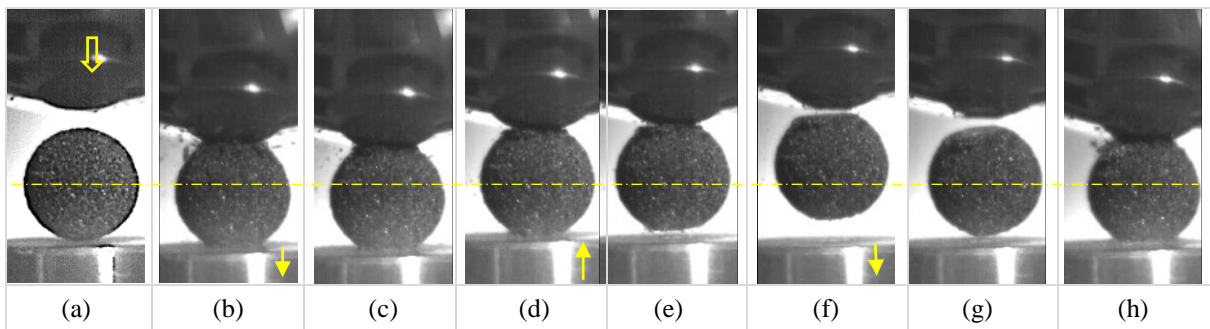


Figure 34 Illustration of dynamic interaction of the striker and the sphere-shaped specimen showing no fracture during a SILC test.

4.6.1 Determination of cross-sectional areas at contact bodies

3DP specimens that did not fail during the impact testing had engraved (indented) marks in the vicinity of the contact bodies, which gives clear evidence of the Hertzian contact mechanics (Goldsmith, 1960; Hertz, 1881). Figure 35 and Figure 36 shows a cross sectional view for the Hertzian hypothesis applied for spheres as observed at 3DP 'group A' (sphere, flattened sphere, and ellipsoid-shaped specimens), and for cylinders as observed at 3DP 'group B' (cylinder-shaped specimens printed vertically and horizontally).

‘Group A’ was represented by a sphere, flattened sphere, and ellipsoid-shaped specimens. The hypothesis applied for ‘group A’ was that a circular contact was formed between all bodies, i.e. the striker against the ‘group A’ specimen, as well as the ‘group A’ specimen against the rod (Figure 35). For calculation purposes, the rod is considered a sphere with an infinitely large radius. Calculation of the cross-sectional circular contact area between the specimen and the rod is presented in Equation (6). And calculation of the cross-sectional circular contact area between the striker (dropped stainless steel ball) and the specimen also utilized Equation (6), except that the effective ratios R is defined as per Equation (7).

$$\begin{aligned}
 a &= (rd)^{1/2} \\
 d &= \left(\frac{9 F_c^2}{16 E^* r} \right)^{1/3} \\
 Area_{circ} &= \pi a^2
 \end{aligned}
 \tag{6}$$

$$\frac{1}{R} = \frac{1}{r} + \frac{1}{r_1}
 \tag{7}$$

Where r is the radius of the specimen, r₁ is the radius of the striker, d is the depth of the indentation, F_c is the fracture force, E* is the elastic modulus of the bodies in contact (E₁, E₂ are the elastic moduli and ν₁, ν₂ the Poisson’s ratios associated with each body).

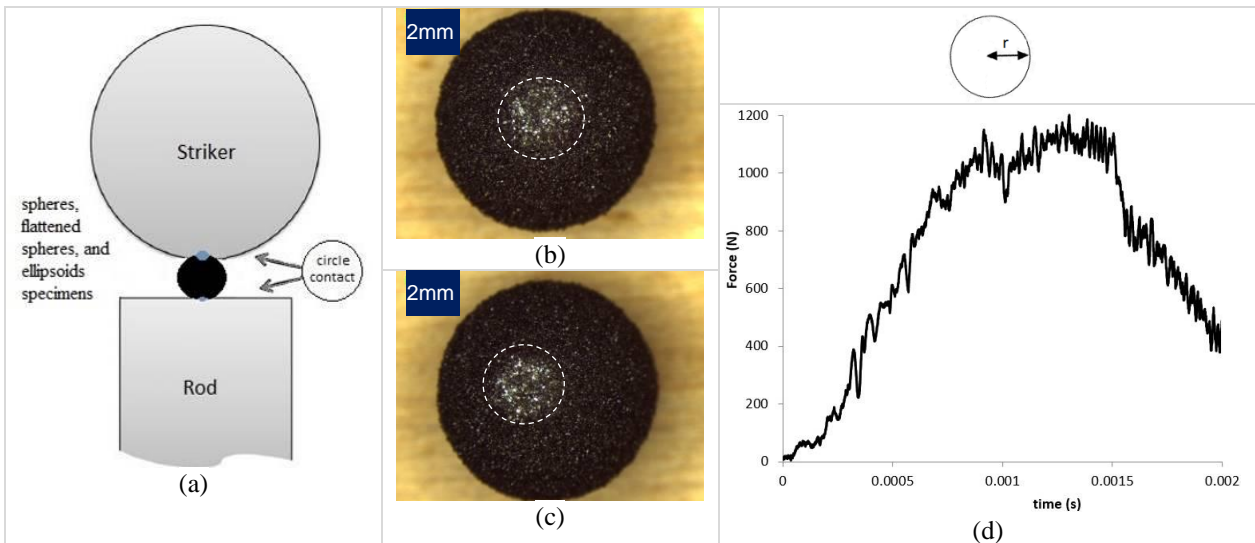


Figure 35 Illustration of the bodies in contact for ‘Group A’: a) striker, ‘group A’ specimen, and rod during breakage in the SILC test, b) evidence for striker against the ‘group A’ specimen, c) the ‘group A’ specimen against the rod, and d) the force-time profile of a sphere-shaped specimen that did not failure.

‘Group B’ was represented by cylinder-shaped specimens. The hypothesis applied for ‘group B’ was that two distinct contacts were formed. Notice that all cylinder-shaped specimens were diametrically loaded/compressed to failure during the test. An elliptical contact occurred between the striker against the ‘group B’ specimen; in addition to that, a rectangular contact was formed at the ‘group B’ specimens against the anvil/rod (Figure 36). Calculation of the cross-sectional elliptical contact area and the cross-sectional rectangular contact area are presented in Equations (8) and (9), respectively. Bonfils’ (2017) calculation accounted for the dimensions of the striker (i.e. D_1 is the steel ball diameter) and the cylinder-shaped specimen tested (i.e. D_2 is the specimen diameter) to provide the three constants: e is the ellipse eccentricity, K and E are the complete elliptic integrals of first and second class, respectively. The elliptical integrals are computed in MatLab for all cylinder-shaped size and ball size combinations. For the cross-sectional rectangular contact area, the rod is considered a cylinder with an infinitely large radius.

$$\begin{aligned}
 a &= b(1 - e^2)^{1/2} \\
 b &= \frac{3F_c K}{2\pi K_e \left(\frac{1}{D_1}\right)^{1/3} \frac{K}{\left(-\frac{1}{e} \frac{dE}{de}\right)^{1/3} \left(\frac{3F_c}{2\pi K_e}\right)^{2/3}} \\
 Area_{ell} &= \pi ab
 \end{aligned} \tag{8}$$

$$Area_{rect} = 2L \left(\frac{\exp(0.5 \ln(2F_c d_p))}{\pi L K_e} \right) \tag{9}$$

where F_c is the fracture force, d_p is the geometrical mean size (diameter/height), L is the specimen length, π is the number PI, and k_e is the local deformation coefficient.

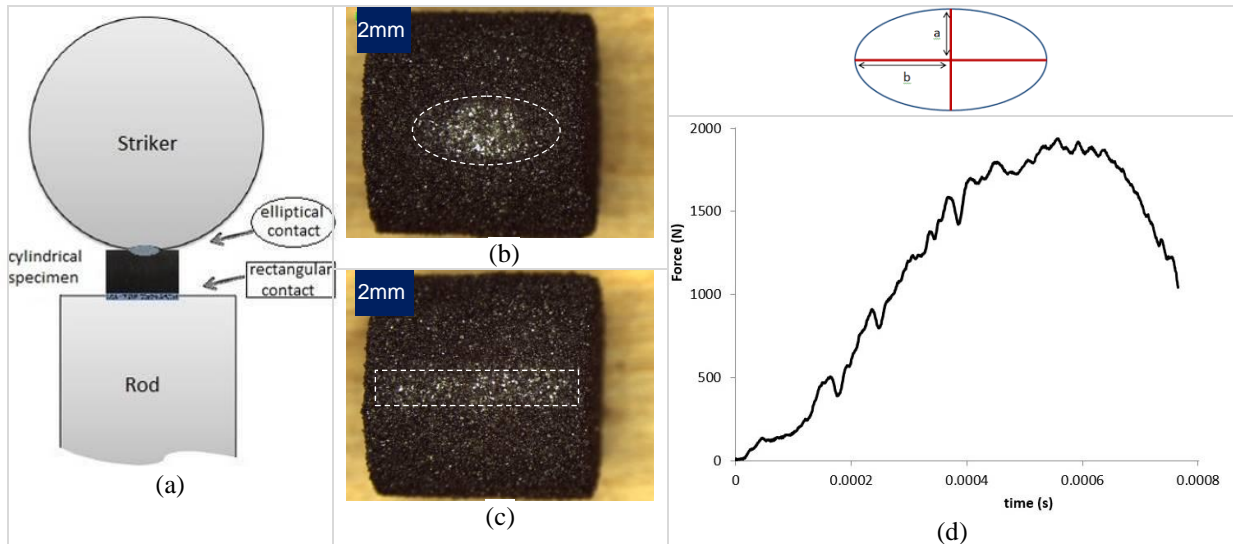


Figure 36 Illustration of the bodies in contact for ‘Group B’: a) striker, ‘group B’ specimen, and rod during breakage in the SILC test (Bonfils, 2017), b) evidence for striker against the ‘group B’ specimen, c) the ‘group B’ specimen against the rod and d) the force-time profile of a cylinder-shaped specimen that did not failure.

4.6.2 Determination of fracture force

A summary of calculations is presented in section 4.6.3. Data processing consisted of analyses of the force-time results from the SILC system, together with information about rod, striker (mass, diameter, and drop height), specimen (diameter, length, and mass), and calibration measurements, all loaded into an Excel spreadsheet. The deconvolution of a typical force-time profile provides information about the fracture force (or force at first fracture, F_c) of each specimen (Tavares, 1997); the fracture event is obtained by direct reading of the peak force on the graphic. It is crucial that results are interpreted by selecting the point on the force–time profile that corresponds to the occurrence of the bulk fracture of the specimen, since it effects further data calculated using the SILC test.

The relationship between the load–displacement profiles can be described using the following regions (Tavares, 1997):

- Region (I): all bodies are in contact, initiation of specimen compression results in relocation of the specimen on the anvil and/or smoothing of asperities on the surface;
- Region (II): deformation stage where specimen behaviour is predominantly elastic, therefore it can provide an estimation of the elastic modulus for the specimen;
- Region (III): damage accumulation and development of a macrocrack in a specimen; and
- Region (IV): rapid reduction of the load with an increase in displacement, growth of a macrocrack through the specimen which leads to failure (breakage).

To illustrate these regions, a typical force-time profile recorded when breaking well-defined sphere-shaped specimen with 10 mm diameter specimen is shown in Figure 37. More intense vibrations on the force-time profile occur for 'group A' specimens whereas 'group B' specimens have less spikey profiles. Unfortunately, none of the recorded videos were able to capture the differences between region II (for this example, $t \approx 350 \mu\text{s}$ assuming deformation and elastic behaviour) and III ($t \approx 700 \mu\text{s}$ for accumulation damage), except for the amount of grains being spread, so these limits are speculations based on time. Figure 37 also illustrates the dynamic nature of the loading where the fracture forces is only observable for less than a microsecond before damage to the specimen becomes evident. The peak corresponding to the fracture force is followed by a steep drop in the force as confirmed on the ultrahigh-speed videos recorded for the specimens tested (Figure 37).

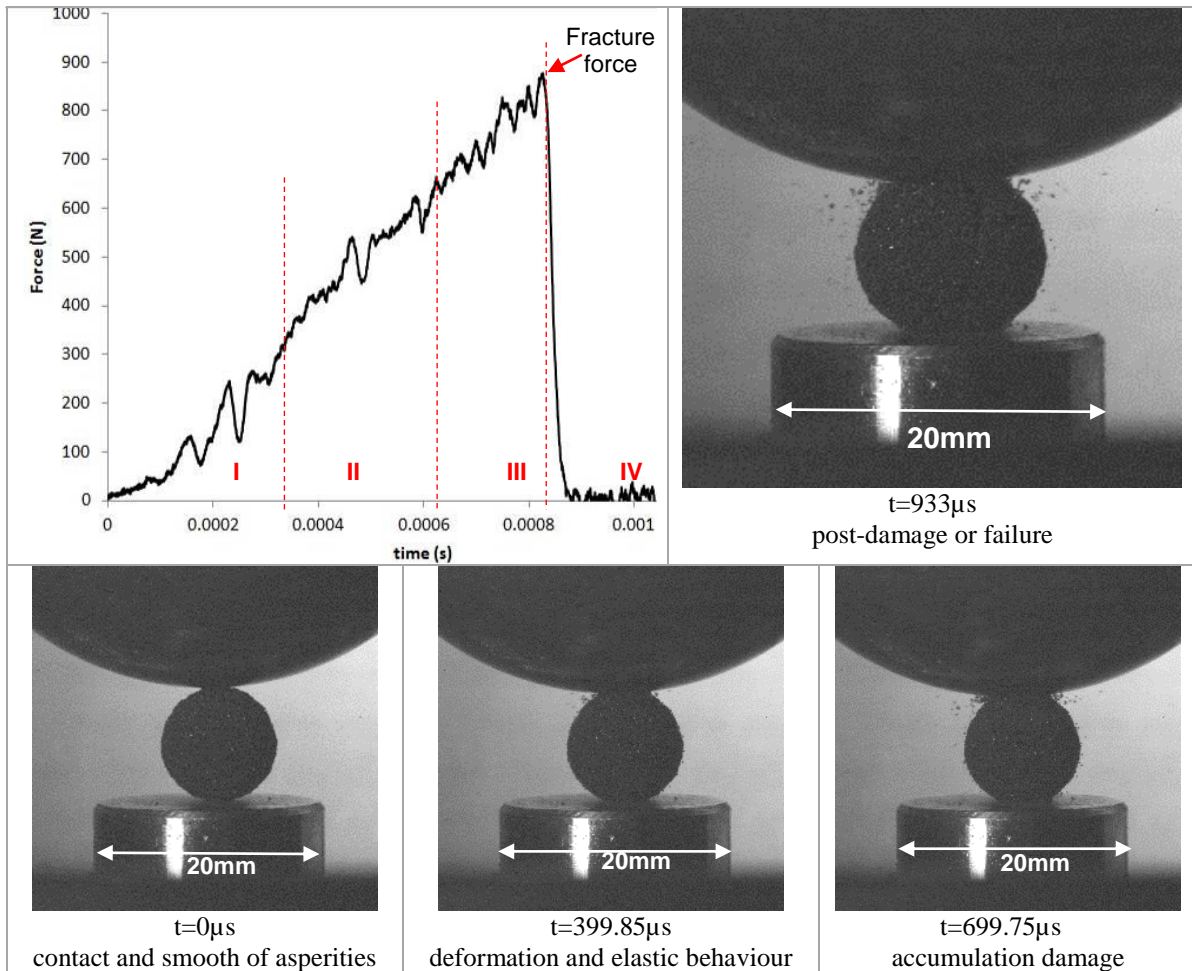


Figure 37 Example of force-time profile of 3DP sphere-shaped specimen with 10 mm in diameter (striker of 2 inches in diameter, 535.25 g) and recorded impact at time equal to 0, 399, 699 and 933 μ s. Regions I to IV are described in the text.

4.6.3 Determination of fracture energy for different settings/conditions

The fracture energy (E') for shaped specimens corresponds to the elastic energy stored within the specimen until the occurrence of fracture and it corresponds to the area below the force-deformation curve (Equation (10)) (Tavares and King, 1998b; Bonfils, 2017):

$$E' = \int_0^{\alpha_c} F d\alpha \quad (10)$$

where α is the deformation (or strain) applied on the specimen, α_c is the deformation at fracture, and F is the force-deformation (applied load or stress).

Notice that measurement of force occur at the strain gauge which is attached to the surface of the steel rod and gets trigger on the contact area between bodies. The force can be calculated based on

the propagation of compressive strain waves through a homogeneous rod (i.e., the longitudinal wave propagation theory) and the Hooke's Law (detailed calculation is presented at Tavares, 1997 and Saeidi, 2016).

Fracture energy calculations for 'group A' specimens

The force-deformation of 'group A' specimens (i.e. circular contact area) is given by Equation (11) (Tavares and King, 1998b). Both the energy absorbed by the specimen, and the energy absorbed by the rod are measured during the breakage test with SILC:

$$F = \left(\frac{K_e d_p^{1/2}}{3} \right) \alpha^{3/2} \quad (11)$$

where K_e is the local deformation coefficient (or critical load) of the Hertzian contact theory (Goldsmith, 1960), d_p is the distance between loading points (specimen height or diameter), and α is the deformation obtained on the impact load cell by accounting for the displacements of the top of the anvil/rod and the deformation of the impacted specimen (Bourgeois and Banini, 2002).

The local deformation coefficient (K_e) is calculated for 'group A' specimens as follow (Equation (12)) (Tavares and King, 1998b):

$$K_e = \sqrt{(0.576 \times F_c^5) / (d_p \times E_c^3)} \quad (12)$$

where F_c is the force at first fracture, E_c is the energy absorbed by specimens at fracture, and d_p is the distance between loading points (specimen height or diameter).

Fracture energy calculations for 'group B' specimens

The deformation (or strain) applied to cylinder-shaped specimens needs to be estimated before calculating the fracture energy (E'). For that, the calculation methodology uses the Hertzian theory of contact for cylinder-shaped specimens which takes into account the bodies in contact. The first contact involves the striker impacting the cylinder-shaped specimen which represents an elliptical contact area (Figure 35) and the deformation for this contact is given by Equation (13) (Bonfils, 2017).

$$\alpha_1 = C \left(\frac{1}{D_1} \right)^{1/3} \left(\frac{3F_c}{2\pi K_{e1}} \right)^{2/3} \quad (13)$$

where α is the cylinder-shaped specimen deformation (or strain) against the striker, C is a constant for a given cylinder and striker (ball) diameter, D_1 is the striker diameter, π is the number PI, F_c is

the force at first fracture, and k_{e1} is the local deformation coefficient is calculated using the Hertzian theory for the contact between the striker and the cylinder-shaped specimen (Equation (14)) (Bonfils, 2017).

$$K_{e1} = \frac{k_1 \times k_2}{k_1 + k_2} \quad (14)$$

where k_1 is the Young's modulus of the striker, and k_2 is the Young's modulus of cylinder-shaped specimen.

The 'apparent' stiffness or stiffness, as defined in the SILC, is also called bulk elastic modulus and is given by (Equation (15)). Notice that bulk modulus is defined for a uniform compression where the pressure is applied from all directions uniformly. And the Young's modulus is defined only for one axis of the material. Therefore, the term Young modulus is assumed along this thesis.

$$k = \frac{Y}{(1 - \mu^2)} \quad (15)$$

where Y is the Young's Modulus and μ Poisson's ratio.

The other side of the contact involves the cylinder-shaped specimen impacting with the planar surface of the rod which represents a rectangular contact area (Figure 36). The deformation of the contact between the cylinder-shaped specimen and the rod (Puttock and Thwaite, 1969) is given by (Equation (16)):

$$\alpha_2 = \frac{F_c}{L\pi K_{e2}} \left(1 + \ln \left(\frac{2\pi K_{e2} L^3}{F_c D_1} \right) \right) \quad (16)$$

where α is the deformation against the planar surface of the rod, F_c is the force at first fracture, L is the length of the cylinder, D_1 is the cylinder-shaped specimen diameter, π is the number PI, k_{e2} is the local deformation coefficient of the Hertzian theory for the contact between the planar surface (rod) and the cylinder-shaped specimen (Equation (17)) (Bonfils, 2017).

$$K_{e2} = \frac{k_1 \times k_2}{k_1 + k_2} \quad (17)$$

where k_1 is the Young's modulus of the rod, and k_2 is the Young's modulus of the cylinder-shaped specimen.

Once the deformations associated with the contact areas of each side of the cylinder-shaped specimen are estimated, the fracture energy for the contact bodies can be calculated. The total fracture energy (E') is a sum of total deformation in the vicinity of the contact (the deformation at the elliptical contact area and the deformation at the rectangular contact area) (Equation (13); (16)).

4.6.4 Estimation of specific fracture energy

The specific fracture energy (E_m) for ‘group A’ and ‘group B’ specimens were simply obtained by dividing the fracture energy (E') by the respective specimen mass (m) given by Equation (18).

$$E_m = \frac{E'}{m} \quad (18)$$

In order to account for the indentation of the striker and the rod in contact with ‘group A’ and ‘group B’ specimens (Tavares and King, 1998; Bonfils, 2017), the corrected specific fracture energy (E'') is shown in Equation (19).

$$E'' = E_m \left(\frac{1}{\frac{K_p}{K_{b,r}} + 1} \right) \quad (19)$$

where K_p is the specimen Young’s modulus and $K_{b,r}$ is the Young’s modulus of the stainless steel (ball and rod).

4.6.5 Estimation of ‘apparent’ stiffness or Young’s modulus

The ‘apparent’ stiffness (SILC literature) or Young’s modulus in this work, is a property of a structure or component of a structure resisting deformation; hence it is influenced by the geometry of the specimen. The ‘apparent’ stiffness or Young’s modulus (K_p) of ‘group A’, and ‘group B’ specimens were calculated by solving the Equation (20) (Tavares and King, 1998b).

$$K_p = \frac{(K_e \times K_{b,r})}{(K_e - K_{b,r})} \quad (20)$$

where K_p is the specimen Young’s modulus, K_e is the local deformation coefficient, and $K_{b,r}$ is the Young’s modulus of the stainless steel (ball or rod).

4.6.6 Estimation of the tensile strength

Tensile strength calculation for ‘group A’ specimens

The tensile strength of sphere and flattened sphere-shaped specimens subject to impact was estimated using the Equation (21) (Tavares and King, 1998a):

$$\sigma_t = 2.8F_c / (\pi \times d_p^2) \quad (21)$$

For ellipsoid-shaped specimen better estimation was obtained taken the length of the specimen into consideration (Equation (22)).

$$\sigma_t = 2.8F_c / (\pi \times d_p \times L) \quad (22)$$

where σ_t is the tensile strength, F_c is the force at first fracture, π is the number PI, d_p is the distance between loading points (specimen height or diameter), and L is the length of the ellipse-shaped specimen. Formerly, d_p is estimated as the geometric mean of the consecutive sieves which bound the size interval for irregular single-particles (Tavares, 1997).

Tensile strength calculation for ‘group B’ specimens

The tensile strength of cylinders-shaped specimens when subject to impact is based on the Brazilian Tensile Strength estimation which is an indirect testing method governed by the ISRM (1978) and ASTM (2008) standards (Equation (23)). Based on this assumption the fracture or failure occurs at the point of maximum tensile stress, i.e. at the center of the cylinder-shaped specimen.

$$\sigma_t = 2F_c / (\pi \times D \times L) \quad (23)$$

where σ_t is the tensile strength, F_c is the force at first fracture, π is the number PI, D is the diameter of the cylinder, and L is the length of the cylinder.

4.6.7 Estimation of the compressive strength

The unconfined compressive strength (UCS) is a measure of a material strength which is not necessarily of main interest in the comminution process, but it is an important geomechanical property. According to Pejchal et al. (2017) there is no well-established method to measure the strength of individual specimens. However, authors such as Altindag and Guney (2010), and Nazir et al. (2013) support that there is a relationship between tensile and compressive strength.

In the present work, UCS (σ_{cUCS}) values of cylinder-shaped specimens are measured using a typical servo-controlled machine. Then, these values are observed against the relationship proposed by Hawkins (1998). Later in this study, the σ_{cUCS} values are compared with tensile strength calculated on SILC, which is measured under dynamic loading conditions. The possibility to estimate UCS from SILC (σ_{cSILC}) is explored using the load and the cross-sectional areas which are dependent upon specimen shape following the contact geometry (Figure 35 and Figure 36). It is emphasized that this correlation will likely be applicable for similar fabricated material, since it will be dependent of the rock/material tested (e.g. surface flaws, bedding, plastic deformation).

Finally, the validity of predicted UCS calculations from the SILC test (σ_{cSILC}) is verified against actual UCS test (σ_{cUCS}). Note that, the calculation of σ_{cSILC} for each shaped specimen tested used the

Hertz law of contact (Goldsmith, 1960; Hertz, 1881) for ‘group A’ and ‘group B’, as it has the potential to predict correctly the contact phenomena occurring experimentally on 3DP specimens. For Hertzian computations, a value of 0.32 has been assumed for Poisson’s ratio of the 3DP specimens. After the σ_{cSILC} is estimated, a correction factor is computed to provide a correlation between distinct tests and shapes on 3DP specimens, similar to approaches proposed by Franklin (1985) and Masoumi et al. (2016). The σ_{cSILC} is calculated as:

Compressive strength calculation

$$\sigma_{cSILC} = 2 \times F_c / (A_{top} + A_{base}) \quad (24)$$

where A_{top} is the cross-sectional contact area between the striker and the specimen and the A_{base} is the cross-sectional contact area between the specimen and the rod. Note that, for ellipsoid-shaped specimens, it is assumed that the average of the semi-minor axis and the semi-major axis gives a practical estimation for the specimen radius.

4.7 UCS APPARATUS AND TESTING

The testing apparatus utilized for UCS testing was an INSTRON 4505 load system and measurements were recorded digitally to obtain stress and strain data (Figure 38). The 3DP cylinder-shaped specimens were tested at room temperature and compressed at a rate of 0.25 mm/min until failure. All specimens underwent an initial load cycle of 0.2 kN to establish close contact between the specimen and INSTRON frame platens prior to loading.

All cylindrical 3DP specimens fabricated for UCS testing were printed in a vertical direction with diameters of 7.3 mm, 10.1 mm, 12.3 mm, 16.5 mm, and 21.6 mm. Overall, the specimen fabrication followed recommendations and guidelines ASTM (1991; 2000; 2013) or ISRM (1979; 1999; 2007) despite the specimen sizes. The compliance for the slenderness ratio (L/D) about 2.3:1 on average also follows the standards (ASTM, 2013). The minimum number of specimens tested for each size was eight. Measurements of Young’s modulus using axial extensometers occurred, except for the two smaller sizes tested (i.e., 7.3 mm and 10.1 mm diameter). The tangent Young’s modulus was calculated following ASTM, passing the initial portion of the stress-strain curve, where the middle (50% or average slope) of the linear pre-peak portion of the stress-strain curve and the end of the stress-strain curve immediately before maximum stress were taken. Table 7 presents a summary for the specimens tested.



Figure 38 The INSTRON 4505 load system.

Table 7 Summary of UCS tests of the 3DP specimens.

	Cylinder-shaped specimens printed vertically				
Size (diameter in mm)	7.3	10.1	12.3	16.5	21.6
Ratio (length/ diameter)	2.2:1	2.2:1	2.2:1	2.2:1	2.2:1
N (number tested)	8	10	10	10	10
Extensometer used	no	no	yes	yes	yes

4.8 RESULTS OF UCS TESTING

In comparison to UCS tests on rocks reported by several authors (Bieniawski, 1984; Santarelli and Brown, 1989; Basu et al., 2013), 3DP sandstones demonstrated consistent failure modes across specimen sizes with a small variability between smaller and larger diameter specimens. Different mechanical behaviour between the fabricated 3DP sandstone and the steel platens of the testing machine resulted in radial shear stresses at their interfaces. For larger diameter specimens (16.5 mm and 21.6 mm), a typical “end cone” failure mode (Figure 39a) resulting from platen end effects (Kwasniewski et al., 2012; Hodder, 2017) was evident and for smaller diameter specimens (7.3 mm, 10.1 mm, and 12.3 mm), the “end cone” failure zone was more rounded (Figure 39b). Because there is no variation on the bedding orientation with respect to loading direction of mini-cylinder specimens tested for UCS, the distinction on failure mode is attributed to a specimen size. For all

diameter specimens, axial cracking occurred along the direction of loading (Hodder, 2017). As shown in Figure 39c, the stress-strain response of the 3DP sandstone specimens did not exhibit a brittle post-peak response. Figure 39c refers to the specimen with 21.6 mm in diameter and 48.7 mm in length, UCS is 35.2 MPa, and estimated Young modulus is 1.9 GPa. The mean time taken to reach a peak stress was 1.3 min and 3.7 min for the smaller and larger diameter specimens, respectively.

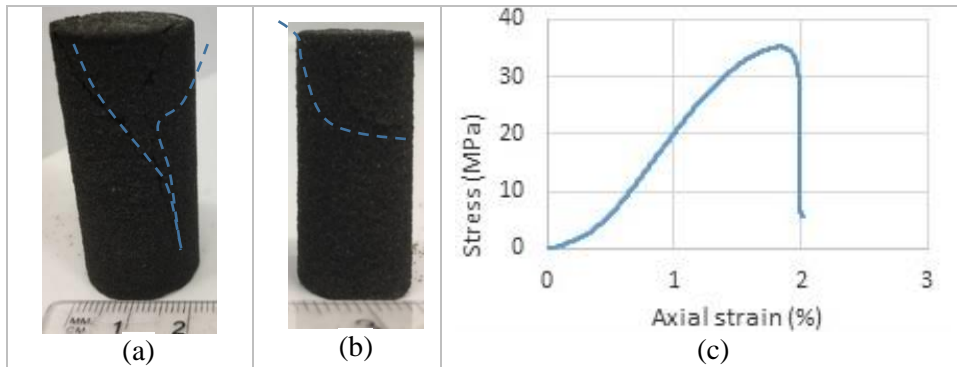


Figure 39 Failure modes observed on 3DP specimens under uniaxial compression a) 21.6 mm specimens, b) 12.3 mm specimens (zoom in photography), and c) example of the axial stress-strain curve for 3DP sandstone (21.6 mm diameter).

Figure 40 illustrates the variation of UCS with the average diameter of the tested specimens clearly showing the expected trend of increasing UCS with the increase in specimen diameter. 3DP specimens demonstrated that the larger the surface area of the specimen in contact with the platens, the better was the weight distributed so the pressure exerted needs to increase to compress the specimen.

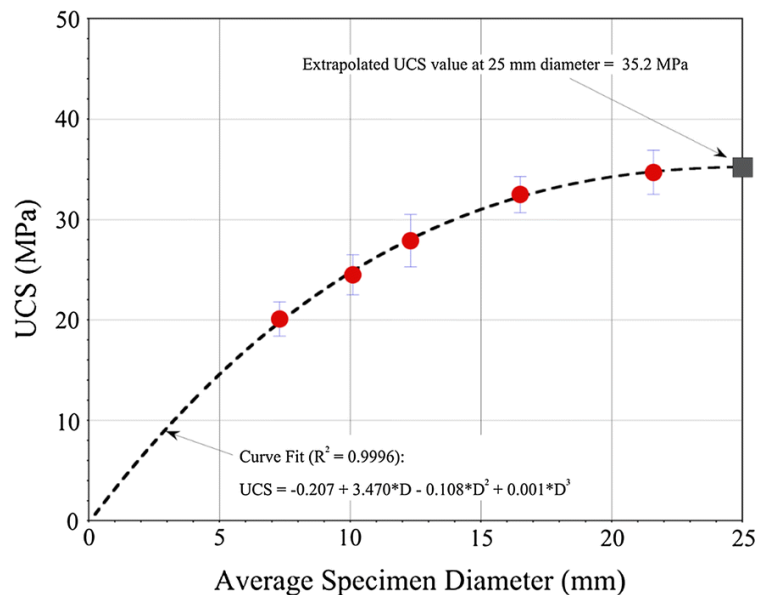


Figure 40 UCS test results for 3DP sandstone specimens of different diameter.

The mechanical properties, including σ_{cUCS} , maximum axial strain (ϵ_A), and Young's modulus (E), are summarized in Table 8. Overall, all results are quite consistent with data reported in the literature (Hodder, 2017; Primkulov et al., 2017), considering that the testing machines were not the same and aspect ratios were slightly different.

Table 8 Mechanical properties of 3DP sandstone obtained from UCS tests.

Specimen diameter (mm)	7.3	10.1	12.3	16.5	21.6
UCS (MPa)	20.1 ± 1.7	24.5 ± 2.0	27.9 ± 2.6	32.5 ± 1.8	34.7 ± 2.2
ϵ_A (%)	2.2 ± 0.4	2.0 ± 0.2	1.9 ± 0.2	1.8 ± 0.2	1.9 ± 0.2
E (GPa)	1.3 ± 0.1	1.8 ± 0.2	2.0 ± 0.3	1.9 ± 0.1	1.9 ± 0.2
N (number tested)	8	10	10	10	10

The suitability of the 3DP sandstone specimens to represent natural sedimentary sandstone was assessed by comparing the UCS measured on the 3DP specimens to UCS measured on natural sandstones by Hawkins (1998). Hawkins tested seven sedimentary rocks at eight different diameters, all with a 2:1 length-to-diameter ratio and presented the results reduced to dimensionless form relative to the strength of the 54 mm diameter specimen (Hawkins' sandstone data is presented below). Here, UCS data was normalized to the UCS measured on 25 mm diameter specimens. A modest extrapolation, as shown in Figure 40, was completed for the 3DP results because the largest 3DP sandstone tested was 21.6 mm. Consequently, the σ_{cUCS} of a 25 mm diameter 3DP specimen was assumed to be equal to 35.2 MPa. Figure 41 shows excellent correspondence in UCS results between the sedimentary sandstone rocks tested by Hawkins (1998) and the 3DP sandstone specimens. While no large diameter 3DP specimens were tested in this study, it is expected that the 3DP specimens would follow the same strength variation determined from Hawkins (1998).

Notice that the results for smaller 3DP specimens and natural sandstone (up to 54 mm) showed comparable ascendant strength which do not support the curved "best fit" line and well-known formulation produced by Hoek and Brown (1980). Hoek and Brown (1980) showed that specimen strength increases progressively as the specimen diameter decreases, but this was for specimens containing flaws and fracture which can be observed on larger size specimens (from 54 to 155 mm in diameter) from Hawkins (1998) (Figure 41).

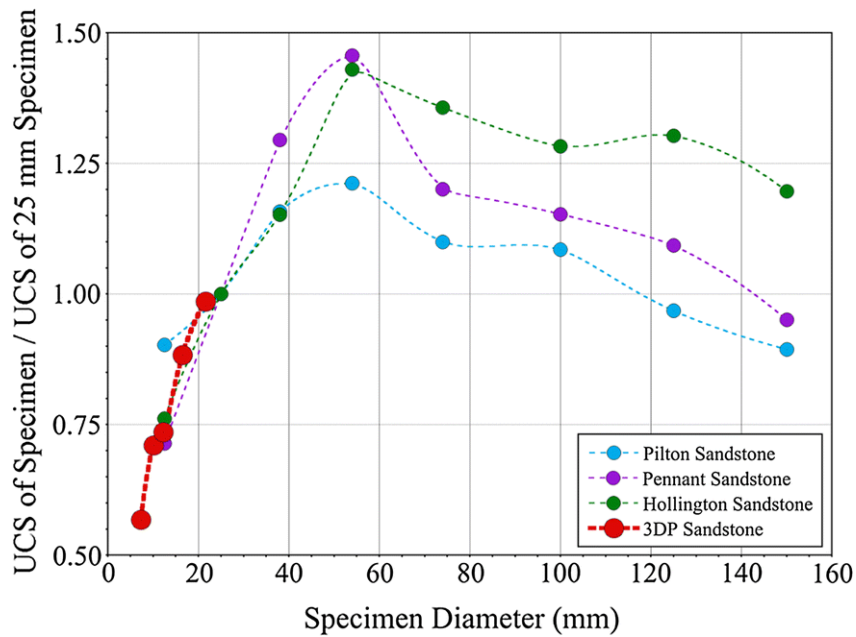


Figure 41 UCS strengths of three sedimentary sandstone rocks (Hawkins, 1998) versus 3DP sandstone.

4.9 RESULTS OF SILC TESTING

4.9.1 Fracture mechanism

In a SILC test, impact from the striker (steel ball) compresses (deforms) the specimen vertically which will induce horizontal deformations and result in horizontal tensile stresses within the specimen (Figure 42a). Vertically oriented fractures are created when this horizontal tensile stress exceeds the specimen tensile strength. This process is very similar to the processing occurring in a Brazilian indirect tensile test. Recorded videos show that the crack initiation position for 3DP specimens definitively starts at the contact surface with the striker (Figure 42b). The first crack propagates perpendicular to the direction of principal tensile stress (Figure 42c). Despite the SILC test being a case of tensile strength dominated failure where specimen shape plays an important role, there is a transition between shear and tensile failure mode. This interpretation is supported by observation of an edge fragment (Figure 42d) systematically formed at the loading contacts, which indicate stress concentration near the loading (striker-specimen contact and rod-specimen contact) that leads to an early shear failure fracture in that localised section of the specimen. The stress concentration induces the propagation of tensile failure zone along the vertical loading diameter.

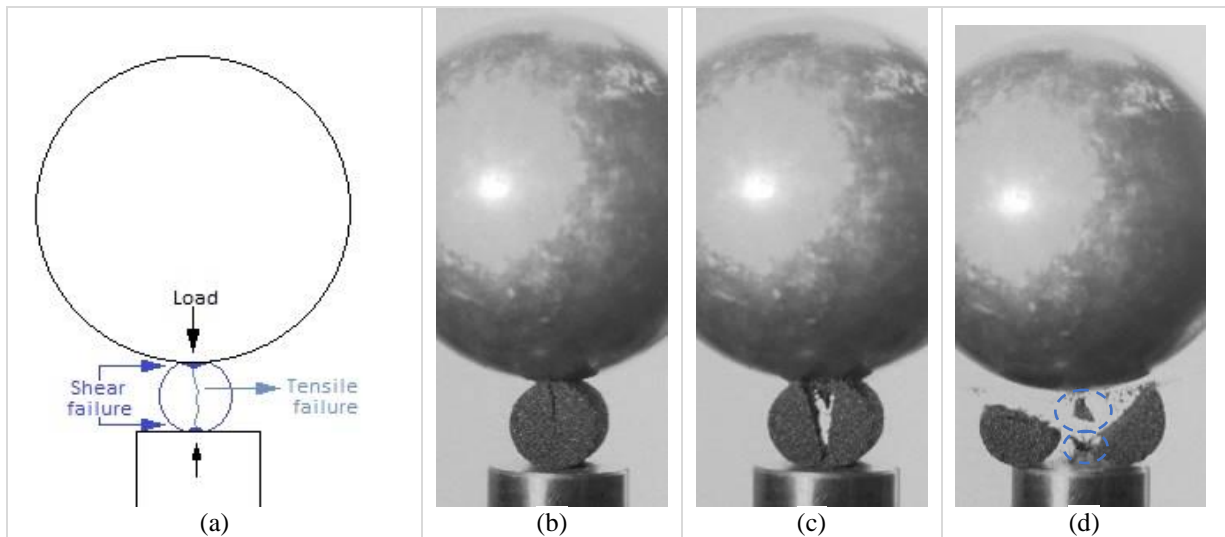


Figure 42 a) Transition between shear and tensile failure modes in 3DP sandstone, modified from the illustration by Li and Wong (2013), b) crack propagation on cylinder-shape specimen diametrically loaded, c) specimen splitting, d) edges from shear failure.

The recording with the monochrome device was set to start when the striker departed its initial position (i.e. free fall) until it touched the rod. Then, the frames of interest would be observed for a shorter interval, e.g. contact striker/specimen and crack propagation which takes up to 1200 μ s. Figure 43 (ultrahigh-speed photography images) illustrates the sequence of fracture generation and propagation as well as the failure pattern for distinct shapes and sizes tested with SILC.

Figure 43a shows a cylinder-shaped specimen with 12.2 mm diameter. The cracks are firstly initiated by the striker at the top loading point, then propagate along the loading plane, and finally split the specimen into two (quasi symmetric) halves. Almost all cylinder-shaped specimens (independent of size and ratio) have a very clear crack initiation and propagation. It may occur that the striker bounced up and down on both halves or on one half before the fragments leave the anvil, particularly for smaller size specimens (\approx 5.2 mm and 7.2 mm diameter). But fragments were completely separated at that instant. Only three cylinder-shaped specimens printed in vertical direction experienced fracture propagation through the banding (i.e., direction of printed layers) resulting in surface chipping or multiple fragments. This is an indication that the fragmentation of cylinder-shaped specimens is influenced by the fabric orientation (Jaeger, 1960; Attewell and Sandsford, 1974; Brown et al., 1977; Al Jassar and Hawkins, 1977, 1979). The anisotropy in properties of the specimens should reflect the bedding structure produced in the 3DP process.

Figure 43b illustrates a sphere-shaped specimen with 5.2 mm diameter where the residual kinetic energy of the striker allowed further breakage of the resulting fragments from the first fracture. It

was observed that smaller specimens (≈ 5.2 mm and 7.2 mm diameter for ‘group A’) might experience some indentation with very small fragments (i.e., grain sized) being generated. For those cases, multiple fragments seemed to be crushed and trapped between the striker and the anvil/rod, even though the test might be compared to an indirect tensile strength test. Overall, a clear crack propagation is not always evident for these smaller sized specimens. Similar observation is reported by Huang et al. (2014) when testing glass spheres of 4.39 mm diameter where slight shape destruction was attributed to Hertzian ring cracks splitting off a shallow slice before the release of the disintegrating cracks.

Figure 43c shows the ellipsoid-shaped specimen with 12.4 mm diameter. The cracks developed by the striker also started at the top loading point, then propagated along the loading plane, and the specimen split into three fragments, about 120° apart. Overall, the fracture seemed to be more evident on larger specimens (≈ 10.1 mm and 12.2 mm diameter for ‘group A’), which behaved more consistently either with a clear split of the specimen (two halves) or three portions/fragments, except for couple specimens experiencing surface chipping.

Figure 43d illustrates the failure pattern of a flattened sphere-shaped specimen with 10.2 mm diameter where splitting into two halves occurred approximately 180° apart. In this case the striker bounced on top of one half while the other half left the anvil.

Figure 43e shows an example of surface chipping on a 10.0 mm diameter sphere-shaped specimen. It is interesting to mention that 5 out of 8 (62.5%) of all those 3DP specimens (from 5.2 mm to 12.2 mm diameter of ‘group A’ and ‘group B’) that chipped on the surface presented the fracture force quite close or within a range to those specimens as bulk fracture. Therefore, each specimen experiencing chipping had the results verified before the decision to reject or keep the test result. According Tavares (1997) a specimen is considered broken if it loses at least 10% of its original weight during impact.

Figure 44 presents a summary of fragmentation characteristics for different specimen shapes and sizes tested with SILC. More frequently, the specimen would separate into two halves and/or three portions but, multiple fragments or one single chip was also observed. For the smaller diameters (5.2 mm and 7.2 mm) of ‘group A’, the number of fragments might be speculative since some of them experience indentation followed by shape destruction. It was observed that ‘group A’ (sphere, flattened sphere, and ellipsoid-shaped) specimens tend to generate more fragments of grain sizes than ‘group B’ (cylinder-shaped) specimens.

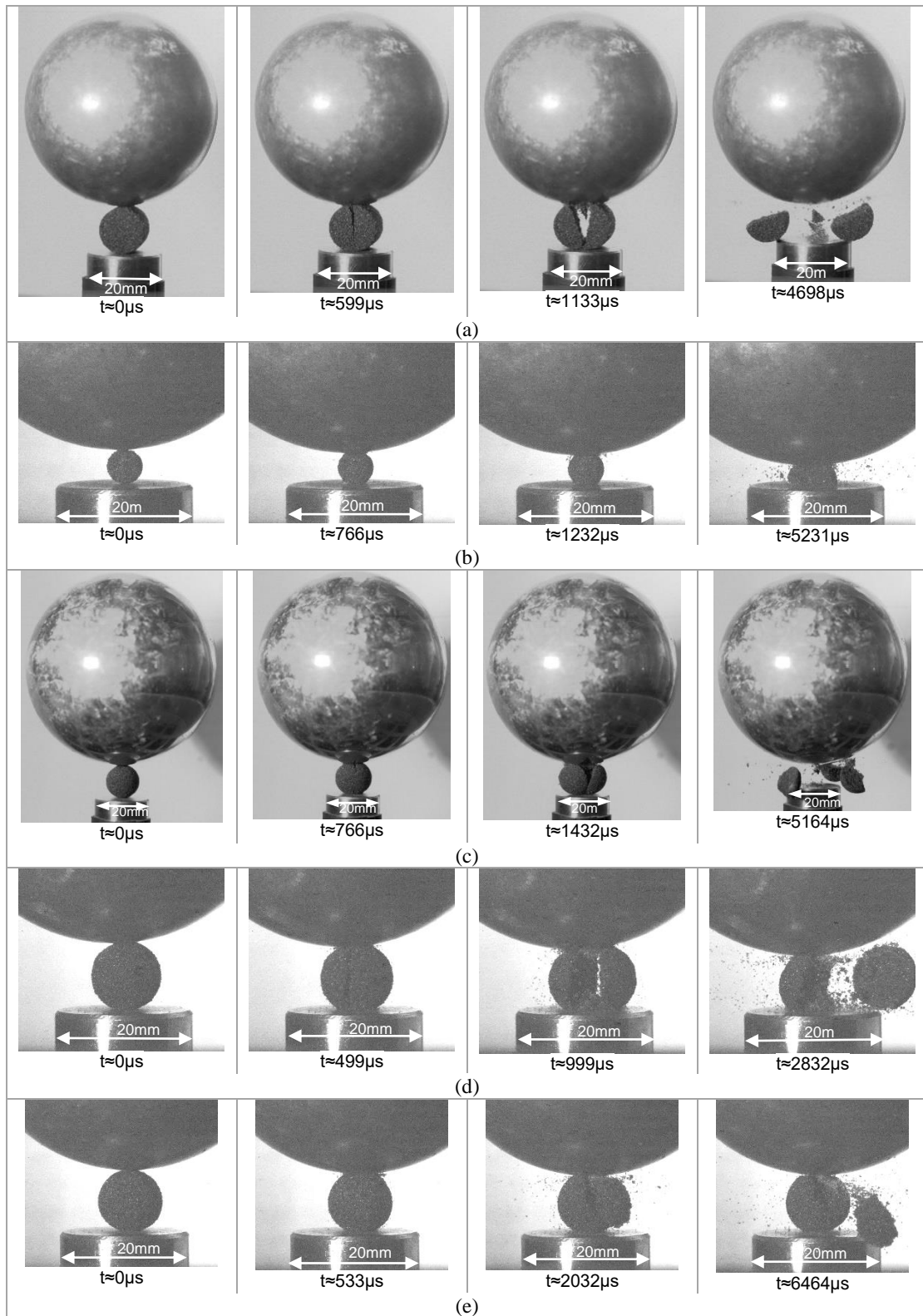


Figure 43 Fracturing process and failure pattern: a) cylinder-shaped specimen (12.2 mm) split into two halves; b) sphere-shaped specimen (5.2 mm) indented and compressed; c) ellipsoid-shaped specimen (12.4 mm) split into three fragments; d) flattened sphere-shaped specimen (10.2 mm) split into two halves, and e) sphere-shaped specimen (10.2 mm) show surface chipping. Selected frames from ultrahigh-speed camera phantom v2011.

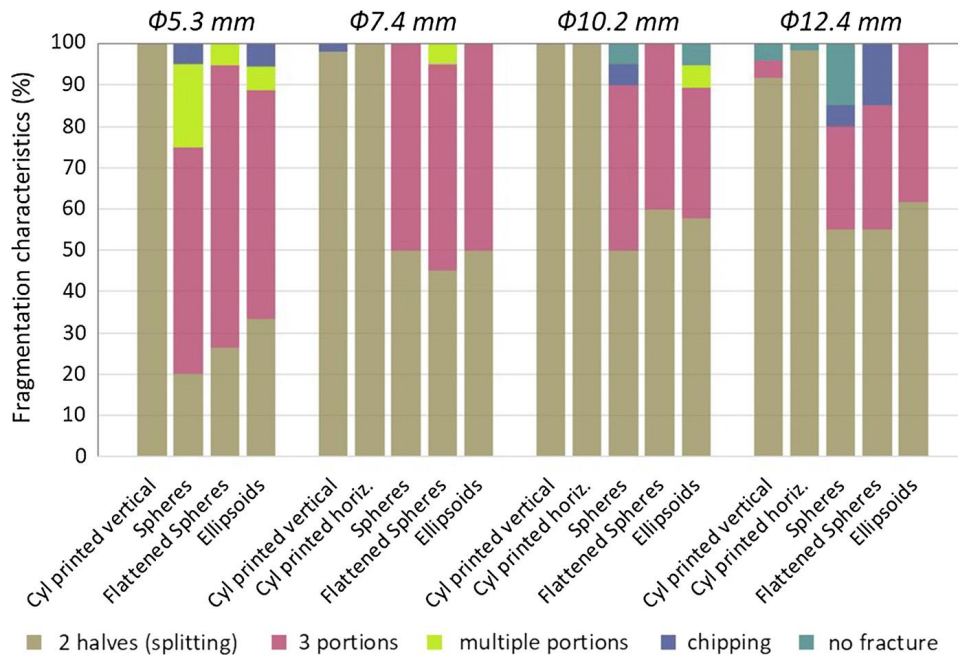


Figure 44 Summary of fragmentation characteristics generated by 3DP specimens tested with SILC.

Overall, the final fracture surface is not perfectly flat even when the striker seems to precisely contact the specimen. Major 3DP fragments from the specimens tested were collected in a plastic bag for each lot (similar shape and size). Two photographs show the pattern fracture for major fragments of cylinder-shaped specimens printed horizontal and sphere-shaped specimens, all with ≈ 12.2 mm diameter (Figure 45).



Figure 45 Pattern fracture for major fragments of 3DP with ≈ 12.2 mm diameter: a) cylinder-shaped specimens printed horizontal and b) sphere-shaped specimens.

4.9.2 Typical force-time profile

Two examples of force-time profiles for 3DP sandstone specimens broken under the same impact conditions (striker size equal to 50.8 mm diameter and drop height of 100 mm) are shown in Figure

46. Figure 46a refers to a cylinder-shaped specimen printed in horizontal direction (10.1 mm diameter, 10.1 mm length and weight of 1.1323 g), and shows that the force at first fracture (i.e., fracture force) is equal to 1139.6 N at 383 μ s. The energy absorbed by the rod and the energy absorbed by the specimen until fracture (i.e., fracture energy) were calculated as 9.5 mJ and 185.8 mJ, respectively. Figure 46b shows the test results for a flattened sphere-shaped specimen (10.0 mm diameter and weight of 0.818 g) and yields a force at first fracture equal to 990.4 N at 868 μ s. The energy absorbed by the rod and the energy stored by the specimen until fracture were calculated as 21.3 mJ and 366.9 mJ, respectively. In general, test results show that although the mass of the cylinder-shaped specimen was about 28% larger than the flattened sphere-shaped specimen, it took about half of the time to fracture the cylinder-shaped specimen when the same energy was applied. This implies that the time interval from the crack initiation to the fragmentation is longer for ‘group A’ shapes. It may be related to the integrity of the specimen’s overall strength and contact areas. Cylinder-shaped specimens are easier to lose integrity once it splits, where the sphere-shaped specimens may be likely to fail at the top, but the overall strength can still remain until the middle part breaks. The fracturing process and failure pattern of ‘group A, and ‘group B’ have a shape dependency as observed in Figure 46.

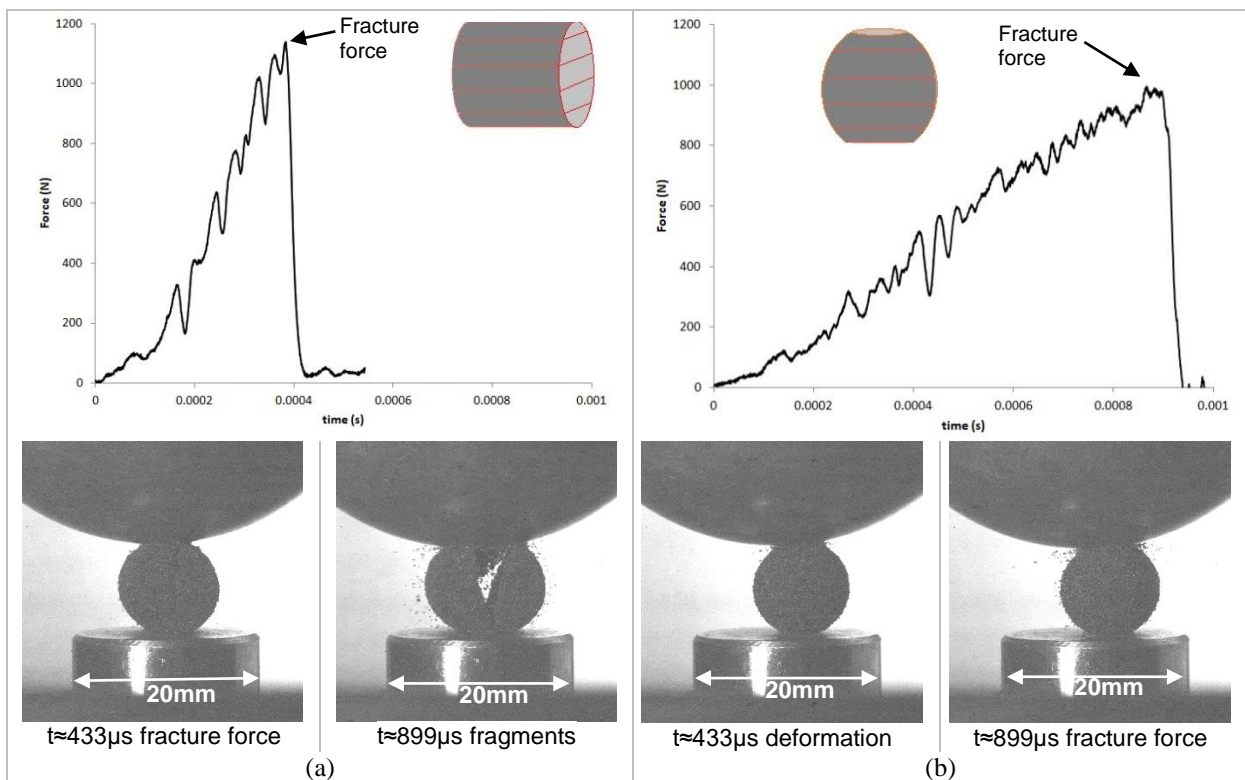


Figure 46 Example of force-time curve of 3DP sandstone with ≈ 10 mm diameter and fractured under same impact conditions: a) cylinder-shaped specimen printed horizontal, and b) flattened sphere-shaped specimen.

4.9.3 Analysis of SILC results

The results for distinct sets of specimens presented in terms of shape, size, and orientation were initially analysed for inherent scatter or variability of specific parameters of interest (fracture force, specific fracture energy, Young's modulus, and tensile strength) by plotting cumulative probability distributions (Equation (25)). This method consists of ranking the test results in ascending order and then assigning $i=1, 2, 3, \dots, N$ to the ranked observations. N is the total number of tests performed per series of experiments.

$$P(E_{m,1}) = \frac{(i - 0.5)}{N} \quad (25)$$

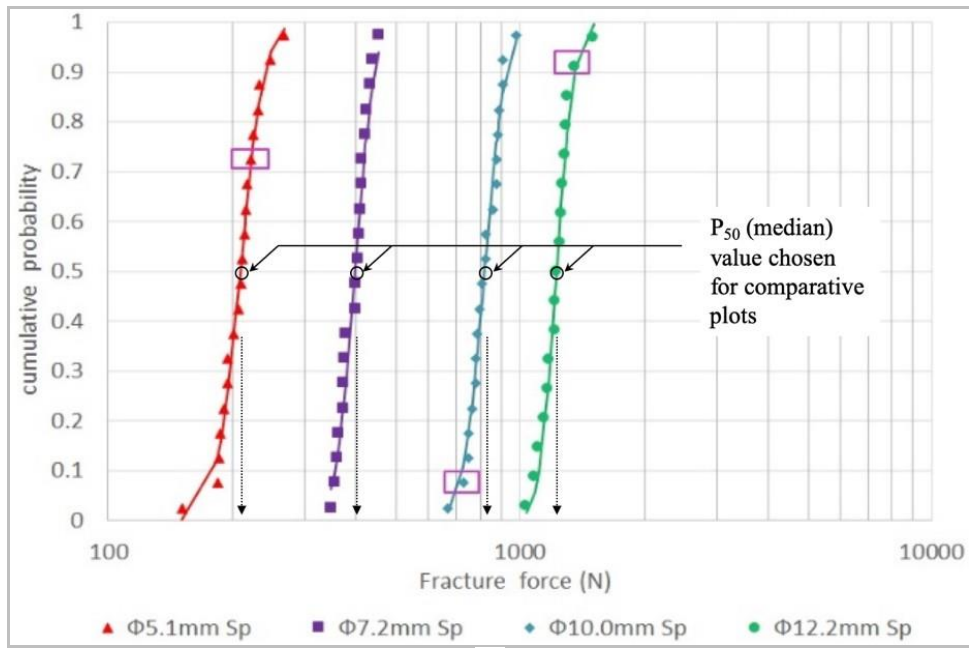
Subsequently, the resulting pairs, i.e., specific fracture energy vs cumulative probability $[E_{m,1}, P(E_{m,1})]$ can be plotted with specific fracture energy presented in a logarithmic scale. Different material can be effectively described fitting a log-normal distribution to the test data (Baumgardt et al., 1975; Dan and Schubert, 1990; King and Bourgeois, 1993; Tavares, 2007; Bonfils, 2017)) given by (Equation (26)). Appendix II shows a comprehensive catalogue of SILC data.

$$P(E_m) = \frac{1}{2} \left[1 + \operatorname{erf} \left(\frac{\ln E_c - \ln E_{m,50}}{\sqrt{2}\sigma_E} \right) \right] \quad (26)$$

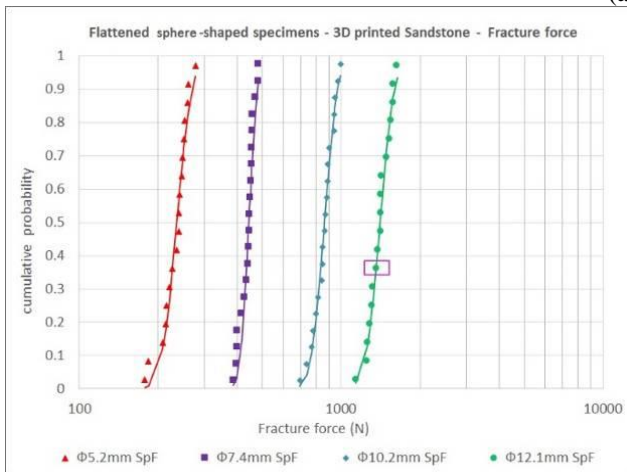
where $E_{m,50}$ is the median specific fracture energy, σ_E^2 is the geometric variance of the distribution.

For example, Figure 47a shows the cumulative probability for the measured fracture force of sphere-shaped specimens per size (i.e., diameter), where the log-normal curve fits are shown for each dataset. These cumulative probability plots also highlight the effect of specimen size on SILC test measurements but to provide a single statistic for exploring these relationships over the entire series of experiments, the corresponding median or P_{50} value for each dataset has been chosen from the curve fits (Figure 47a). Symbols are individual specimens and lines are log-normal distribution curve fits. The pink rectangles indicate specimens that were chipped.

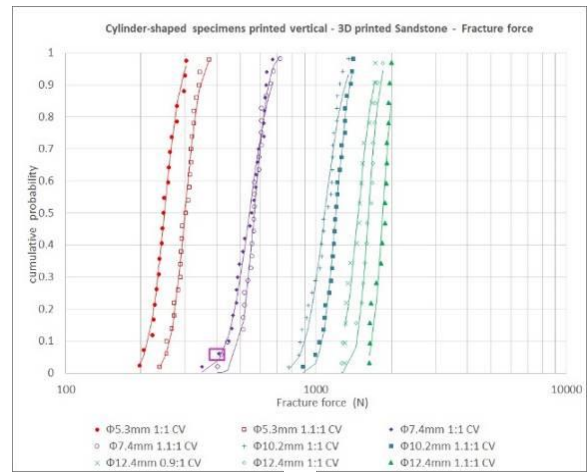
Overall, the cumulative probability plots for all shaped specimens (sphere, flattened sphere, ellipsoid, cylinder printed vertically, and cylinder printed horizontally) showed good reproducibility for tests conducted on 3DP specimens with a defined geometry (Figure 47). All cylinder-shaped specimens were tested for some small variation on the length-to-diameter ratio (1:1 and 1.1:1, while specimens with 12.2 mm diameter were also tested for 0.9:1), and the ratio variation was captured on SILC tests (Figure 47d, e).



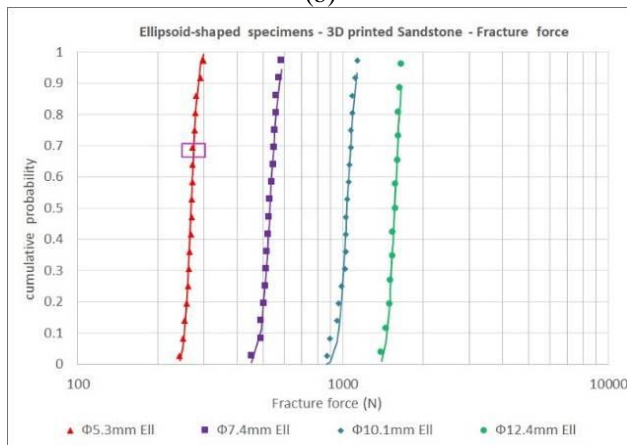
(a)



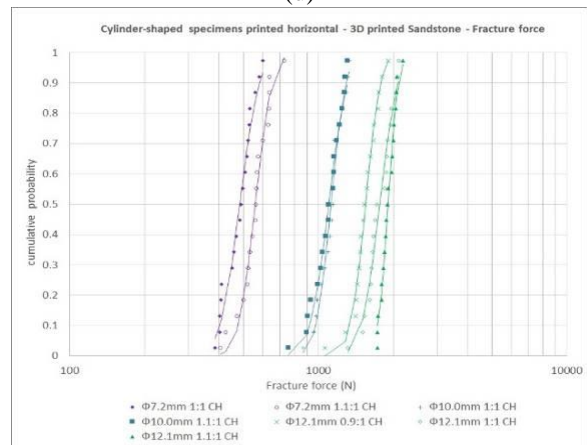
(b)



(d)



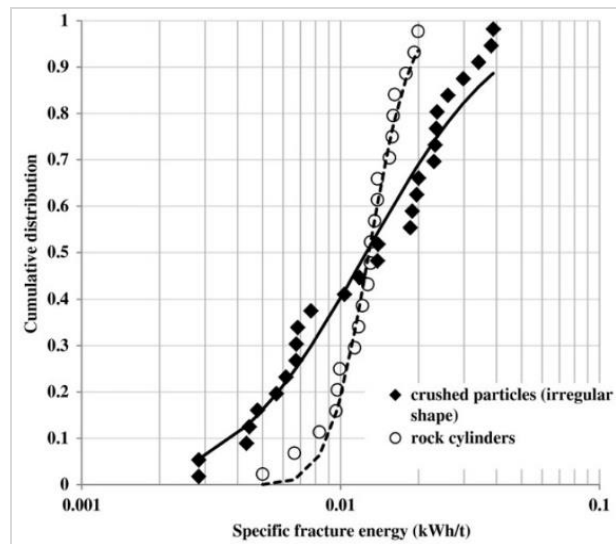
(c)



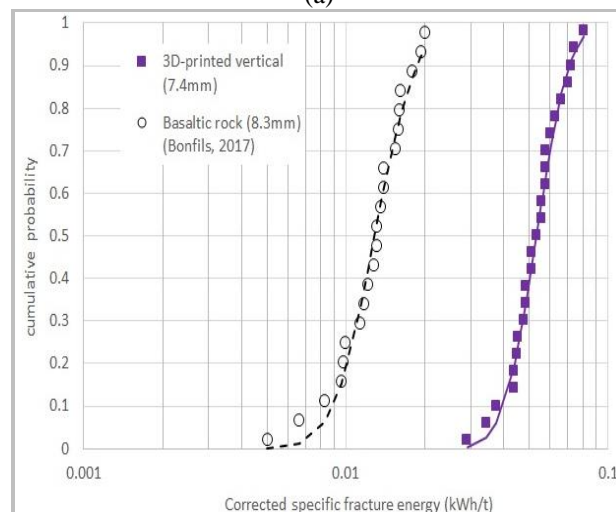
(e)

Figure 47 Cumulative distributions of force at first fracture of: a) sphere-shaped, b) flattened sphere, c) ellipsoid, d) cylinder printed vertical, and e) cylinder printed horizontal.

To better understand the fracture behaviour of 3DP specimens under SILC test conditions, a comparison of cumulative distributions between natural rocks tested by Bonfils (2017) and the fabricated 3DP specimens was conducted (Figure 48). Despite the resolution of the strain gauge and digitalisation equipment utilized, the scattered data observed from SILC tests is attributed to both the shape and the intrinsic material variability of tested specimens (Bonfils, 2017). Figure 48a shows the log-normal distributions for specific fracture energy (or corrected specific fracture energy) comparing results of irregular crushed particles and cylinders-shaped for basaltic rock plotted by Bonfils (2017). It demonstrates that a defined shape certainly contributes to reduce the scatter. Figure 48b illustrates that cylinder-shaped specimens of basaltic rock (Bonfils, 2017) and 3DP specimens showed quite similar scatter. Typical basalt rocks have a fine-grained mineral texture, which may contribute to the consistency of the two sets of results.



(a)



(b)

Figure 48 Cumulative distribution of the specific fracture energies: a) irregular crushed particles versus cylinder-shaped specimens of basaltic rock (Bonfils, 2017), b) cylinder-shaped specimens of basaltic rock versus cylinder-shaped specimens of 3DP.

Figure 49 shows the median results of fracture force for all shapes and sizes tested. The fracture force increases with increasing specimen size, with cylindrical specimens ('group B') following a slightly different trend than the non-cylindrical specimens ('group A'). An interesting result was that trend for ellipsoid-shape specimens are positioned between cylinder shape-specimens and sphere-shaped specimens. Also, the influence of fabric orientation relative to impact direction influenced the breakage properties. For instance, the median fracture force for flattened sphere-shaped specimens (marked as triangles) is larger than sphere-shaped specimens (marked as squares) (Figure 49). When referring to cylinder-shaped specimen printed vertical (marked as dots) and horizontal (marked as diamonds), the larger specimens (≈ 12.2 mm diameter) tend to present more variability in the median fracture force. The observations for cylinder-shaped specimens should take the information of aspect ratio into consideration. It was observed that each small increment (≈ 0.1 increment) on the aspect ratio resulted in an increase of median force at first fracture for cylinders printed with the same fabric.

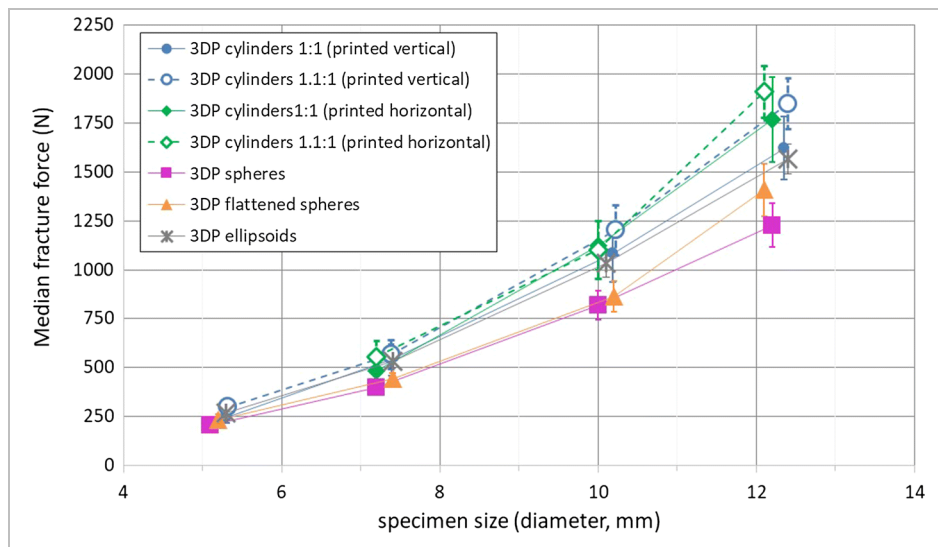


Figure 49 Variation of median force at first fracture with specimen size for 3DP specimens.

Figure 50 shows that, when cylinder-shaped specimens (≈ 12.2 mm diameter) are compared for same aspect ratio (for instance 1:1), then the SILC test measurements show the influence of fabric orientation (i.e., variation of bedding direction) relative to impact on 3DP sandstone. Although distinction about the fabric was not visible on the 3DP specimens, cylinder-shaped specimens printed vertical or horizontal were not mixed when tested. The results showed, for the same aspect ratio (1:1), that cylinder-shaped specimens printed horizontal (striker impacting layers/bedding varying from 0° to 90°) present slightly larger fracture force than those printed vertical (striker

impacting layers/bedding at 90°). On the other hand, the median results for smaller sizes (≈ 7.3 mm and 10.1 mm diameter) are not always behaving as expected (Figure 50). The recommended aspect ratio (1:1) when testing cylinder-shaped specimens on SILC should be perceived as small variations will reflect on the results. However, it seems to be acceptable to utilize cylinder-shaped specimens with ratio varying from 0.9:1 to 1.1:1. For further ratio variation it is suggested that the results be factored to suit the actual recommended ratio.

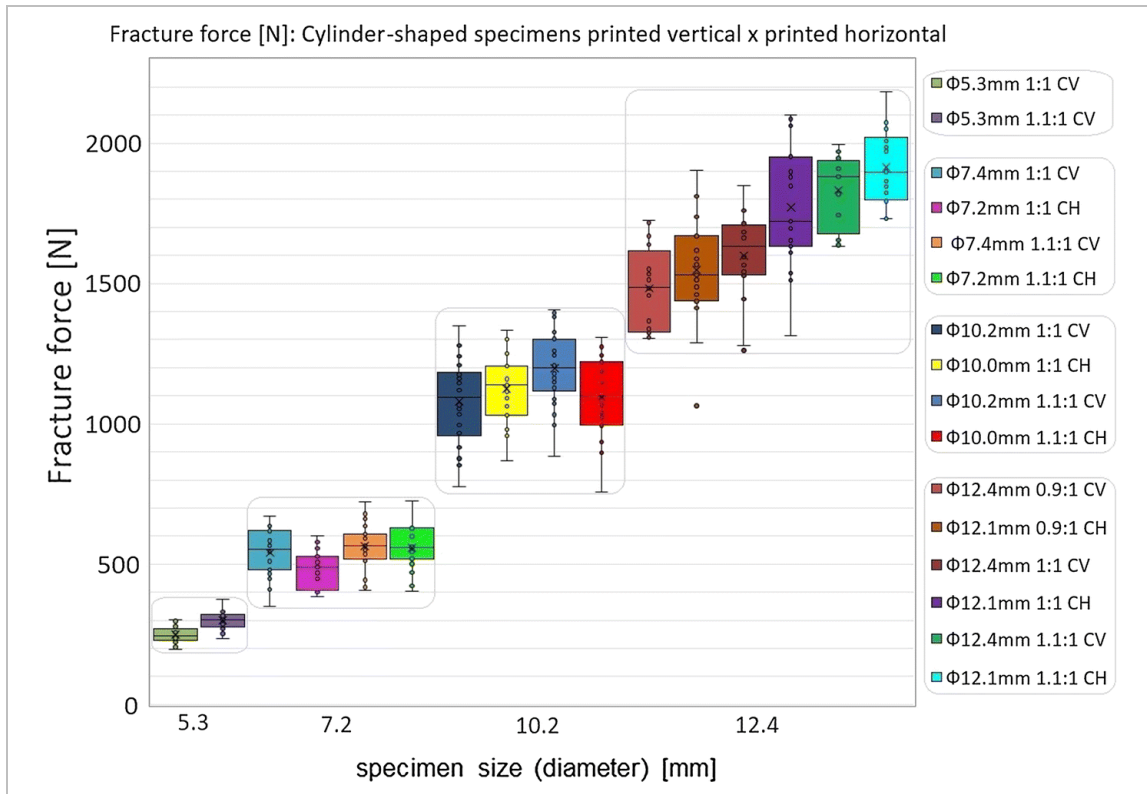


Figure 50 Impact of fabric orientation on the fracture force for cylinder-shaped specimens.

4.9.4 Interpretation of mechanical properties from SILC tests

The mechanical properties of a specimen are uniquely related, given the Young's modulus of the striker and the rod are known (Tavares, 1997). Figure 51 shows the median results of fracture energy for 3DP sandstone with distinct shapes and sizes. The stored fracture energy was demonstrated to be slightly larger for 'group A' subjected to impact load prior to fracture when compared with 'group B' (both printed vertical and horizontal) of similar diameter.

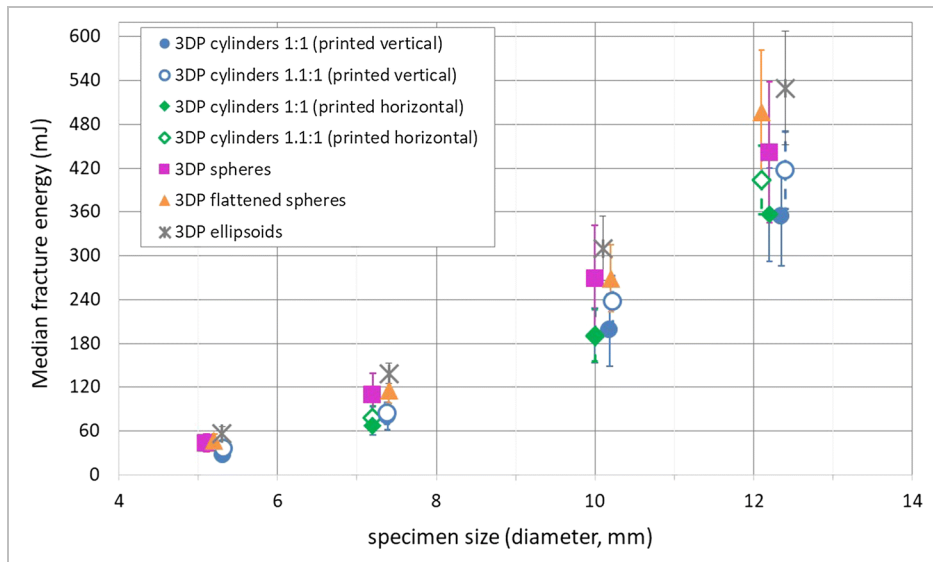


Figure 51 Variation of median fracture energy with specimen size for 3DP sandstone.

Figure 52 shows the median results of corrected specific fracture energy for 3DP sandstone with distinct shapes and sizes. When the specimen mass is taken out of consideration, the minimum energy required to fracture ‘group A’ was about double the energy for ‘group B’ of similar sizes. Note that the fracture energy corresponds to the minimum energy required to fracture a brittle specimen (Baumgardt et al., 1975) and corresponds to the area below the force-deformation curve. The force-time profile (previously illustrated in Figure 46) has similar plotting characteristics to the force-deformation curve. As observed before, the force-time profile for ‘group B’ specimens yielded a reduced area when compared to ‘group A’ specimens. Thus, the size and most importantly the shape of the specimens tested with SILC have a strong influence on the results of corrected specific fracture energy regardless of the impact conditions (ball size and drop height). Overall, differences between shape and size of the tested specimen are very influential for the determination of geomechanical parameters; therefore, they cannot be ignored.

Figure 53 demonstrates the size dependence of an equivalent ‘Young’s modulus’ (stiffness or ‘apparent’ stiffness in previous publications) for SILC test. There is an increase in the Young’s modulus with increasing specimen size. In terms of shape variation for 3DP specimens, the estimated values of ‘Young’s modulus’ for cylinders and ellipsoids are greater than for sphere and flattened sphere-shaped specimens. Moreover, looking at the fabric orientation relative to impact direction, it was observed that the ‘Young’s modulus’ estimated for large cylinder-shaped specimens (10.1 mm and 12.2 mm diameter) printed vertically was smaller than that one printed horizontally. It is consistent with the effect of bedding orientation (Attewell and Sandsford, 1974;

Brown et al., 1977; Al Jassar and Hawkins, 1977, 1979). But better similarity for the equivalent ‘Young’s modulus’ between ‘group A’ and ‘group B’ was expected. Upcoming publication from Lois-Morales et al. (2019) is addressing issues in the calculations proposed for cylinder-shaped specimens.

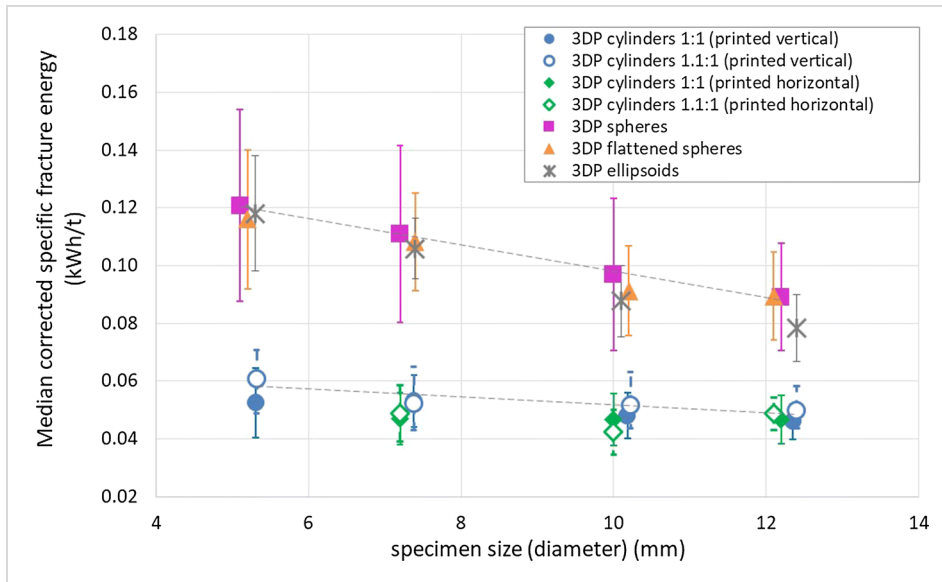


Figure 52 Variation of median corrected specific fracture energy with specimen size for 3DP sandstone.

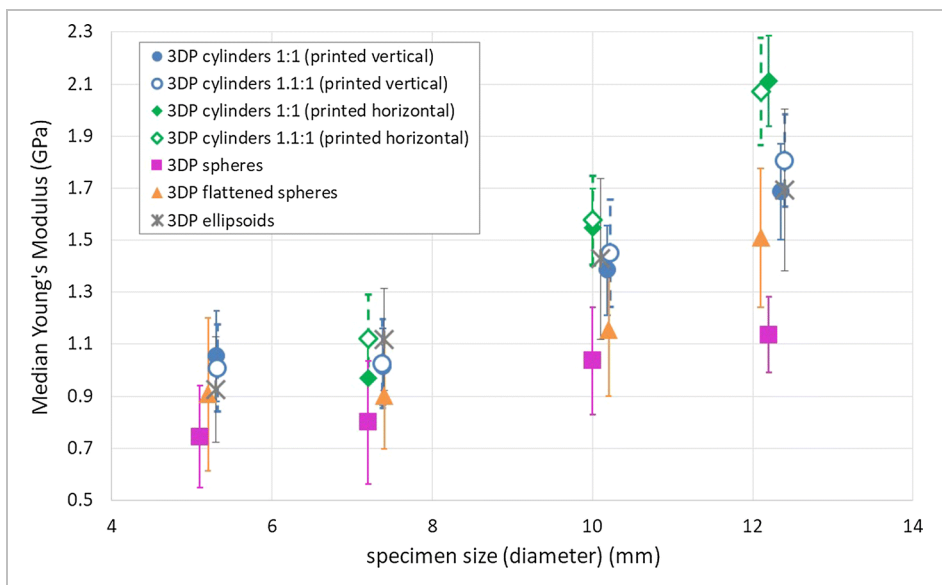


Figure 53 Variation of median ‘Young’s Modulus’ with specimen size for 3DP sandstone.

Figure 54 illustrates the median values of tensile strength distributions for 3DP sandstone with distinct shapes and sizes. Again, size dependent results were demonstrated as the tensile strength increased with increased 3DP specimen. It was observed that the median values for tensile strength between shapes varied up to 26%. It is supposed that ‘group A’ with 5.2 mm diameter might be influenced by a grain size issue causing offset of the results. Recommended diameter for core specimens (prepared for standard triaxial or uniaxial tests) is to be at least six to ten times that of the largest fragment/grain within the rock (ASTM and ISRM). Recorded videos of SILC test showed that sphere and flattened sphere-shaped specimens with 5.2 mm diameter tend to be indented resulting into several small fragments/grains.

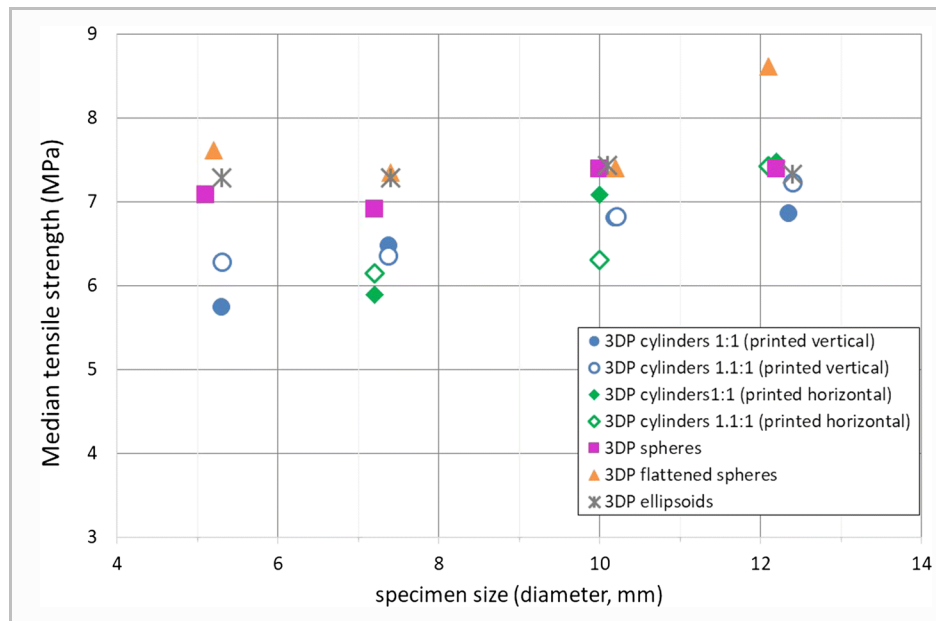


Figure 54 Variation of median tensile strength with specimen size for 3DP sandstone.

It is known that the ratio of UCS to tensile strength typically varies between 8:1 and 15:1 for most of the rock materials (Perras and Diederichs, 2014; Komurlu et al., 2017; Konietzky and Ismael, 2017). Figure 55 shows the experimental results of average UCS estimated from the conventional UCS test and average tensile strength estimated from the SILC tests. The average ratio of UCS to tensile strength ($\bar{\sigma}_c(UCS)/\bar{\sigma}_t(SILC)$) is around 2:1 to 4:1 as the specimen size increases. Therefore, if a typical 61 mm diameter specimen was tested, it is anticipated, by extrapolation of $\bar{\sigma}_c(UCS)/\bar{\sigma}_t(SILC)$, to vary between 9:1 and 11:1 conditional to shape.

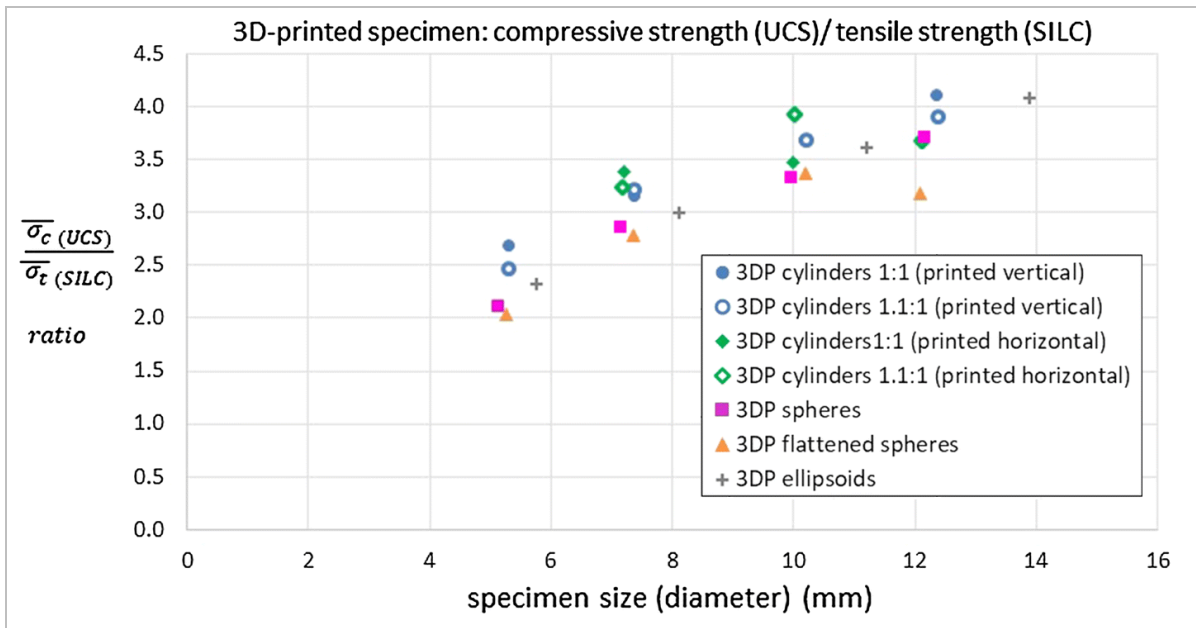


Figure 55 Variation of average uniaxial compressive strength and average tensile strength ratio with specimen size for 3DP sandstone.

4.9.5 Assessment of compressive strength from SILC tests

Direct measurements of UCS values sometime can be difficult due to the limited samples available and costs to core representative specimens. For this reason, preliminary attempt will be sought next to estimate UCS values from SILC data. Uncertainties for this task are related to (i) utilisation of a tensile dominant failure mode test, (ii) the experimental investigation be conducted on distinct shape (cylindrical and non-cylindrical specimens), and (iii) combined with its nonlinearity, the Hertz relation does not account for energy dissipation during the impact process. Nonetheless, for estimation of the compressive strength on SILC test (σ_{cSILC}), the contact areas related to bodies interaction are needed. The median results of the calculated contact area (top and bottom contacts) for each lot following the contacting bodies are presented for ‘group A’ and ‘group B’ in Figure 56. Note that quantification of contact areas for shaped specimens differ mostly for ‘group B’.

Next, using the applied load and the estimated contact areas, the possibility to estimate the UCS value for each shaped specimen is verified. The compressive strength (σ_{cSILC}) of median values for distinct specimen sizes and shape (‘group A’ and ‘group B’) is shown in Figure 57.

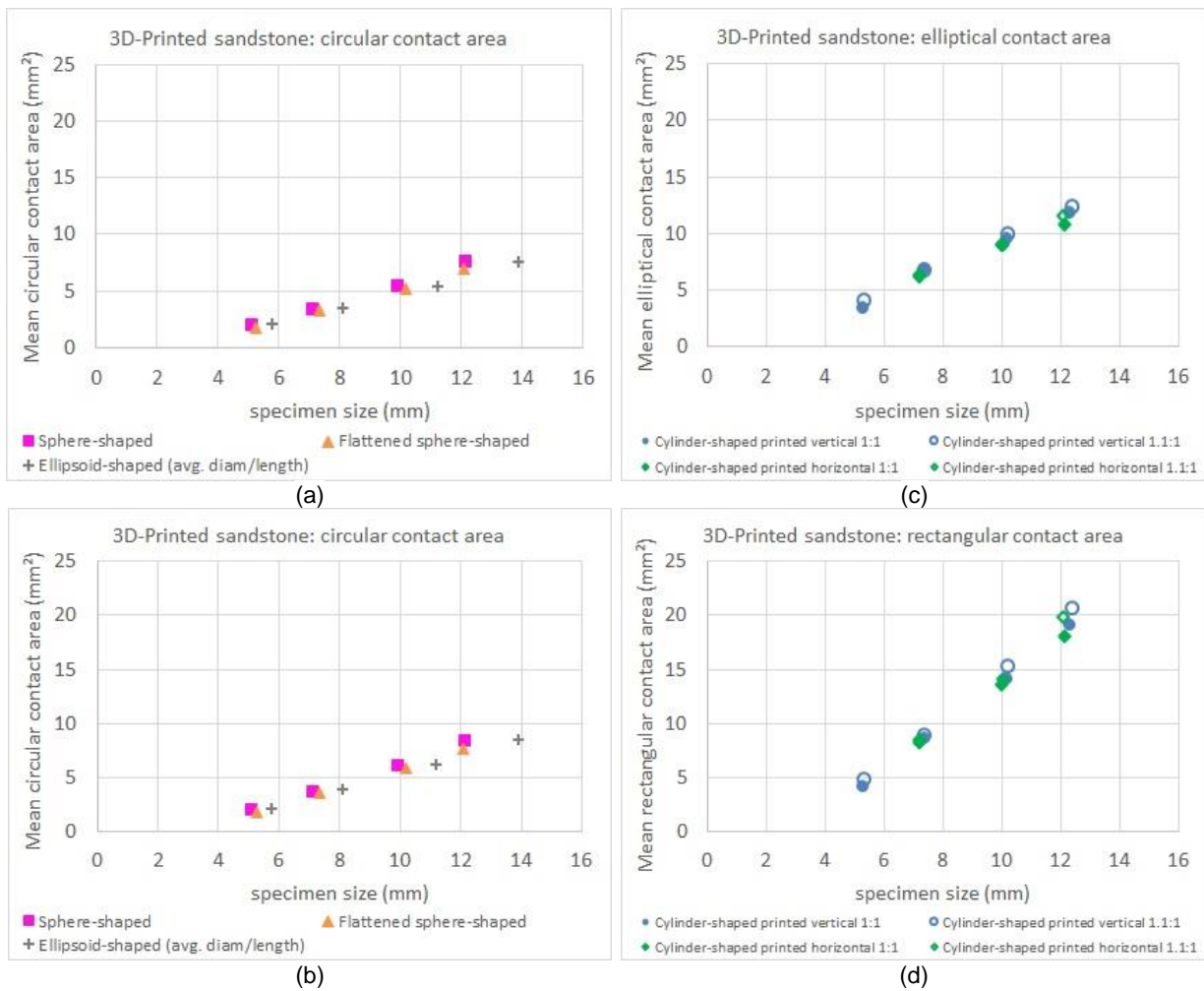


Figure 56 Median results for 3DP of ‘group A’ and ‘group B’ specimens: a) circular contact area for striker versus specimen, b) circular contact area for specimen versus rod, c) elliptical contact area for striker versus specimen, and d) rectangular contact area for specimen versus rod.

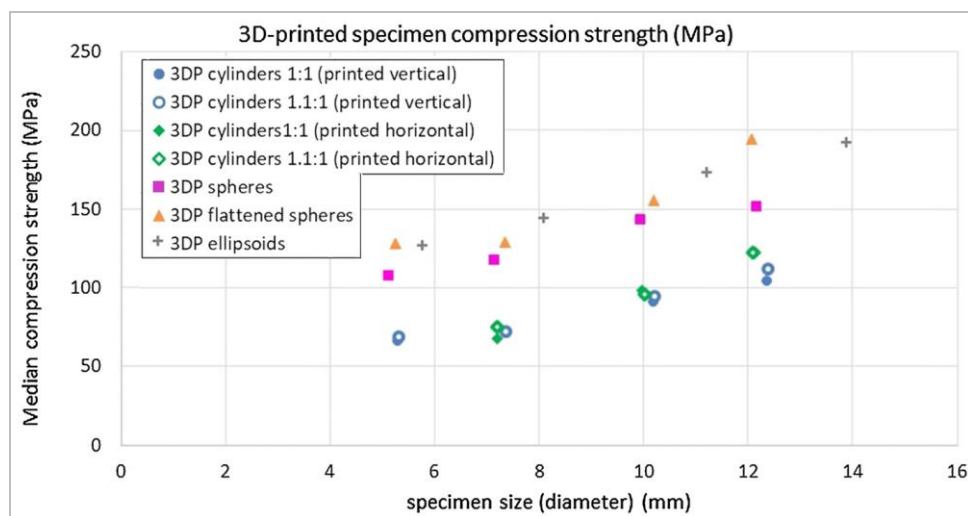


Figure 57 Variation of median compressive strength for ‘group A’ and ‘group B’ of 3DP sandstone.

Because the UCS results shown in Figure 41 confirmed the similarity between 3DP sandstone and real sandstone rock (Hawkins 1998). Also, the average ratio between compressive strength, again from conventional UCS test, and tensile strength from SILC ($\bar{\sigma}_c(UCS)/\bar{\sigma}_t(SILC)$) seemed to be consistent. Confidence of UCS for 3DP sandstone specimens determined directly from UCS tests (σ_{cUCS}) at distinct size (Figure 40) allows for verification of correlation to UCS values from SILC tests (σ_{cSILC}), if any.

It was found that estimation of σ_{cSILC} does not reflect a straight forward prediction of σ_{cUCS} . The simple solution, which can contribute for this approach, is to introduce a correction factor. It is anticipated that the correction factor must vary as function of the specimen shape and type of material tested. Figure 58 shows a proposed correlation factor valid for 3DP specimens, indicating the size has little effect but the shape is quite strong by comparison. The median ratio for cylinder-shaped specimens is 3.9, which is the lowest among the four shapes. Flattened sphere and ellipsoid-shaped specimens have the highest ratio of 6.8, followed by sphere-shaped specimens with ratio of 5.8 (median values).

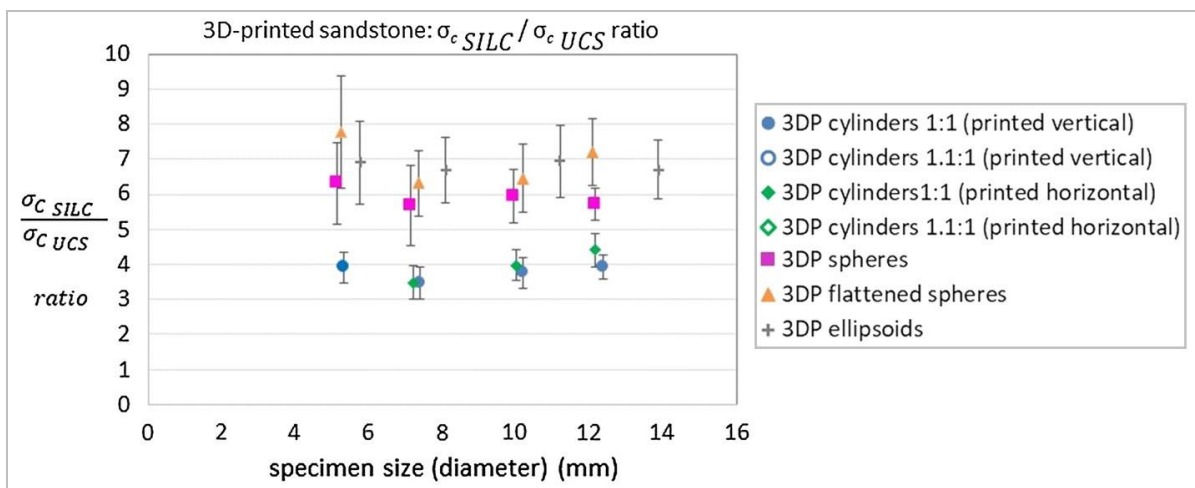


Figure 58 Comparison of the strength ratios between SILC method (σ_{cSILC}) and standard UCS method (σ_{cUCS}) for ‘group A’ and ‘group B’ of 3DP sandstone.

4.10 CONCLUSIONS AND RECOMMENDATIONS

This study details an experimental method using the SILC test to investigate the mechanical and fracture properties of fabricated 3DP sandstone. The tested specimen is a brittle, intact and homogeneous rock-like with defined size, shape, and fabric orientation. Typical force-time profiles

recorded when breaking well-defined shaped specimens have the advantage of evident peak corresponding to the fracture force which is critical for the data generated. This is an important outcome of this study as it not only reviews the mathematical assumptions, which were unchanged, but the basic criteria of measurement which could change the absolute values measured for irregular shaped materials. Furthermore, it gives confidence to the geomechanical properties to be estimated.

During the SILC test, the fracture initiated, in shear at the top loading of the specimens and grows in tension, so the propagated crack within the 3DP moves towards the anvil/rod vertically. There is a strong influence of shape effect on the fragmentation. A global knowledge and understanding of fracture mechanics, shape, size, fabric orientation, and ratio dependence on SILC test using 3DP sandstone is critical to demonstrate the experimental contributions and limitations.

SILC tests conducted under controlled conditions (preferential cylinder-shaped specimens of specific aspect ratio, which can be checked against some conventional experiments) do appear to provide quite reasonable estimates of rock properties. It is emphasized the valuable contribution of SILC test for measuring tensile strength and specific fracture energy (related to fracture toughness) and offering promise as a relatively quick and inexpensive alternative to the Brazilian test. Estimated rock properties can be used for practical applications at the mining and the oil and gas industries, such as prediction of blast fragmentation, fraccing, and numerical modelling simulations.

The variability on the compressive strength results occurred for both SILC and UCS tests on 3DP specimens, while the repeatability still seems to be good when specimens are tested under different conditions. Then, comparison of UCS values shows that σ_{cSILC} regression is much higher than that from conventional σ_{cUCS} measurements on 3DP sandstone. The ratio between the methods is almost constant independent of specimen size, but the ratio shows strong dependence of shape.

It is suggestive that a standard procedure for using the SILC might need to be developed to specify the dimensions of specimens tested as well as the impact conditions to be employed. Then databases for shaped-specimens of varied rocks can be tested and compared.

SILC ON COAL AND MUDSTONE

Karina Barbosa (PhD candidate) conducted specimen preparation and testing, interpreted data, prepared figures and graphics, and wrote the manuscript.

Benjamin Bonfils escorted the experimental work, reviewed, discussed and edited the manuscript.

Joan Esterle (Principal PhD supervisor) proposed the experiment, reviewed, discussed and edited the manuscript.

Zhongwei Chen (Associate PhD supervisor) reviewed, discussed, and edited the manuscript.

Summary

Rock specimens of coal lithotypes and mudstone were selected and prepared based on availability of material, to perform the laboratory SILC tests. SILC was selected as an alternative to other geomechanical tests as it captures fracture energy and toughness, which are important inputs to hydrofracturing simulations. If successful, the small specimens are easy to prepare and there is a potential to use rotary drilled chip specimens. Low energy impact or breakage tests were utilised not only to test smaller specimens, but for investigation of sub-bituminous coal tensile strength, specific fracture energy, and Young's modulus that could also be compared to a previous database across a range of coal ranks and lithotypes. Although cleats are poorly developed in low rank coal, the presence of microfractures, microlithotype fabrics, and mineral matter, played a role in coal deformation response to impact energy. It is anticipated that rather than a well-defined planar fracture feature (as observed on 3D-printed sandstone cylinder-shaped specimens) promoting the specimen separation, SILC tests on coal should be able to capture the micromechanics of brittle fractures on coal. The investigation involved testing a range of shapes and sizes. For cylinder-shaped specimens (i.e. same size and lithotype) small variation for the impact conditions affect the results of Young's modulus. It is suggested that available database for distinct rock material cannot be compared in terms of Young's modulus since the specimens are most likely to be fractured by varied range of drop height and striker mass combinations.

The use of short impact load cell to derive geomechanical properties of sub-bituminous coal and mudstone

*Karina Barbosa^{ab}, Joan Esterle^{ab}, Benjamin Bonfils^d and
Zhongwei Chen^c*

- a. School of Earth and Environmental Sciences, The University of Queensland, St. Lucia 4072, QLD, Australia*
- b. UQ Centre for Coal Seam Gas, The University of Queensland, St. Lucia 4072, QLD, Australia*
- c. School of Mechanical and Mining Engineering, The University of Queensland, St. Lucia 4072, QLD, Australia*
- d. Julius Kruttschnitt Minerals Research Centre, The University of Queensland, Indooroopilly 4068, QLD, Australia*

Abstract

This study estimates the geomechanical properties of coal of varied ply lithotypes and mudstone by using the experimental Short Impact Load Cell (SILC) test. SILC is an alternative laboratory test for measuring tensile strength, Young's modulus, and specific fracture energy (fracture toughness). Available coal data is rare for low rank sub-bituminous coals that are the target for coal seam gas stimulation and extraction in the Surat Basin, Australia. Tested specimens include mini-core (11.7 mm in diameter) and irregular particles (3.35 - 9.5 mm in diameter). The results demonstrate geomechanical properties can be derived and used in the reservoir numerical modelling investigation.

Keywords: impact breakage; lithotypes; tensile strength; specific fracture energy

5.1 INTRODUCTION

In coal seam gas (CSG) reservoirs, gas is mainly contained under pressure in isolated submicroscopic pores and released by reservoir pressure depletion (i.e. unloading or dewatering of the coal seam). Following desorption and diffusion, this causes an oriented system of natural fractures to form an interconnected system of flow paths allowing for gas extraction. It is anticipated that coal undergoes tensile failure to promote the flow of desorbed gas through an interconnected system of natural fractures, whereas the stability of a borehole is controlled by shear and compression. It is important to know coal strength (i.e. both tensile and compression) and fracture toughness to predict coal reservoir behaviour, especially if fractures are stimulated. Incorrect estimation of coal strength could lead to formation damage from drilling fluid invasion or complete wellbore collapse (Deisman et al., 2008).

The coal strength is conditioned by a combination of lithotypes and microlithotypes with variable natural fractures, cleat spacing, and bedding thickness as per rank class. Strength and fracture toughness increase with decreasing coal rank (thermal maturity) and banding. The influence of coal strength by rank (thermal maturity) is shown in Figure 59 (Palmer et al, 2005 cited in Deisman, 2016). This can be observed on the boundary from low to medium volatile bituminous up until the high volatile bituminous (Stach et al., 1982; Medhurst and Brown, 1998; Palmer et al., 2005; Esterle, 2008; Deisman, 2016), which is evident in tests such as Hardgrove grindability index and hardness (Ting, 1977; Stach et al., 1982; Hower et al., 1987; Hower and Wild, 1988; Narayanan et al., 1988; Van Krevelen, 1993; Conroy, 1994; Barton et al., 1994; Klawitter et al., 2015). Furthermore, strength also varies with confining stress or depth (Bieniawski, 1968b; Wagner, 1974; Bieniawski and Van Heerden, 1975; Trueman and Medhurst, 1994; Medhurst, 1996; Medhurst and Brown, 1998; Scholtès et al., 2011; Poulsen and Adhikary, 2013). The specific fracture energy is an important aspect of describing the fracture energy consumption rate required to create new surfaces in the comminution process. Donovan (2003) showed that there is a strong relationship between fracture toughness and specific fracture energy.

Because coal banding is complex, the number of specimens required at laboratory tests to estimate the range in values across the lithotypes may be prohibitive. Also, it could be argued that coal core specimens are not intact (see Gonzalez-Garcia, 2012 definition for intact). The interbedded and banded nature of coal plies make upscaling from laboratory tests to the coal mass a more challenging task. Other aspects influencing the strength values for laboratory test, include rock or

coal type, specimen shape, aspect ratio (length-to-diameter), orientation of the test loading to the specimen fabric or structure, and moisture content (Al Jassar and Hawkins, 1977, 1979; Norbury, 1986; Forster, 1983). The general prediction of the geomechanical behaviour of coal seams and rock strata is a function of the intact rock strength and the fracture density. This discounts the strength when being upscaled (i.e. downgrading properties values) to the rock mass. Thus, strength values increase as specimen size decrease (Hoek and Brown, 1980). Moreover, it is difficult to conduct direct tensile strength experiments, and the Brazilian test (an indirect testing method) is utilised. However, most strength studies have been conducted on bituminous coals, at least in Australia. There have been a small number conducted on sub-bituminous coals in which cleats are poorly developed, but larger scale joints are prevalent.

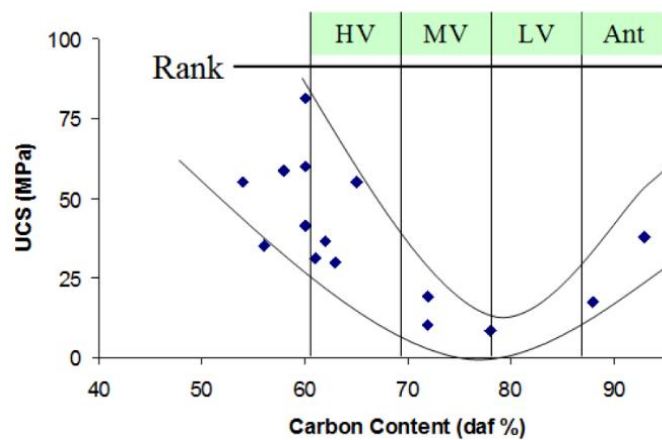


Figure 59 Variation in coal strength relative to rank as estimated by carbon content.

From Palmer et al, 2005 cited in Deisman, 2016.

Looking for alternative laboratory experiments, the Short Impact Load Cell (SILC) test provides a measurement of force and energy (King and Bourgeois, 1993; Tavares and King, 1998, 2004; Bourgeois and Banini, 2002; and Bonfils, 2017). Along with other impact breakage techniques, it is commonly used in mineral processing. SILC can be used to analyse a range of specimen sizes and shapes (mini-cylinders and particles/chip specimens from rotary drilling recovery) and may be advantageous when standard to large intact core specimens are difficult to obtain and measure.

Although distinct applied strain rates (static, quasi-static, and dynamic) can be associated with different types of loading and equipment. The effect of applied strain rate appears to be insignificant for brittle material (Antonyuk et al., 2005; Schönert, 1988; Tavares, 2007; Yashima et al., 1979). While the effect of applied strain rate appears to be significant when the material under investigation exhibits inelastic behaviour (e.g. marble, limestone). Saeidi et al. (2017) compared the rate of breakage between slow compression and SILC (impact mechanism) for brittle material.

According to Saeidi et al. (2017) the primary breakage characteristics can be employed to represent the material properties. The primary breakage characteristics are nearly identical for both compression and impact mechanisms, as they are function of the material properties rather than the stressing conditions (Saeidi et al., 2017). Therefore, the information derived from breakage testing using SILC devices have the potential to estimate other mechanical properties (Bonfils, 2017; Saeidi et al., 2017) such as coal strength and, in particular, fracture strength, fracture energy, specific fracture energy, and Young's modulus.

While the SILC test is meant to be used for brittle material, the Basin of interest comprises extremely heterogeneous rock contrast between coal and mudstone (brittleness/ductility) varying from meter to centimetre scale. Mudstones and shales are both made of clay and silt, and the strength properties of the rocks are dependent on the water content, perhaps making it more or less ductile. Therefore, whether the SILC test could be used to characterise geomechanical properties of mudstone is questionable, but an observation of any contrast coal/mudstone could be useful.

In this study, the sampling approach tested impact breakage signatures for different lithotypes and mudstone partings in sub-bituminous coal from the Surat-Clarence-Moreton Basin in Australia. As target seams for CSG become deeper, hydraulic stimulation may be required. The primary aim of the laboratory testing is to demonstrate the feasibility and applicability of the SILC test (Bourgeois and Banini, 2002) on particles and cylinder-shaped of mudstone and sub-bituminous coal. Moreover, the cylinder-shaped specimens (Bonfils, 2017) are a relatively inexpensive, reliable and practical shape to gather requisite geomechanical properties to provide more accurate input data for the numerical modelling investigation of CSG reservoirs.

5.2 SHORT IMPACT LOAD CELL TEST SETTINGS AND OUTPUT

The impact load cell device is based on a hybrid concept between Hopkinson (1914) bar and drop weight tester. A smaller version known as the Short Impact Load Cell (SILC) was designed by Bourgeois and Banini (2002). It is located at The University of Queensland Julius Kruttschnitt Mineral Research Centre (UQ JKMRC), Australia, where all tests for this work were performed. Main components of this instrumented machine include the rod/anvil (cold-rolled stainless steel), stainless steel balls (strikers), load cell, strain gauges, pneumatic clamps, voltage amplifier, and data acquisition system (previously presented in Figure 32). The Young's modulus for both the stainless-steel strikers and rod utilised, which is required for the calculations, is 230 GPa. Before the SILC

tests start, the rod was calibrated. Measurements of the bridge factor (i.e. the change in resistance, that in turn results in a voltage change in the Wheatstone bridge, is outputted as an amplified voltage) (Bourgeois and Banini, 2002) were recorded during calibration to be imputed in the calculation. The striker drop height is utilised to obtain the impact velocity of a body at free-fall conditions (Tavares, 1997). When utilizing the SILC, the impact conditions (striker's diameter, weight, and drop height) should be enough to promote the breakage of the material without over breaking the specimen or failing to fracture it. The details about the impact load cell device and calculations methodology can be referred to King and Bourgeois (1993), Tavares and King (1998, 2004), Bourgeois and Banini (2002), and Bonfils (2017).

5.3 SAMPLING

5.3.1 Sample collection

The coal samples were collected from freshly-exposed blocks in a mine from the Surat-Clarence-Moreton Basin in Australia. Reported rank of the coal at the sample location is sub-bituminous (maximum vitrinite reflectance, $R_{vmax} = 0.50\%$) and have a high overall vitrinite content (i.e. >60% vitrinite content). In this Basin coal seams are jointed; they show multiple thin beds (about 0.4 m average thickness), contain abundant thin partings, and are interbedded with variable soft strata such as bands of carbonaceous mudstone, tuffaceous claystone or siltstone (Figure 8). The samples originated from small to large blocks ($5 \times 5 \times 5$ to $30 \times 30 \times 30$ cm) of different end-member (bright to dull) coal lithotypes were representative of four plies within a seam. The four coal plies were named (i) C8 ply banded (PC8-B), (ii) C8 ply banded with white marks comprising clay lenses (PC8-WB), (iii) C6 ply dull (PC6-D), and (iv) D8 ply banded low ash (PD8-BLA). Mudstone blocks were also collected in the same location, but the intercalated tuffaceous claystones were too thin for collection. All block samples collected were wrapped in plastic, sealed in boxes and transported to UQ JKMRC for preparation and testing.

5.3.2 Specimen preparation

In this study, the specimen preparation for SILC takes into consideration mini-core specimens and irregular single-particles described as follows:

a) Mini-core specimens

For a regular cylinder-shape or mini-core specimens (Bonfils, 2017), large hand-picked blocks were selected and cut into brick size blocks (about $12 \times 7 \times 5$ cm) (Figure 60a). Then, mini-core specimens were drilled using diamond drill bits (Figure 60b). Both the top and base of the mini-core specimens were also prepared to obtain the parallelism of faces (i.e. parallel specimens' ends). The final diameter of the mini-core specimens is about 11.7 mm with lengths varying between 10 and 14.5 mm. The length-to-diameter ratio or aspect ratio is 0.8:1 to 1.2:1 (note that suggested ratio for SILC test is 1:1). Mini-core specimens with visual cracks or flaws were excluded from testing. Preparation of mini-core specimens also takes into consideration the orientation of banding relative to impact loading energy, therefore specimens were drilled perpendicular and parallel to bands (Figure 60c). Because specimen preparation involves water during the drilling operation, drilling on mudstone was not attempted and the mechanical interaction of coal with water cannot be quantified.

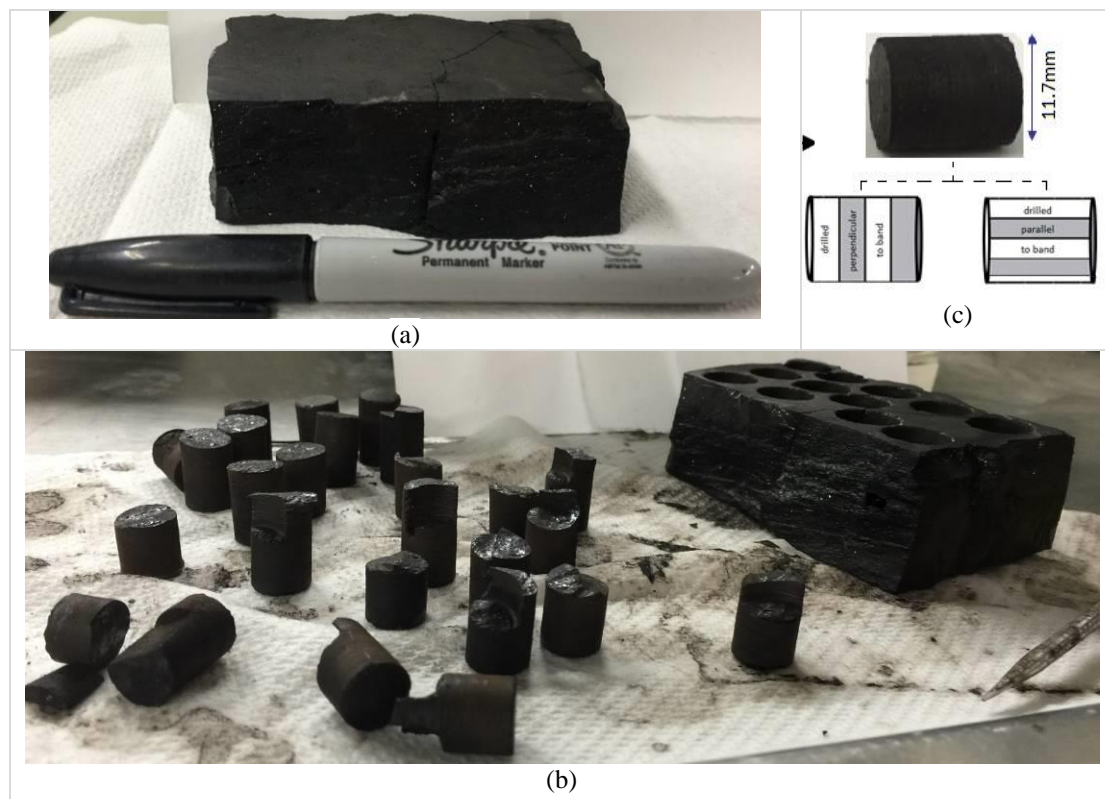


Figure 60 Illustration of samples shape preparation into mini-core specimens of coal tested on SILC.

b) Irregular-particle specimens

For irregular single-particles, specimens with a shape that best approximates a spherical geometry were selected. For that, small to large blocks from the same rock type (or ply if coal) were reduced into smaller irregular-particles using the DWT (JK Drop Weight Test) and then sieved using round-mesh precision. Classified irregular-particles were packed by size, type/ply, and initial size and drop

energy used into the DWT. Figure 61 shows the DWT equipment utilized and the fragmentation characteristics of tested irregular-particles. For instance, $63 \times 53_E = 0.25$, indicate the origin size ($63 \times 53\text{mm}$) prior to DWT reduction/fragmentation, and the drop energy (0.25 kWh/t). It is supposed that the irregular-particles should respond differently based on their size and energy applied on the DWT, which influence the presence of more or less flaws (cracks). Thus, the results would provide some indication of cumulative damage. The DWT was performed on two distinct coal plies, PC6-D and PD8-BLA, and the mudstone specimens. The selected size fractions of irregular-particles tested on SILC were 3.35, 4.75, 6.7, and 9.5 mm (mesh size based on dimensions of mesh size opening, following the ASTM E11 standard) (Figure 61).



Figure 61 Illustration of the DWT used for fragmentation of distinct size distribution and varied energy in preparation for the irregular-particle specimens of coal tested on SILC.

Same procedure was applied to coal and mudstone. It is relevant to highlight that there is no current technique to determine the comminution characteristics of mudstone (e.g. crushing, grinding). This is essentially due to the ductile characteristic of this material, as observed during the attempt to fragment mudstone using the DWT. Commonly, mudstone bends or flows in response to energy applied (Figure 62).



Figure 62 Evidence of ductile deformation for mudstone during fragmentation. a) before DWT test, b) after DWT test.

Therefore, only fragments sustained some ‘round’ shape (i.e. non-squashed/non-flat) after fragmentation and sieving were selected as irregular-particles for the SILC test (Figure 63 show an example for the 9.5 mm mesh size).



Figure 63 Illustration of irregular single-particles of mudstone tested on SILC.

A total of 142 drilled mini-core specimens of coal belonging to PC6-D, PC8-B, and PC8-WB were tested on SILC. Additionally, 1250 irregular-particles of coal belonging to PC6-D and PD8-BLA,

and 580 irregular-particles of mudstone were also tested on SILC. A summary of the size, shape, breakage direction and lithology tested during this study is shown in Table 9. Despite careful preparation and selection of mini-core and irregular-particle specimens, some of the results showed invalid force-time profiles, which were excluded in the statistical analysis and Table 9. Notice that, SILC can demonstrate the influence of a specimen's size and shape, allowing for a direct quantitative measure of properties for the material being tested. Overall, SILC is relatively simple and easy to conduct, but it can be time consuming due specimen preparation and data processing.

Table 9 Number of specimens used to conduct SILC tests following the rock material and specimen features.

		Shape	Mini-core specimens		Irregular-particle specimens			
			Breakage direction	Perpendicular to band	Parallel to band	Indistinct/ unknown		
		height or diameter (mm)	11.7	11.7	3.35	4.75	6.70	9.50
Rock material	South pit	Coal PD8-BLA (Low ash banded)	-	-	118	152	195	200
	North pit	Coal PC6-D (Dull)	14	-	146	231	-	208
		Coal PC8-B (Banded)	91	13	-	-	-	-
		Coal PC8-WB (Banded with white marks /clay lenses)	-	24	-	-	-	-
	West pit	Mudstone	-	-	30	79	227	244

5.4 SILC FAILURE MODE

The description reported for failure are based on observations during test and/or similarities with other material recorded with a camera. Unfortunately, an ultra-high-speed video camera was not available during this study of coal and mudstone with SILC. Also, it is cogitated that the description of failure, together with a representation of the force-time profile and the characteristic of fragments can assist in analysis of the results.

5.4.1 Coal

Ideally, SILC testing should be performed on brittle materials which deform elastically until failure. During breakage of brittle material, such as coal, it is anticipated that the crack initiation and propagation occurs as follows: a) the crack generated by the striker starts at the top loading point (upon contact between striker and specimen); b) then the crack rapidly grows and tends to propagate along a vertical plane towards the centre of the specimen; c) until it encounters natural

fractures (cleats, discontinuities) or a contrast between weaker and stronger materials including mineral grains, perhaps change on microlithotype/band which might change the fracture path; and d) then the specimen splits into various fragments. There is a mechanism of shear along the plane formed by jointing the loadings (striker and rod) followed by tensile failure.

Figure 64 shows the force-time profile of two specimen drilled perpendicular to band with a 1:1 ratio where the first fracture was identified. The tortuosity observed on the fracture surface of fragments from mini-core specimens photographed before and after test (Figure 64) indicates microscopic deviation of the crack from its intended/initial path, and coal fragments may be ejected far from the testing machine. At least four large fragments or multiple smaller ones were observed for sub-bituminous coal. The photos highlight the natural variability of coal demonstrated by the amount and the size of fragments generated as well as the value of the fracture force itself.

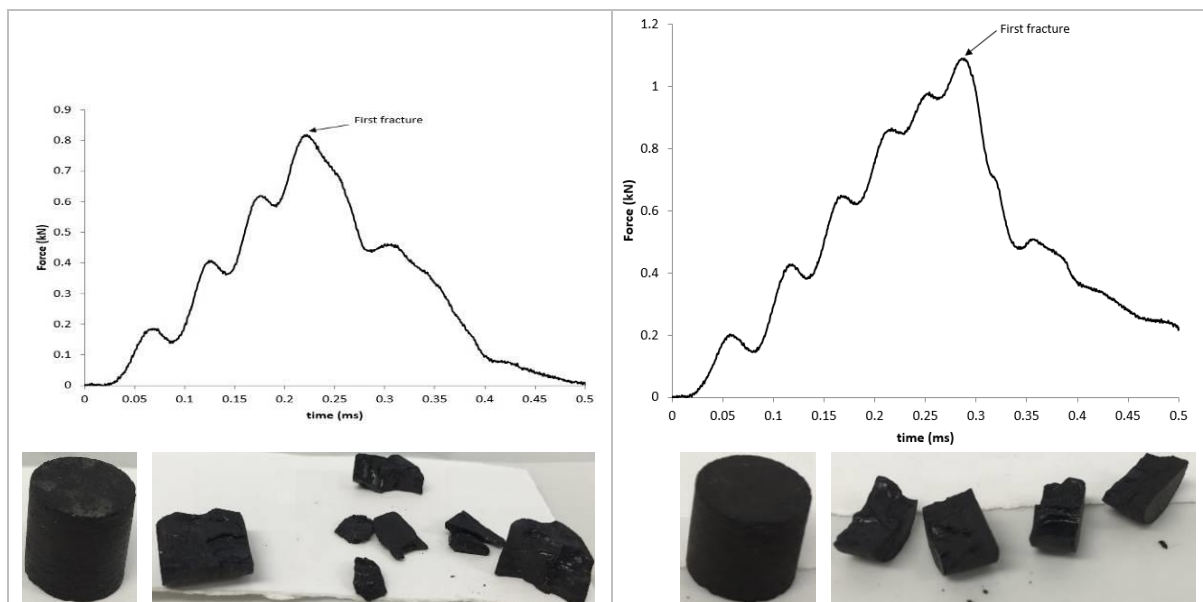


Figure 64 The force-time profile for mini-core specimens drilled perpendicular to band and their conditions before (cylinder-shape) and after (fragments) the SILC test.

The crack initiation and propagation on irregular single-particles of sub-bituminous coal should occur as described for mini-core specimens, but it can be expected that the irregular surface of the particle might cause further deviation of the crack propagation path. The irregular-particles of sub-bituminous coal tested showed a more abrupt and powerful energy release, including few re-breakages, and splitting into more fragments compared with mini-core specimens. Where fragments may be ejected far from the testing machine. According to Tavares (2007), the irregular-particle fracture process does not terminate after first failure at a flaw because kinetic energy may still be available either from the tools that apply the stresses or from the flying fragments of the particles. This remaining energy must be dissipated during the second stage of the process, which results in

secondary fracture of the initial progeny and possibly several further stages of sequential fracture as well (Tavares, 2007). Figure 65 shows two examples of the force-time profile where the first fracture was pointed for irregular-particles of sub-bituminous coal, and supplementary peaks are attributed to secondary fracture.

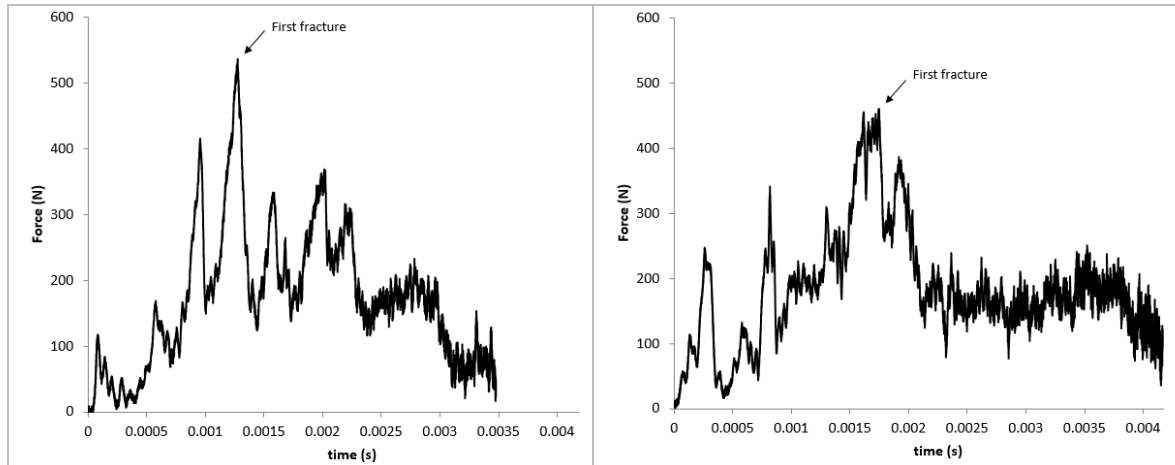


Figure 65 Impact signal showing the force-time profile for irregular-particles of sub-bituminous coal with 9.5 mm in height on SILC test.

5.4.2 Mudstone

Due to the fine-grained characteristics of the mudstone tested (comprising of clays or muds), it is assumed that the crack initiation and propagation on irregular single-particles also started at the top loading point, and the crack propagated within the particle towards the anvil/rod vertically growing in tension. The particles of mudstone allowed for some ductile deformation to occur during the breakage process. For ductile material, energy associated with plastic deformation needs to be taken into consideration. The ductile behaviour of mudstone did not seem to invalidate the results for the particles tested on SILC. Perhaps, the fine layers of clay present in the particle surface are permanently deformed to assume a flattened format, where fragments tend either to break gently into pieces or to stick together rather than ejected. It could be assumed that the kinetic energy from the striker (applied stress) is completely absorbed by single-particles of mudstone.

Figure 66 shows two examples of the force-time profile where the first fracture was selected for irregular single-particles of mudstone. It is interesting that the force-time profiles shows a clear peak (Figure 66). Few secondary fractures occur associated with cracks or fissures on mudstone. Despite having some ductile behaviour, the SILC test gave consistent results for the mudstone.

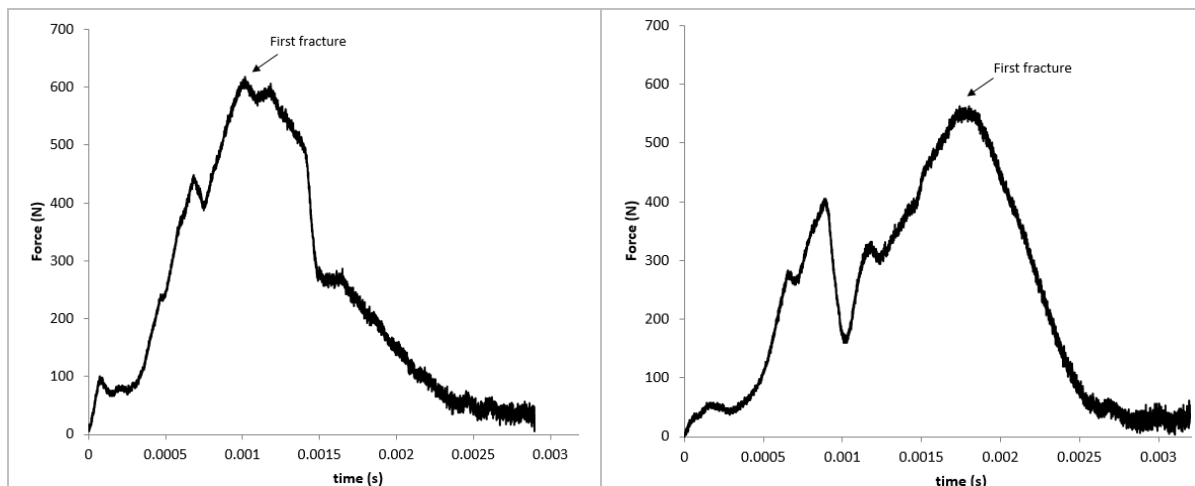


Figure 66 Impact signal of two irregular-particles of mudstone with 9.5 mm in height showing the force-time profile from SILC test.

5.5 DATA PROCESSING METHODS

Fundamentally, SILC measures fracture force and gives information about actual fracture energy consumed by each specimen during breakage and estimates the deformation of fracture. The fracture force (force required to generate the first fracture) of each specimen being impacted is estimated from the force-time profile of the fracture event by a direct reading of the peak force on the graphic. Comparison of the force-time profile of an impact directly on the anvil is predicted under Hertzian impact (Goldsmith, 1960). Whilst the hypothesis for the contact geometry between the bodies (striker-specimen as well as specimen-rod) is applied, it is conditional to the specimen shape. Valid contact geometry resulting for mini-core specimens is an elliptical and rectangular contact area; while irregular-particles specimens result in circular contact areas (Tavares, 2007; Bonfils, 2017). Also, the extent of the deformation depends on the mechanical properties of the bodies in contact. Therefore, the calculation methodology and interpretation of results must take those into account.

Data processing consists of the analyses of the signal results from SILC test, in addition to recorded information from impact energy (mass, diameter, and drop height of the striker) together with the specimen geometrical mean size (i.e. mass, diameter, and length of the specimen). Figure 67 illustrates a typical valid force-time profile with an estimation of first fracture for sub-bituminous coal: mini-core specimen (Figure 67a) and irregular-particle specimen (Figure 67b). Note that controlled shapes (e.g. mini-core specimen) tend to generate more uniform curves which improve the confidence of identification of the first fracture. It occurred that, irregular-particle specimen

with 9.5 mm in diameter (or height) required the impact conditions to be superior than that needed to fracture mini-core specimen with 11.7 mm in diameter. Furthermore, the time to fracture a mini-core specimen tend to be shorter than for an irregular-particle specimen.

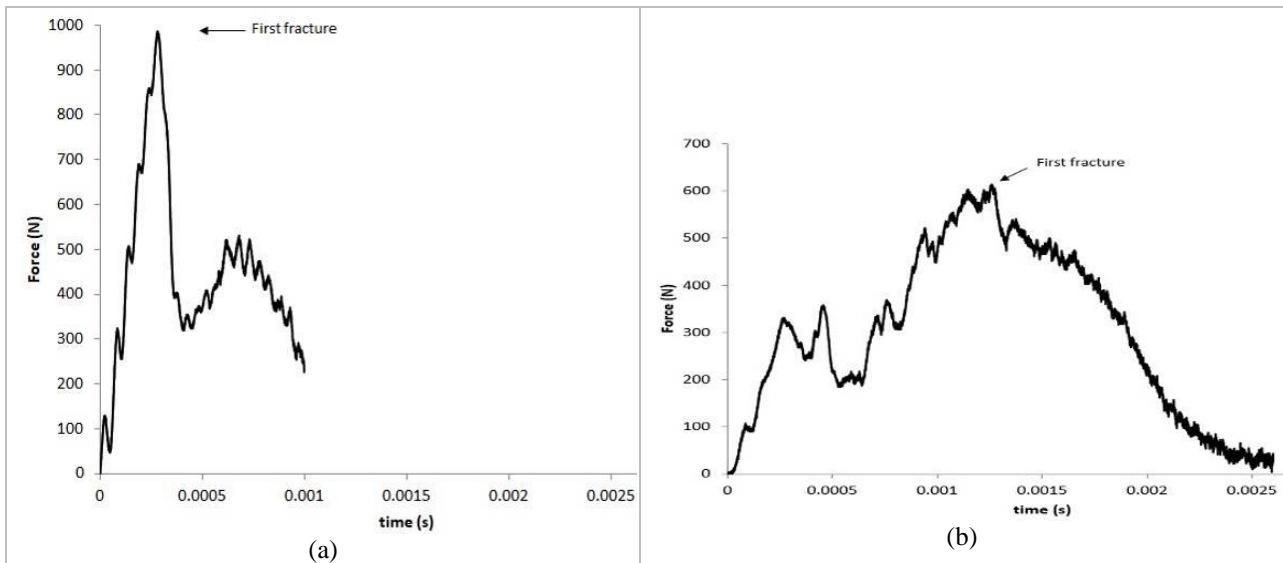


Figure 67 Example of impact signal showing the force-time profile where the first fracture was selected for sub-bituminous coal: (a) mini-core specimen with 11.7 mm in diameter, (b) irregular-particle with 9.5 mm in diameter.

SILC results are strongly dependent on shape, size, ratio, fabric orientation relative to loading direction, and impact energy. Table 10 shows a list of parameters estimated for specimens tested on SILC (see King and Bourgeois, 1993; Tavares and King, 1998, 2004; Bourgeois and Banini, 2002; and Bonfils, 2017 for detailed calculations). The table shows the mini-core specimen and the irregular-particle of coal plotted for the force-time profiles in Figure 67. This study is focused to present results for specific fracture energy (an indication of toughness), tensile strength, and Young's modulus ('apparent' stiffness as per SILC literature).

The statistical analyses adopted in this study are the same described in Chapter 4 (section 4.6). Once each specimen of a selected series of experiments is evaluated separately, then it is included in the statistical analysis. Subsequently, the data can be effectively described using the log-normal distribution (Baumgardt et al., 1975; Dan and Schubert, 1990; King and Bourgeois, 1993; Bonfils, 2017). The method based on order statistics and the cumulative probability distribution for the measured variable is described in section 4.9.3. Note that, very steeper curves for cumulative probability demonstrate a tendency of less heterogeneous specimens and/or better shape control of the specimens.

Lastly, two lots might be compared and interpreted on a statistical basis to decide whether the independent distributions are equal or not following Milin and King (1994). Milin and King (1994) statistics are based on three tests: the ‘median’ test; the ‘number of runs’ test and the ‘Mann-Whitney-Wilcoxon’ test. The T-test for the difference of means gives the value of T from the data, and the critical value of T for 95% of confidence to draw a decision about equality of the means for two distributions measured with SILC.

Table 10 List of parameters obtained using SILC, the example illustrates experiments on sub-bituminous coal.

Terminology	symbol	unit	a) mini-core specimen	b) single-particle
Fracture force (first fracture)	F_c	N	985.8	613.9
Fracture energy	E'	mJ	84.30	381.96
Specific fracture energy	E_m	kWh/t	0.0121	0.0861
Tensile strength	σ_t	MPa	3.8	6.6
Local deformation coefficient	K_e	GPa	3.92	0.31
Total energy	E	mJ	160.78	458.05
% energy used	-	%	90.62	95.99
Energy absorbed by rod up to fracture	-	mJ	6.705	13.065
Total energy absorbed by rod	-	mJ	18.66	24.54
Young's modulus	K_p	GPa	3.99	0.32
Corrected specific fracture energy	E''	kWh/t	0.0120	0.0859

a) mini-core specimen (11.7 mm diameter), and b) single-particle (9.5 mm height).

5.6 SILC RESULTS ON MINI-CORE SPECIMENS OF COAL

Next in this study, each series of test results on mini-core specimens was organised and analysed based on the influence of the drop mass/height combinations; the aspect ratio of specimens; the lithotype; and the orientation of banding relative to impact loading energy affecting the mechanical properties of interest. In the graphics, the legend displays the lithotype, followed by the specimen orientation, and aspect ratio (e.g. PC8-B perp 0.9:1). Symbols denote individual mini-core specimens tested i.e., data points and solid lines denote the fitted experimental log-normal distribution.

5.6.1 Influence of drop mass and height combinations on mini-core specimens of coal

The selected impact conditions should be enough to promote the breakage of the material without over breaking or failing to fracture it. The influence of drop mass and height combinations was observed for 49 mini-core specimens of PC8-B (banded), drilled perpendicular to the band, aspect ratio 1:1 (average), and tested on SILC. The mini-core specimens were sourced from two single blocks, which provided multiple specimens of very similar characteristics. Results are plotted to compare 22 data points from block 1, where specimens were fractured by a 535.25 g striker released from 45.5 mm height, against 27 data points from block 2 using the same striker but released from 63.1 mm height.

Figure 68 shows the cumulative distributions of Young's modulus for mini-core specimens fractured with distinct impact velocities. Because PC8-B is a similar material with equivalent characteristics, it is observed that the Young's modulus is influenced by the impact conditions on SILC. Figure 68 shows that an increase in the drop height of the striker (represented by circle symbols on the left) shows less resistance to the deformation (i.e. amount of compression hold by the specimen at fracture). By looking at the fitted median values (i.e. corresponding Young's modulus value for P_{50}), the difference between the Young's modulus values is about 37%, which appears to be significant. The statistical basis showed the distributions as being distinctly different. The fitted median values are 2.38 GPa if the striker is dropped from 63.1 mm in height, and 4.0 GPa if the striker is dropped from 45.5 mm in height. It highlights concerns on the calculation of Young's modulus for mini-core specimens tested on SILC.

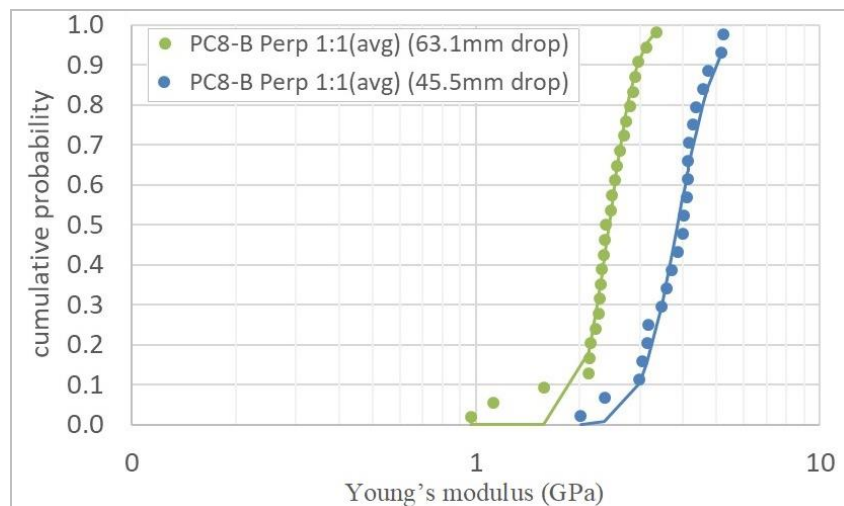


Figure 68 Cumulative distributions of Young's modulus for PC8-B mini-core specimens drilled perpendicular to band and compared for impact velocity variation on SILC test.

Besides, comparison was made with laboratory tests using UCS on the same onshore eastern Australian basin, where the Young's modulus of coal (unknown lithotype) range from 2.0 to 3.2 GPa for varies of depths (2.7 GPa in average) (Parotidis et al., 2016). It is reasonable to suggest that mini-core specimens of PC8-B coal with 11.7 mm in diameter provides a better estimation of Young's moduli on average, when a striker with 535.25 g is released from 63.1 mm rather than 45.5 mm in height. Therefore, all the following analysis for mini-core specimens presented in this study refer to a drop height of 63.1 mm. The calculations for Young's modulus (or 'apparent stiffness) requires further investigation (Lois-Morales et al., 2019) to provide measurements that are comparable to standard triaxial or uniaxial tests.

However, other parameters such as the fracture force, the fracture energy, the tensile strength, and the corrected specific fracture energy were not affected by an increase or decrease in the drop height of the striker when performing the SILC test. Figure 69 shows the cumulative distributions of tensile strength for mini-core specimens fractured with distinct impact velocities. Using the statistical basis from Milin and King (1994), the test did not reject the null hypotheses, given the distributions are identical. Also, the test did not reject the hypothesis that the means are equal. The tensile strength is about 4.2 MPa for sub-bituminous coal PC8-B with 11.7 mm in diameter.

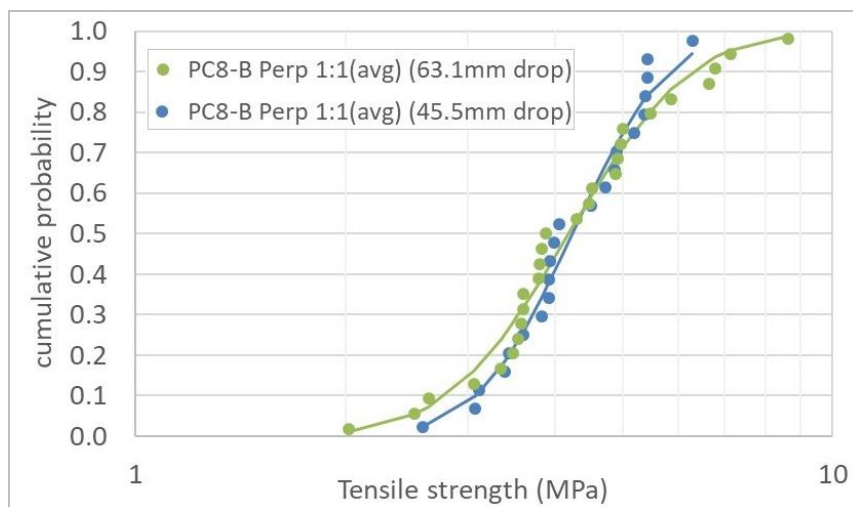


Figure 69 Cumulative distributions of tensile strength for PC8-B mini-core specimens drilled perpendicular to band and compared for impact velocity variation on SILC test.

5.6.2 Aspect ratio effect on mini-core specimens of coal

The mini-core specimens tested on SILC are 11.7 mm in diameter and their length-to-diameter ratio varies between 0.8 and 1.2, as observed for 135 mini-core specimens of PC8-B (banded). Each was drilled perpendicular to the band before being tested on the SILC. The mini-core specimens were

grouped based on the aspect ratio of PC8-B. Therefore, results are plotted for 17 data points of 0.8:1; 24 data points of 0.9:1; 38 data points of 1:1; 29 data points of 1.1:1; and 27 data points of 1.2:1, reflecting similar bedding orientation. The mini-core specimens were then observed independent of the drop mass and height combination utilised. It was anticipated that the influence of drop mass and height combinations would present a minor impact, as the majority of the mini-core specimens (83% of the population) was fractured under similar impact conditions.

Figure 70 shows cumulative distributions of corrected specific fracture energy for mini-core specimens with aspect ratios varying from 0.8:1 to 1.2:1. Note that, the fracture energy represents the minimum energy required to fracture a brittle specimen, while the specific fracture energy is obtained by dividing the fracture energy by the respective specimen mass. Thus, a corrected specific fracture energy is calculated to account for the indentation of the striker and the rod in contact with specimens (Tavares and King, 1998; Bonfils, 2017). The corrected specific fracture energy is influenced by the ratio where slender specimens (1.2:1 ratio) require less energy to fracture while the robust specimens (0.8:1 ratio) need more energy.

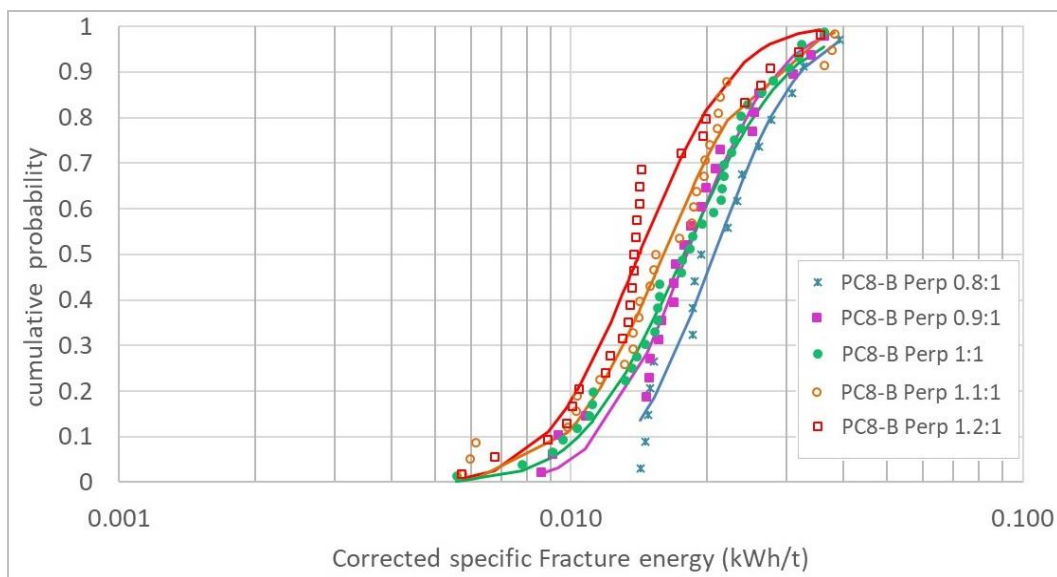


Figure 70 Cumulative distributions of correct specific fracture energy for PC8-B mini-core specimens drilled perpendicular to band and sorted by ratio on SILC test.

During the analysis for corrected specific fracture energy, it was observed that the difference of fitted median is considered significant when the specimens with 0.8:1 and 1.2:1 ratios were compared. However, if the aspect ratio is narrowed down, and the cumulative distributions for the aspect ratios of 0.9:1 and 1.1:1 are compared instead, then the hypothesis that the distributions are

identical cannot be rejected. Also, it does not reject the hypothesis that the means are equal. Those interpretations were supported by statistics (Milin and King, 1994).

Similar observations were found by analysing cumulative distributions and fitted median values for other properties. Figure 71 shows cumulative distributions of Young's modulus for mini-core specimens of PC8-B with aspect ratios varying from 0.8:1 to 1.2:1. Again, the statistical basis demonstrates equal distributions for specimens of aspect ratio varying from 0.9:1 to 1.1:1 (total of 91 data points). Therefore, the limits of 0.9:1 to 1.1:1 aspect ratio are suggested as cut off ratios when testing SILC on mini-core specimens. Furthermore, it is assumed that results for this aspect ratio range (0.9:1 to 1.1:1) might be grouped together in order to refine the interpretation for a median (or P_{50} value) value.

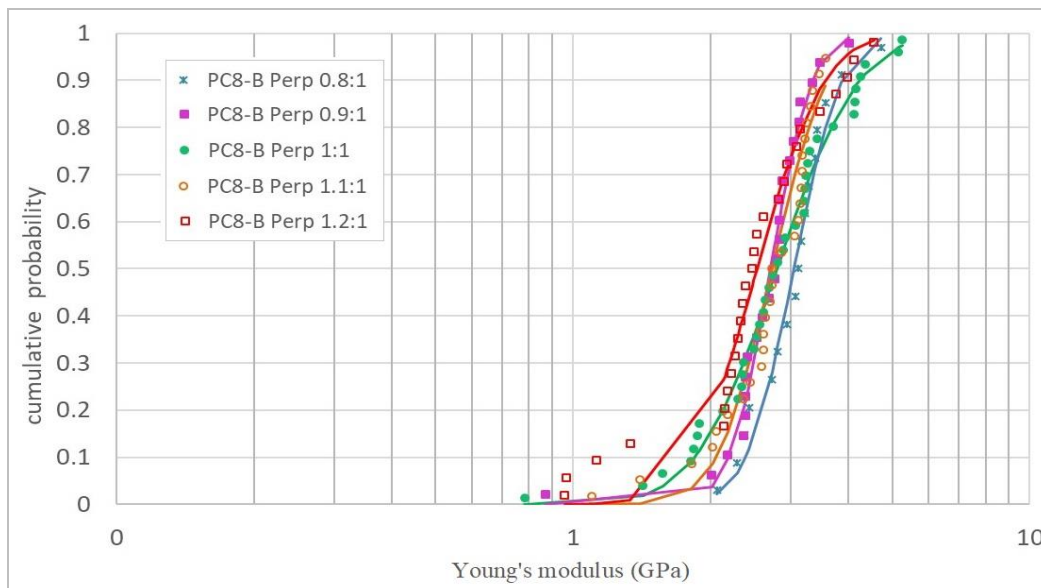


Figure 71 Cumulative distributions of Young's modulus for PC8-B mini-core specimens drilled perpendicular to band and sorted by ratio on SILC test.

5.6.3 Lithotype effect on mini-core specimens of coal

The influence of lithotype was observed on SILC testing of mini-core specimens of PC8-B (banded) and PC6-D (dull), all of which were drilled perpendicular to banding. In order to compare groups of similar number of data points, PC8-B with aspect ratio of 0.9:1 (24 data points) and PC6-D (dull) with aspect ratio of 0.9:1 to 1.1:1 (14 data points) were used. Note that, less specimens from dull (PC6-D) were prepared since the variability for dull band was expected to be smaller if compared to banded (PC8-B). However, because a population of 14 specimens (dull) should not be compared to a population of 91 specimens (banded), then specimens with a ratio 0.9:1 were selected (recall from

the previous section that this aspect ratio provides a good representation for banded as well as 1:1 or 1.1.1). A 535.25 g striker was dropped from a height of 63.1 mm when testing mini-core specimens of PC8-B and PC6-D.

Figure 72 presents the cumulative distributions of corrected specific fracture energy for PC8-B (banded) and PC6-D (dull). The statistical basis supported that the distributions are marginally equal for the corrected specific fracture energy. The mini-core specimens of PC8-B (banded) require less energy (0.018 kWh/t) to fracture while PC6-D (dull) need slightly more energy (0.0194 kWh/t). This outcome is advantageous and followed expectations. SILC was able to capture that a banded coal should be more brittle (require less energy to fracture) than a dull coal, even though cleats are reported as very poor in banded sub-bituminous coal.

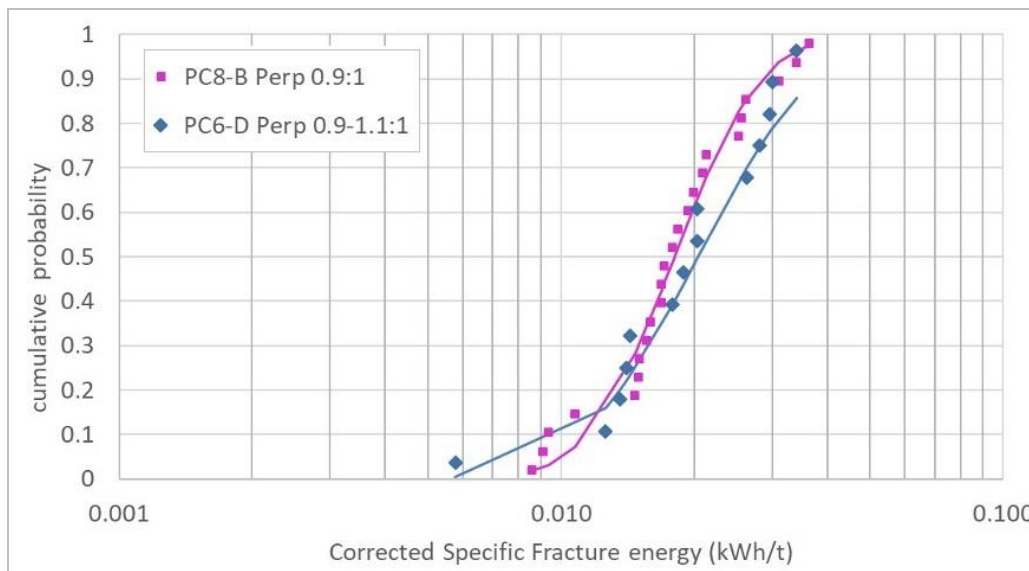


Figure 72 Cumulative distributions of correct specific fracture energy for PC8-B with aspect ratio of 0.9:1 and PC6-D with aspect ratio from 0.9:1 to 1.1:1, all mini-core specimens drilled perpendicular to band.

The experimental cumulative distribution of tensile strength is also observed. Figure 73 shows that the fitted median values were 4.5 MPa for PC8-B and 5.1 MPa for PC6-D, using mini-core specimens 11.7 mm in diameter drilled perpendicular to the band. The hypothesis that the means are statistically equal was not rejected. While the test did not reject the null hypothesis of two distributions being identical for tensile strength, it did reject the null hypothesis that the means are equal for the fracture force (0.89 kN for PC8-B versus 1.19 kN for PC6-D). This indicates that coal lithotype matters, even though not all parameters are statistically distinct.

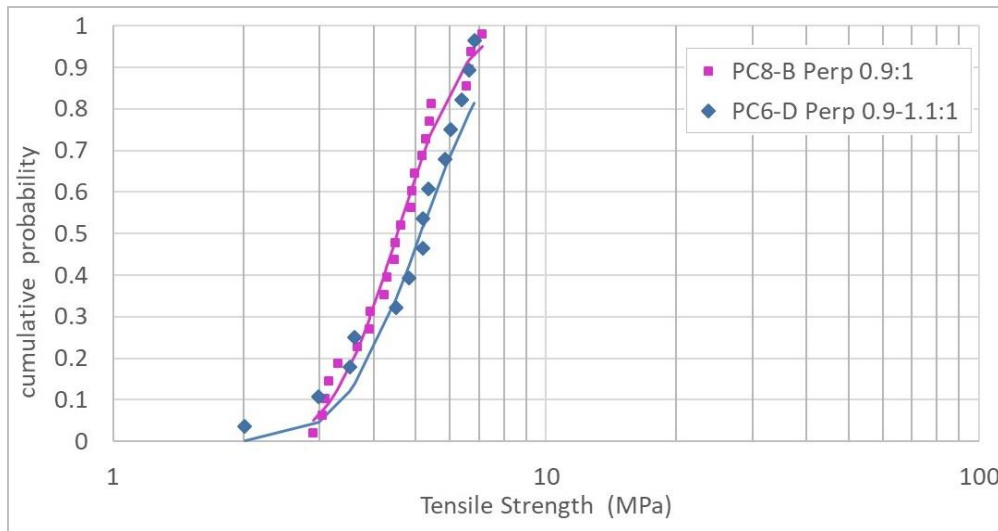


Figure 73 Cumulative distributions of tensile strength PC8-B with aspect ratio of 0.9:1 and PC6-D with aspect ratio from 0.9:1 to 1.1:1, all mini-core specimens drilled perpendicular to band.

Next, the influence of lithotype was then observed during SILC testing of mini-core specimens for PC8-B (banded) and PC8-WB (banded with white marks/clay lenses), all of which were drilled parallel to banding. The lithotype effect was demonstrated with 13 data points of PC8-B and 24 data points of PC8-WB, both with an aspect ratio from 0.9:1 to 1.1:1. While one or two tests rejected the null hypothesis showing the distributions are marginally equal, it is quite clear from the overall results that the means are different. Figure 74 shows the cumulative distributions of corrected specific fracture energy where PC8-B, which is richer in vitrain (more brittle), required much less energy to fracture than PC8-WB.

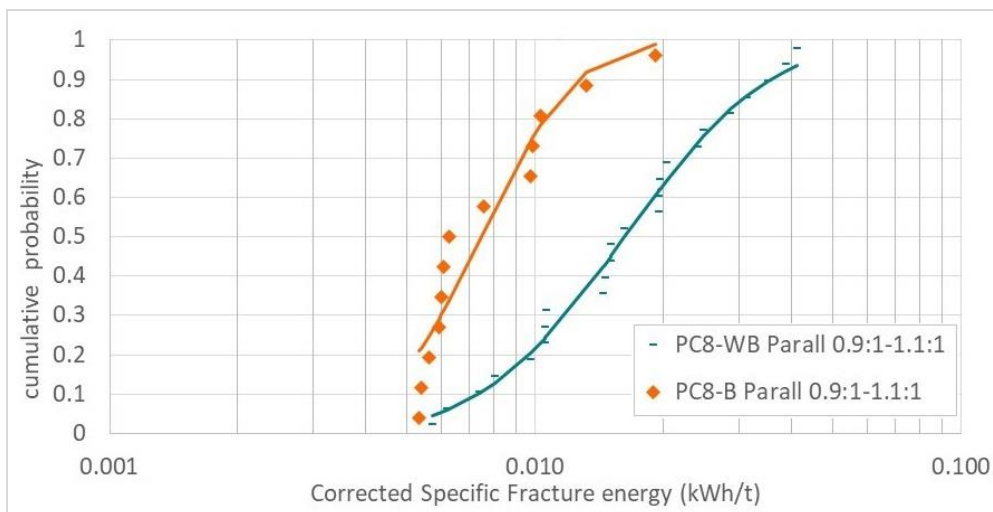


Figure 74 Cumulative distributions of correct specific fracture energy for PC8-B and PC8-WB both with an aspect ratio from 0.9:1 to 1.1:1, all mini-core specimens drilled parallel to band.

Then, Figure 75 illustrates the experimental cumulative distribution of tensile strength for PC8-B and PC8-WB. The fitted median values for tensile strength are 2.9 MPa for PC8-B and 4.7 MPa for PC8-WB, using mini-core specimens of 11.7 mm in diameter drilled parallel to band.

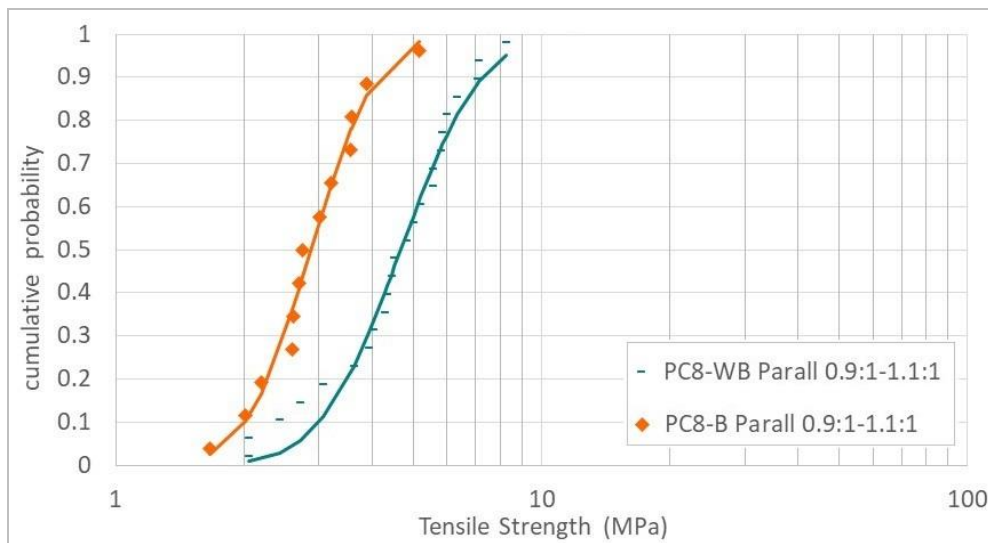


Figure 75 Cumulative distributions of tensile strength for PC8-B and PC8-WB both with an aspect ratio from 0.9:1 to 1.1:1, all mini-core specimens drilled parallel to band.

5.6.4 Orientation of bands relative to impact loading on mini-core specimens of coal

The fabric orientation relative to impact loading during SILC testing was investigated for mini-core specimens of PC8-B (banded) drilled perpendicular and parallel to bands. The influence of fabric orientation was demonstrated for 24 data points with aspect ratio of 0.9:1 drilled perpendicular to band and 13 data points with an aspect ratio from 0.9:1 to 1.1:1 drilled parallel to the band.

Figure 76 presents the cumulative distributions of corrected specific fracture energy for PC8-B (banded), where less energy to fracture is required for mini-core specimens drilled parallel to bands than those drilled perpendicular to bands. Again, using the statistical bases, the two distributions plotted are marginally different, but the means are not equal for the same lithotype when tested at distinct directions. In this context, the amount of energy required to fracture a coal seam is strongly dependent of the fabric orientation when referring to the same lithotype (0.0194 kWh/t for PC8-B drilled perpendicular versus 0.0074 kWh/t for PC8-B drilled parallel).

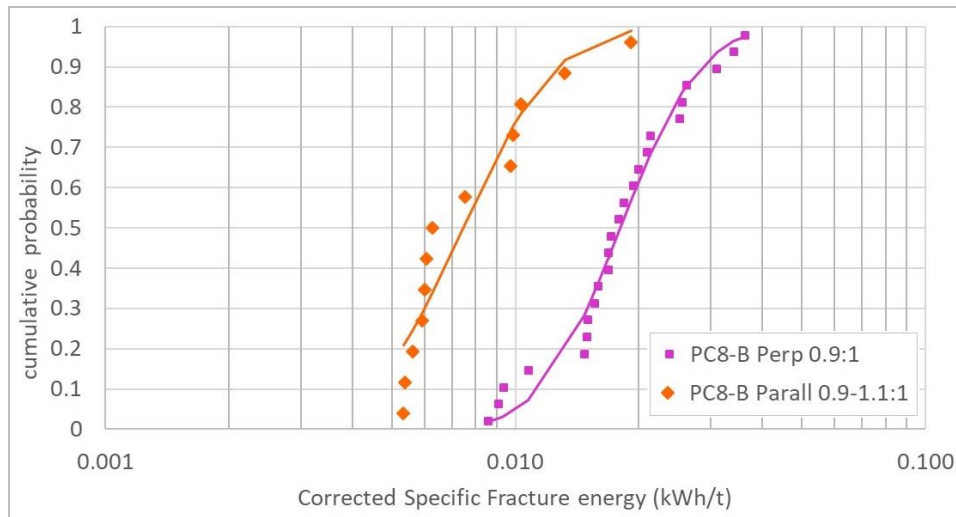


Figure 76 Cumulative distributions of correct specific fracture energy for PC8-B with aspect ratio of 0.9:1 drilled perpendicular to band and PC8-B with aspect ratio from 0.9:1 to 1.1:1 drilled parallel to band.

Figure 77 shows the cumulative distributions of tensile strength for lithotype PC8-B, where mini-core specimens drilled parallel to banding are weaker (or fail more easily) than those mini-core specimens drilled perpendicular to banding. The fitted median values for tensile strength are 2.9 MPa for specimens drilled parallel to bands and 4.5 MPa for those drilled perpendicular to bands (i.e. a 35% difference based on the coal banding orientation) when comparing mini-core specimens of 11.7 mm in diameter. The low values of the tensile strength for specimens drilled parallel to bands may be due to the low cohesion existing between the coal bands and/or and the generation of micro-cracks aligned parallel to the preferential failure plan when the tensile failure mode dominates.

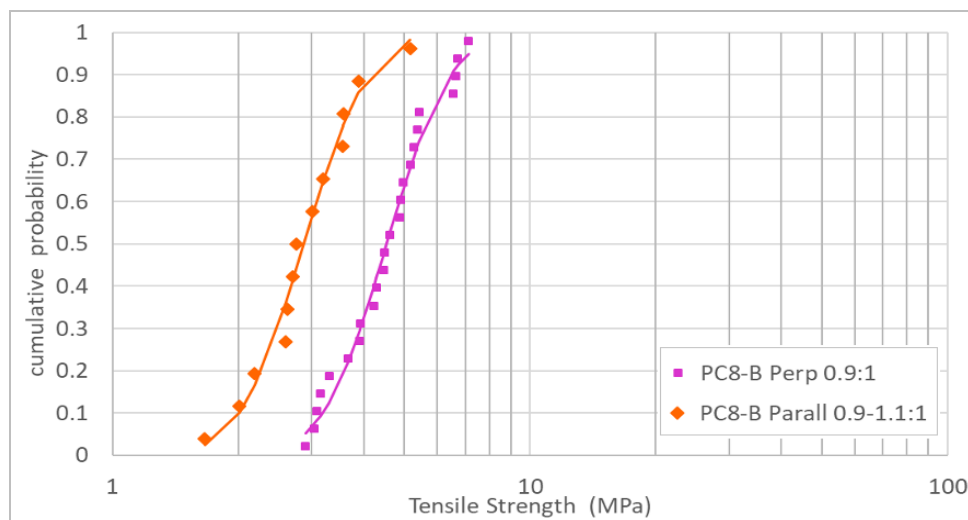


Figure 77 Cumulative distributions of tensile strength for PC8-B with aspect ratio of 0.9:1 drilled perpendicular to band and PC8-B with aspect ratio from 0.9:1 to 1.1:1 drilled parallel to band.

5.7 SILC RESULTS ON IRREGULAR-PARTICLES OF COAL AND MUDSTONE

The irregular single-particles tested on the SILC were made up of the specimens retained at mesh sized 3.35, 4.75, 6.7 and 9.5 mm (Table 9). It was observed that when sub-bituminous coal is reduced into those size fractions, the irregular-particles tend to be an angular product with prominent corners and edges (Figure 61) while the SILC calculations assume a sphere-shape. It should be questioned how much effect a variation in specimen shape might have on SILC test results when using irregular-particles of coal. Note that, when mudstone is reduced into those size fractions, the irregular-particles appeared slightly more uniform (or round) than coal particles.

The breakage of irregular-particles was performed using a striker of 66.78 g or 535.25 g in weight and released from a varied height (45.5 mm - 125 mm) depending on the particle size. Detailed impact conditions for each set of particles tested are presented in the Appendix II. The irregular single-particles were positioned on its most stable surface on top of the anvil (i.e. attempting to avoid particles moving or rolling over) during the SILC test. The unknown orientation of the fabric relative to impact load tends to increase the variability of the test results for irregular-particles when compared with mini-core specimens. Testing a large number of irregular-particles is a method to minimise the test variability.

Initially each series of test results on irregular-particles was organised following the lithotype, mesh size, and energy distribution/size combination from the DWT (e.g. PD8-BLA 9.5 mm₆₃ × 53_E = 0.25). However, it was not possible to distinguish between the presence of flaws in the irregular-particles or cumulative damage arising from the DWT, as the variability associate to particles randomly oriented during testing cannot be isolated. This was concluded after the results for each series were processed, and no relationship about the potential of existing flaws were explicitly observed. Therefore, it is assumed irrelevant to plot the original names (i.e. energy distribution/size combination from the DWT) into the graphic analysis below, although each data point can be back correlated/verified in the Appendix II. In the graphics, the symbols correspond to the fitted median value from the log-normal distribution for each series tested. The results were represented by lithology/lithotype name (e.g. PD8-BLA) for analysis and display as per the chart legend. The graphics show the irregular-particles analysed to test the influence of size and lithology/lithotype. The work with irregular single-particles of coal and mudstone focused on fracture force, fracture energy, and tensile strength.

5.7.1 Size and lithology/lithotype effect on irregular-particles of coal and mudstone

The influence of size and lithology/lithotype was observed on SILC test of irregular-particles for PC6-D (dull coal), PD8-BLA (low ash banded coal) and mudstone. Each lithology/lithotype belonged to a distinct pit location (Table 9) while represented by: PC6-D (585 irregular-particles, averaging 37 particles per symbol), PD8-BLA (665 irregular-particles, averaging 35 particles per symbol), and mudstone (580 irregular-particles, averaging 41 particles per symbol). However, PC6-D is not available at the 6.7 mm mesh size; and smaller irregular-particles (mesh sized 3.35 mm) for coal and mudstone might present issues associated with the particle size/grain diameter. In the future, it may be considered that the SILC test be expanded to include larger irregular-particle sizes (e.g. 16 mm and 22.4 mm sieve mesh size), which could contribute to establishing a better correlation between particle size (scale effect) and the parameters of interest.

Figure 78 shows the fitted median from log-normal distribution of force at first fracture for irregular-particles of PC6-D, PD8-BLA, and mudstone. Median fracture force represents the force required to create the first fracture on coal plies and mudstone. The fracture force increased with increasing particle sizes. More significant variability is observed for larger particles (9.5 mm in diameter) of PC6-D, while all series of mudstone of larger size particles showed some discrepancy on fracture force. The force required to fracture the mudstone is higher than for coal but, it seems to lean towards convergence for particles of increasing size. Perhaps the ductile behaviour is less prominent on large particles of mudstone. Also, it is speculated that the increase in the coal particle size tended to increase the differences in the aspect ratio (length-to-diameter) as well as shape of the particle, exacerbating the variability in the fracture force for the largest size series tested.

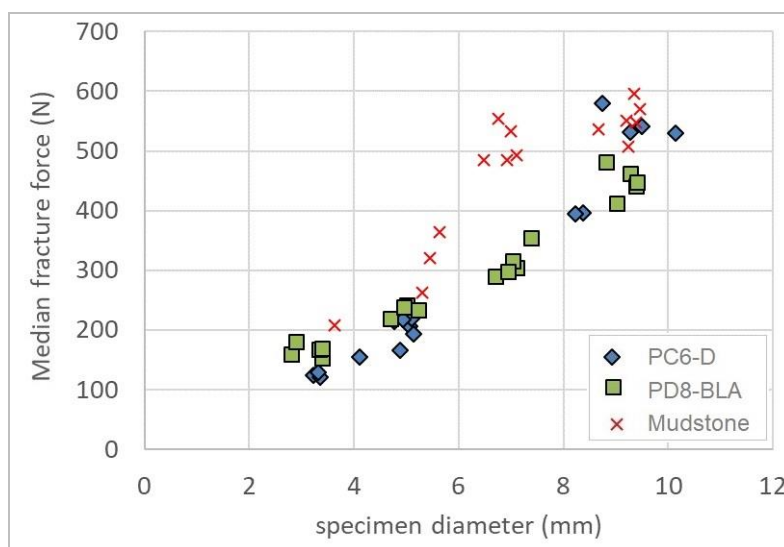


Figure 78 Variation of median fracture force against specimen diameter for irregular-particles of coal plies PC6-D, PD8-BLA and mudstone.

Next, the contrast between distinct rock and size is described for the tensile strength of irregular-particles. Coal's innate tendency to reduce in strength (compressive or tensile) with increased specimen size is well known (Bieniawski, 1968a; Medhurst, 1996; and Song et al., 2018). This is also the case for other rock types (Hoek and Brown, 1980). This behaviour was confirmed with the irregular-particles tested on the SILC. Figure 79 presents the fitted median from log-normal distribution of tensile strength for PC6-D, PD8-BLA, and mudstone. The median tensile strength of coal plies (PC6-D and PD8-BLA) and mudstone follow trends. Here the data was analysed using the method of least squares regression. The best approximation equation with the highest correlation coefficient was achieved using the power regression. The equation's correlating tensile strength and irregular-particle size might be used to quantify the observations. The tensile strength of coal plies PC6-D and PD8-BLA was weaker than mudstone for the tested fractions but could potentially be more similar for particles of increasing size (above 8 mm in diameter).

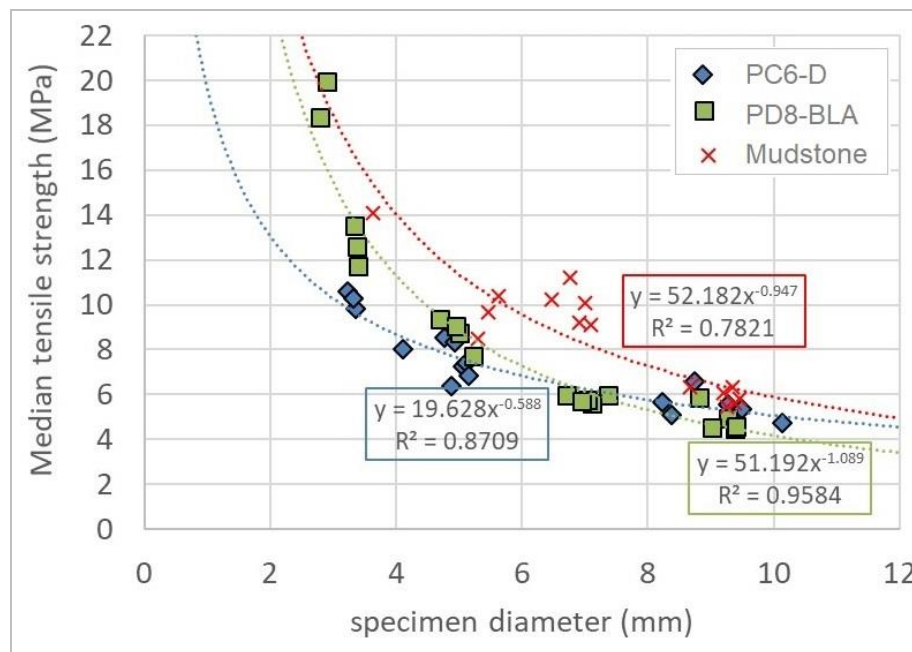


Figure 79 Variation of median tensile strength for irregular-particles of coal plies PC6-D, PD8-BLA and mudstone by size.

Last, the fracture energy, which is also size dependent (King and Bourgeois, 1993; Tavares and King, 1998), was plotted for irregular-particles of coal and mudstone (Figure 80). Parallel trends were observed for all particles tested. Between the coal plies, irregular-particles of PC6-D were able to store less elastic energy until the occurrence of the fracture, when compared with the PD8-BLA specimens. Again, the data was analysed using the method of least squares regression, and best approximation was achieved using the power regression. The equation's correlating fracture energy

for irregular-particle size for coal and mudstone are presented. Overall, as coal and mudstone specimen size increases, higher fracture energy is required for crack extension and propagation. The mudstone shows an accentuated increase of fracture energy for larger dimensions (>8 mm in diameter) when compared with coal. Figure 80 shows that anisotropic behaviour between plies and different lithology of distinct thickness can be interpreted for a variety of scenarios applied to reservoir geomechanics. For example, using this data set, it can be interpreted that the fracture energy utilised to fracture 9–10 mm (in diameter) of coal PC6-D might also extend up to 5 mm of mudstone, causing some over breaking/fracture, if it is the interbedding. It must be noted that the mudstone would have a mechanical-chemical interaction with the water in the reservoir (i.e. it could slake), but this study focussed on the mechanical aspects only.

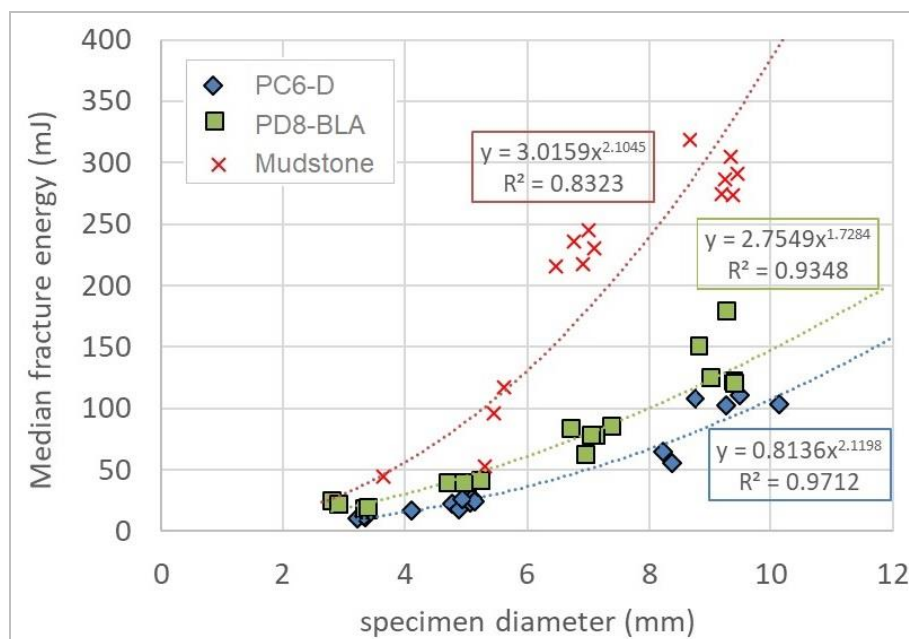


Figure 80 Variation of median fracture energy for irregular-particles of coal plies PC6-D, PD8-BLA and mudstone by size.

5.8 COMPARISON OF IRREGULAR PARTICLES AND MINI-CORE SPECIMENS ON COAL

The influence on the shape-dependent properties was observed for irregular-particles and mini-core specimens. This time, in order to reduce the variability of distinct series of irregular-particles tested, each specimen result was grouped by size (i.e. disregarding the initial series) but considering the lithotype. The fitted median value from log-normal distribution was then obtained for each size tested, which became hundreds of particles instead of groups of 35 particles on average.

For example, irregular-particles with 3.35 mm mesh size were grouped, then PC6-D includes 146 data points and PD8-BLA comprise 118 data points as illustrated in Figure 81. After getting the fitted median values per size (P_{50} value about 10.9 mJ and 20.4 mJ for PC6-D and PD8-BLA, respectively) the size sequence was correlated using the method of least squares regression and a trend line was assigned for irregular-particles belonging to a ply.

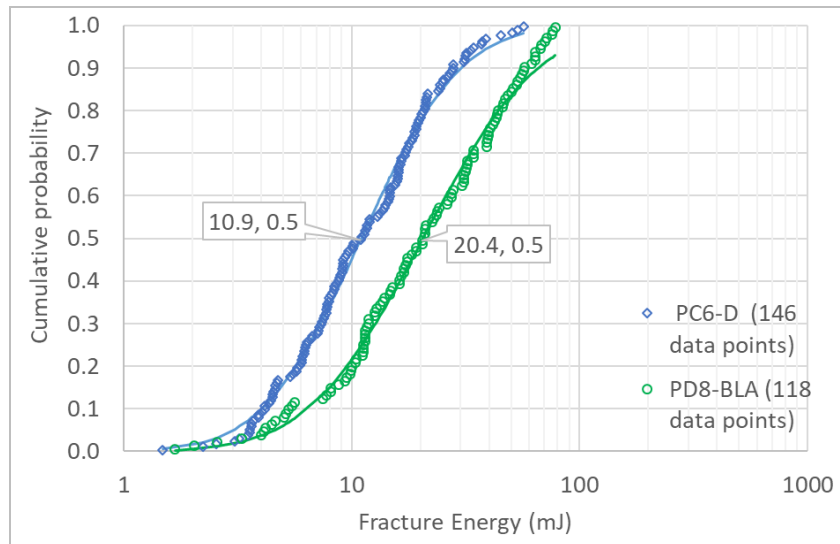


Figure 81 Median values of cumulative distributions of fracture energy for PC6-D and PD8-BLA for lots of irregular particles retained at 3.35 mm mesh size.

Figure 82 shows that the tensile strength estimated on SILC test might be considered independent of the specimen shape as well as the loading condition. The lithology/lithotype allowing for this observation is PC6-D which was the only one tested for both shapes (mini-core specimens and irregular-particles). Therefore, PC6-D is used to guide the observations here. The fitted median values of tensile strength for PC6-D, irregular-particles and mini-core specimens, are found to be generally similar, as they follow the same trend. The tensile strength for coal particles of PC6-D was about 5.1 MPa for specimens 10 mm in diameter or by extrapolation using the power law regression curve, 1.9 and 1.7 MPa for specimens with 50 and 61 mm in diameter, respectively. Note that, PC6-D mini-core specimen (see symbol \diamond in Figure 82) induces a slight ramp up in the curve for specimens of increasing size. Therefore, if another trend for the power law regression curve is calculated to include the irregular-particles and the mini-core specimen for coal PC6-D, then the tensile strength is expected to be 2.2 and 2.0 MPa for specimens with 50 and 61 mm in diameter, respectively. On the other hand, the PD8-BLA is stronger than PC6-D when smaller particles (<7 mm in diameter) are compared. It then starts behaving weaker as the size increases. The tensile strength for coal PD8-BLA is expected to be 0.8 and 0.6 MPa for specimens with 50 and 61 mm in diameter respectively, again by extrapolation using the power law regression curve.

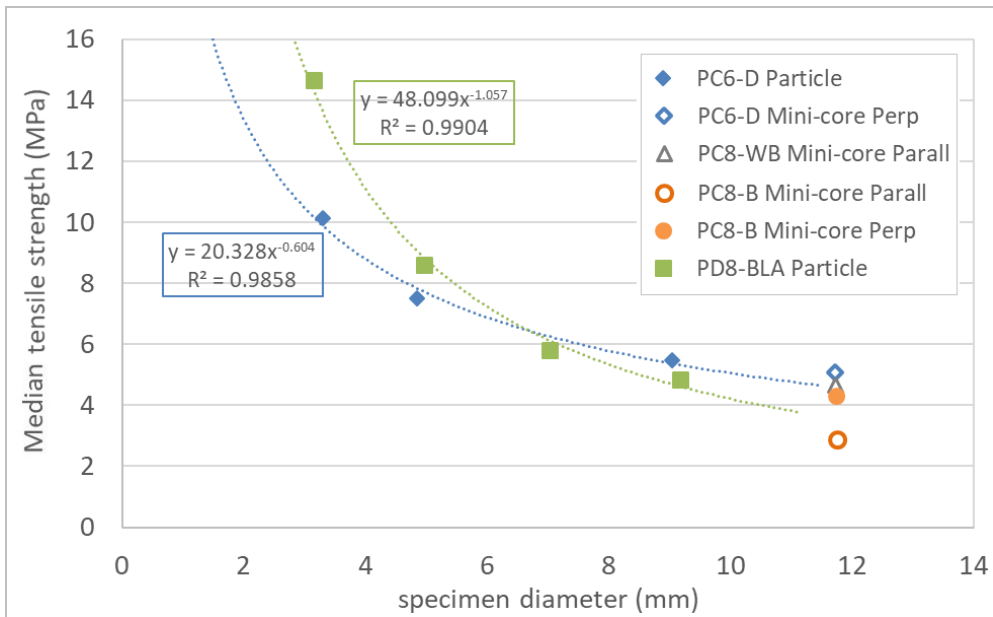


Figure 82 Variation of median tensile strength for sub-bituminous coal on SILC influenced by shape.

Figure 83 shows that the highest fracture force is required for mini-core specimens. This is close to 71% larger in magnitude than the fitted median value of force at fracture required to break irregular-particles of PC6-D of a similar size (1189.4 N versus 694.1 N for 11.7 mm in diameter). There is a strong shape dependence influencing results of fracture force on SILC.

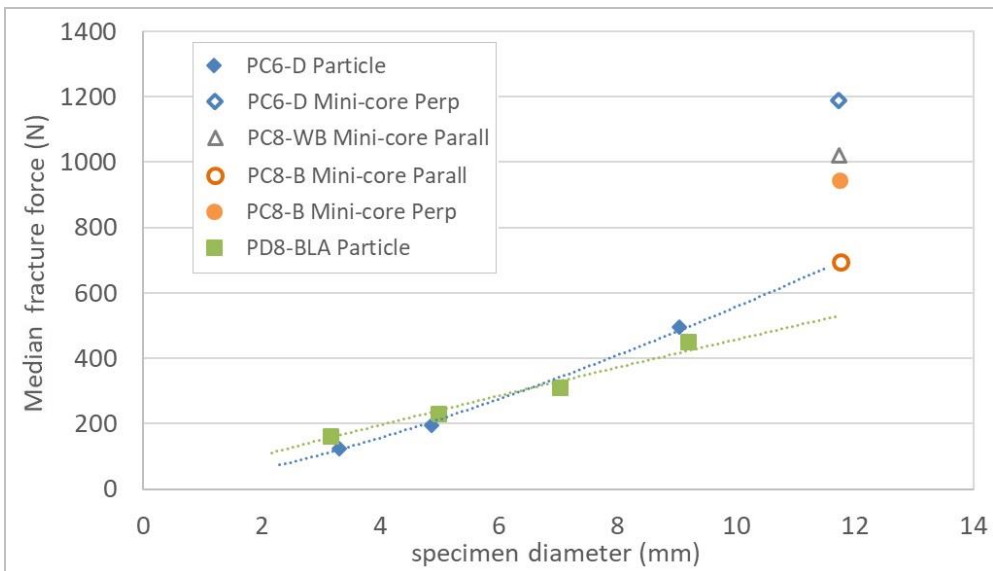


Figure 83 Variation of median fracture force for sub-bituminous coal on SILC influenced by shape.

In brittle material such as coal, the fracture energy is expected to be low. Figure 84 shows that the trend in coal has an upward slope with increasing specimen size, but the upward trend for irregular-particles of PC6-D did not deviate significantly from mini-core specimens of PC6-D (148.9 mJ versus 124.4 mJ for 11.7 mm in diameter).

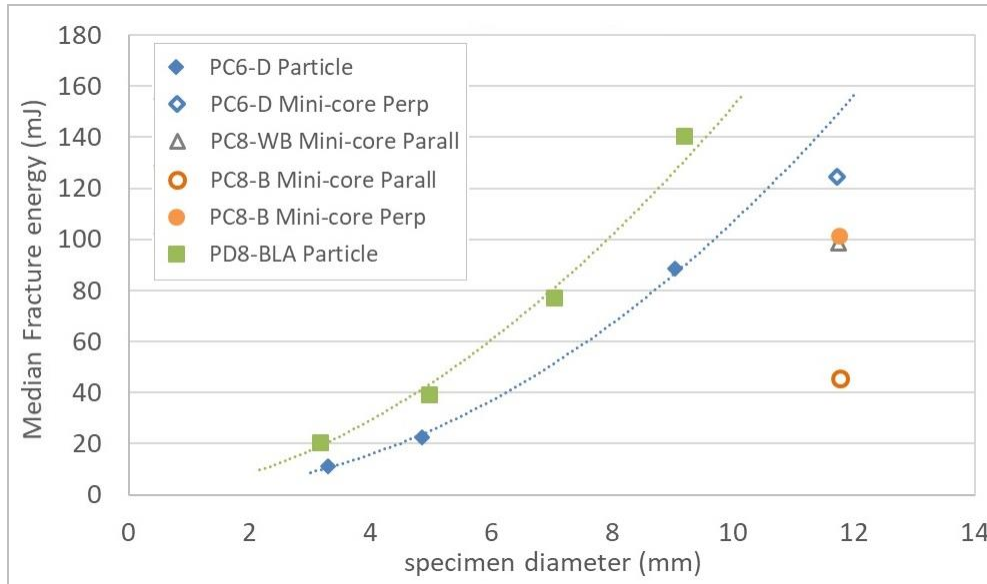


Figure 84 Variation of median fracture energy for sub-bituminous coal on SILC influenced by shape.

Figure 85 shows similar observations about trend for specific fracture energy of coal when irregular-particles and mini-core specimens are compared. Thus, the specific fracture energy still can be used as an indication for toughness, independent of the shape tested for heterogeneous rock material on SILC.

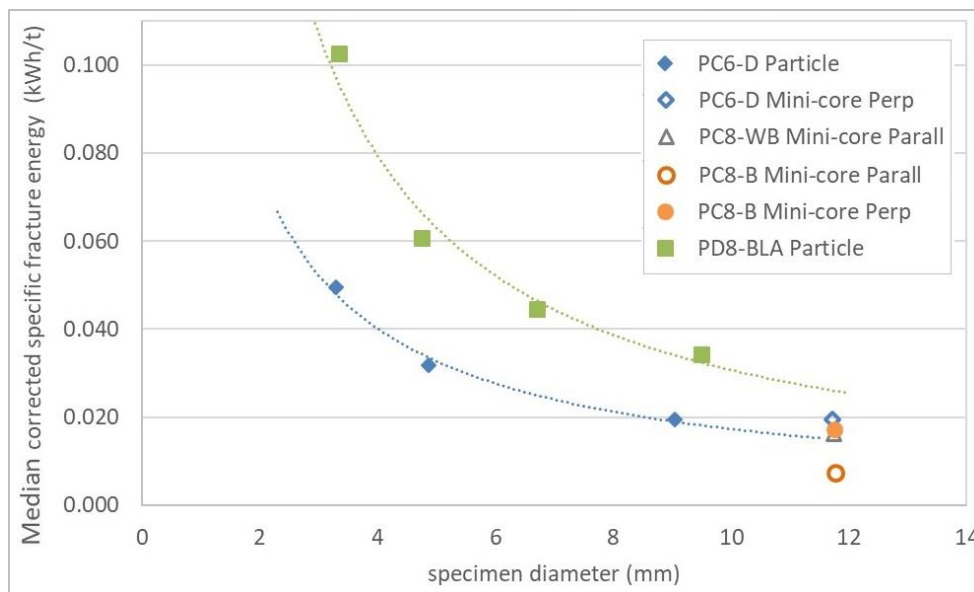


Figure 85 Variation of median corrected specific fracture energy for sub-bituminous coal on SILC influenced by shape.

5.9 CONCLUSIONS AND RECOMMENDATIONS

Based on SILC testing of mineral ores, the geomechanical properties of rocks can be influenced by the specimen shape, size, impact orientation, type of material, and impact conditions, which contributes to highlight similarities with standard geotechnical tests (e.g. Brazilian tensile strength). This work focused on testing and analysing data for irregular single-particles of mudstone and both mini-core specimens and irregular single-particles of sub-bituminous coal. The inherent material contrast between brittle coal containing natural defects including differences for plies and ductile mudstone rock was demonstrated when specimens collected from the Surat-Clarence-Moreton Basin in Australia, were tested using the SILC. The key findings are listed:

1. Measurements of Young's modulus (or 'apparent' stiffness as called for publication on SILC), deformation, and contact areas post-impact are conditioned by the SILC test impact conditions while fracture force, tensile strength, and specific fracture energy appeared not to be influenced. Caution is required when interpreting results from different impact combinations and/or incorporating data from other studies. Moreover, further investigation about the 'apparent' stiffness calculation for mini-core specimens is required.
2. The coal anisotropy was observed for mini-core specimens (11.7 mm in diameter), where specimens drilled parallel to bands require considerably lower fracture energy (at least 44% less) than those drilled perpendicular to the band for the same coal lithotype. For geomechanical purposes, the controlled specimen shape (cylinder/mini-core specimens) show an advantage associated to more uniform force-time profiles, and less variability of the data, in contrast to irregular-particles, while the P50 values might be equivalent. The results of tensile strength and specific fracture energy for mini-core specimens followed the trends of irregular-particles. Then, it is expected that for heterogeneous brittle material, the specific fracture energy is independent of the shape tested (which might not be the case for homogeneous specimens too). A strong correlation between fracture toughness and specific fracture energy is reported in the literature, which is of interest for the CSG.
3. The scale effect on strength and specific fracture energy was explored by observing specimens of distinct sizes (from 3.35 to 11.7 mm in diameter both irregular-particles and mini-core specimens) and both producing consistent results when testing coal on the SILC. Therefore, difficult associated to test standard core specimens, particularly for measurement of tensile strength can be overcome.

For future studies related to CSG, although specimen collection as well as preparation can be a challenge, it is suggested that SILC experiments be performed using specimens of composite lithology, i.e. specimens formed by half coal and half mudstone.

LITHOTYPES AND MICROLITHOTYPES MATTER

Karina Barbosa (PhD candidate) conducted specimen preparation and testing, interpreted data, prepared figures and graphics, and wrote the manuscript.

Joan Esterle (Principal PhD supervisor) proposed the experiment, assisted on microlithotype classification, reviewed, discussed and edited the manuscript.

Zhongwei Chen (Associate PhD supervisor) reviewed, discussed, and edited the manuscript.

Summary

Coal cannot be assumed a single rock type in the rock mechanics context, since the lithotypes (biochemical composition) matter when observing the geomechanical behaviour of bituminous coal. In other to test for lithotypes and microlithotypes at low rank, sub-bituminous coal, this chapter presents a series of Shore Scleroscope Rebound Hardness test results performed on polished surface of coal lithotype specimens. The experimental study is designed to address hardness properties that can demonstrate the brittle and ductile behaviour of coal on microscopic scale. It investigates whether or not a microlithotype is capable to undergo substantial permanent damage without presenting a microscopic fracture; and if the microstructural physics and interactions can be simplified in terms of hardness. This study is useful for fracture stimulation by the coal seam gas industry, while it also might bring interest of the mining industry when studying coal bursts.

Shore hardness measurements of sub-bituminous coal microlithotypes

*Karina Barbosa^{ab}, Joan Esterle^{ab}, Nikola Van De Wetering^a, and
Zhongwei Chen^c*

- a. School of Earth and Environmental Sciences, The University of Queensland, St. Lucia 4072, QLD, Australia*
- b. UQ Centre for Coal Seam Gas, The University of Queensland, St. Lucia 4072, QLD, Australia*
- c. School of Mechanical and Mining Engineering, The University of Queensland, St. Lucia 4072, QLD, Australia*

Submitted to International Journal of Coal Geology

Abstract

This study presents the results of the surface hardness of coal, estimated with the Shore Scleroscope Rebound Hardness tester. The Shore hardness can be related to fracture toughness and tensile strength, which are important input parameters for fracture stimulation design of coal seam gas reservoirs. The Shore hardness experiments were performed on low rank coal specimens from an open cut mine from the Surat-Clarence-Moreton Basin, and a borehole from the Surat Basin, Australia. All measurements were conducted on polished coal surface confined within epoxy blocks following similar preparation required for coal petrographic analyses. The resulting indentations and microlithotypes were analysed under the microscope, then associated to the Shore hardness number. Three common microlithotypes were identified for the sub-bituminous specimens tested: vitrite, clarite and carbominerite. Results indicate the hardest microlithotype is clarite, followed by vitrite, and then carbominerite. Quantification of the micromechanical properties is possible using simple Shore hardness tests, and opportunities to improve fracture propagation may be further explored from this work.

Keywords: scleroscope; coal microlithotype; mechanical properties; fracture propagation.

6.1 INTRODUCTION

Coal is a complex heterogeneous material with distinct characteristics reflecting hardness, tenacity, and fracture which are influenced by rank (thermal maturity), lithotype (biochemical composition), and grade (amount and type of minerals) (Hower et al., 1987; Hower and Wild, 1988; Barton et al., 1994; Bailey and Hodson, 1994; Conroy, 1994; Rubiera et al., 1999). Hardness is a function of the elastic resistance of a surface to the local penetration of another body, and can be measured by different tests using scratch, rebound, impact or indentation (Taylor et al., 1998; Altindag and Güney, 2006). Micro-indentation, e.g. Vickers microhardness, is often used to illustrate the changes in surface hardness related to coal rank, maceral or microlithotype distribution, and mineral composition (e.g. Hower et al., 2008; Kozusnikova, 2009; Borodich et al., 2015; and references therein). The organic components, or macerals, and minerals occurring in association as microlithotypes are commonly layered at the millimetre scale and reflect the original plant matter and its degree of decay. The individual macerals are non-uniform in structure, can contain inorganic inclusions, internal cracks and micro-pores which contributes to their gross mechanical properties (Macmillan and Rickerby, 1979; Epshtein et al, 2015). Moreover, the porosity of the coal decreases with rank advance as moisture decreases, resulting in hardness differences between lithotypes and microlithotypes. Whether these differences are significant at lower sub-bituminous ranks is examined in this study using an indenter test, the Shore Scleroscope Rebound Hardness (SSRH or SH as referred to in this study). Note that sub-bituminous coals in Australia are not commonly tested for hardness or other geomechanical properties. The SH is a simple test that has been used previously (e.g. Klawitter et al., 2015 and references therein) to illustrate differences in hardness between lithotypes and their maceral components (Figure 86). However, the results of this hardness test are influenced by sample preparation, creating a level surface through polishing, and a degree of confinement imposed by epoxy binding (Klawitter et al., 2015).

In this study, SH is used to test the variability in hardness relative to maceral and microlithotype in the different lithotypes occurring in the sub-bituminous coals of the Walloon Coal Measures. The Walloon coal measures in the Surat Basin are currently produced for gas, and as target depth increases they may require fracture stimulation. Knowing the variation in hardness (Das, 1972; Mukherjee et al., 1989; Hower et al., 2008; Kozusnikova, 2009; Epshtein et al, 2015; Manjunath and Nair, 2015; Klawitter et al, 2015; Shi et al., 2017; Kossovich et al., 2019) as a function of microlithotype can contribute to understanding the mechanical behaviour of coal seam gas reservoirs, and assist in designing stimulations. Information about hardness may also be utilised for

the prediction of outburst, breakage and grindability (Peters et al., 1962; Hower and Lineberry, 1988) that contributes to the mining operation and coal product preparation.

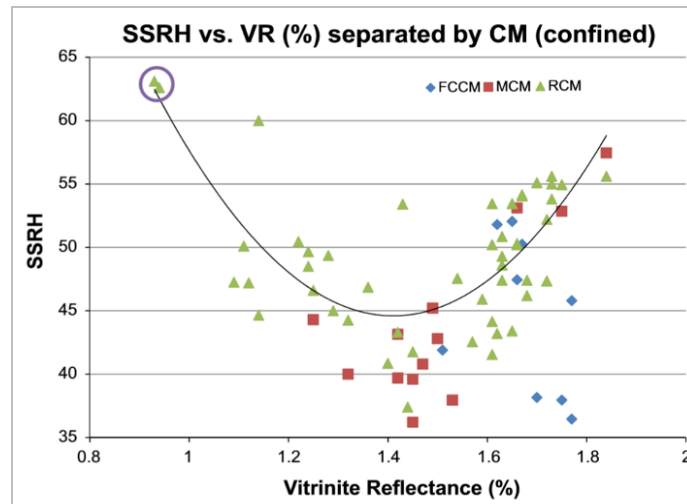


Figure 86 SSRH versus VR (%) on confined (epoxy block) specimens, separated by coal maceral (CM) where MCM stands for Moranbah Coal Measures; FCCM for Fort Cooper Coal Measures, and RCM for Rangal Coal Measures (Klawitter et al., 2015).

6.2 RESEARCH METHODOLOGY

6.2.1 Hardness testing

The surface hardness or the material response to the indentation was obtained using the Shore Scleroscope Rebound Hardness. The SH tester is a non-destructive index test, convenient technique, and low budget method which provides a straight forward estimation of hardness (Altindag and Güney, 2006). The SH tester involves dropping a diamond-tipped metallic hammer made of pure hardened high-carbon steel onto the polished specimen surface. The spherical diamond-tipped hammer falls under the force of its own weight from a fixed height and rebounds, imprinting an indentation on the specimen surface. The instrument setup consists of adjustment of the level vial, to guarantee a free vertical drop of the hammer. The rebound height is measured on the dial gauge (a graduated scale) on the scleroscope. The scale of the rebound consists of Shore units, divided into 140 parts. The Shore (dynamic) Hardness (denoted SH) is a measure of the elasticity of the material; the harder (more competent) the material, the higher the rebound and its measurement number (Honda and Sanada, 1956; Hucka, 1991). In this study, the SH test was performed at The University of Queensland using the IMAI SIKENKI Co. equipment (Tokyo – Nov. 1970, No 700756) (Figure 87), which produces a spherical indenter (i.e. circular shape imprinted).



Figure 87 Shore scleroscope rebound hardness made by IMAI SIKENKI Co.

A conversion table is supplied with this equipment, correlating the graduated scale for SH with an equivalent estimation of Vickers scale (which uses a square-base diamond pyramid indenter) as well as tensile strength (σ_t). For example, an average SH of 80, is approximately 680 Vickers, or $\sigma_t = 232 \times 10^3$ psi (1.6 GPa) (values corresponding to $\times 10^3$ psi as per Arbtin and Murphy, 1953). While a hardness number can be converted to other hardness numbers or to some mechanical property if appropriate charts or equations are known, Arbtin and Murphy (1953) also showed that an exclusive hardness conversion chart should not be used for different materials. Thus, the information on the conversion table is for guidance only. The provided conversion table only includes SH < 80, therefore an extrapolation curve was used to extend the Shore values up to 100 (see Figure 88), which was required in this study.

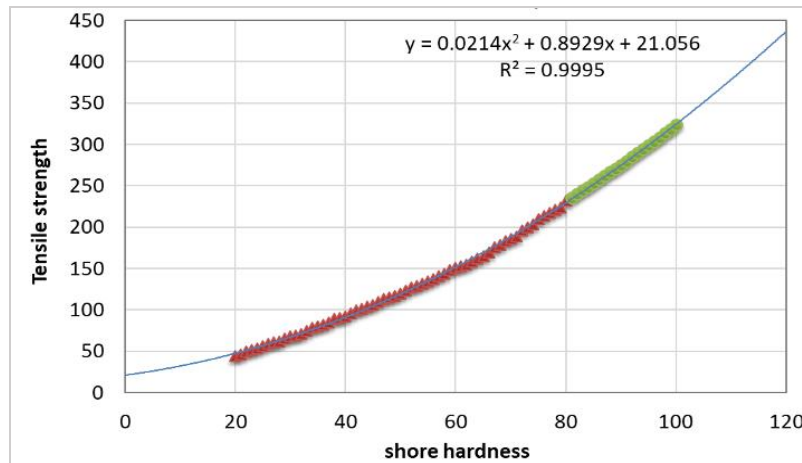


Figure 88 SH conversion table - IMAI SIKENKI Co. equipment, in red values from the original conversion table, and in green values extrapolated for SH > 80.

6.2.2 Sample collection

The low rank, sub-bituminous coal samples were collected from two locations:

- The first, an open cut mine in the Surat-Clarence-Moreton Basin with a maximum vitrinite reflectance of 0.50 %. The following plies were collected: C8 ply banded (PC8-B), C8 ply white marks banded (PC8-WB), and C6 ply dull (PC6-D). All three plies belong to the same pit (north pit) with minimal depth variation. Note that the “white marks” are clay blebs.
- In addition to the open cut mine specimens, samples were collected from a borehole named Guluguba-2 in the Surat Basin, with a maximum vitrinite reflectance of 0.43-0.47 %. The specimens were collected at different depths within the Walloon Coal Measures. The specimens were called GG- followed by a specimen number e.g. GG-4 and had been previously studied for petrology by Hentschel et al. (2016).

6.2.3 Specimen preparation

During the SH test, the rebound of the hammer is affected by the smoothness of the material surface. Therefore, all specimens were prepared as ground and polished coal surface at epoxy-set blocks. According to Klawitter et al. (2015), the epoxy confinement in blocks of similar dimensions contributes to improved reproducibility of SH tests, although it is acknowledged that increasing confinement pressure reduces dilatant fracture propagation and therefore increases the strength of the coal under test (Hobbs, 1964). Therefore, this study examines relative rather than absolute differences in hardness for the different lithotypes and their components. The polished epoxy was also indented for comparison to the coal, and the samples were observed in white and blue light excitation to demonstrate that the indenter was indeed measuring the coal surface without visible impregnation by the epoxy as might expected with lower rank porous lignites. The epoxy has a bright green fluorescence as compared to the orange to yellow colours of liptinite group macerals in these coals. The vitrinite group macerals showed no excitation in blue light. An added advantage to the epoxy-set blocks is that the specimen preparation follows the same procedure used for petrographic analyses. The specimens were placed into moulds exposing the coal layering, embedded in epoxy, and dried for 24 hours. Specimens were then ground and polished to 0.04 μm grit, exhibiting a clean, flat polished coal surface (Taylor et al., 1998). The coal specimens were prepared to fit regular blocks sized 50×30×10-12 mm. A total of 43 confined coal block specimens were tested.

6.2.4 Hardness testing procedure

To perform the SH test, each sample was positioned manually on the flat base of the instrument. The resulting distance of the rebound for each indentation should be recorded, then later averaged.

Procedures for classic analysis suggest collecting and averaging 20 randomly placed measurements on a homogeneous rock, to account for any variation, following calibration on the quenched and tempered steel standard which measures 81.4 ± 2.5 (ISRM, 1978; Rabia and Brook, 1979; Altindag and Güney 2006; Yarali, and Soyer, 2011; Klawitter et al., 2015). As an additional calibration, 20 indentations were measured on the polished epoxy only, which showed an average of 60.8 ± 4 .

As coal is a heterogeneous rock, this study followed a different procedure for data collection. The SH values were recorded in transects to encapsulate changes in microlithotype within a block (Figure 89a), or as a random 20 indentations within a given microlithotype on selective areas (Figure 89b), and the results are compared to understand the range of hardness variability in sub-bituminous rank coals. The transects comprised 16 to 30 measurements depending on the specimen size. A summary of testing conditions and number of specimens is shown in Table 11.

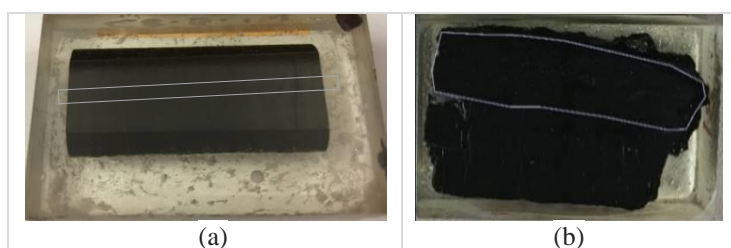


Figure 89 Photographs of polished coal blocks illustrating a) transect, and b) selected lithotype within a block.

Table 11 Number of specimens and testing conditions per location.

Location	Coal measures	Ply/ seam	Number of specimens	
			Transects	Selected lithotypes
Open cut mine	Acland seams (~Taroom)	PC8-B	7	-
		PC8-WB	1	-
		PC6-D	5	-
Borehole Guluguba-2	Juandah	various	-	17
	Taroom	various	1	4
	unknown	various	1	7

6.2.5 Microscopic analysis

Following SH testing, the specimens were examined under a reflected-light microscope (Leica DM 6000M) equipped with the Hilgers' Diskus Fossil computer program for image capture. The microlithotype was identified for each SH test point to determine a relationship to surface hardness values. By definition, microlithotypes are assemblages of macerals occurring within a $50 \mu\text{m}$ area or layer (Falcon and Snyman, 1986); in this study the area of indentation ($\sim 600 \mu\text{m}$) was classified to a microlithotype as follows:

- Vitrite (monomacerite vitrinite, commonly telovitrinite >95%);
- Clarite (bimacerite vitrinite plus liptinite >95%);
- Carbominerite (vitrite or clarite comprising 20-60% of minerals).

Photomicrographs were taken using a 5× objective in air, resulting in ~50× magnification. Microlithotype/ lithotype bands in these coals are of variable thickness, between 50-600 µm; though thicker bright bands do occur, they are rare (Afonso, 2014; Hentschel, 2018). The approach for measurement along transects, gave a precise SH value for each indentation, allowing for a match between the SH number and microlithotype. The histograms for transect investigations presented uni, bi, or trimodal distribution, for each clustered average in SH. Measurements identified on epoxy were removed from the analysis, as well as any overlapping indentations. Comparison of SH values mode, mean, and range utilising box-and-whisker plots was conducted for the different populations.

6.3 RESULTS AND DISCUSSION

SH values ranged from 39 to 94 across all specimens tested, with a gross average value of 75 ± 6 for the open cut mine specimens, and 68 ± 6 for the borehole specimens. A summary of the SH results for each microlithotype, at each sample location is summarised in Table 12. The variation in SH values between different microlithotypes appears to be consistent despite a slight variation in rank between the open cut mine and borehole sub-bituminous coal specimens.

Table 12 Summary of SH values measured conditional to microlithotype.

	Outcrop data (open cut mine)				Borehole data (Guluguba-2)			
	Min	Max	SH avg (StDev)	tensile strength (GPa)*	Min	Max	SH avg (StDev)	tensile strength (GPa)*
carbominerite	51	78	70.2 (6.8)	1.28	39	58	47.7 (4.5)	0.78
vitrite	56	82	71.3 (6.9)	1.30	52	83	68.8 (6.8)	1.23
clarite	74	94	84.0 (3.6)	1.72	73	94	84.5 (4.6)	1.73
clarite increase mineral matter	-	-	-	-	60	85	74.8 (5.0)	1.45
clarite increase cracks/fractures	-	-	-	-	44	82.5	65.1 (8.2)	1.14

*approximated tensile strength based on average SH values.

6.3.1 Correlation between hardness and microlithotype for specimens from the open cut mine

The SH trend for each observed lithotype (from least to most hard) is: carbominerite (70.2 ± 6.8), vitrite (71.3 ± 6.9), clarite (84.0 ± 3.6). Each of these microlithotypes exhibited some variation in

SH dependent on their maceral composition. The variability of coal microlithotypes and their associated SH value was observed for three distinct plies (PC8-B, PC8-WB, and PC6-D).

Figure 90 shows specimen PC6-D #M5 composed of clarite and carbominerite, with a minor proportion of vitrite. The vitrite in this specimen was thin and not indented during SH testing. The majority of the indentations (76 %) were performed on clarite, and the remainder on carbominerite for this specimen. The SH for carbominerite ranged from 64 to 78, with an average of 74.4 ± 4.9 . SH for clarite ranged from 82 to 92, with an average of 86.9 ± 2.7 . As clarite accounted for the larger population of measurement in the specimen, the distribution observed on the histogram is negatively skewed, showing a mode of 90.

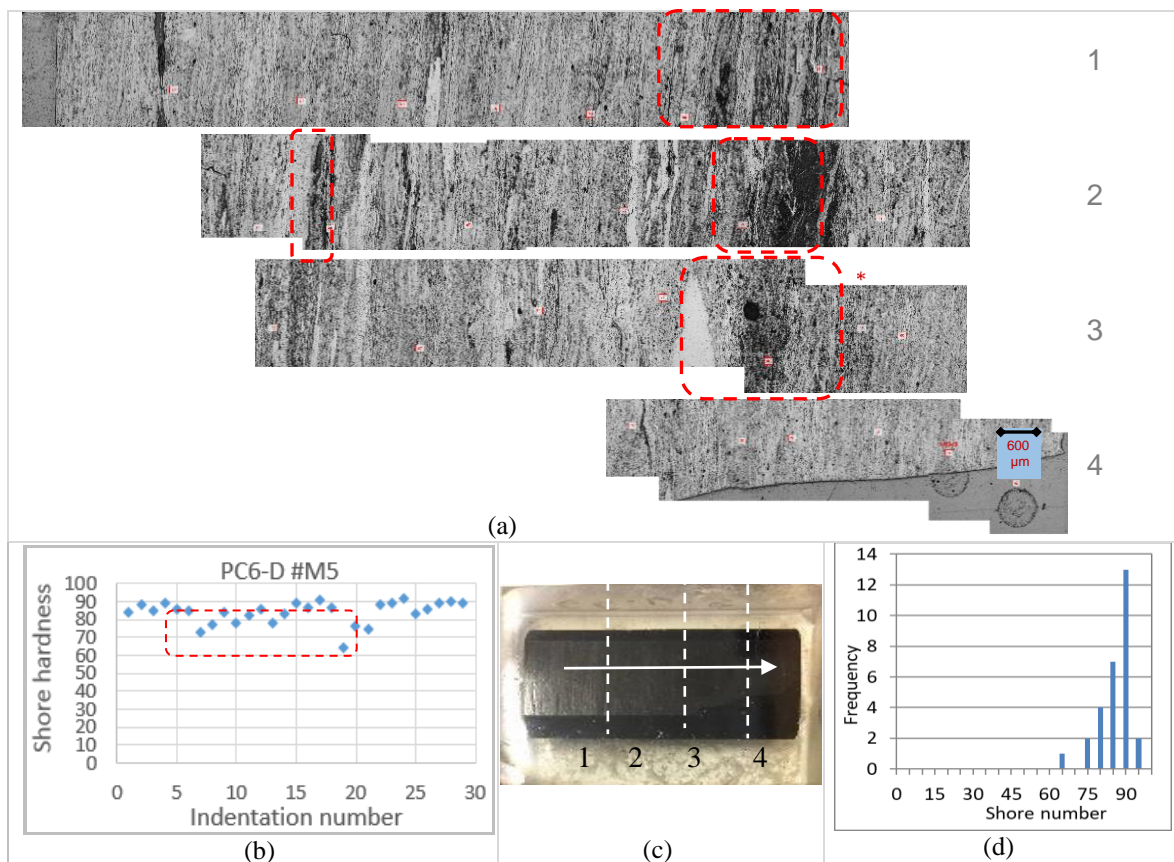


Figure 90 Ply PC6-D, specimen M5 tested for SH in a transect. a) photomicrographs 1, 2, 3, and 4 representing the sections across the whole specimen as per photo of polished coal surface (c); b) graphic sequence of indentations in terms of Shore hardness (SH); and d) SH values plotted on a histogram. Note that carbominerite areas highlighted on photomicrographs 1, 2, and 3 correspond to drop on SH values as observed in the graphic sequence of indentations.

Figure 91 shows specimen PC8-WB #M1, predominately comprised of clarite, with minor carbominerite. The distribution for PC8-WB #M1 is unimodal showing broadly symmetrical clustering. The data distribution for the sequence of indentations, indicates consistent SH along the specimen, due to clarite-dominant microlithotypes. SH values ranging from 74 to 88, with an average of 82.6 ± 3.4 .

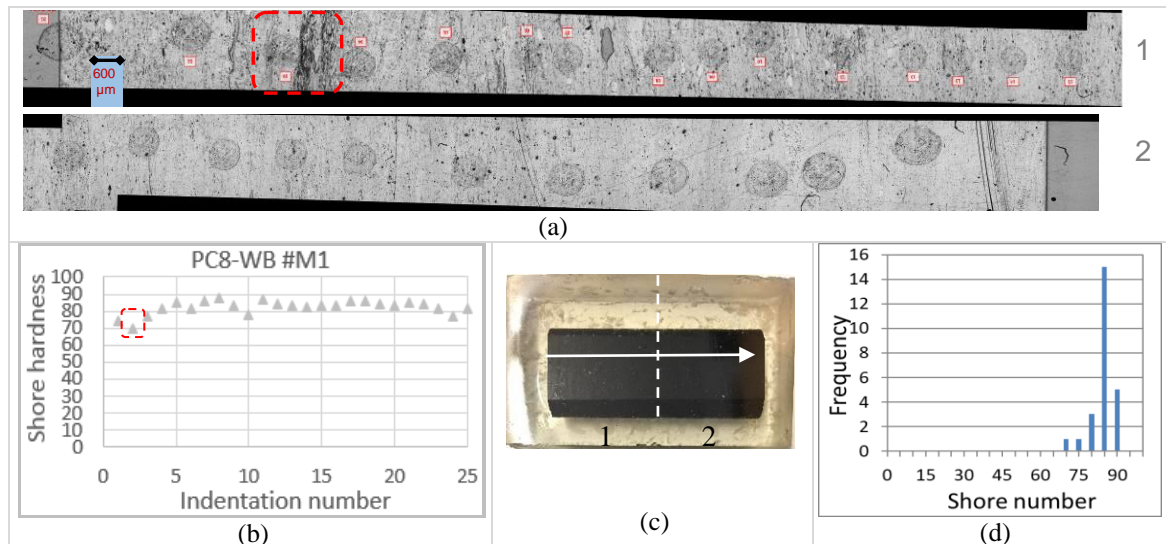


Figure 91 Ply PC8-WB, specimen M1 tested for SH in a transect. a) photomicrographs 1 and 2 representing the sections across the whole specimen as per photo of polished coal surface (c); b) graphic sequence of indentations in terms of SH; and d) SH values plotted on a histogram.

Figure 92 shows PC8-B #M2 comprised of carbominerite (43 %) and clarite (57 %). SH for clarite ranged from 76 to 89, with an average of 81.9 ± 3.7 . SH for carbominerite ranged from 51 to 71, average 63.9 ± 6.2 . The variation of SH for carbominerite is attributed to clay rich intervals (confirmed using Scanning Electron Microscope, SEM). Isolated mineral grains or cracks/fractures may have also contributed to lower SH values, as observed under the microscope. A bimodal distribution for PC8-B #M2 is observed in the histogram, reflecting the two dominant microlithotypes.

Overall, the results of transects illustrate a strong correlation between hardness and microlithotype (Figure 93).

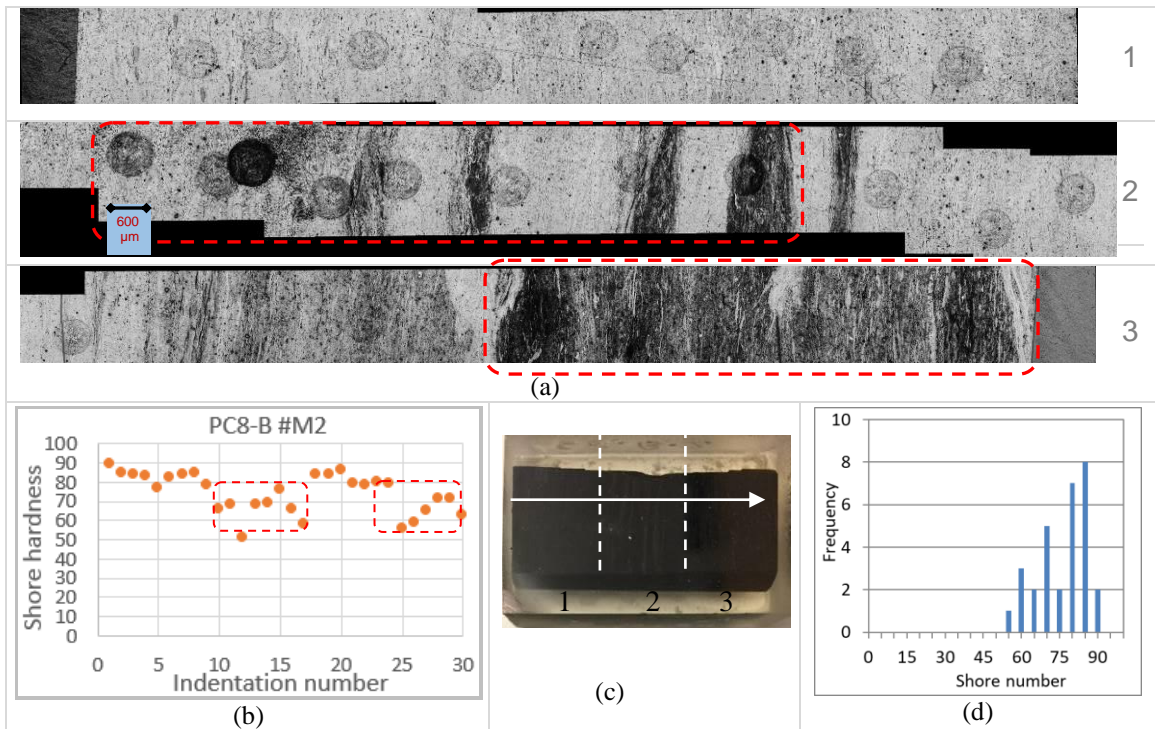


Figure 92 Ply PC8-B, specimen M2 tested for SH in a transect. a) photomicrographs 1, 2, and 3 representing the sections across the whole specimen as per photo of polished coal surface (c); b) graphic sequence of indentations in terms of SH; and d) SH values plotted on a histogram.

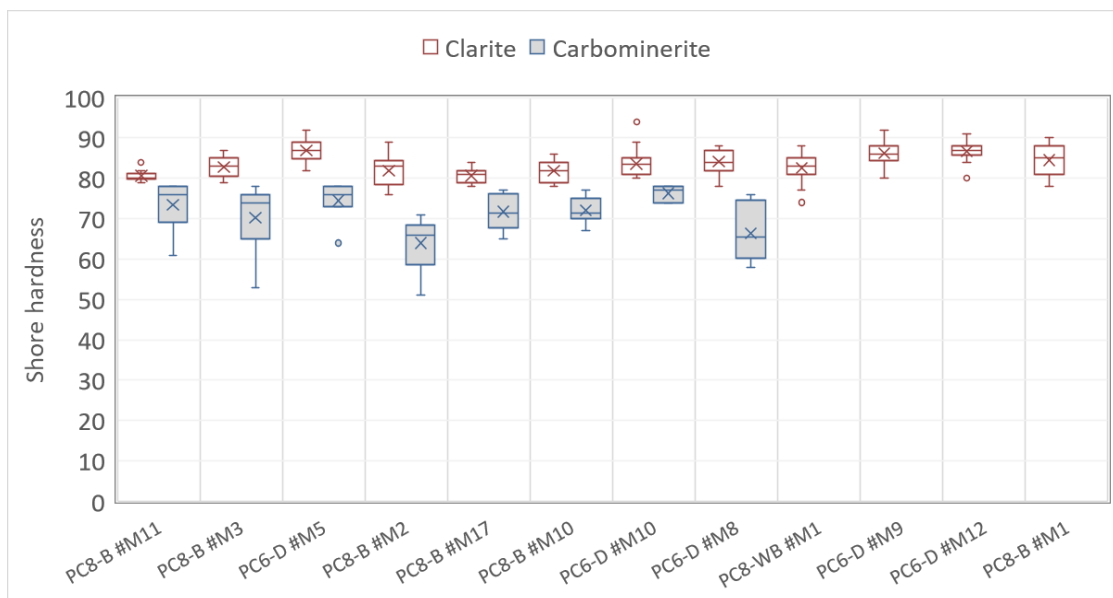


Figure 93 Shore hardness limits for clarite and carbominerite in fine controlled specimens from open cut mine.

6.3.2 SH behaviour of vitrite for specimens from the open cut mine

There is a lack of representative data for vitrite in the above specimens. According to Macmillan and Rickerby (1979), one reason coal hardness is difficult to determine, particularly when the individual coal macerals are very brittle, is because vitrite is very prone to form cracking and chipping around the indentations, and in cases of extensive elastic and/or inelastic recovery during unloading can produce a misleading result.

In the specimens PC6-D #M9 and PC8-B#M3, some thin vitrite bands were observed and indented. Because vitrite bands tend to present cracks, it is difficult to affirm if cracks/fractures occurred pre- or post-indentation. Nonetheless, vitrite observed in specimens PC6-D #M9 and PC8-B#M3, indicate that cracks and chips are exacerbated by multiple surrounding cracks and/or thick cracks/fractures, in addition to a slight overlapping indentation. The SH reached values of 71 and 77 on the vitrite for PC8-B#M3 and PC6-D #M9, respectively (Figure 94a, b). Overall, it seems that vitrite is more likely to propagate a crack than carbominerite or clarite.

PC8-B #6a shows a distinct vitrain band (approx. 4 mm thick), the specimen was tested and analysed for indentations performed inside this band only (i.e. selective indentation on vitrite). A population of eleven ($n = 11$) SH indentations were recorded and observed with photomicrographs. SH values of 56 and 58 were measured when the indenter reached a pre-existing crack which may have contributed to chipping observed on the specimen surface (Figure 94c). SH values of 74 and 82 showed spread/propagation of the cracking, and no chipping, as no fractures were observed proximal to the indented marks (Figure 94e). Other values of SH measured ($n = 7$) range from 61 to 71, where the majority of the indented marks were surrounding pre-existing fractures, some of them fairly opened. The cracks generated by the indentation appeared to propagate from the indentation, showing scattered breakage and crack growth (Figure 94d).

Overall, higher vitrinite (corresponding to vitrite microlithotype) content in coal, results in higher HGI (Hardgrove Grindability Index) (i.e. measurement of resistance to grinding coal, where the higher the HGI value, less elastic-plastic the coal bands behave and are easier to grind, as it cracks and fractures), consistent with the observations of this study. About 15 % of the indentations on vitrite showed a propagation of fractures, resulting in a higher SH (the higher the rebound) than for clarite-dominated specimens.

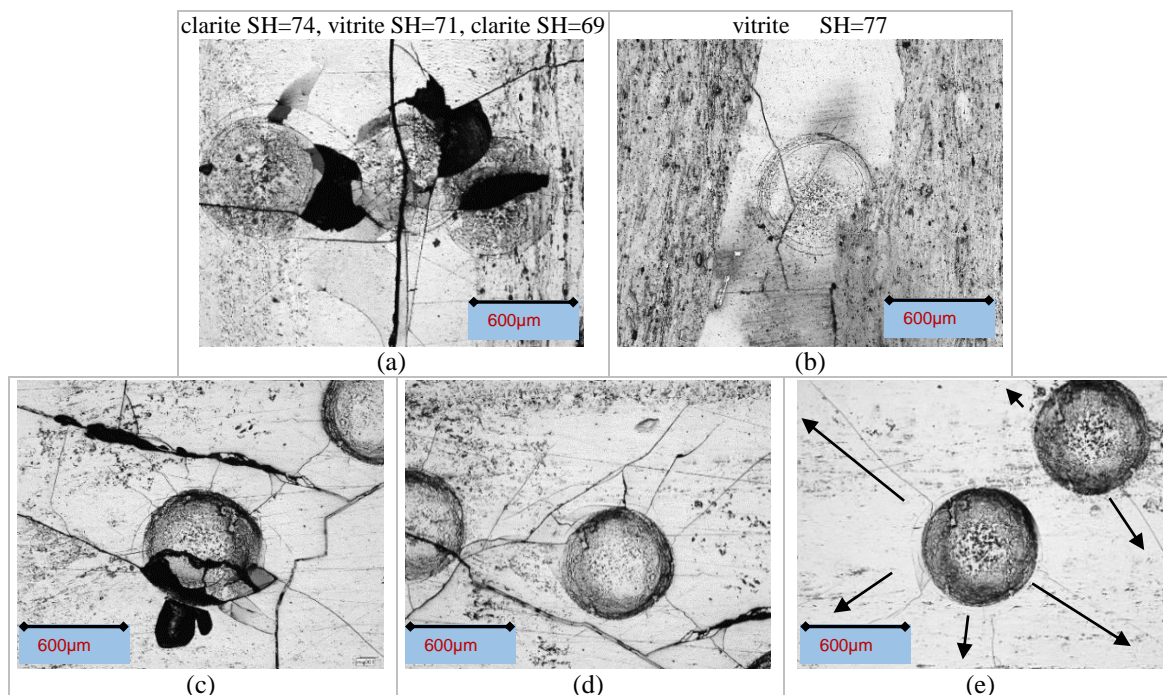


Figure 94 Representative photomicrographs of SH indentation on vitrite for the following specimens: a) PC8-B#M3; b) PC6-D #M9; c) PC8-B #6a, lower SH value; d) PC8-B #6a, medium SH value; and e) PC8-B #6a, higher SH value.

6.3.3 Correlation between hardness and microlithotype for specimens from borehole

Sub-bituminous coals samples with slightly lower reflectance were tested from exploration borehole, Guluguba-2, from 138 m to 486 m depth. The interpretation includes 30 specimens in total, where 2 specimens were tested using transects (GG-16 and GG-27), while the other 28 specimens were indented selectively by microlithotype.

For specimen GG-16, the microlithotype variability was observed using three transects parallel to each other, to ensure repeatability of results. The indentations represented a population of 59 SH values measured. Figure 95a shows the SH data for all three transects are quite similar, and present a bimodal distribution with modes at 60 and 90 (Figure 95b). As with open cut mine specimens, the SH data from these specimens indicate carbominerite showed lower SH values, 43 to 66 with average of 56.7 ± 5.9 , than the vitrite, 69 to 79 with average of 74.3 ± 3.8 and clarite, 80 to 93 with an average of 87.6 ± 3.3 (Figure 95c). Note the vitrite occurred in thin bands (<5 mm), and variability was sometimes caused by pre-existing fractures being indented (see small interval between two areas delineated in Figure 95d).

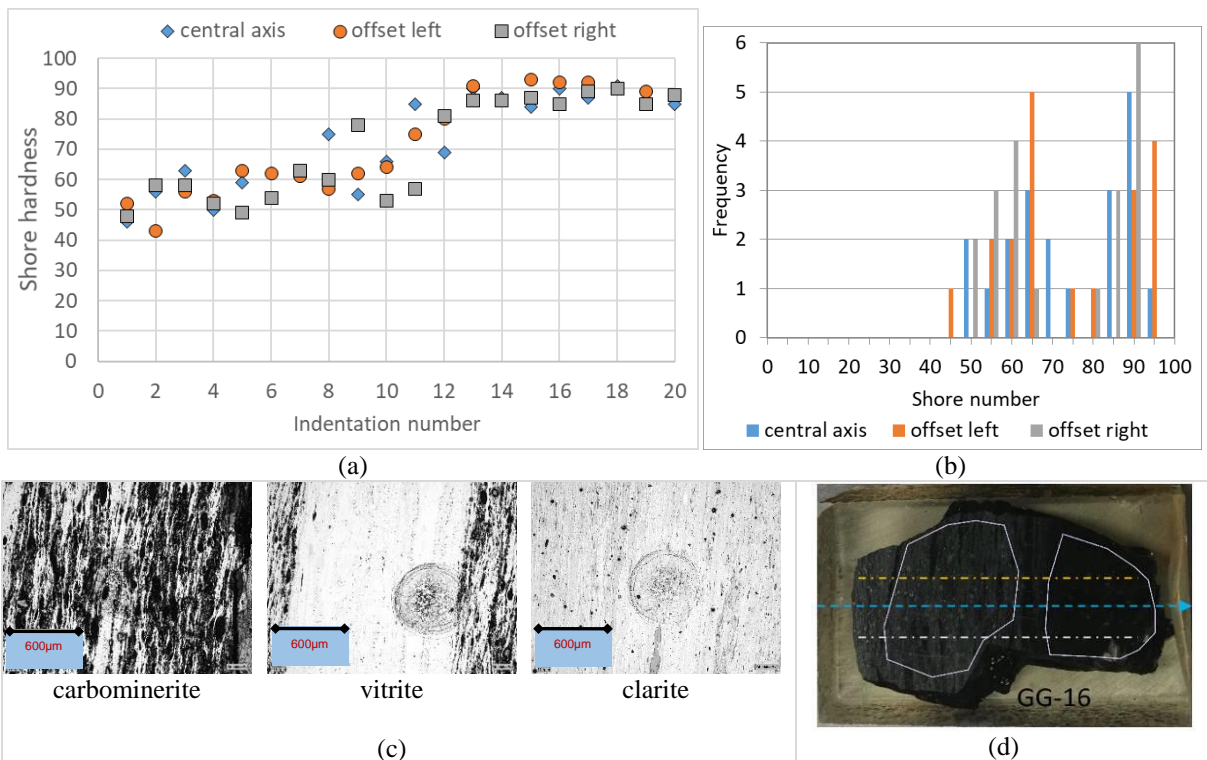


Figure 95 Guluguba-2, specimen GG-16, Taroom Coal Measures, 415.5m depth. a) graphic sequence of indentations in terms of SH for the transects; b) SH values plotted on a histogram; c) representative photomicrographs for visualization of microlithotype as it occurred along the transects; and d) the polished coal surface showing location of transects as well as distinct lithotypes delineated. Note that the blue transect follows along the specimens' central axis, then an orange one offsets the central axil towards the left side, while the light grey one offsets the central axil towards the right side.

The entire specimen GG-27 is a vitrain band with small cracks/fractures distributed across the polished surface. For GG-27, the coal variability was observed using four transects, three of them parallel to each other and one perpendicular, where the vitrite microlithotype could be tested. The indentations represented a population of 69 measurements. Results for this specimen are consistent with previous observations, but exhibit higher variation when indentations punch pre-existing cracks/fractures (Figure 96a, b). SH ranged from 29 to 75; average of 55.7 ± 10.7 . It was observed that the lower range values for SH (<50) correspond to indentations reaching large or open cracks/fractures (Figure 96c).

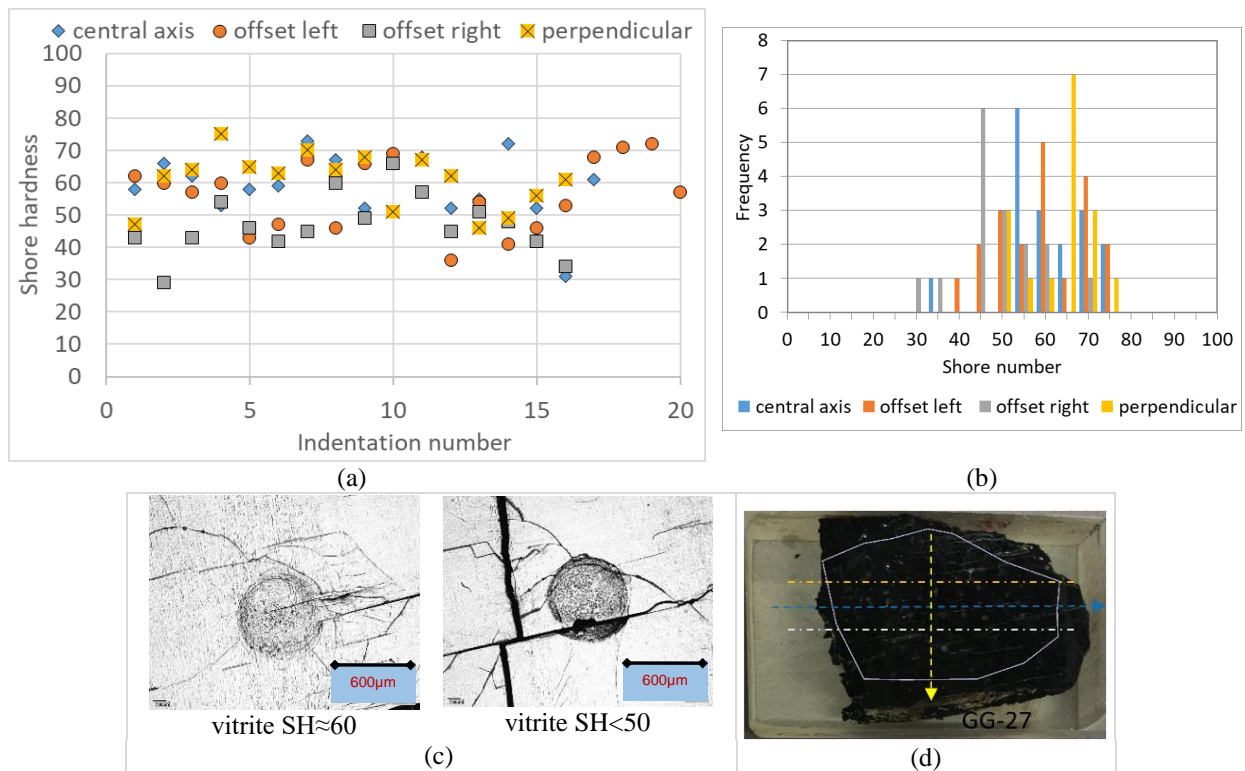


Figure 96 Guluguba-2, specimen GG-27 (unknown depth). a) graphic sequence of indentations in terms of SH for the transects; b) SH values plotted on a histogram; c) representative photomicrographs for visualization of microlithotype as it occurred along the transects; and d) the polished coal surface showing location of transects.

For Guluguba-2, a total of 24 specimens, from distinct depths, were tested for the clarite lithotype within a block (similar to Figure 89b). Figure 97 shows a box-and-whisker plot which summarizes the results observed for all SH values across specimens reaching the clarite. A gradual decrease of average SH values across indentations observed on clarite is attributed to distinct texture (mostly mineral matter) and/or integrity (cracks and fractures) which are not related to a distinct depth or stratigraphic interval.

For Guluguba-2, the SH values on clarite can be grouped as consistently hard (higher rebound, SH values >80) across 13 specimens. The SH ranged from 73 to 94, average of 84.5 ± 4.6 see Figure 97 for results from GG-18 until GG-21. The remaining specimens show an increase in the estimated mineral matter percentage and/or presence of cracks/fractures surrounding the indentations on clarite. Then, for those specimens the percentage estimation for mineral matter is based on visual observation using a comparison chart (Folk, 1951). SH ranged from 60 to 85, average of 74.8 ± 5.0 . The influence of mineral matter and fractures dropped the SH values by approx. 10, for results from GG-5 until GG-20 (Figure 1 as highlighted). Next, GG-24 shows an isolated case where various

thin vitrain bands are intersected with small cleats surrounding the indentations resulting in a relatively lower SH value. The results for GG-24 which correspond to an SH value of 69.7 on average and standard deviation of 3.7. Though Afonso (2014) observed that cleats appear to increase with depth for the sub-bituminous coal, no relationship of SH with depth can be expressed. Then, the final 4 specimens exhibit lower SH values for clarite ranged from 44 to 82.5, average of 65.1 ± 4.7). These values are attributed to increasing occurrence of cracks/fractures (last section highlighted in Figure 97).

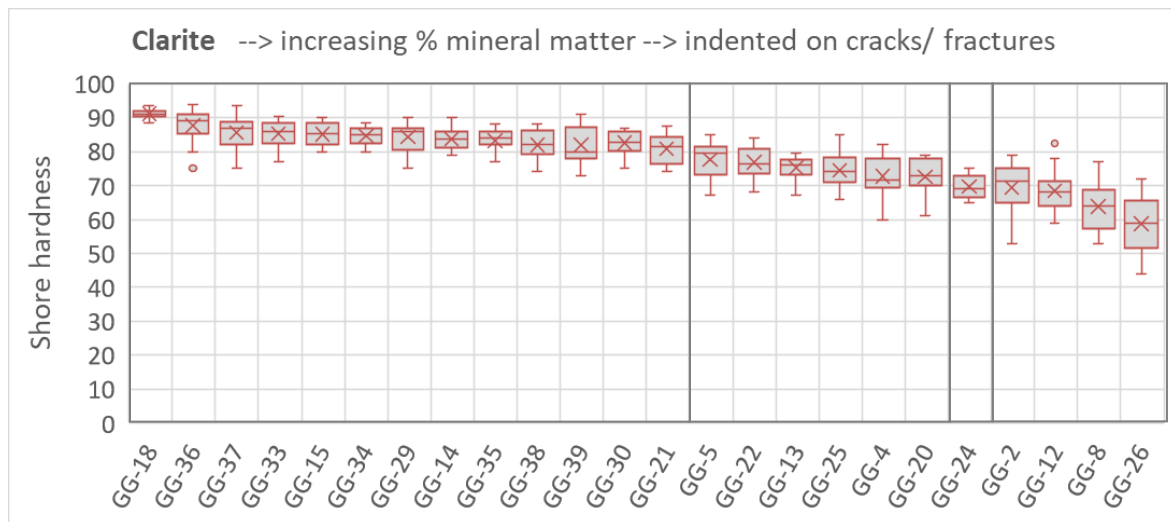


Figure 97 Shore hardness limits for clarite in selected lithotypes of specimens from borehole Guluguba-2. Cross symbols represent the average.

For Guluguba-2, only 3 specimens are used for the selected indentations on vitrite. The SH ranged from 52 to 83, average of 68.8 ± 6.8 on vitrite for tested specimens. Again, it is observed that the cracks influence the SH values measured (i.e. specimens with more cracks surrounded or reached by the indenter showed large variability).

SH values measured on Guluguba-2 carbominerite microlithotype indicate values ranging from 39 to 58, average of 47.7 ± 4.5 (again, SH measured for 3 specimens only). Note that SH values are much lower than observed for the open cut mine (average of 70.2 ± 6.8).

6.3.4 Comparison of SH values across specimens

From observing the summarised data for both open cut and borehole specimens, there is a clear, and consistent relationship between SH and microlithotype. The series of indentations made on the three microlithotypes (clarite, carbominerite, and vitrite) exhibit different values of yield strength/Young's modulus, therefore growth of fracture patterns is expected upon fracture

stimulation or loading. Table 12 indicates that there is a significant difference between the hardness of the different microlithotypes, particularly for specimens tested from the borehole than the open cut mine specimens, also indicating large variation within clarite-dominated microlithotypes. Therefore, it can be concluded that hardness is influenced by the composition that is inherited from the biochemical precursors (i.e. vegetation) and mineralogy of existing mineral matter of each microlithotypes.

Clarite can be really hard, like pure hardened high-carbon steel (SH equal to 82.3 ± 3.0). Clarite is the most heterogeneous microlithotype observed in this study, therefore its hardness must be the higher. The energy applied by the Shore scleroscope dissipates through the microlithotype heterogeneity and prevents fractures and cracks from propagating through the coal. In another microlithotype, the occurrence of clay minerals in the carbominerite absorbs the energy applied by the Shore scleroscope. While it might exhibit some indentation mark, evidence of fracture and crack propagation/ growth through the coal is less common. Last, the vitrite is the homogeneous microlithotype, and the applied energy cannot dissipate without changing the material characteristics. Chips surrounding the indentation and fracture propagation showing the crack growth onto vitrite are quite common. Also, because cleat systems can be developed on brighter vitrite, they might assist to create a pathway for fracture propagation, reducing the Shore hardness values.

The specimens from the open cut mine correspond to a reflectance of 0.5 % while those prepared from Guluguba-2 showed a reflectance range of 0.43-0.47 %. While photomicrographs displayed the differences in texture between both specimens' locations, the difference in rank (thermal maturity) which is still sub-bituminous (roughly for purpose of comparison) does not seem to be an issue. It is suggested that the SH values for vitrite and clarite microlithotypes at these locations are statistically the same, though Guluguba-2 is affected by clay rich (mineral matter) and fractures (natural and/or pre-existing). The carbominerite is slightly softer in Guluguba-2 which again seemed be an influence of clay rich minerals where Guluguba-2 tends to comprise the highest end (percentage) of mineral matter.

Figure 98 shows the SH for all the specimens tested in this study against the plot from Klawitter et al. (2015) (both performed on polished coal surface confined into epoxy blocks, using same SSRH equipment). Note this plot consider the average SH by microlithotype rather than an average of random SH measurements (Klawitter et al., 2015). The overall range confirms an increase of SH for low rank coals, but also shows them to be very hard and highly variable. This is also visible in the

indentations left from the test. The tables summarizing the SH for all specimens observed including the depth sequence if applicable; photos of the polished coal surface showing the selective areas delineated; and photomicrographs of representative microlithotypes can be found in the Appendix III.

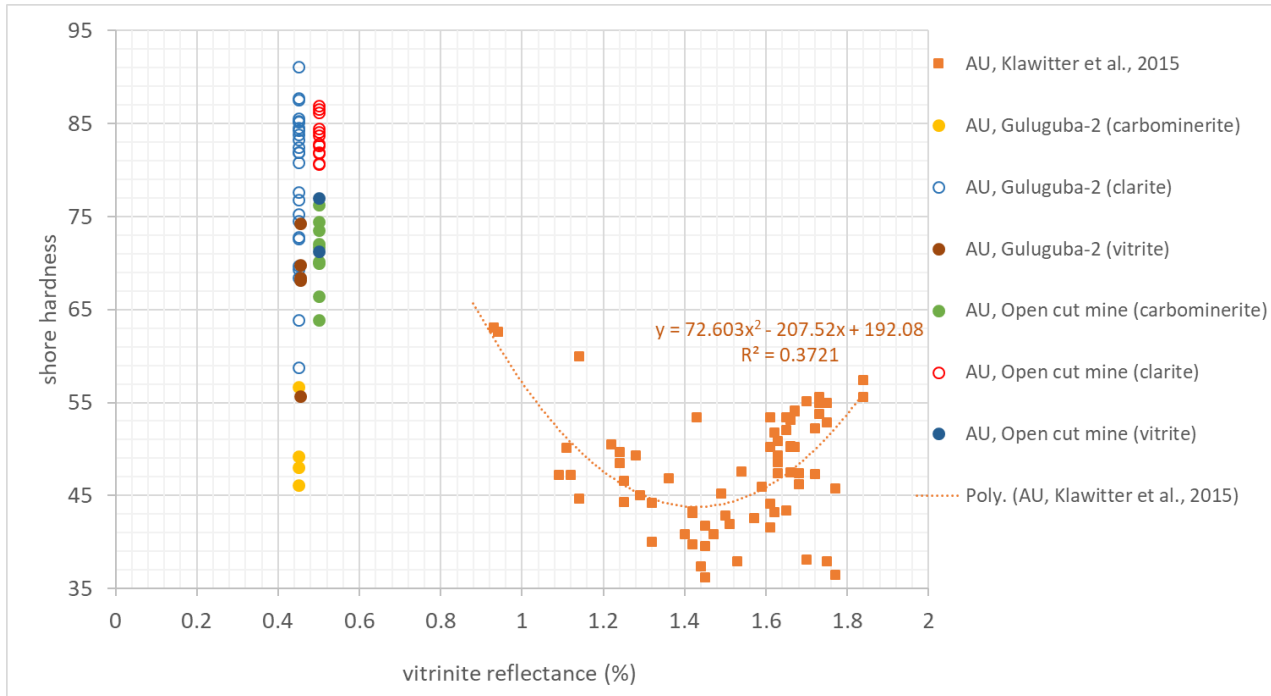


Figure 98 Shore hardness for specimens tested in this study compared with Klawitter et al. (2015) database.

6.4 CONCLUSIONS AND RECOMENDATIONS

This work addressed the hardness response of the microlithotype in sub-bituminous collected from two locations (open cut mine and borehole) for low rank sub-bituminous coal. Three microlithotypes were identified for the sub-bituminous specimens tested: vitrite, clarite and carbominerite. Quantification of the micromechanical properties is possible using such a simple test, and opportunities to improve fracture propagation can be further explored.

Results suggested that a strong correlation exists between microlithotype and hardness when interpreting thin weak and bedding plane surface of sub-bituminous coal. Specifically,

1. The microstructural heterogeneity and anisotropy of the coal can be captured by the variation in hardness when transects or selective measurements are performed.

2. The variation in Shore Hardness (SH) is a function of the presence of cleats, cracks/fractures, different textures and mineral matter.
3. The harder microlithotype is clarite, followed by vitrite, and then carbominerite. The Shore hardness values decrease from clarite with an increase in mineral matter towards carbominerite. However, measurements of Shore hardness by itself give no evidence about micro-brittle (vitrite) or micro-ductile (carbominerite) behaviour of coal. It happens that vitrite displays purely brittle behaviour, while carbominerite has a ductile component.
4. The differences between microlithotypes are not small enough to be ignored in numerical modelling simulations, as the variation occur at centimetre to millimetre scale it has implications for fracture propagation across bands in a coal seam.

Further studies are required to determine how these properties can be better represented and upscaled from the microstructural observations to the rock mass depending on the numerical modelling approach and aim. Lastly, the band thickness distributions were not accounted for in this study and could be the subject of further work. Also, a comparison between similar microlithotype for other ranks would be of interest to describe the hardness behaviour by microlithotype across rank.

SYNTHESIS, CONCLUSIONS AND FUTURE WORK

7.1 SUMMARY AND SIGNIFICANCE

A number of non-conventional experimental laboratory tests were performed, to attend the need of the coal seam gas (CSG) industry, to test small size specimens as plugs from core or as chips/particles from exploration drilling. The tests selected from mineral processing and rock mechanics disciplines, allow for estimation of hardness, fracture energy, toughness, and strength, which were thought applicable to fracture stimulation of CSG reservoirs. Output from the tests were validated and compared to mechanical properties available in literature datasets, and the successes and pitfalls of each test were pointed out.

It is relevant that numerical modelling to predict the geomechanical behaviour of coal during gas extraction or mining design and stability, can only be achieved by understanding the mechanical properties of the coal at different scales. Whereas a well-known approach is to treat the rock mass as a large volume of indistinct rock, this thesis explored the anisotropic behaviour of coal strength as a function of its different lithotypes, microlithotypes, and inter-bandings of stone. Laboratory testing of individual lithotypes, regardless of the test, resulted in significant differences in strength and hardness, but when looking at the additivity or upscaling of the results to larger rock masses, these differences tend to decline. In other words, the rock mass concept is a fair reliable approach for some situations where the coal behaves “en masse”. Therefore, testing large coal specimens must lead to a better understand whether pillars or boreholes continue to deform and take load without reaching a defined peak strength. When looking at the phenomenon of pillars and/or thin coal seams with very large width-to-height ratios, these rocks (pillars or seams) are virtually ‘indestructible’ and the stability of the support structure (roof, coal pillar, and floor) is governed by the pillar deformation and the strength of the surrounding strata (Wagner and Madden, 1984). In

this context, one should take advantage of testing smaller specimens of coal as well as the surrounding rock which is often missed. Then, scaling from the laboratory, considering that a sequence of increasing size is established, to any other scale including the rock mass can be successful. Justification for any concern about not strictly following the standards of specimens' preparation related to rock 'grain size' rely on the fact that coal has more fibre than grains, and about the specimen mass of rock tested, clarification is made that the recommended aspect ratio applies. However, where specific layers are targeted for fracture stimulation, the rock mass approach is insufficient to predict induced fracture propagation.

In the gas fields of low rank, sub-bituminous coal in the Surat-Clarence-Moreton Basin, Australia, the seams and plies are considered as 'indestructible' thin pillars with poor cleats developed, and pervasive, wide joints (as observed at mine exposures). The coal seams in this Basin are comprised of multiple thin layers that vary from millimetres to decimetres over some metres or tens of metres. The seams show both brittle and ductile contrasting behaviours interbedded by distinct combination of coal lithologies and rocks including sandstone, mudstone, and claystone. In this scenario, the mechanical properties need to be characterized by different methods to capture the heterogeneity of the seams at the relevant scale of interest. In addition to logistical problems of getting intact coal core specimens or cutting disks in an inherently fractured material, the number of tests and the range of coal lithotypes that comprise a seam at a given rank is onerous and potentially not feasible. While the common test for rock is the Uniaxial Compressive Strength (UCS), for some applications, understanding the tensile behaviour with SILC (Short Impact Load Cell) and hardness with SSRH (Shore Scleroscope Rebound Hardness) are very important.

In this thesis, the information from UCS to derive the intact strength of coal and fabricated material was investigated, also the correlations between tensile and compressive strength were observed. The amount of energy required to induce fracture in coal can be found, while fracture in the vicinity of sandstone and mudstone can be evaluated for extension damage. Textural properties manifested in the microlithotypes might control fracture distributions and patterns resulting in a diverse fracture network propagation within the formation. It is anticipated that the fracturing propagation relative to the stimulation should be controlled by the rock strength, the amount of energy injected, the presence of microlithotypes, the natural fractures and other geological discontinuities. The results of this thesis are promising for future applications, and might be utilized in simulation models, providing more reliable estimates of hydraulic fracture and borehole stability in CSG reservoirs.

7.2 MAIN FINDINGS FROM THIS RESEARCH

Chapter 3: Mini-cylinder specimens scaled

The validity of testing mini-cylinder specimens, the Young's modulus, the effect of fractures on strength results, and the scaling properties of coal were all successfully demonstrated in this thesis. Mini-cylinder specimens of coal from increasing, non-standard sizes (between 9.3 and 22.6 mm in diameter) were tested for UCS, where the resistance of a material to breaking under compression showed the fracture propagation during loading. While the aim was to test mini-cylinder specimens to be intact, the non-intact (visible fractures) could not be avoided, and they also retain useful information.

The specimens with pre-existing fractures are the weaker, while the ones classified as 'intact' (but having flaws and cleats), still present some variation in the results which is expected. Despite the strong correlation with size, for both the sub-bituminous coal of mini-cylinder specimens and the medium-rank coal from standard to large specimens, when scaled to the rock mass the differences attributable to type and to rank might reduce; hence averaged "coal values" may suffice. It triggers that upscaling by itself does not allow for characterisation of the seams in the Surat Basin, albeit not all tens of metres were captured in the testing. The size effect for specimen strength is significant and different strength should be assigned based not so much on lithotype, but on the thickness of the coal and rock layers. Whether the assignment of different strengths by coal and rock layers would result in diminished returns for effort was not tested, and this is recommended for future work, probably via numerical modelling. Furthermore, the observation of failure mode with specimens failing in a dynamic brittle fashion while others did not show such explosive/abrupt behaviour, still deserves further attention in modelling. Unfortunately, the relationship between strength and maceral subgroup distribution showed inconclusive results for UCS, as the presence of fractures was more important to failure. To extract gas, the rock should fail in tension (not in compression), and a relationship between tensile and compression strength for low rank coal needed to be established, therefore the interest at using the impact load cell for further characterisation.

Chapter 4: A test of fracture, shape, and size using 3D-printed sandstone

3D-printed sandstone (3DP), a fabricated homogeneous rock was chosen to test the repeatability and performance of the SILC test, and to verify assumptions and pre-established calculations for sphere and cylinder-shaped specimens without the influence of flaws. The methodology and

calculations for the SILC test (Tavares, 1997; Bonfils, 2017) are based on specimen shape contact, the Hertzian impact was confirmed on specimens that did not fail. The SILC test can estimate tensile strength and fracture energy by a dynamic impact against small single particles and/or shaped specimens. By removing the intrinsic material variability, the influence of specimen size, shape, and fabric orientation relative to the impact was investigated. The impact conditions were the same for all specimens except for larger diameter of sphere-type specimens that required an increased stress.

Fundamentally, the fracture initiated, in shear, in the top loading of the specimens and grows in tension, while the fragmentation is influenced by the specimen shape. Different shaped specimens lead for some variation in the results which is independent of the rock material, also differences seemed to increase with an increase of the specimen size. When specific fracture energy is estimated from SILC there is a significant difference in the property attributed to shape, perhaps due to a dependence on grain size. The use of shaped specimens highlights the need to develop standards for SILC in order to guarantee a single outcome that can be comparable. For instance, it is suggested that the ratio variation 0.9:1 to 1.1:1 should be adopted as limits for mini-core specimens tested on SILC, as part of the standard procedures. The 3DP was also tested for UCS, then compared to data from literature (Hodder, 2017) and real sandstone (Hawkins, 1998). This outcome also confirmed that UCS can be successfully estimated using mini-core specimens. The 3DP increases in strength for all sizes tested. Following that, the relationship between the average ultimate tensile and the compressive strengths of 3DP derived from UCS and SILC test, seems concordant with the literature. This confirmation lends confidence to the use of SILC tests on natural rocks to capture geomechanical properties.

Chapter 5: SILC on coal and mudstone

Coal (complex heterogeneous rock of brittle behaviour) and mudstone (ductile behaviour rock) were tested on SILC, to answer questions about fracture propagation across seams, tensile strength as well as specific fracture energy. Capturing the differences between lithotypes and lithology of distinct thickness revealed the contrasts of materials behaviour, assigned by size and recorded for sub-bituminous coals from the Surat Basin. The coal breakage is influenced by the specimen shape, besides the presence of fractures, mineral grains, and lithotype bands, all together induce some microscopic deviation of the crack path. Overall, sub-bituminous coal specimens tested on SILC exhibited a deformation mechanism type cataclasis which is abrupt, powerful energy release with many fragments of very irregular surface being generated. The properties of Young's modulus

(‘apparent’ stiffness) were shown to be influenced by the impact conditions on SILC which was not expected, therefore calculations for cylinder-shaped specimens need to be corrected. The validity of fracture force, specific fracture energy, and tensile strength is indifferent (or independent) to the test impact conditions. It was also observed that specific fracture energy from SILC, which can be correlated to fracture toughness, did not show significant variation or dependence by shape when testing heterogeneous rock. The coal plies were tested for UCS and SILC (Chapter 1 & 5), both tests showed that PC8WB > PC6-D > PC8-B in terms of strength, and this is interpreted to arise from their composition and texture. It is also thought that the presence of clays in the PC8-WB allows more compression than does the dull and bright lithotypes. Although the differences of strength values between all three plies are not very expressive, the SILC test seemed to capture it effectively. Also, SILC captured well the influence of coal bedding orientation relative to impact conditions (or fracture stimulation). The relationship between the average ultimate tensile and the compressive strengths of low rank can be derived. Another valuable outcome from SILC was the graphic representation of fracture energy plotted for increasing specimen size, as it provides interpretation for varied seam thickness. Overall, the energy required to fracture the coal is much lower than that necessary to fracture a sandstone or a mudstone specimen of similar thickness. For seams comprising multiple thinner beds and layers, by reducing the scale of observation allows for better interpretation.

Chapter 6: Lithotypes and microlithotypes matter

Because the coal’s surface varies with different bands, the texture and composition of these as microlithotypes was explored. To measure and observe any physical change at this scale, an assessment for individual values of coal hardness was conducted with the Shore Scleroscope Rebound Hardness (SSRH or SH). It turned out quite evident that both brittle and ductile behaviours observed on sub-bituminous coal are conditioned by microlithotypes, and these ultimately manifest at larger scales into lithotypes. Also, the hardness is also sensible to the presence of natural and induced fractures. The three microlithotypes identified for the sub-bituminous lithotype specimens were: (i) Vitrite (pure vitrain) was the less frequent microlithotype in the specimens tested, but of dominant brittle behaviour as large tension cracks tend to develop on the surface indented (i.e., irradiate, spread out and get connected), while fragments might move apart. The deformation mechanism of vitrite was the cataclasis, a kind of explosive/abrupt fracture which is very sensitive to pressure. (ii) Carbominerite (vitrite plus mineral matter) was the moderately frequent microlithotype in the specimens tested, and tend to behave like a ductile

material where the indenter could be pushed inside the specimen for longer; the indentation seemed to respond as a plastic flow deformation. After indented, perhaps due to a redistribution of grain minerals, a dark indentation mark became imprinted (i.e. no cracks or chips tend to develop), which was more evident when the percentage of mineral matter was at the lower limits ($\approx 20\%$). The minerals were most likely to be clay, as observed with the scanning electron microscope (SEM). (iii) Clarite (vitrinite plus liptinite $>95\%$) was the most frequent microlithotype, it is the hardest between those tested. It was observed that an indentation on clarite surrounded by very thin vitrite bands containing non-persistent cleats, showed a drop in the SH measurements (i.e., influence on hardness). Notice that, the microlithotypes carbominerite and clarite can both be deformed, while the vitrite is simple brittle. Moreover, the complexity of sub-bituminous coal was also attributed to the fact that neighbours microlithotypes maybe of comparable hardness (e.g. clarite and vitrite) but completely opposite fracture mode that occur in centimetre to millimetre scale.

7.3 CONCLUDING REMARKS

The key points arising from this thesis are:

- Pre-existing fractures, either natural or induced by specimen preparation, influence the properties results as observed on the experimental studies for compressive strength.
- The mini-cylinder specimens of coal tested at UCS showed high strength which decreases as the specimens' size increases. It is expected that same dimensions will be even strong under confining stresses.
- The mini-cylinder specimens are able to emulate/ scale to standard or large cores following a power regression.
- The macroscopic failure mode of coal might be influenced by the microscopic behaviour, banding texture and/or pattern locations (high stress regions versus low strain in the centre) of the specimens. Following on that, the combination of microlithotypes in those locations of mini-cylinder specimens should be the one accounting for variation on strength results.
- 3D-printed sandstone (3DP) behaved similar to smaller specimens of real sandstone rock, following literature database in terms of compressive uniaxial strength.
- Proposed calculations for SILC test are unchanged, but Young's modulus ('apparent' stiffness) for cylinder-shaped specimens needs further consideration as observed on 3DP.

- The specimen shape influences the material properties results on SILC, as demonstrated with 3DP, which produced slightly distinct results, moreover when specimens increase in size.
- SILC captures the effects of material microstructure. Breakage of 3DP showed a brittle fracture controlled by the crack initiation and propagation, resulting in less fragmentation when compared with coal which has much complex microstructure and natural fractures.
- Fracture energy obtained on SILC is relevant for the CSG while the crack propagation on coal appears to be strongly conditioned by microlithotype.
- When testing irregular single-particles, it is recommended that measurements of height and length dimensions be taken into consideration for calculations on SILC tests.
- The coal anisotropic behaviour is observed on laboratory experiment with SILC when testing specimens with distinct orientation of bedding planes and cleats. A significant variation on behaviour occurred which have implications for hydraulic fracturing stimulation.
- 3DP specimens tested on SILC showed a shape dependency when specific fracture energy is estimated, whereas for heterogeneous specimens no significant shape dependency is observed which may be due the grain size.
- Though coal contains more macerals (fibres) than minerals (grains), the Surat Basin coals showed quite good representation of grains in the form of mineral matter which changes the coal behaviour when compared to other basins and rank.
- The coal behaviour is influenced by changes on centimetre to millimetre basis, as observed on distinct microlithotypes. The hardness measurements might be of similar magnitude but different strain response to indentation. Therefore, brittleness and ductility occur together at low rank and are inherent of rheological characteristics of coal in the Surat Basin.
- Hardness by microlithotype might be a more appropriate measurement to understand coal rather than elastic deformation.
- It is difficult to precisely work out the additivity of microlithotypes and their degree of heterogeneous deformation to produce a single strength value in a UCS tests.
- Distinct failure mode, hardness, strength, and fracture energy of coal are conditioned by the wide spectrum of maceral and subgroup maceral inside the specimens observed, in addition to the amount of natural or induced fractures on specimens of low rank sub-bituminous coal.

7.4 RECOMMENDATIONS FOR FUTURE WORK

This research showed experimental observations for small specimens where the low rank coal behaviour is still complex in the Surat Clarence-Moreton basins. The mechanical properties of the formation are very critical for fracture stimulation, also influenced by the contrast of soft and competent materials at thin intervals. Despite the experimental work does not consider the effect of confining stress and the pore-pressure changes within the seams (i.e. sorption-induced coal matrix swelling/shrinkage), it is relevant to understand the coal brittle and ductile behaviour when fracture arise. Some technical challenges remain unresolved particularly in the area of coal rock behaviour in laboratory and require further investigation, some of which are listed below:

- A study to consider the impact of scale on coal mechanical properties and how to better represent the scale impact when inputting parameters values into numerical models.
- While advanced numerical modelling might be available, development of robust models that can deal with the complexity of coal and the interbedded rock for gas simulation, including more realistic constitutive models might be required for optimization of fracture stimulation.
- Application of the experimental procedures (UCS, SILC, and SSRH) is recommended for other ranks, in order to improve understanding on coal heterogeneity at similar scale.
- It might be suggested that small portions of vitrite (>10% of the specimen) can contribute to trigger a deformation mechanism type cataclasis as observed in all tests (UCS, SILC, and SSRH), but further investigation is still needed.
- It is suggested that macroscopic failure mode and strength of coal might be influenced by the location/concentration of specific microlithotypes in mini-cylinders. Therefore, an investigation to map the microlithotypes of each specimen before conducting a UCS test might help to draw some conclusions.
- Variation in deformation of thin coal seams can be attributed to the interbedded material. Further studies for characterization of interbedded material utilizing UCS, SILC, and SSRH, wherever applicable for the rock type, is recommended.
- There are more to be explored utilizing the microlithotypes. Because the vitrite tend to be more intensely fractured, it would be of interest an observation of the fracture propagation displaced along the bedding planes of mudstone and sandstone layers. Further studies considering the

rock-type assemblage (e.g. soft/hard or soft/ soft) and the fracture growth are strongly suggested.

- It is recommended that the rebound location on the coal specimen be further investigated using calibrations of ultrasonic wave speeds to verify the influence of different microlithotypes on varied of coal specimens.

List of References

- AFONSO, J.M.S., 2014. Electrical resistivity measurements in coal: assessment of coal-bed methane content, reserves and coal permeability. PhD thesis. Leicester: The University of Leicester
- AL JASSAR S.H. and HAWKINS A.B., 1977. Some geotechnical properties of the main carbonate lithologies within the Carboniferous Limestone Formation of the Clifton Gorge, Bristol. In: Proceedings of the Conference of Rock Engineering, Newcastle upon Tyne, 393-405
- AL JASSAR S.H. and HAWKINS A.B., 1979. Geotechnical properties of the Carboniferous Limestone of the Bristol area – the influence of petrography and chemistry. 4th Conference International Society of Rock Mechanics, Montreaux, 1, 3-14
- ALTINDAG R. and GÜNEY A. 2006. ISRM suggested method for determining the Shore hardness value for rock. International Journal of Rock Mechanics and Mining Sciences. 43, 19-22
- ALTINDAG, R. and GUNAY, A., 2010. Predicting the relationships between brittleness and mechanical properties (UCS, TS and SH) of rocks. Scientific research and essays, 5(16), 2107-2118
- AMERICAN SOCIETY FOR TESTING AND MATERIALS, 1985. ASTM D4543. Standard practice for preparing rock core specimens and determining dimensional and shape tolerances
- AMERICAN SOCIETY FOR TESTING AND MATERIALS, 1991. ASTM D2938-86/95. Standard test method for unconfined compressive strength of intact rock core specimens
- AMERICAN SOCIETY FOR TESTING AND MATERIALS, 2000. ASTM D4543-85. Practice for preparing rock core specimens and determining dimensional and shape tolerances
- AMERICAN SOCIETY FOR TESTING AND MATERIALS, 2008. ASTM D3967-08. Standard Test Method for Splitting Tensile Strength of Intact Rock Core Specimens
- AMERICAN SOCIETY FOR TESTING AND MATERIALS, 2009. ASTM E11. Standard specification for woven wire test sieve cloth and test sieves

- AMERICAN SOCIETY FOR TESTING AND MATERIALS, 2013. ASTM D7012-13. Standard Test Methods for Compressive Strength and Elastic Moduli of Intact Rock Core Specimens under Varying States of Stress and Temperatures. West Conshohocken, PA
- AMMOSOV, I.I. and EREMIN, I.V., 1963. Fracturing in Coal. Israel Program for Scientific Translations 112
- ANTONYUK, S., TOMAS, J., HEINRICH, S., and LOTHAR MORL, L., 2005. Breakage behaviour of spherical granulates by compression. Chem. Eng. Sci. 60, 4031-4044
- APPEA website accessed 2019. https://www.appea.com.au/wp-content/uploads/2019/06/APPEA_Key-Statistics_2019.pdf
- ARBIN, E.Jr. and MURPHY, G., 1953. Correlation of Vickers hardness number, modulus of elasticity, and the yield strength for ductile metals. Ames Laboratory ISC Technical Reports. 50. http://lib.dr.iastate.edu/ameslab_iscreports/50
- ATTEWELL, P.B. and SANDSFORD, M.R., 1974. Intrinsic shear strength of a brittle anisotropic rock. International Journal of Rock Mechanics and Mining Sciences and Geomechanics Abstracts, 11, 423-430
- AUSTRALIAN GOVERNMENT - DEPARTMENT OF ENVIRONMENT AND ENERGY – website accessed 2019. <http://www.environment.gov.au/system/files/pages/63b569ff-ae63-4d7b-be54-16f2e79900e0/files/nga-factsheet7.pdf>
- BAILEY, J.G. and HODSON, A., 1994. The effect of coal grindability on pulverised fuel combustion. Proceedings of the 6th Australian Coal Science Conference, Newcastle, AIE, Australia, 40-47
- BARTON, W.A., CONDIE, D.J., and LYNCH, L.J., 1994. Coal grindability: relationships with coal composition and structure. Proceedings of the 6th Australian Coal Science Conference, Newcastle, AIE, Australia, 55-64
- BASU, A., MISHRA, D.A., and ROYCHOWDHURY, K., 2013. Rock failure modes under uniaxial compression, Brazilian, and point load tests. Bulletin of Engineering Geology and the Environment. 72 (3-4), 457-475
- BAUMGARDT, S., BUSS, B., MAY, P. and SCHUBERT, H., 1975. On the comparison of results in single grain crushing under different kinds of load. Proceedings of the 11th International Mineral Processing Congress. Instituto di Arte Mineraria e Preparazione dei Minerali, Cagliari, Sardinia. 1-32
- BEARMAN, R.A., PINE, R.J. and WILLS, B.A., 1989. Use of fracture toughness testing in characterizing the comminution potential of rock. Proceedings of MMIj/IMM Joint Symposium, Kyoto, 161-180
- BIENIAWSKI, Z.T., 1967a. Mechanism of brittle fracture of rock. Part I. Theory of the fracture process; Part II. Experimental studies; Part III. Fracture in tension and under long-term loading. International Journal of Rock Mechanics and Mining. 4, 395-430
- BIENIAWSKI, Z.T., 1967b. Mechanism of brittle fracture of rock, D.Sc. (Eng.) Thesis, University of Pretoria, August 1967
- BIENIAWSKI, Z.T., 1968a. The effect of specimen size on compressive strength of coal. International Journal of Rock Mechanics and Mining Sciences and Geomechanics Abstracts, 5 (4), 325-35
- BIENIAWSKI, Z.T., 1968b. In situ strength and deformation characteristics of coal. Engineering Geology. 2, 325-340

- BIENIAWSKI, Z.T. and VAN HEERDEN W.L., 1975. The significance of in situ tests on large rock specimens. *International Journal of Rock Mechanics and Mining Sciences and Geomechanics Abstracts*, 12 (4), 101-13
- BIENIAWSKI, Z.T. and BAUER, J., 1982. Discussion of empirical strength criterion for rock masses. *Journal of Geotechnical Engineering Division. ASCE*. 108 (4), 670-673
- BIENIAWSKI, Z.T., 1984. *Rock mechanics design in mining and tunneling*. A.A. Balkema, Rotterdam, 272
- BOMBOLAKIS, E.G., 1964. Photoelastic investigation of brittle crack growth within a field of uniaxial compression. *Tectonophysics* 1, 343-351
- BONFILS, B., 2017. Quantifying of impact breakage of cylindrical rock particles on an impact load cell. *International Journal of Mineral Processing*. 161, 1-6
- BOURGEOIS, F.S. and BANINI, G.A., 2002. A portable load cell for in-situ ore impact breakage testing. *International Journal of Mineral Processing*. 65 (1), 31-54
- BRACE, W.F., 1960. An extension of the Griffith theory of fracture to rocks. *Journal of Geophysical Research*. 65, 3477-3480
- BRACE, W.F., 1964. Brittle fracture of rocks. In: Judd WR (ed) *State of stress in the Earth's crust*. American Elsevier, New York, 111-174
- BRACE, W.F. and BOMBOLAKIS, E.G., 1963. A note on brittle crack growth in compression. *Journal of Geophysical Research*. 68, 3709-3713
- BRACE, W.F., WALSH, J.B., and FRANGOS, W.T., 1968. Permeability of granite under high pressure. *Journal of Geophysical Research*. <https://doi.org/10.1029/JB073i006p02225>
- BRADY, B.H.G. and BROWN, E.T., 1985. *Rock mechanics for underground mining*. London: George Allen and Unwin
- BRIDGMAN, P.W., 1949. Volume changes in the plastic stages of simple compression. *Journal of Applied Physics*. 20, 1241-1251
- BROWN, E.T., RICHARDS, L.R. and BARR, M.V., 1977. Shear strength characteristics of the Delabole Slates. In: *Proceedings of Conference on Rock Engineering, Newcastle upon Tyne*, 31-51
- BROWN, E.T., 2008. Estimating the mechanical properties of rock masses. In: Potvin, Y., Carter, J., Dyskin, A. and Jeffrey, R. (eds) *Proceedings of the First Southern Hemisphere Rock Mechanics Symposium*. Perth: Australian Centre for Geomechanics
- BUZZI, O., SIEFFERT, Y., MENDES, J., LIU, X. A, GIACOMINI, A., and SEEDSMAN, R., 2014. Strength of an Australian coal under low confinement. *Rock Mechanics and Rock Engineering*. 47 (6), 2265-2270
- CADY, G.H., 1942. Modern concepts of physical constitution of coal. *Journal of Geology*, 50, 337-356
- CLOSE, J.C., 1993. Natural fractures in coal. B.E. Law, D.D. Rice (Eds.), *Hydrocarbons from Coal*, American Association of Petroleum Geologists, Tulsa, Oklahoma. 119-132
- CONROY, A., 1994. Impact of coal quality on grinding characteristics. *Combustion News*, Australian Combustion Technology Centre Company Publication. 1-4
- CUTHBERTSON, R.J., 1990. The Seismo-tectonics of Southeast Queensland, Bureau of Mineral Resources Bulletin, Australia, 232, 67-81

- DAN, C.C., and SCHUBERT, H., 1990. Breakage probability, progeny size distribution and energy utilization of comminution by impact. *Aufbereitungs-Technik*. 31, 241-247
- DAS, B., 1972. Microhardness of abnormally metamorphosed coal. *Fuel*. 51(1), 52-3
[http://dx.doi.org/10.1016/0016-2361\(72\)90038-5](http://dx.doi.org/10.1016/0016-2361(72)90038-5)
- DAVIS, A., 1978. Compromise in coal seam description. In: Dutcher, R.R. (ed.) *Field Description of Coal*. American Society for Testing Materials (ASTM) STP 661. Philadelphia: ASTM
- DAWSON, G.K.W. and ESTERLE, J.S., 2010. Controls on coal cleat spacing. *International Journal of Coal Geology*, 82 (3-4), 213-218
- DAY, R.W., WHITAKER, W.G., MURRAY, C.G., WILSON, I.H., and GRIMES, K.G., 1983. *Queensland Geology*, Geological Survey of Queensland Publication. 383
- DEISMAN, N., GENTZIS, T., and CHALATURNYK, R.J., 2008. Unconventional geomechanical testing on coal for coalbed reservoir well design. The Alberta foothills and plains. *International Journal of Coal Geology*. 75 (1), 15-26
- DEISMAN, N., 2016. Geomechanical characterization of coal for CBM reservoir engineering. University of Alberta PhD thesis
- DIESSEL, C.F.K., 1982. An appraisal of coal facies based on maceral characteristics. *Australian Coal Geology*, 4, 474-483
- DONOVAN, J.G., 2003. Fracture toughness based models for the prediction of power consumption, product size, and capacity of jaw crushers. Doctor of philosophy dissertation, Mining and Mineral Engineering, Virginia Tech, Blacksburg
- DRON, R.W., 1925. Notes on cleat in the Scottish coalfield. *Transactions of the Institution of Mining Engineers*, 70, 115-7
- EPSHTEIN, S.A., BORODICH, F.M., and BULL, S.J., 2015. Evaluation of elastic modulus and hardness of highly inhomogeneous materials by nanoindentation. *Applied Physics A*. 119, 325–335. doi: 10.1007/s00339-014-8971-5
- ESTERLE, J.S. 1994. Personal communication. CSIRO Division of Exploration and Mining
- ESTERLE, J.S., 2008. Mining and beneficiation in Suarez-Ruiz, I. and Crelling, J.C. (eds) *applied coal petrology: The role of petrology in coal utilisation*. Elsevier 61-83
- EXON, N.F., 1976. *Geology of the Surat Basin in Queensland*. Department of national resources bureau of mineral resources, geology and geophysics. Australian government publishing service, bulletin 166, Canberra
- EXON, N.F. 1980. The stratigraphy of the Surat basin, with special reference to coal deposits. *Coal Geology*, 1(3): 57-69
- FAIRHURST, C. and COOK, N.G.W., 1966. The phenomenon of rock splitting parallel to the direction of maximum compression in the neighbourhood of a surface. In: *Proceedings of 1st Congress of International Society of Rock Mechanics*, Lisbon, I, 687-692
- FALCON, R.M.S. and SNYMAN, C.P., 1986. An introduction to coal petrography: Atlas of petrographic constituents in the bituminous coals of Southern Africa: Johannesburg, South Africa. The Geological Society of South Africa. Review paper No. 2, 27
- FARAJ, B.S.M., FIELDING, C.R. and MACKINNON, I.D.R., 1996. Cleat mineralisation of Upper Permian Baralaba/Rangal Coal Measures, Bowen Basin, Australia. In: *Coalbed Methane and Coal*

- FIELDING, C. R., GRAY, A. R. G., HARRIS, G. I., and SALOMON, J. A., 1990. The Bowen Basin and overlying Surat Basin. In: Finlayson, D.M. (Ed.), *The Eromanga–Brisbane geoscience transect: a guide to basin development across Phanerozoic Australia in southern Queensland*. 105-116
- FIELDING, C.R., 1996. Mesozoic sedimentary basins and resources in eastern Australia - a review of current understanding. In: *Mesozoic Vol. 96. Proceedings of the Mesozoic Geology of the Eastern Australia Plate Conference*. Geological Society of Australia, Extended Abstracts. Brisbane, QLD. 180-185
- FLORES, R.M., 2014. *Coal and coalbed gas: fueling the future*. ISBN: 9780123969729. First edition. Waltham, Massachusetts: Elsevier
- FOLK, R.L., 1951. A comparison chart for visual percentage estimation. *Journal of sedimentary petrology*. The Pennsylvania State College, 21 (1), 32-33
- FORSTER, I.R., 1983. Influence of core sample geometry on the axial point-load test. Technical note: *International Journal of Rock Mechanics and Mining Sciences*. 20 (6), 291-295
- FRANKLIN, J. A. 1985. Suggested method for determining point load strength. *International Journal of Rock Mechanics and Mining Sciences*. 22(2), 51-60
- GALLAGHER K. 1990. Permian–Cretaceous subsidence history along the Eromanga–Brisbane geoscience transect. In: Finlayson D.M. ed. *The Eromanga–Brisbane geoscience transect: a guide to basin development across Phanerozoic Australia in southern Queensland*. Bureau of Mineral Resources Bulletin. 232, 133-151
- GAMSON, P.D., BEAMISH, B.B., and JOHNSON, D.P., 1993. Coal microstructure and micropermeability and their effects on natural gas recovery. *Fuel*, 72 (1), 87-99
- GAO, F., STEAD, D., and KANG, H., 2014. Numerical investigation of the scale effect and anisotropy in the strength and deformability of coal. *International Journal of Coal Geology*. 136, 25-37 <http://dx.doi.org/10.1016/j.coal.2014.10.003>
- GENTZIS, T., DEISMAN, N., and CHALATURNYK, R.J., 2006. Geomechanical properties and permeability of coals from the Foothills and Mountain regions of western Canada. *International Journal of Coal Geology*, 69 (3), 153-64
- GEORGE, A.M., 1975. Brown coal lithotypes in the Latrobe Valley deposits. Victoria State Electricity Commission, Planning and Investigation Department, petrological report number 17. Melbourne: Planning and Investigation Department
- GOLDSMITH, W., 1960. *Impact: The theory and physical behaviour of colliding solids*. Edward Arnold Ltd. (Ed.), London
- GONZALEZ-GARCIA, A. J., 2012. Rock strength and failure: Some common and uncommon issues. *Harmonising Rock Engineering and the Environment – Qian and Zhou (eds)* Taylor and Francis Group, London, ISBN 978-0-415-80444-8
- GRAMBERG, J., 1965. Axial cleavage fracturing, a significant process in mining and geology. *Engineering Geology*. 1, 31-72
- GRAMBERG, J., 1970. The ‘ellipse-with-notch’ theory to explain axial cleavage fracturing of rocks (a natural extension to the first Griffith theory). *International Journal of Rock Mechanics and Mining Sciences*. 7, 537-559

- GRAY I., 2015. Outburst risk determination and associated factors. ACARP Project report C23014
- GREEN, P.M., HOFFMANN, K.L., BRAIN, C.G., and GRAY, A.R.G., 1997. Project aims and activities, exploration history and geological investigations in the Bowen and overlying Surat Basins, Queensland. In: The Surat and Bowen Basins, Southeast Queensland, Queensland Minerals and Energy Review Series, Queensland Department of Natural Resources and Mines. 41-108
- GRIFFITH, A.A., 1924. The theory of rupture. In: Biezeno CG, Burgers JM (eds). Proceedings of the 1st International Congress of Applied Mechanics. Delft, Tech. Boekhandel en Drukkerij J. Waltman Jr., 54-63
- GRIGGS, D.T., and HANDIN, J., 1960. Observations on fracture and a hypothesis of earthquakes. In: Griggs D., Handin J. (eds) Rock deformation. Geological Society of America Memoranda. 79, 347-364
- GROSS, J., 1938. Crushing and grinding. *Crushing and grinding*. 402, 1-148
- GURDAL, G. and YALCIN, M.N., 2001. Pore volume and surface area of the carboniferous coals from the Zonguldak basin (NW Turkey) and their variations with rank and maceral composition. *International Journal of Coal Geology*. 48, 133-144
- GURNEY, C. and ROWE, P.W., 1948a. The effect of radial pressure on the flow and fracture of reinforced plastic rods. Aero. Research Council. London: H.M. Stationary Office, Reports and Memoranda No. 2283, May 1945, 10 pp
- GURNEY, C. AND ROWE, P.W., 1948b. Fracture of glass rods in bending and under radial pressure. Aero. Research Council. London: H.M. Stationary Office, Reports and Memoranda No. 2284, Nov. 1945, 5 pp
- HAMILTON, S.K., ESTERLE, J.S., and GOLDING, S.D., 2012. Geological interpretation of gas content trends, Walloon Subgroup, eastern Surat Basin, Queensland, Australia. *International Journal of Coal Geology*, 101, 21-35
- HAMILTON, S.K., 2014. Controls on spatial variability of methanogenesis in the Walloon Subgroup, eastern Surat Basin, Queensland. PhD Thesis, University of Queensland
- HANCOCK, P.L. and ENGELDER, T., 1989. Neotectonic joints. *Bulletin of the Geological Society of America*. 101, 1197-1208
- HAWKES, I. and MELLOR, M., 1970. Uniaxial testing in rock mechanics laboratories. *Engineering Geology*. 4:177-285
- HAWKINS, A.B., 1998. Aspects of rock strength. *Bulletin of Engineering Geology and the Environment*. (57), 17–30. <https://doi.org/10.1007/s100640050017>
- HAWLADER, H.M., 1990. Petrology, Diagenesis, and Reservoir Potential of the Surat Basin Sandstones with special reference to hydrocarbon exploration. PhD thesis, Macquarie University, School of Earth Sciences
- HEIDBACH, O., TINGAY, M., BARTH, A., REINECKER, J., KURFEß, D., and MÜLLER, B., 2010. Global crustal stress pattern based on the World Stress Map database release 2008. *Tectonophysics* 482, 3-15. <https://doi.org/10.1016/j.tecto.2009.07.023>
- HEIDBACH, O., RAJABI, M., CUI, X., FUCHS, K., MÜLLER, B., REINECKER, J., REITER, K., TINGAY, M., WENZEL, F., XIE, F., ZIEGLER, M.O, ZOBACK, M-L., and ZOBACK, M., 2018. The World Stress Map database release 2016: Crustal stress pattern across scales. *Tectonophysics* 744, 484-498

- HENTSCHEL, A., 2013. Geochemical characterisation of Surat Basin coal cores for gas origin assessment. MSc thesis, RWTH Aachen University of Technology, Aachen, Germany, unpublished
- HENTSCHEL, A., ESTERLE, J.S., GOLDING, S.D., and PACEY, D., 2016. Petrologic and stable isotopic study of the Walloon Coal Measures, Surat Basin, Queensland: peat accumulation under changing climate and base level. *International Journal of Coal Geology*, 160-161, 11-27
- HENTSCHEL, A., 2018. Integrating coal petrology, geochemistry and geochronology to understand spatial variation in the Walloon Subgroup. PhD Thesis, School of Earth and Environmental Sciences, The University of Queensland. <https://doi.org/10.14264/uql.2018.483>
- HERTZ, H., 1881. On the contact of elastic bodies. *J. für die reine und angewandte Mathematik*, 92, 56-171
- HILLIS, R.R., MEYER, J.J., and REYNOLDS, S.D., 1998. The Australian stress map. *Exploration Geophysics*. 29 (4), 420-427
- HILLIS, R.R., ENEVER, J.R., and REYNOLDS, S.D., 1999. In situ stress field of eastern Australia. *Australia Journal of Earth Sciences*. 46 (5), 813-825
- HILLIS, R.R. and REYNOLDS, S.D., 2000. The Australian Stress Map. *Journal of the Geological Society*, 157(5), 915-921
- HILLIS, R.R. and REYNOLDS, S.D., 2003. In situ stress field of Australia Geological Society of America Special Paper. 372, 49-58
- HOBBS, D.W., 1964. The Strength and the Stress-Strain Characteristics of Coal in Triaxial Compression. *The Journal of Geology* 72 (2), 214-231 <http://doi.org/10.1086/626977>
- HODDER, K., 2017. Fabrication, characterization and performance of 3D-Printed Sandstone models. PhD thesis. Department of Chemical and Materials Engineering. University of Alberta
- HOEK, E., 1983. Strength of jointed rock masses. *Geotechnique*, 23(3), 187-223
- HOEK, E. and BIENIAWSKI, Z.T., 1965. Brittle fracture propagation in rock under compression. *International Journal of Fracture Mechanics*. 1, 137-155
- HOEK, E. and BROWN, E.T., 1997. Practical estimates of rock mass strength. *International Journal of Rock Mechanics and Mining Sciences*, 34(8), 1165-1186
- HOEK, E. and BROWN, E.T., 1980. Underground excavations in rock. The Institution of Mining and Metallurgy (IMM), London, 155-156
- HOEK, E. and BROWN, E.T., 1982. Empirical strength criterion for rock masses. Discussion and closure. *Journal of the Geotechnical Engineering Division, ASCE*, 108 (GT4), 670-3
- HOFFMANN, K.L., TOTTERDELL, J.M., DIXON, O., SIMPSON, G.A., BRAKEL, A.T., WELLS, A.T., and MCKELLAR, J.L., 2009. Sequence stratigraphy of Jurassic strata in the lower Surat Basin succession, Queensland. *Australian Journal of Earth Sciences*. 56, 461-476
- HOLZHAUSEN, G.R. and JOHNSON, A.M. 1979. Analysis of longitudinal splitting of uniaxially compressed rock cylinders. *International Journal of Rock Mechanics and Mining Sciences*. 16, 163-177
- HONDA, H. and SANADA, Y., 1956. Hardness of coal: *Fuel*, 36, 451-461
- HOPKINSON, B., 1914. A method for measuring the pressure produced in the detonation of High Explosives or by the Impact of Bullets. *Philosophical Transactions of the Royal Society London Series A*, 213, 437-456

- HOSKINS, E.R., 1969. The failure of thick-walled hollow cylinders of isotropic rock. *International Journal of Rock Mechanics and Mining Sciences*. 6, 99-125
- HOUPERT, R. 1974. Le rôle du temps dans le comportement à la rupture des roches. In: *Advances in Rock Mechanics. Proceedings of the 3rd International Congress of Rock Mechanics, Denver, 1974.* Washington, D.C., Nat. Acad. Sci. (Ed.), 325–329
- HOWER, J.C. and LINEBERRY, G.T., 1988. The interface of coal lithology and coal cutting: study of breakage characteristics of selected Kentucky coals. *Journal of Coal Quality*. 7, 88-95
- HOWER, J.C., ESTERLE, J.S., WILD, G.D. and POLLOCK, J.D., 1990. Perspectives on coal lithotype analysis. *Journal of Coal Quality*, 9 (2), 48-52
- HOWER, J.C., GRAESE, A.M., and KLAPHEKE, J.G., 1987. Influence of microlithotype composition on Hardgrove Grindability Index for selected eastern Kentucky coals. *International Journal of Coal Geology* 7(3), 227-244
- HOWER, J.C. and WAGNER, N.J., 2012. Notes on the methods of the combined maceral/ microlithotype determination in coal. *International Journal of Coal Geology*, 95, 47-53
- HOWER, J.C. and WILD, G.D., 1988. Relationships between Hardgrove Grindability Index and petrographic composition for high-volatile bituminous coals from Kentucky. *Journal of Coal Quality*. 7, 122-126
- HOWER, J.C., TRINKLE, E.J., and RAIONE, R.P., 2008. Vickers microhardness of telovitrinite and pseudovitrinite from high volatile bituminous Kentucky coals. *International Journal of Coal Geology*. 75(2), 76-80
- HUANG, J., XU, S., YI, H., and HU, S., 2014. Size effect on the compression breakage strengths of glass particles. *Powder Technology*. 268, 86–94. <http://dx.doi.org/10.1016/j.powtec.2014.08.037>
- HUCKA, B.P., 1991. Coal hardness and rank relationships of some Utah and Colorado coals. *Utah Geological Association Publication*. 19, 183-192
- INTERNATIONAL COMMITTEE FOR COAL AND ORGANIC PETROLOGY, 1998. ICCP. The new vitrinite classification (ICCP System 1994), *Fuel* 77, 349-358
- INTERNATIONAL COMMITTEE FOR COAL AND ORGANIC PETROLOGY, 2001. ICCP. The new inertinite classification (ICCP System 1994), *Fuel* 80, 459-471
- INTERNATIONAL SOCIETY FOR ROCK MECHANICS, 1978. ISRM suggested methods for determine hardness and abrasiveness of rocks. Commission on standardization laboratory and field results. *International Journal of Rock Mechanics and Mining Sciences and Geomechanics Abstracts*. 15, 89-97
- INTERNATIONAL SOCIETY FOR ROCK MECHANICS, 1978. ISRM - suggested methods for determining tensile strength of rock materials. *International Journal of Rock Mechanics and Mining Sciences and Geomechanics Abstracts*. 15 (3), 99-103. [http:// dx.doi.org/10.1016/0148-9062\(78\)90003-7](http://dx.doi.org/10.1016/0148-9062(78)90003-7)
- INTERNATIONAL SOCIETY FOR ROCK MECHANICS, 1979. ISRM - suggested methods for determining the uniaxial compressive strength and deformability of rock materials
- INTERNATIONAL SOCIETY FOR ROCK MECHANICS, 1999. ISRM suggested method for the complete stress-strain curve for intact rock in uniaxial compression. *International Journal of Rock Mechanics and Mining Sciences*. 36, 279-289

- INTERNATIONAL SOCIETY FOR ROCK MECHANICS, 2007. ISRM the complete ISRM suggested methods for rock characterization, testing and monitoring: 1974-2006. In: Ulusay R, Hudson JA (eds) Suggested methods prepared by the commission on testing methods, ISRM, Compilation arranged by the ISRM Turkish National Group, Kozaoffset, Ankara
- JAEGER, J.C., 1960. Shear failure of anisotropic rocks. *Geological Magazine*. 97, 65-72. <http://dx.doi.org/10.1017/S0016756800061100>
- JAEGER, J.C., 1971. Friction of rocks and stability of rock slopes. *Géotechnique* 21, 97-134. <http://dx.doi.org/10.1680/geot.1971.21.2.97>
- JAEGER, J.C. and COOK N.G.W., 1979. *Fundamentals of rock mechanics*, 3rd ed. Chapman and Hall, London, 1-593
- JELL, P.A., 2013. *Geology of Queensland*, Geological Survey of Queensland, Brisbane, QLD.
- KAISER, P.K., AMANN, F., and BEWICK, R.P., 2015. Overcoming challenges of rock mass characterization for underground construction in deep mines. *ISRM Congress 2015 Proceedings - International Symposium on Rock Mechanics - ISBN: 978-1-926872-25-4*
- KHAVARI-KHORASANI, G.K., 1987. Oil-prone coals of the Walloon Coal Measures, Surat Basin, Australia. In: Scott, A.C. (Ed.), *Coal and Coal-Bearing Strata: Recent Advances: Geological Society of London, Special Publication*. 32, 303-310
- KING, R.P. and BOURGEOIS, F.S., 1993. Measurement of fracture energy during single particle fracture, *Minerals Engineering*, 6 (4), 353-367
- KLAWITTER, M., ESTERLE, J., and COLLINS, S., 2015. A study of hardness and fracture propagation in coal. *International Journal of Rock Mechanics and Mining Sciences* 76, 237-242
- KOENIG, R.A. and STUBBS, P.B., 1986. Interference testing of a coalbed methane reservoir. *Proceedings of the SPE Unconventional Gas Technology Symposium, Louisville, Kentucky, 18-21 May. Society of Petroleum Engineers*
- KOMURLU, E., KESIMAL, A., and DEMIR, A.D., 2017. Dogbone-shaped specimen testing method to evaluate tensile strength of rock materials. *Geomechanics and Engineering*, 12 (6), 883-898 <https://doi.org/10.12989/gae.2017.12.6.883>
- KONIETZKY, H. and ISMAEL, M. 2017. Failure Criteria for Rocks – an Introduction. In: *Introduction into Geomechanics*, (Griebsch, A. (ed.)), Geotechnical Institute TU Bergakademie Freiberg
- KORSCH, R.J. and TOTTERDELL, J.M. 1996. Mesozoic deformational events in eastern Australia and their impact on onShore sedimentary basins. In: *Mesozoic 96. Proceedings of the Mesozoic geology of the Eastern Australia Plate Conference. Geological Society of Australia*. 308-318
- KORSCH, R.J., BOREHAM, C.J., TOTTERDELL, J.M., SHAW, R.D., and NICOLL, M.G., 1998. Development and petroleum resource evaluation of the Bowen, Gunnedah and Surat basins, eastern Australia. *APPEA Journal* 38, 199-236
- KORSCH, R.J., TOTTERDELL, J.M., FOMIN, T., and NICOLL, M.G., 2009. Contractional structures and deformational events in the Bowen, Gunnedah and Surat Basins, eastern Australia. *Australian Journal of Earth Sciences*. 56, 477-499
- KORSCH, R.J. and TOTTERDELL, J.M., 2009. Subsidence history and basin phases of the Bowen, Gunnedah and Surat Basins, eastern Australia. *Australian Journal of Earth Sciences*. 56, 335-353

- KOSSOVICH, E.L., BORODICH, F.M., EPSHTEIN, S.A., GALANOV, B.A., MININ, M.G., and PROSINA, V.A., 2019. Mechanical, structural and scaling properties of coals: depth-sensing indentation studies. *Applied Physics A*. 125, 195. <https://doi.org/10.1007/s00339-018-2282-1>
- KOZUSNIKOVA, A. 2009. Determination of microhardness and elastic modulus of coal components by using indentation method. *Geolines (Prague)*. 22, 40-43
- KWASNIEWSKI, M., LI, X., and MANABU, T., 2012. True Triaxial Testing of Rocks, vol. 4 of Geomechanics Research Series, CRC Press, Taylor and Francis Group
- KULANDER, B.R., DEAN, S.L., and WARD Jr, B.J., 1990. Fractured Core Analysis: Interpretation, Logging, and Use of Natural and Induced Fractures in Core. PDF reprint on CD. Tulsa: American Association of Petroleum Geologists
- LAUBSCHER, D.H. and JAKUBEC J., 2001. The MRMR rock mass classification for jointed rock masses. In: Hustrulid WA, Bullock RL, eds. *Underground mining methods: engineering fundamentals and international case studies*. Littleton, CO: Society for Mining, Metallurgy, and Exploration, Inc., pp. 475-481
- LAUBACH, S.E. and TREMAIN, C.M., 1991. Regional coal fracture patterns and coalbed methane development. The 32nd US Symposium on Rock Mechanics (USRMS), Norman, Oklahoma, 10-12 July. American Rock Mechanics Association, 10
- LAUBACH, S.E., MARRETT, R.A., OLSON, J.E., and SCOTT, A.R., 1998. Characteristics and origins of coal cleat: a review. *International Journal of Coal Geology*, 35 (1-4), 175-207
- LAW, B.E., 1993. The relation between coal rank and cleat spacing: implications for the prediction of permeability in coal. *Proceedings of the International Coalbed Methane Symposium, II*, 435-42. Tuscaloosa, Alabama: University of Alabama
- LEBLANG, G.M., RAYMENT, P.A., and SMYTH, M., 1981. The Austinvale Coal Deposit - Wandoan: A Palaeoenvironmental Analysis. *Coal Geology*. 1, 185-195
- LI, H., SHIMADA, S., and ZHANG M., 2004. Anisotropy of gas permeability associated with cleat pattern in a coal seam of the Kushiro coalfield in Japan. *Journal of Environmental Geology*. 47, 45-50
- LI, D. and WONG, L.N.Y., 2013. The Brazilian Disc Test for Rock Mechanics Applications: Review and New Insights. *Rock Mechanics and Rock Engineering*. 46, 269-287
- LOIS-MORALES, P., EVANS, C., BONFILS, B., and WEATHERLEY, D., 2019. The impact load cell as a tool to link comminution properties to geomechanical properties of rocks (draft manuscript-personal communication)
- LUCIA, F.J., 1983. Petrophysical parameters estimated from visual descriptions of carbonate rocks: a field classification of carbonate pore space. SPE Paper 10073. *Journal of Petroleum Technology* 35 (3), 629-637
- MACMILLAN, N.H. and RICKERBY, D.G., 1979. On the measurement of hardness in coal. *Journal of Materials Science*. 14 (1), 242-246
- MANJUNATH, G.L. and NAIR, R.R., 2015. Implications of the 3D micro scale coal characteristics along with Raman stress mapping of the scratch tracks. *International Journal of Coal Geology*. 1(141), 13-22
- MARK, C. and BARTON, T.M., 1996. A new look at the uniaxial compressive strength of coal. In: *Proceedings of the 2nd North American rock mechanics symposium*, Rotterdam: Balkema. 405-412

- MASOUMI, H., SAYDAM, S., and HAGAN, P.C., 2016. Unified size-effect law for intact rock. *International Journal of Geomechanics*. 16 (2), 04015059
- MATTHEWS, K.J., HALE, A.J., GURNIS, M., MÜLLER, R.D., and DICAPRIO, L., 2011. Dynamic subsidence of eastern Australia during the Cretaceous. *Gondwana Research*. 19 (2), 372-383
- MCKELLAR, J.L., 1998. Late Early to Late Jurassic palynology, biostratigraphy and palaeogeography of the Roma Shelf area, northwestern Surat Basin, Queensland, Australia. PhD thesis. Brisbane: The University of Queensland, 515
- MEDHURST, T.P., 1996. Estimation of the in-situ strength and deformability of coal for engineering design. PhD thesis. Brisbane: The University of Queensland
- MEDHURST, T.P., BROWN, E.T. and TRUEMAN, R., 1995. Experimental studies of the effects of scale on the strength of coal. In *Proceedings of the 8th International Congress of Rock Mechanics*. Balkema, Rotterdam.1, 347-351
- MEDHURST, T.P. and BROWN, E.T., 1998. A study of the mechanical behaviour of coal for pillar design. *International Journal of Rock Mechanics and Mining Sciences and Geomechanics Abstracts*. 35 (8), 1087-105
- MILIN, L. and KING, R.P., 1994. Testing the equality of two independent distributions of data on the ultrafact load cell. The Utah Comminution Centre, University of Utah, U.S.A. 1-36
- MUKHERJEE, A.K., ALAM, M.M., and GHOSE, S., 1989. Microhardness characteristics of Indian coal and lignite. *Fuel*. 68(5), 670-3 [http://dx.doi.org/10.1016/0016-2361\(89\)90172-5](http://dx.doi.org/10.1016/0016-2361(89)90172-5)
- NARAYANAN, S.S., LIRA, B.B., and RONG, R.X., 1988. A single particle breakage technique for the determination of comminution characteristics of coal. *Coal Preparation*, 5(3-4), 211-227 [doi:10.1080/07349348808945566](https://doi.org/10.1080/07349348808945566)
- NAZIR, R., MOMENI, E., ARMAGHANI, D.J., and AMIN, M.F.M., 2013. Correlation between unconfined compressive strength and indirect tensile strength of limestone rock samples. *The Electronic Journal of Geotechnical Engineering* 18, 1737-1746
- NORBURY, D.R., 1986. The point load test. Geological Society, Engineering Geology Special Publication No. 2
- PACEY, D., 2011. An investigation of macroscopic and microscopic vertical trends, characteristics and cyclicity in the Jurassic age Walloon Coals, Surat Basin, Queensland. BSc Hons Thesis, The University of Queensland, Brisbane, Queensland, Australia, unpublished
- PALMER, I., MOSCHOVIDIS, Z.A., and CAMERON, J., 2005. Coal failure and consequences for coalbed methane wells. SPE No. 96872, Society of Petroleum Engineers Annual Technical Conference and Exhibition. Dallas, Texas, USA, Oct. 9-12
- PAN, J., MENG, Z., HOU, Q., JU, Y., and CAO, Y., 2013. Coal strength and Young's modulus related to coal rank, compressional velocity and maceral composition. *Journal of Structural Geology*. 54, 129-135. <http://dx.doi.org/10.1016/j.jsg.2013.07.008>
- PAROTIDIS, M. HUMMEL, N., GRAHAM, J., WHEELER, J., and PRITCHARD, T., 2016. Unconventional plays, various lithologies – constant stress gradients. SPE-180075MS. 78th EAGE conference and exhibition, Vienna, Austria
- PATTISON, C.I., FIELDING, C.R., MC WATTERS, R.H., and HAMILTON, L.H., 1996. Nature and origin of fractures in Permian coals from the Bowen Basin, Queensland, Australia. In: Gayer, R. and Harris, I. (eds) *Coalbed Methane and Coal Geology*. Geological Society Special Publication 109, 133-150

- PATERSON, M.S., and WONG, T., 2005. Experimental rock deformation – The brittle field. Book chapter micromechanics of brittle fracture. Berlin, Heidelberg: Springer. 115-145
- PEJCHAL, V., ŽAGAR, G., CHARVET, R., DÉNÉRÉAZ, C., and MORTENSEN, A., 2017. Compression testing spherical particles for strength: Theory of the meridian crack test and implementation for microscopic fused quartz. *Journal of the Mechanics and Physics of Solids*. 99, 70-92 <https://doi.org/10.1016/j.jmps.2016.11.009>
- PENG, S.S., 1973. Time-dependent aspects of rock behaviour as measured by a servo-controlled hydraulic testing machine. *International Journal of Rock Mechanics and Mining Sciences* 10, 235-246
- PERRAS, M.A. and DIEDERICHS, M.S., 2014. A Review of the Tensile Strength of Rock: Concepts and Testing. *Geotechnical and Geological Engineering*, 32 (2), 525-546 <https://doi.org/10.1007/s10706-014-9732-0>
- PETERS, J.T., SCHAPIRO, N., and GRAY, R.J., 1962. Know your coal. *Transactions of the American Institute of Mining and Metallurgical Engineers*. 223, 1-6
- POTYONDY, D.O., 2015. The bonded-particle model as a tool for rock mechanics research and application: current trends and future directions. *Geosystem Engineering*. 18(1), 1-28
- POULSEN, B.A. and ADHIKARY, D.P., 2013. A numerical study of the scale effect in coal strength. *International Journal of Rock Mechanics and Mining Sciences*, 63 (1), 62-71 <http://dx.doi.org/10.1016/j.ijrmms.2013.06.006>
- PRIMKULOV, B., CHALATURNYK, J., CHALATURNYK, R.J., and ZAMBRANO NARVAEZ, G., 2017. 3D Printed Sandstone Strength: Curing of Furfuryl Alcohol Resin-Based Sandstone. *3D Printing and Additive Manufacturing*. 4 (3), 149-155
- PUTTOCK, M.J. and THWAITE, E.G., 1969. Elastic Compression of Spheres and Cylinders at Point and Line Contact. CSIRO, National Standards Laboratory Technical Paper No. 25
- RABIA, H. and BROOK, N., 1979. The Shore hardness of rock. Technical Note. *International Journal of Rock Mechanics and Mining Sciences and Geomechanics Abstracts*.16, 335-6
- RAJABI, M., TINGAY, M., HEIDBACH, O., HILLIS, R., and REYNOLDS, S., 2017. The present-day stress field of Australia. *Earth-Sciences. Rev.* 168, 165–189. <https://doi.org/10.1016/j.earscirev.2017.04.003>
- RAMAMURTHY, T., 1993. Strength and modulus responses of anisotropic rocks. *Comprehensive Rock Engineering*. 1 (1), 313-329
- REYNOLDS, S.D., COBLENTZ, D.D., and HILLIS, R., 2002. Tectonic forces controlling the regional intraplate stress field in continental Australia: results from new finite element modeling. *Journal of Geophysical Research. Solid Earth*. 107 (B7), ETG 1-1 to 1-15 <https://doi.org/10.1029/2001JB000408>
- REYNOLDS, S.D., COBLENTZ, D.D., and HILLIS, R., 2003. Influences of plate-boundary forces on the regional intraplate stress field of continental Australia. *Geological Society of America Special Publication*. 372, 59-70
- RIGBY, S.M. and KANTSLER, A.J., 1987. Marilla Creek – An untested stratigraphy play in the Surat Basin. *The APPEA Journal*, 27 (1), 230-44
- RODRIGUES, C.F. and LEMOS DE SOUSA, M.J., 2002. The measurement of coal porosity with different gases. *International Journal of Coal Geology*. 48, 245-251

- ROSHAN, H., MASOUMI, H., and REGENAUER-LIEB, K., 2017. Frictional behaviour of sandstone: A sample-size dependent triaxial investigation. *Journal of Structural Geology*. 94, 154-165
- RUBIERA, F., ARENILLAS, A., FUENTE, E., MILES, N., and PIS, J.J., 1999. Effect of the grinding behaviour of coal blends on coal utilisation for combustion. *Powder Technology*. 105, 351-356
- RUSNAK J., 2018. Coal strength variation by lithotype for High-Volatile A Bituminous coal in the Central Appalachian Basin. 36th International conference on ground control in mining
- RUSSELL, M. and GURNIS, M., 1994. The platform of epeirogeny: Vertical motions of Australia during the Cretaceous. *Basin Research*. 6, 63-76
- SAEIDI, F., 2016. New approach for characterising a breakage event as a multi-stage process. PhD thesis, SMI, JKMRC, The University of Queensland
- SANTARELLI, F.J. and BROWN, E.T., 1989. Failure of three sedimentary rocks in triaxial and hollow cylinder compression tests. *International Journal of Rock Mechanics and Mining Sciences and Geomechanics Abstract*, 26 (5), 401-413
- SCHOPF, J.M., 1960. Field description and sampling of coal beds. US Geological Survey Bulletin 111B. Washington, D.C.: US Government Printing Office
- SCOTT, A.R., 2002. Hydrogeologic factors affecting gas content distribution in coal beds. *International Journal of Coal Geology*, 50, 363-387
- SCOTT, S., ANDERSON, B., CROSDALE, P., DINGWALL, J., and LEBLANG, G., 2007. Coal petrology and coal seam gas contents of the Walloon Subgroup - Surat Basin, Queensland, Australia. *International Journal of Coal Geology*. 70, 209-222
- SCHOLTÈS L., DONZÉ, F.-V. and KHANAL, M., 2011. Scale effects on strength of geomaterials, case study: coal. *Journal of the Mechanics and Physics of Solids*, 59 (5), 1131-1146 <http://dx.doi.org/10.1016/j.jmps.2011.01.009>
- SCHOLZ, C.H., BOITNOTT, G., and NEMAT-NASSER, S., 1986. The Bridgman ring paradox revisited. *Pure Applied Geophysics*. 124, 587-599
- SCHONERT, K., UMHAUER, H., and RUMPF, H., 1962. Die Festigkeit kleiner Glaskugeln. *Glastech. Ber.*, 35, 272-278
- SCHONERT, K., 1986. Advances in the physical fundamentals of comminution. In *Advances in Mineral Processing*, ed. P. Somasundaran. Society of Mining Engineers, 19-32
- SHI, Q., QIN, Y., LI, J., WANG, Z., ZHANG, M., and SONG, X., 2017. Simulation of the crack development in coal without confining stress under ultrasonic wave treatment. *Fuel*. 205, 222-231
- SLIWA, R. and ESTERLE, J.S., 2008. Re-evaluation of structure and sedimentary packages in the eastern Surat Basin. In: Blevin, J.E., Bradshaw, B.E., Uruski, C. (Eds.), *Eastern Australasian Basins Symposium III*. Petroleum Exploration Society of Australia, Special Publication, 527
- SMITH, T., BIANCHI, V., CAPITANIO, F., and VERDEL, C., 2017. Subduction controls on dynamic topography: Implications for the Jurassic Surat Basin. *Australian Journal of Earth Sciences*
- SONG, H., JIANG, Y., ELSWORTH, D., ZHAO, Y., WANG, J., and LIU, B., 2018. Scale effects and strength anisotropy in coal. *International Journal of Coal Geology*. 195, 37-46 <https://doi.org/10.1016/j.coal.2018.05.006>

- STACH, E., MACKOWSKY, M-TH., TEICHMULLER, M., TAYLOR, G.H., CHANDRA, D., and TEICHMULLER, R., 1982. Stach's textbook of coal petrology. (eds.) Gebrüder Borntraeger, Berlin - Stuttgart, 535
- STANDARDS ASSOCIATION OF AUSTRALIA, 1993. AS 2519. Guide to the technical evaluation of higher rank coal deposits. Sydney: Standards Association of Australia
- STOPEs, M.C., 1919. On the four visible ingredients in banded bituminous coals. Proceedings of the Royal Society B, 90 (633), 497-508
- SU, X., FENG, Y., CHEN, J. and PAN, J., 2001. The characteristics and origins of cleat in coal from Western North China. International Journal of Coal Geology, 47, 51-62
- TAVARES, L.M., 1997. Microscale investigation of particle breakage applied to the study of thermal and mechanical predamage. PhD thesis. Department of Metallurgical Engineering. The University of Utah
- TAVARES, L.M. and KING, R.P., 1998a. Microscale investigation of thermally assisted comminution. Proceedings of the XIX International Mineral Processing Congress (IMPC), 36, 203-208
- TAVARES, L.M. and KING, R.P., 1998b. Single-particle fracture under impact loading. International Journal of Mineral Processing, 54, 1-28
- TAVARES, L.M. and KING, R.P., 2004. Measurement of the load–deformation response from impact-breakage of particles. International Journal of Mineral Processing. 74, S267-S277
- TAVARES, L.M., 2007. Handbook of powder technology. Chapter 1 Breakage of single particles: quasi-static. Vol 12, 3-68
- TAYLOR, G.H., TEICHMÜLLER, M., DAVIS, A., DIESSEL, C.F.K., LITKE, R., and ROBERT, P., 1998. Organic petrology: a new handbook incorporating some revised parts of Stach's Textbook of coal petrology. Contributions by Glick, D.C., Smyth, M., Swaine, D.J., Vandenbroucke, M., Espitale, J. Berlin: Gebrüder Borntraeger. 438-441
- TEICHMÜLLER, M., 1989. The genesis of coal from the viewpoint of coal petrology. International Journal of Coal Geology. 12, 1-87
- TERZAGHI, K., PECK, R.B. and G. MESRI, G., 1996. Soil Mechanics in Engineering Practice, John Wiley & Sons, New York, NY
- TING, F.T.C., 1977a. Origin and spacing of cleats in coal beds. Journal of Pressure Vessel Technology. 99, 624-626 doi:10.1115/1.3454584
- TING, F.T.C., 1977b. Microscopical investigation of the transformation (diagenesis) from peat to lignite. Journal of Microscopy. 109, 75-83
- TING, F.T.C., 1982. Coal macerals. In: R.A. Meyers (Editor), Coal Structure
- THIESSEN, R. and SPRUNK, G.C. 1935. Microscopic and petrographic studies of certain American coals. Washington DC: U.S. Bureau of the Mines Technical paper, 71
- TREMAIN, C.M., LAUBACH, S.E., and WHITEHEAD, N.H., 1991. Coal fracture cleat patterns in upper cretaceous fruitland formation, San Juan Basin, Colorado and New Mexico: implications for exploration and development. In: Schwochow, S., Murray, D.K., Fahy, M.F. (eds.), Coalbed methane of Western North America. Rk. Mt. Association of Geology, Field Conference, 49-59

- TRUEMAN, R. and MEDHURST, T.P., 1994. The influence of scale effects on the strength and deformability of coal. IV CSMR/ Integral Approach to Applied Rock Mechanics, ed. M. Van Sint Jan., 1, 103-114. Santiago: Sociedad Chilena de Geotecnia
- TURNER, W.T. and SECOR, D.T., Jr., 1974. Effective Confining Pressure and Fluid Discharge Along Fractures. *Eos, Transactions, American Geophysical Union*, 55(4), 431
- VAN KREVELEN, D.W., 1993. Coal: typology physics chemistry constitution. 3rd ed. Amsterdam: Elsevier
- VEEVERS, J. J., 1984. Phanerozoic Earth History of Australia. Clarendon Press, Oxford, 418
- WAGNER, H., 1974. Determination of the complete load-deformation characteristics of coal pillars. In: Fairhurst, C. (ed) Proceedings of the 3rd International Congress of Rock Mechanics. 1-B, 1,076–81. Washington D.C.: National Academy of Sciences
- WAGNER, H. and MADDEN, B.J. 1984. Fifteen years' experience with the design of coal pillars in shallow South African collieries: an evaluation of the performance of the design procedures and recent improvements. Design and Performance of Underground Excavations, ed. E.T. Brown E.T., and Hudson J.A., 391-399. London: British Geotechnical Society
- WARD, C.R., 1984. Coal geology and coal technology. Oxford: Blackwell Scientific Publications, 345
- WASCHBUSCH, P., BEAUMONT, C., and KORSCH, R.J., 1999. Geodynamic modelling of aspects of the New England Orogen and adjacent Bowen, Gunnedah and Surat basins. In: Flood P. G. ed. New England Orogen, eastern Australia. Department of Geology and Geophysics, University of New England, Armidale. 203-210
- WASCHBUSCH, P., KORSCH, R.J., and BEAUMONT, C., 2009. Geodynamic modelling of aspects of the Bowen, Gunnedah, Surat and Eromanga Basins from the perspective of convergent margin processes. *Australian Journal of Earth Sciences*. 56, 309-334
- WOLD, M., DAVIDSON, S., WU, B., CHOI, S., and KOENIG, R., 1995. Cavity completion for coalbed methane stimulation - an integrated investigation and trial in the Bowen Basin, Queensland. Proceedings of the SPE Annual Technical Conference and Exhibition, Dallas, Texas, 22-25 October. Society of Petroleum Engineers
- YAGO, J.V.R. and FIELDING, C.R., 1996. Sedimentology of the Middle Jurassic Walloon Coal Measures in the Great Artesian Basin, eastern Australia. In: Mesozoic 96. Proceedings of the Mesozoic Geology of the Eastern Australia Plate Conference, Brisbane, 1996: Geological Society of Australia, Extended Abstracts. 43, 574-575
- YARALI, O. and SOYER, E., 2011. The effect of mechanical rock properties and brittleness on drillability. *Scientific Research and Essays*. 6(5), 1077-1088 doi: 10.5897/SRE10.1004
- YASHIMA, S., KANDA, Y., and SANO, S., 1987. Relationships between particle size and fracture energy or impact velocity required to fracture as estimated from single particle crushing. *Powder Technology*. 51, 277-282
- ZHAO, Y., LIU, S., ZHAO, G.-F., ELSWORTH, D., JIANG, Y., and HAN, J., 2014a. Failure mechanisms in coal: dependence on strain rate and microstructure. *Journal of Geophysical Research. Solid Earth* 119, 6924-6935 <http://dx.doi.org/10.1002/2014JB011198>
- ZHAO, Y., ZHAO, G.F., JIANG, Y., ELSWORTH, D., and HUANG, Y., 2014b. Effects of bedding on the dynamic indirect tensile strength of coal: laboratory experiments and numerical simulation. *International Journal of Coal Geology*. 132, 81-93 <http://dx.doi.org/10.1016/j.coal.2014.08.007>

- ZHAO, S. and MÜLLER, R.D., 2001. The Tectonic Stress Field in Eastern Australia, Eastern Australasian Basins Symposium, A Refocussed Energy Perspective for the Future. Petroleum Exploration Society of Australia Special Publication. 61-70
- ZIEGLER, M. and HEIDBACH, O., 2017. Manual of the Matlab script Stress2Grid. In: World Stress Map Technical Report. GFZ German Research Centre for Geosciences, Potsdam, 33 <https://doi.org/10.2312/wsm.2017.002>
- ZOBACK, M.D. and BYERLEE, J.D., 1975. The effect of microcrack dilatancy on the permeability of Westerly granite. *Journal of Geophysical Research*. 80 (5), 752–755

Appendix I

3D-PRINTED SANDSTONE PROPERTIES

Table 13 Summary of UCS measurements on 3D-printed sandstone from UCS test.

	Diameter (mm)	Height (mm)	Maximum load (kN)	Time at maximum comp. load (min)	Extension at maximum comp. load (mm)	Compressive strength (MPa)	Extensometer (yes/ no)
	21.53	48.62	12.80	3.39	0.92	35.16	Yes -25mm
	21.65	48.72	12.61	3.53	0.88	34.26	Yes -25mm
	21.61	48.78	13.02	3.96	0.99	35.5	Yes -25mm
	21.62	48.73	12.92	3.57	0.89	35.19	Yes -25mm
	21.54	48.77	12.94	3.59	0.83	35.52	Yes -25mm
	21.54	48.77	12.94	3.42	0.86	35.51	Yes -25mm
	21.59	48.74	11.89	3.54	0.88	32.49	no
	21.55	48.78	13.48	3.86	0.97	36.94	no
	21.54	48.65	13.18	3.97	0.99	36.16	no
	21.66	48.71	13.12	4.04	1.01	35.6	no
avg	21.6					35.2 ± 1.2	
	16.57	37.27	7.34	2.82	0.70	34.05	Yes - 12.5mm
	16.53	37.18	7.26	2.74	0.69	33.84	Yes - 12.5mm
	16.53	37.23	7.22	2.73	0.68	33.64	Yes - 12.5mm
	16.54	37.2	6.98	2.56	0.64	32.5	Yes - 12.5mm
	16.56	37.21	6.72	2.70	0.68	31.2	Yes - 12.5mm
	16.53	37.21	7.27	2.83	0.71	33.88	Yes - 12.5mm
	16.58	37.21	6.62	2.77	0.69	30.67	no
	16.38	37.18	7.23	2.93	0.73	34.31	no
	16.54	37.21	6.84	2.95	0.74	31.83	no
	16.43	37.2	6.55	2.49	0.62	30.91	no
avg	16.5					32.7 ± 1.4	
	12.38	27.48	3.10	2.75	2.51	25.74	Yes
	12.35	27.58	3.04	1.88	0.57	25.35	Yes
	12.37	27.46	3.42	1.97	0.54	28.43	Yes
	12.35	27.52	3.28	2.20	0.55	27.38	Yes
	12.32	27.48	3.64	2.20	0.55	30.51	Yes
	12.33	27.48	3.51	2.18	0.55	29.41	Yes
	12.35	27.52	3.19	2.12	0.53	26.66	no
	12.29	27.51	3.25	1.96	0.49	27.39	no
	12.32	27.46	3.41	1.92	0.48	28.57	no
	12.29	27.4	3.09	2.28	0.57	26	no
avg	12.3					27.5 ± 1.7	

Diameter (mm)	Height (mm)	Maximum load (kN)	Time at maximum comp. load (min)	Extension at maximum comp. load (mm)	Compressive strength (MPa)	Extensometer (yes/ no)
10.07	22.15	1.97	1.67	0.42	24.72	no
10.17	22.26	1.99	1.99	0.50	24.47	no
10.02	22.27	2.06	1.66	0.42	26.07	no
10.05	22.22	2.03	1.71	0.43	25.63	no
10.06	22.28	2.11	1.83	1.28	26.56	no
10.12	22.29	2.01	1.62	0.40	25.01	no
10.07	22.23	1.79	1.62	0.41	22.46	no
10.08	22.22	1.99	1.78	0.44	24.98	no
10.09	22.21	2.06	1.62	0.41	25.77	no
10.14	22.25	1.98	1.75	0.44	24.53	no
avg	10.1				25.0 ± 1.1	
7.34	16.04	0.89	1.68	0.42	20.99	no
7.44	16.03	0.90	1.28	0.32	20.62	no
7.4	16.09	0.84	1.58	0.40	19.62	no
7.27	15.89	0.91	1.29	0.32	21.84	no
7.3	15.89	0.77	1.30	0.33	18.43	no
7.32	15.95	0.84	1.04	0.28	19.9	no
7.4	15.96	0.80	1.14	0.28	18.56	no
7.26	15.9	0.81	1.25	0.31	19.62	no
avg	7.3				19.9 ± 1.2	

Table 14 Summary for SILC test results on 3D-printed sandstone.

Specimen	Impact conditions		Specimen dimension: (average)			Impact velocity (m/s)	Number of specimens tested	
	Ball mass (g)	Drop height (mm)	Mass (g)	Height/diameter (mm)	Length (mm)			
Cylinder-shaped printed vertical	535.25	25.07	0.149	5.31	5.19	0.70	21	VC (Φ5.3 mm 1:1)
	535.25	25.07	0.166	5.32	5.70	0.70	25	VC (Φ5.32 mm 1.1:1)
	535.25	63.33	0.421	7.38	7.23	1.11	25	VC (Φ7.38 mm 1:1)
	535.25	63.33	0.448	7.38	7.69	1.11	26	VC (Φ7.38 mm 1.1:1)
	535.25	100	1.144	10.18	9.94	1.40	26	VC (Φ10.18 mm 1:1)
	535.25	100	1.273	10.22	10.97	1.40	26	VC (Φ10.22 mm 1.1:1)
	535.25	125.11	1.904	12.35	10.92	1.57	16	VC (Φ12.35 mm 0.9:1)
	535.25	125.11	2.131	12.36	12.17	1.57	16	VC (Φ12.36 mm 1:1)
	535.25	125.11	2.319	12.40	13.18	1.57	16	VC (Φ12.4 mm 1.1:1)
Cylinder-shaped printed horizontal	535.25	63.33	0.398	7.20	7.27	1.11	19	HC (Φ7.2 mm 1:1)
	535.25	63.33	0.446	7.19	8.03	1.11	19	HC (Φ7.19 mm 1.1:1)
	535.25	100	1.133	9.98	10.13	1.40	19	HC (Φ9.98 mm 1:1)
	535.25	100	1.244	10.01	11.08	1.40	19	HC (Φ10.01 mm 1.1:1)
	535.25	125.11	1.923	12.21	11.24	1.57	19	HC (Φ12.21 mm 0.9:1)
	535.25	125.11	2.111	12.15	12.38	1.57	19	HC (Φ12.15 mm 1:1)
	535.25	125.11	2.291	12.10	13.53	1.57	19	HC (Φ12.1 mm 1.1:1)
Sphere-shaped	535.25	25.07	0.100	5.12	-	0.70	20	Sp (Φ5.1 mm)
	535.25	63.33	0.274	7.15	-	1.11	20	Sp (Φ7.2 mm)
	535.25	100	0.767	9.95	-	1.40	20	Sp (Φ10.0 mm)
	1399.8	100	1.414	12.17	-	1.40	17	Sp (Φ12.2 mm)
Flattened Sphere-shaped	535.25	25.07	0.110	5.26	-	0.70	18	SpF (Φ5.2 mm)
	535.25	63.33	0.297	7.35	-	1.11	20	SpF (Φ7.4 mm)
	535.25	100	0.815	10.18	-	1.40	20	SpF (Φ10.2 mm)
	1399.8	100	1.533	12.08	-	1.40	18	SpF (Φ12.1 mm)
**Ellipsoid-shaped average	535.25	25.07	0.134	5.77	-	0.70	18	Ell (Φ5.3 mm)
	535.25	63.33	0.363	8.10	-	1.11	18	Ell (Φ7.4 mm)
	535.25	100	0.976	11.20	-	1.40	18	Ell (Φ10.1 mm)
	1399.8	100	1.862	13.88	-	1.40	13	Ell (Φ12.4 mm)

Specimen	Specimen fracture force (N)			Specimen fracture energy (mJ)			Specimen tensile strength (MPa)			Specimen compression strength (MPa)			Specimen Young's modulus (GPa)			
	\bar{F}_c	$F_{c,50}$	$\sigma_{F_c}^2$	\bar{E}'	E'_{50}	$\sigma_{E'}^2$	$\bar{\sigma}_p$	$\sigma_{p,50}$	$\sigma_{\sigma_p}^2$	$\bar{\sigma}_c$	$\sigma_{c,50}$	$\sigma_{\sigma_c}^2$	\bar{k}_p	$k_{p,50}$	σ_k^2	
Cylinder-shaped printed vertical	250.23	247.98	0.014	28.22	28.29	0.036	5.79	5.74	0.014	73.4	66.4	0.017	1.06	1.05	0.033	VC
	300.02	299.56	0.012	35.67	36.40	0.025	6.30	6.28	0.013	69.2	68.9	0.012	1.04	1.01	0.017	VC
	540.83	541.84	0.026	82.13	80.65	0.050	6.45	6.48	0.026	70.8	70.9	0.019	1.01	1.01	0.019	VC
	564.55	566.79	0.010	85.97	84.29	0.024	6.33	6.35	0.012	72.1	72.0	0.016	1.04	1.02	0.024	VC
	1079.10	1084.29	0.021	204.13	198.41	0.059	6.79	6.81	0.021	90.5	90.6	0.014	1.39	1.38	0.020	VC
	1198.12	1201.39	0.010	236.73	236.99	0.021	6.80	6.82	0.011	94.5	94.1	0.015	1.47	1.45	0.023	VC
	1483.13	1473.96	0.013	306.38	295.61	0.024	7.00	6.96	0.013	105.2	104.9	0.007	1.74	1.74	0.005	VC
	1598.98	1620.68	0.007	352.36	353.98	0.034	6.77	6.86	0.007	103.9	103.9	0.008	1.70	1.69	0.013	VC
	1832.99	1847.43	0.006	415.83	417.23	0.021	7.14	7.22	0.005	111.3	111.7	0.007	1.81	1.81	0.009	VC
Cylinder-shaped printed horizontal	483.59	482.81	0.021	69.16	67.77	0.041	5.88	5.89	0.020	66.8	67.3	0.016	0.97	0.97	0.021	HC
	557.64	557.64	0.015	79.89	78.53	0.046	6.15	6.15	0.014	75.1	75.4	0.010	1.13	1.12	0.026	HC
	1124.84	1124.62	0.012	196.92	191.24	0.033	7.08	7.08	0.012	98.6	98.7	0.010	1.56	1.55	0.021	HC
	1094.27	1101.10	0.019	187.05	190.53	0.029	6.28	6.30	0.018	94.6	95.9	0.007	1.56	1.58	0.013	HC
	1547.38	1547.70	0.012	303.98	304.59	0.025	7.18	7.17	0.013	110.9	110.0	0.013	1.86	1.84	0.011	HC
	1770.72	1765.35	0.018	355.87	356.28	0.033	7.50	7.48	0.018	122.5	122.5	0.016	2.10	2.11	0.014	HC
	1914.40	1907.89	0.006	405.12	403.36	0.021	7.44	7.42	0.006	122.3	122.5	0.005	2.07	2.07	0.009	HC
Sphere-shaped	209.63	208.85	0.012	45.41	43.72	0.074	7.12	7.08	0.012	107.4	107.2	0.038	0.75	0.74	0.069	Sp
	397.55	397.31	0.007	114.46	109.64	0.077	6.93	6.92	0.009	115.7	117.3	0.036	0.80	0.80	0.095	Sp
	822.10	819.44	0.009	280.63	269.05	0.080	7.40	7.39	0.010	144.5	143.2	0.018	1.05	1.04	0.054	Sp
	1230.56	1226.49	0.006	471.95	455.62	0.034	7.41	7.39	0.007	154.0	151.5	0.005	1.16	1.14	0.013	Sp
Flattened Sphere-shaped	233.54	235.88	0.011	45.01	46.41	0.034	7.53	7.62	0.008	134.2	128.0	0.028	0.97	0.91	0.062	SpF
	441.17	444.35	0.003	118.41	116.19	0.021	7.28	7.35	0.003	130.1	128.9	0.012	0.92	0.90	0.022	SpF
	861.93	863.83	0.008	271.99	269.06	0.031	7.41	7.40	0.008	158.3	155.8	0.029	1.20	1.16	0.052	SpF
	1410.49	1407.11	0.010	498.09	496.75	0.033	8.62	8.61	0.011	193.2	194.8	0.012	1.52	1.51	0.024	SpF
**Ellipsoid-shaped average	267.91	267.52	0.002	57.95	56.47	0.011	7.18	7.14	0.002	125.0	126.5	0.012	0.89	0.89	0.023	EII
	529.46	530.18	0.004	138.27	138.32	0.014	7.20	7.19	0.005	145.1	144.2	0.012	1.08	1.07	0.022	EII
	1025.18	1034.28	0.004	310.09	307.78	0.017	7.28	7.36	0.003	179.1	173.6	0.013	1.44	1.37	0.018	EII
	1556.43	1562.72	0.002	530.40	522.59	0.028	7.20	7.23	0.002	193.7	192.2	0.024	1.65	1.63	0.051	EII

Appendix II

SILC ON COAL AND MUDSTONE

Table 15 Summary of fracture characteristics for mini-cylinder specimens (11.7 mm in diameter, aspect ratio varying from 0.9:1 to 1.1:1) of coal on SILC. Impact conditions utilising a 535.25 g strike dropped from 63.1 mm in height.

Drilled direction	Ply	Data points	Mean fracture force (N)	Mean fracture energy (mJ)	Mean corrected spec. fract. energy (kWh/t)	Mean tensile strength (MPa)
Perpendicular to band	PC6-D	14	1189.4	124.4	0.0194	5.06
	PC8-B	91	945.05	101.65	0.0173	4.32
Parallel to band	PC8-B	13	656.8	45.4	0.0074	2.87
	PC8-WB	24	1020.5	98.5	0.0162	4.67

Table 16 Summary of fracture characteristics for irregular-particles (retained at 3.35, 4.75, 6.7, and 9.5 mm mesh sized) of coal plies PC6-D, PD8-BLA and mudstone on SILC.

Ply	Impact conditions		Number of particles tested	Particle height (avg) (mm)	Mean fracture force (N)	Mean corrected spec. fract. energy (kWh/t)	Mean fracture energy (mJ)	Mean tensile strength (MPa)
	Ball mass (g)	Drop height (mm)						
PC6-D	66.78	100	146	3.30	125.1	0.0495	11.0	10.1
	66.78	125	231	4.86	195.2	0.0318	22.5	7.5
	535.25	80	208	9.04	495.6	0.0194	88.7	5.5
PD8-BLA	66.78	125	118	3.16	164.1	0.1027	20.5	14.7
	535.25	45.5	152	4.97	231.7	0.0608	39.4	8.6
	535.25	80	195	7.03	310.5	0.0446	77.2	5.8
	535.25	100	200	9.18	450.2	0.0343	140.5	4.9
Mudstone	66.78	100	30	3.64	207.7	0.1157	44.0	14.1
	535.25	45.5	79	5.54	343.4	0.0873	106.1	10.0
	535.25	80	227	6.85	506.4	0.0751	228.7	9.8
	535.25	100	244	9.22	553.2	0.0437	290.6	5.9

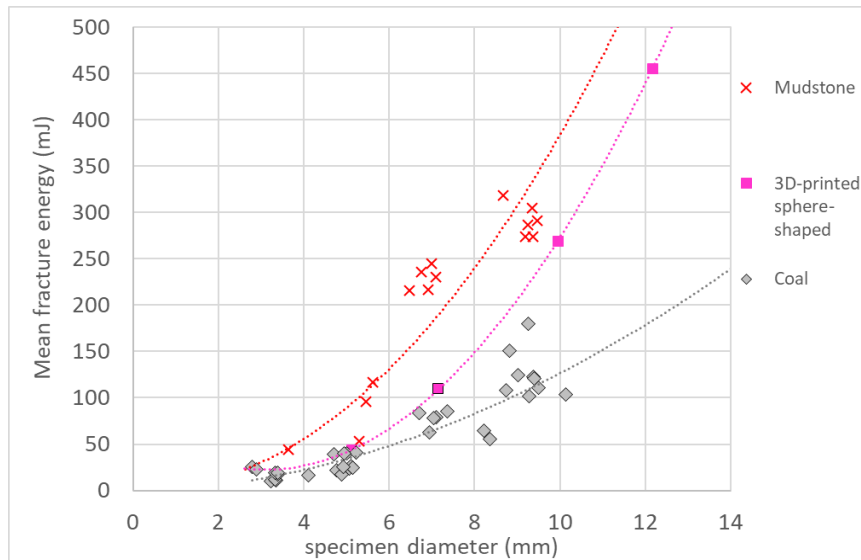


Figure 99 Variation of mean fracture energy for irregular-particles of coal plies PC6-D, PD8-BLA, 3D-printed sphere-shaped specimens, and mudstone by size, all tested on SILC.

Detailed results for each series of sub-bituminous coal and mudstone are presented below. The tables present: \bar{F}_c average fracture force; $F_{c,50}$ mean fracture force; $\sigma^2_{F_c}$ variance of the log-normal distribution of fracture force (-); \bar{E}' fracture energy; E'_{50} mean fracture energy; $\sigma^2_{E'}$ variance of the log-normal distribution of fracture energy (-); $\bar{\sigma}_p$ tensile strength (MPa); $\sigma_{p,50}$ mean tensile strength (MPa); $\sigma^2_{\sigma_p}$ variance of the log-normal distribution of tensile strength(-); \bar{k}_p Young's modulus (GPa); $k_{p,50}$ mean Young's modulus (GPa); σ^2_k variance of the log-normal distribution of Young's modulus (-).

Table 17 Fracture characteristics for irregular-particles of sub-bituminous coal PC6-D on SILC.

Irregular single-particles of sub-bituminous coal PC6-D																		
Specimen fracture force (N)			Specimen fracture energy (mj)			Specimen tensile strength (MPa)			Specimen Young's modulus (GPa)			Impact conditions		Specimen dimension: (avg)		Impact velocity (m/s)	Number of spec. tested	DWT size/ energy combinations
\bar{F}_c	$F_{c,50}$	$\sigma_{\bar{F}_c}^2$	\bar{E}'	E'_{50}	$\sigma_{E'}^2$	$\bar{\sigma}_p$	$\sigma_{p,50}$	$\sigma_{\sigma_p}^2$	\bar{k}_p	$k_{p,50}$	σ_k^2	Ball mass (g)	Drop height (mm)	Mass (g)	Height / diam (mm)			
135.56	124.74	0.235	12.24	10.27	0.490	12.8	10.6	0.291	2.68	2.35	0.338	66.78	100	0.061	3.22	1.40	43	PC6-D_63x53_E 0.1
127.95	121.52	0.169	14.10	10.90	0.564	10.4	9.8	0.103	2.14	1.92	0.387	66.78	100	0.064	3.35	1.40	42	PC6-D_63x53_E 0.4
137.88	128.18	0.227	15.51	11.77	0.774	11.2	10.3	0.114	2.32	1.94	0.453	66.78	100	0.062	3.33	1.40	61	PC6-D_22.4x19_E 1.0
134.3	125.1	0.211	14.1	11.0	0.620	11.4	10.1	0.145	2.4	2.1	0.397				3.30		146	PC6-D 3.35mm
223.41	213.92	0.138	25.22	21.95	0.335	9.0	8.5	0.130	2.42	2.34	0.165	66.78	100	0.201	4.76	1.40	39	PC6-D_65x53_E 0.4
227.32	218.40	0.151	29.62	26.83	0.267	8.1	7.4	0.136	2.14	1.76	0.655	66.78	125	0.241	5.11	1.57	35	PC6-D_65x53_E 0.25
216.76	205.65	0.131	28.58	23.58	0.494	7.7	7.3	0.149	2.05	1.81	0.333	66.78	125	0.208	5.06	1.57	30	PC6-D_65x53_E 0.1
204.61	192.65	0.107	27.76	24.55	0.293	7.3	6.8	0.272	1.78	1.48	0.418	66.78	125	0.207	5.15	1.57	31	PC6-D_45x37.5_E 0.25
171.86	166.55	0.128	21.19	17.74	0.598	6.5	6.4	0.115	1.97	1.72	0.415	66.78	125	0.200	4.88	1.57	33	PC6-D_45x37.5_E 1.0
236.26	218.18	0.159	27.07	25.73	0.215	9.1	8.3	0.252	2.49	1.92	0.295	66.78	125	0.205	4.93	1.57	35	PC6-D_31.5x26.5_E 0.25
164.58	154.25	0.115	18.05	16.41	0.419	9.1	8.0	0.209	2.25	1.84	0.593	66.78	125	0.146	4.11	1.57	28	PC6-D_22.4x19_E 1.0
208.1	195.2	0.148	25.5	22.5	0.360	8.1	7.5	0.171	2.2	1.9	0.417				4.86		231	PC6-D 4.75mm
558.33	541.10	0.099	113.43	110.51	0.170	6.1	5.3	0.346	1.89	1.57	0.302	535.25	80	1.348	9.50	1.25	34	PC6-D_63x53_E 0.10
602.06	580.07	0.148	122.66	108.30	0.390	7.2	6.6	0.992	2.08	1.79	0.365	535.25	80	1.351	8.75	1.25	34	PC6-D_63x53_E 0.40
560.21	529.74	0.166	116.92	103.41	0.496	5.0	4.8	0.179	1.85	1.55	0.253	535.25	80	1.475	10.14	1.25	40	PC6-D_63x53_E 0.25
437.63	394.99	0.190	77.24	64.64	0.362	5.8	5.6	0.119	1.92	1.63	0.330	535.25	80	1.125	8.22	1.25	30	PC6-D_45x37.5_E 0.1
571.39	531.99	0.219	122.33	101.95	0.586	6.1	5.6	0.188	1.86	1.60	0.535	535.25	80	1.493	9.28	1.25	37	PC6-D_45x37.5_E 0.25
414.88	396.06	0.183	66.50	55.59	0.460	5.5	5.1	0.233	2.20	1.96	0.279	535.25	80	1.041	8.37	1.25	33	PC6-D_31.5x26.5_E 0.25
528.0	495.6	0.182	104.5	88.7	0.515	5.9	5.5	0.205	2.0	1.7	0.350				9.04		208	PC6-D 9.5mm

Table 18 Fracture characteristics for irregular-particles of sub-bituminous coal PD8-BLA on SILC.

Irregular single-particles of sub-bituminous coal PD8-BLA																		
Specimen fracture force (N)			Specimen fracture energy (mJ)			Specimen tensile strength (MPa)			Specimen Young's modulus (GPa)			Impact conditions		Specimen dimension: (avg)		Impact velocity (m/s)	Number of spec. tested	DWT size/ energy combinations
\bar{F}_c	$F_{c,50}$	$\sigma_{\bar{F}_c}^2$	\bar{E}'	E'_{50}	$\sigma_{\bar{E}'}^2$	$\bar{\sigma}_p$	$\sigma_{p,50}$	$\sigma_{\sigma_p}^2$	\bar{k}_p	$k_{p,50}$	σ_k^2	Ball mass (g)	Drop height (mm)	Mass (g)	Height/diam (mm)			
163.65	159.19	0.107	33.77	25.25	0.963	20.55	18.37	0.311	2.26	1.15	2.018	66.78	125	0.045	2.80	1.57	24	3.35mm_22.4x19_E=2.5
185.47	181.19	0.141	30.15	22.70	0.986	21.09	19.94	0.270	2.86	2.06	1.099	66.78	125	0.048	2.90	1.57	24	3.35mm_22.4x19_E 1.0
155.98	152.37	0.058	22.07	17.71	0.811	12.53	11.74	0.140	2.80	1.74	1.260	66.78	125	0.062	3.39	1.57	26	3.35mm_22.4x19_E 0.25
174.49	167.46	0.131	23.79	18.86	0.646	15.34	13.50	0.274	2.66	1.69	0.932	66.78	125	0.066	3.34	1.57	28	3.35mm_45x37.5_E 0.25
167.46	168.84	0.092	24.82	19.26	0.952	13.84	12.60	0.154	2.26	1.79	0.469	66.78	125	0.062	3.39	1.57	16	3.35mm_45x37.5_E 0.1
<i>169.5</i>	<i>164.1</i>	<i>0.114</i>	<i>26.9</i>	<i>20.5</i>	<i>0.829</i>	<i>16.7</i>	<i>14.7</i>	<i>0.294</i>	<i>2.60</i>	<i>1.69</i>	<i>1.153</i>				<i>3.16</i>		<i>118</i>	<i>3.35mm</i>
250.05	241.55	0.062	55.61	39.78	0.573	10.23	8.73	0.269	1.74	1.27	1.019	535.25	45.5	0.201	5.01	0.94	36	4.75mm_63x53_E 0.25
221.95	218.67	0.076	48.09	39.49	0.740	9.61	9.34	0.226	1.73	1.17	1.127	535.25	45.5	0.159	4.70	0.94	37	4.75mm_45x37.5_E 1.0
242.83	233.06	0.088	58.65	41.25	0.939	8.55	7.72	0.185	1.73	1.05	1.572	535.25	45.5	0.203	5.22	0.94	39	4.75mm_45x37.5_E 0.25
250.08	238.30	0.055	53.05	40.10	0.658	9.44	9.05	0.094	1.75	1.25	0.745	535.25	45.5	0.183	4.95	0.94	40	4.75mm_45x37.5_E 0.1
<i>241.4</i>	<i>231.7</i>	<i>0.068</i>	<i>53.9</i>	<i>39.4</i>	<i>0.693</i>	<i>9.4</i>	<i>8.6</i>	<i>0.182</i>	<i>1.74</i>	<i>1.16</i>	<i>1.052</i>				<i>4.97</i>		<i>152</i>	<i>4.75mm</i>
325.35	315.03	0.083	97.94	77.98	0.608	6.02	5.75	0.106	1.17	0.76	1.218	535.25	80	0.505	7.04	1.25	40	6.7mm_63x53_E 0.4
362.42	354.06	0.102	112.35	85.72	0.643	6.19	5.95	0.164	1.22	0.84	1.052	535.25	80	0.517	7.37	1.25	38	6.7mm_63x53_E 0.25
304.43	297.40	0.066	83.03	62.45	0.591	5.88	5.72	0.128	1.26	0.91	0.894	535.25	80	0.503	6.94	1.25	40	6.7mm_63x53_E 0.1
319.81	304.42	0.114	102.21	78.87	0.635	5.88	5.58	0.179	1.03	0.69	1.162	535.25	80	0.476	7.11	1.25	36	6.7mm_45x37.5_E 0.25
298.66	290.68	0.099	103.32	84.06	0.602	6.16	5.96	0.114	0.84	0.55	1.170	535.25	80	0.453	6.71	1.25	41	6.7mm_45x37.5_E 0.1
<i>321.6</i>	<i>310.5</i>	<i>0.094</i>	<i>99.6</i>	<i>77.2</i>	<i>0.620</i>	<i>6.0</i>	<i>5.8</i>	<i>0.135</i>	<i>1.10</i>	<i>0.74</i>	<i>1.154</i>				<i>7.03</i>		<i>195</i>	<i>6.7mm</i>
438.45	413.06	0.126	172.76	124.92	0.913	5.39	4.53	0.222	1.10	0.65	1.439	535.25	100	1.099	9.02	1.40	41	9.5mm_45x37.5_E 0.25
450.91	440.71	0.064	160.04	122.90	0.700	4.80	4.49	0.141	1.25	0.73	1.633	535.25	100	1.252	9.39	1.40	37	9.5mm_45x37.5_E 0.1
493.48	481.13	0.057	175.99	151.12	0.446	5.93	5.87	0.123	0.99	0.71	0.832	535.25	100	1.060	8.82	1.40	42	9.5mm_63x53_E 0.4
470.25	462.54	0.071	208.72	179.62	0.439	5.13	4.97	0.137	0.74	0.44	1.359	535.25	100	1.122	9.27	1.40	42	9.5mm_63x53_E 0.25
468.68	447.83	0.119	153.62	120.70	0.684	4.88	4.56	0.110	1.23	0.76	0.982	535.25	100	1.308	9.40	1.40	38	9.5mm_63x53_E 0.1
<i>464.7</i>	<i>450.2</i>	<i>0.087</i>	<i>175.0</i>	<i>140.5</i>	<i>0.635</i>	<i>5.2</i>	<i>4.9</i>	<i>0.167</i>	<i>1.05</i>	<i>0.65</i>	<i>1.267</i>				<i>9.18</i>		<i>200</i>	<i>9.5mm</i>

Table 19 Fracture characteristics for irregular-particles of mudstone on SILC.

Irregular single-particles of mudstone																		
Specimen fracture force (N)			Specimen fracture energy (mJ)			Specimen tensile strength (MPa)			Specimen Young's modulus (GPa)			Impact conditions		Specimen dimension: (average)		Impact velocity (m/s)	Number of spec. tested	DWT size/ energy combinations
\bar{F}_c	$F_{c,50}$	$\sigma_{F_c}^2$	\bar{E}'	E'_{50}	$\sigma_{E'}^2$	$\bar{\sigma}_p$	$\sigma_{p,50}$	$\sigma_{\sigma_p}^2$	\bar{k}_p	$k_{p,50}$	σ_k^2	Ball mass (g)	Drop height (mm)	Mass (g)	Height / diam (mm)			
213.77	207.68	0.039	43.09	44.03	0.080	15.8	14.1	0.165	1.13	1.00	0.413	66.78	100	0.105	3.64	1.40	30	Mudstone 45x37.5_E=0.25
274.36	263.24	0.093	53.35	53.12	0.081	9.1	8.5	0.198	1.37	1.03	0.768	66.78	125	0.285	5.30	1.57	46	Mudstone 31.5x26.5_E 1.0
347.69	320.60	0.182	104.18	95.50	0.328	10.8	9.6	0.277	1.12	0.62	0.859	535.25	45.5	0.324	5.46	0.94	40	Mudstone 63x53_E 0.1
377.89	364.03	0.099	122.84	117.12	0.231	11.3	10.4	0.182	1.00	0.66	0.643	535.25	45.5	0.348	5.63	0.94	39	Mudstone 45x37.5_E=1.0
<i>362.6</i>	<i>343.4</i>	<i>0.139</i>	<i>113.4</i>	<i>106.1</i>	<i>0.280</i>	<i>11.0</i>	<i>10.0</i>	<i>0.231</i>	<i>1.06</i>	<i>0.64</i>	<i>0.749</i>				<i>5.54</i>		<i>79</i>	<i>Mudstone 4.75mm</i>
584.70	554.29	0.174	233.08	235.78	0.152	12.7	11.2	0.488	1.17	0.73	1.673	535.25	80	0.824	6.76	1.25	45	Mudstone 45x37.5_E=1.0
513.07	485.15	0.081	221.86	217.05	0.208	10.3	9.2	0.166	0.87	0.53	0.939	535.25	80	0.864	6.92	1.25	52	Mudstone 45x37.5_E=0.25
552.15	493.02	0.145	238.25	230.37	0.139	10.6	9.1	0.254	0.94	0.48	1.532	535.25	80	0.887	7.10	1.25	46	Mudstone 31.5x26.5_E=0.25
492.43	484.21	0.086	220.38	215.92	0.232	11.6	10.2	0.239	0.85	0.51	0.934	535.25	80	0.760	6.47	1.25	40	Mudstone 31.5x26.5_E=1.0
542.87	532.70	0.087	244.45	245.30	0.162	10.7	10.1	0.211	0.79	0.54	0.596	535.25	80	0.904	7.00	1.25	44	Mudstone 63x53_E=0.1
<i>537.3</i>	<i>506.4</i>	<i>0.114</i>	<i>231.5</i>	<i>228.7</i>	<i>0.177</i>	<i>11.1</i>	<i>9.8</i>	<i>0.266</i>	<i>0.92</i>	<i>0.55</i>	<i>1.135</i>				<i>6.85</i>		<i>227</i>	<i>Mudstone 6.7mm</i>
629.62	595.72	0.080	308.52	305.02	0.103	6.8	6.4	0.211	0.61	0.44	0.614	535.25	100	1.833	9.36	1.40	41	Mudstone 63x53_E=0.1
580.17	547.16	0.153	281.36	273.77	0.189	6.3	5.6	0.213	0.64	0.41	0.822	535.25	100	1.940	9.38	1.40	42	Mudstone 31.5x26.5_E=0.25
580.08	536.15	0.190	302.52	318.40	0.098	7.3	6.3	0.199	0.61	0.41	1.374	535.25	100	1.724	8.67	1.40	40	Mudstone 22.4x19.0_E=0.25
581.03	570.12	0.055	290.51	290.94	0.121	6.2	5.8	0.129	0.58	0.43	0.530	535.25	100	2.086	9.46	1.40	45	Mudstone 45x37.5_E=0.25
548.30	506.94	0.166	292.43	286.23	0.134	6.0	5.5	0.200	0.54	0.32	1.255	535.25	100	1.720	9.25	1.40	39	Mudstone 45x37.5_E=0.1
592.70	550.33	0.160	280.67	274.18	0.181	7.0	6.0	0.340	0.70	0.44	1.366	535.25	100	1.788	9.20	1.40	37	Mudstone 45x37.5_E=1.0
<i>585.4</i>	<i>553.2</i>	<i>0.126</i>	<i>292.7</i>	<i>290.6</i>	<i>0.143</i>	<i>6.6</i>	<i>5.9</i>	<i>0.204</i>	<i>0.61</i>	<i>0.41</i>	<i>0.939</i>				<i>9.22</i>		<i>244</i>	<i>Mudstone 9.5mm</i>

Appendix III

MICROLITHOTYPE MATTER

Table 20 Summary of specimens from open cut mine tested for SH hardness in a transect line.

Walloon Coal Measures	Data points	Carbominerite		Vitrite		Clarite	
		SH avg (StDev)	(%)	SH avg (StDev)	(%)	SH avg (StDev)	(%)
PC6-D #M5	29	74.4 (4.9)	24	-	-	86.9 (2.7)	76
PC6-D #M8	25	66.4 (7.1)	40	-	-	84.1 (3.2)	60
PC6-D #M12	22	-	-	-	-	86.6 (2.7)	100
PC6-D #M9	26	-	-	77	4	86.2 (2.7)	96
PC6-D #M10	23	76.3 (2.1)	13	-	-	83.7 (3.7)	87
PC8-WB #M1	25	70	4	-	-	82.6 (3.4)	96
PC8-B #M2	30	63.9 (6.2)	43	-	-	81.9 (3.7)	57
PC8-B #M10	21	72.1 (3.3)	38	-	-	81.8 (2.7)	62
PC8-B #M11	23	73.5 (5.7)	57	-	-	80.6 (1.5)	43
PC8-B #M3	33	70.2 (7.4)	52	71.3 (2.5)	9	82.8 (2.5)	39
PC8-B #M1	22	-	-	-	-	84.5 (3.5)	100
PC8-B #M17	22	71.7 (4.3)	55	-	-	80.7 (1.9)	45

Table 21 Summary of specimens from borehole Gulugula-2 tested for SH in a transect line.

	depth (m)	Data points	Carbominerite		Vitrite		Clarite	
			SH avg (StDev)	(%)	SH avg (StDev)	(%)	SH avg (StDev)	(%)
GG #16	415.5	59	56.7 (5.9)	49	74.3 (3.8)	7	87.6 (3.3)	44
GG #27	unknown	69	-	-	55.7 (10.7)	100	-	-

Table 22 Summary of specimens from borehole Gulugula-2 tested for SH on selected lithotype.

		depth (m)	Carbominerite SH avg (StDev)	Vitrite SH avg (StDev)	Clarite SH avg (StDev)
Juandah Coal Measures	GG #2	138.38			69.3 (7.8)
	GG #4	155.26			72.8 (5.1)
	GG #21	156.67			80.8 (4.4)
	GG #20	157.49			72.6 (5.3)
	GG #22	158.86			76.8 (4.9)
	GG #23	162.60	49.2 (5.1)		
	GG #24	163.53			69.7 (3.5)
	GG #26	165.38			58.8 (7.8)
	GG #5	168.15			77.6 (5.2)
	GG #8	178.82			63.9 (7.2)
	GG #9	207.32	46.1 (3.8)		
	GG #11	226.08		68.2 (5.7)	
	GG #34	280.02			84.6 (2.8)
	GG #12	297.06			68.4 (5.9)
	GG #13	318.60		69.8 (7.3)	75.3 (3.0)
GG #14	337.42			83.8 (3.3)	
GG #15	351.43			85.2 (3.3)	
Taroom Coal Measures	GG #36	404.07			87.7 (4.7)
	GG #18	432.66			91.1 (1.4)
	GG #38	449.33			81.9 (4.3)
	GG #39	486.37			81.9 (5.4)
Unknown depth	GG #3	-	48.0 (4.0)	68.4 (7.5)	
	GG #30	-			82.5 (3.4)
	GG #25	-			74.5 (4.8)
	GG #29	-			84.3 (4.3)
	GG #33	-			85.3 (4.0)
	GG #35	-			83.3 (3.6)
	GG #37	-			85.6 (4.6)

Figure 100 shows a series of photomicrographs of clarite and carbominerite, and their corresponding SH values recorded for other specimens from the open cut mine.

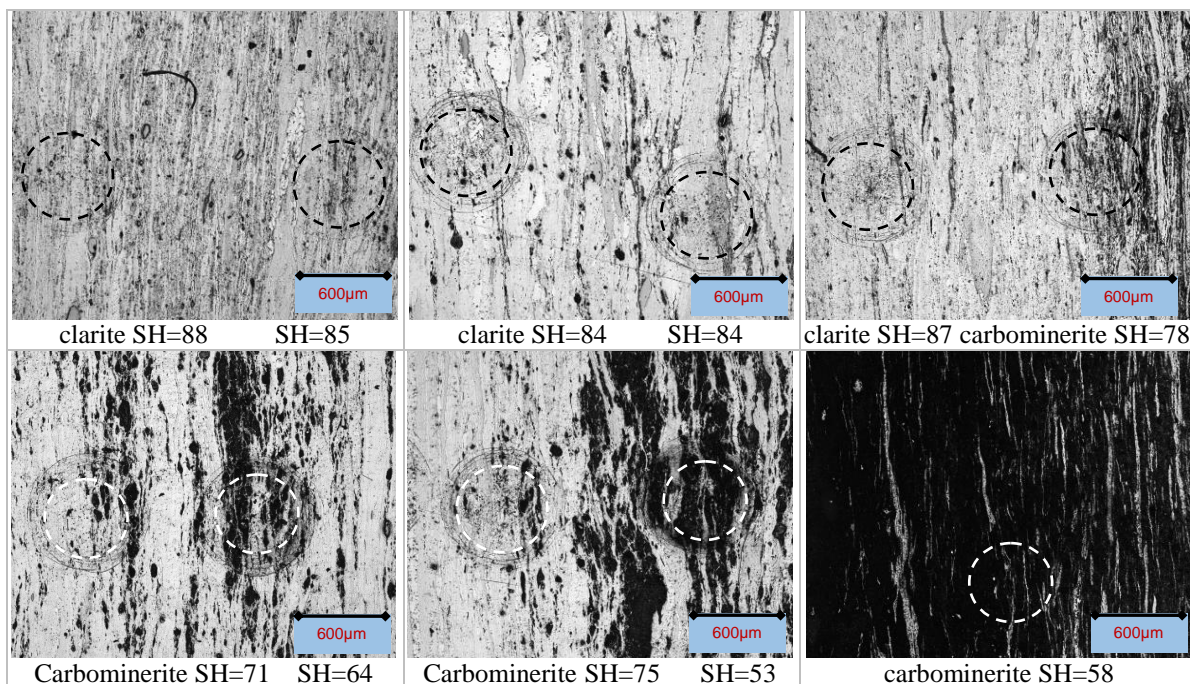


Figure 100 Representative photomicrographs of SH indentation on clarite and carbominerite showing the banding structure for specimens of open cut mine.

Figure 101 shows a series of photomicrographs of vitrite and carbominerite, and their corresponding SH values recorded for other specimens from Guluguba-2.

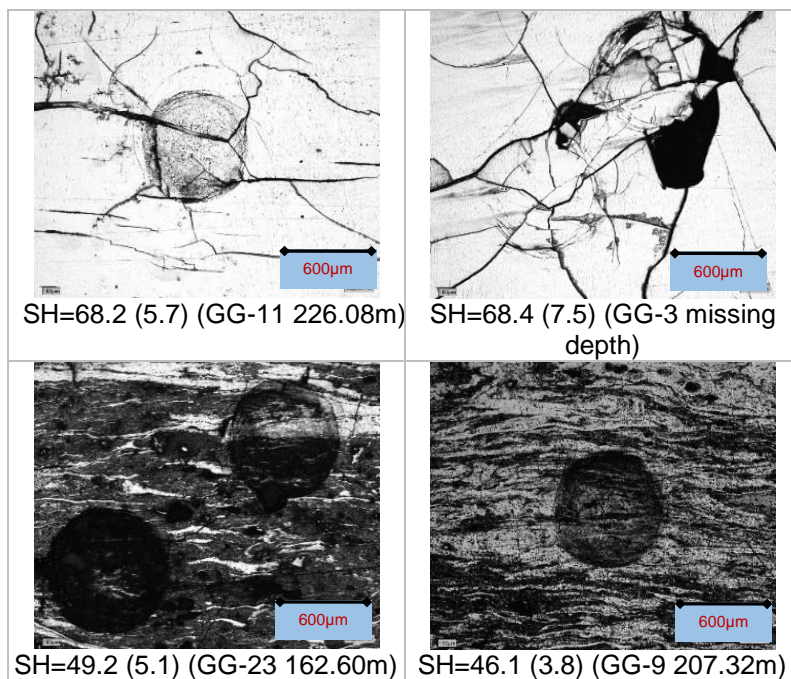


Figure 101 Representative photomicrographs of SH indentation on vitrite and carbominerite showing the banding structure for specimens of Guluguba-2.

Figure 102 shows representative photomicrographs for visualization of clarite with distinct SH values. These results represented a sequence of observations compiled in Figure 97.

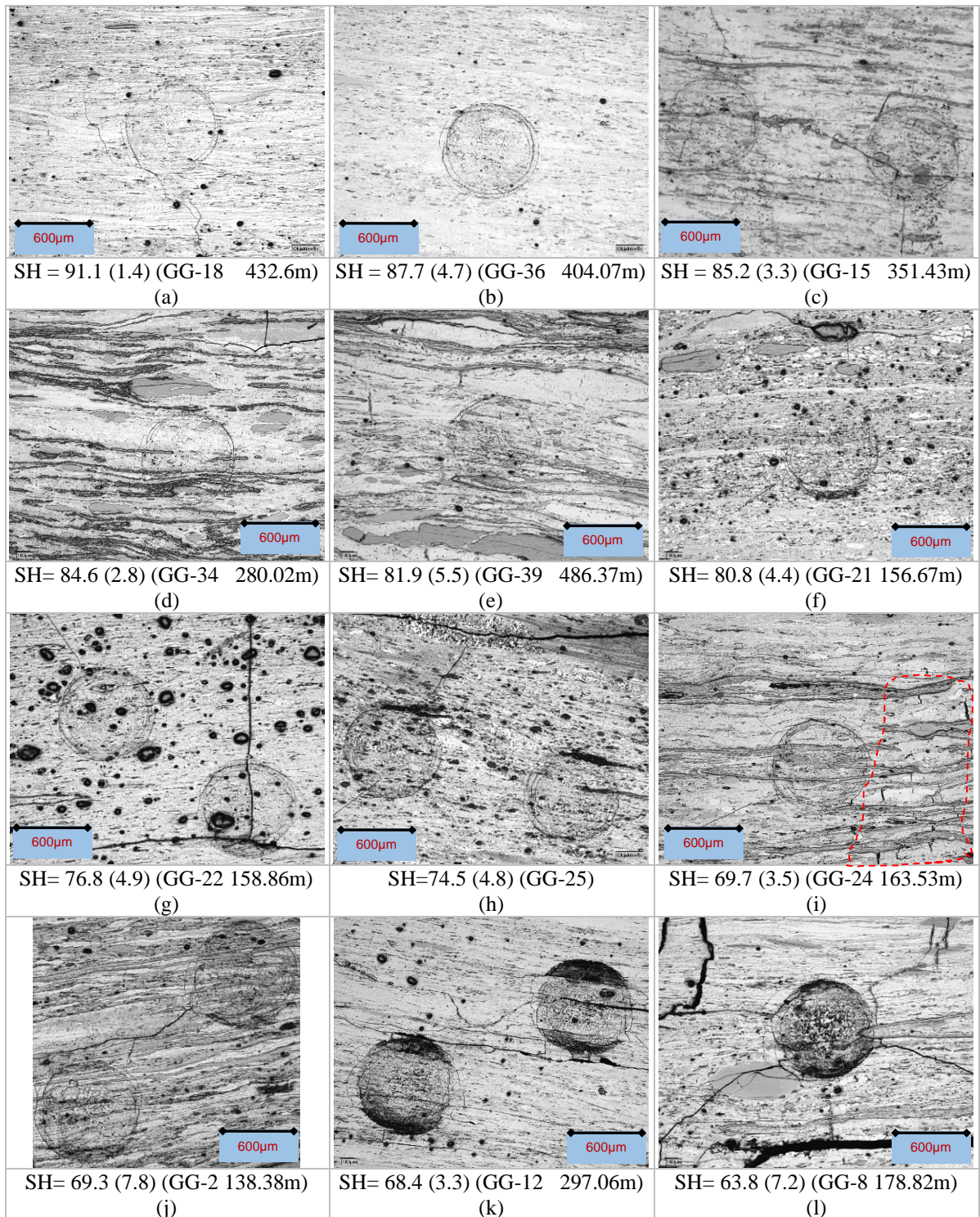


Figure 102 Representative photomicrographs of SH indentation for clarite (average/standard deviation) at Guluguba-2.

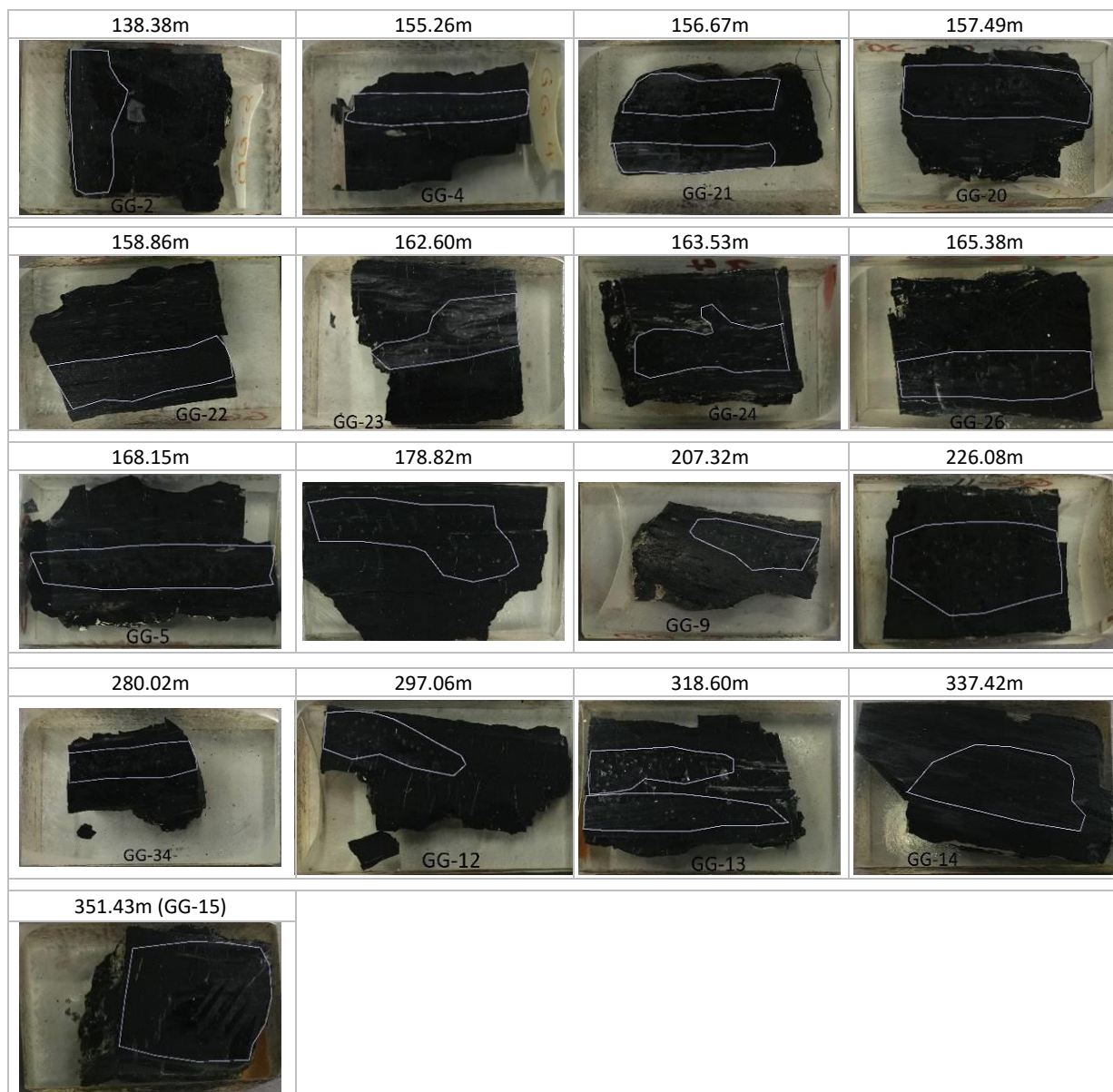


Figure 103 Guluguba-2, Juandah Coal Measures, specimens tested for Shore hardness.

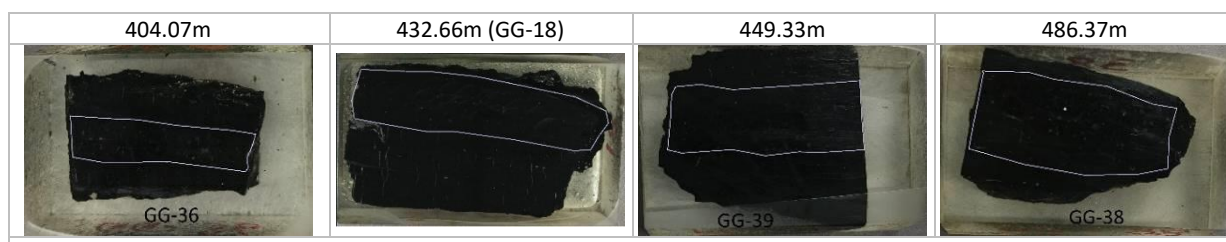


Figure 104 Guluguba-2, Taroom Coal Measures, specimens tested for Shore hardness.

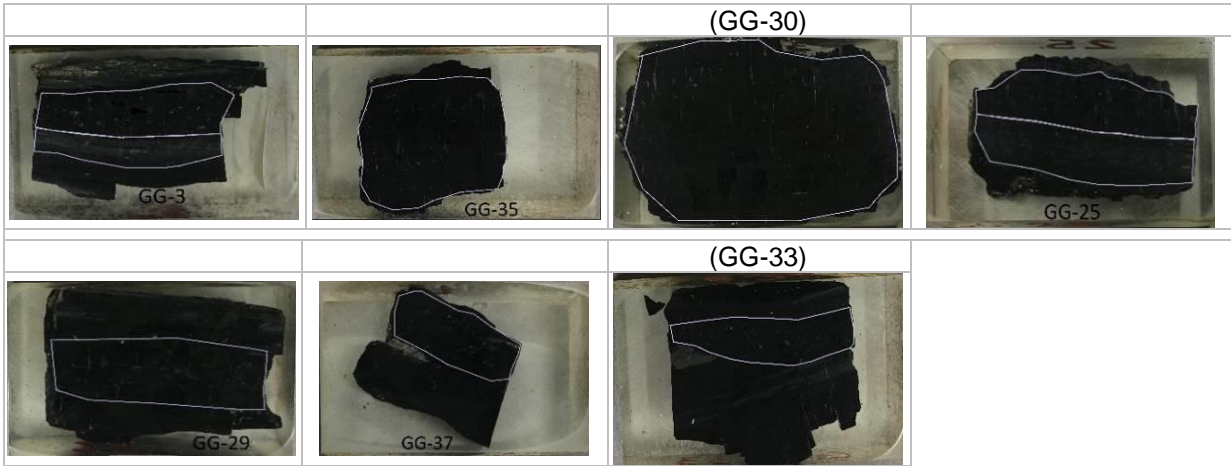


Figure 105 Guluguba-2, unknown depth, coal specimens tested for Shore hardness.